CWP-395
November 2001

Microlocal analysis of wave-equation imaging and generalized-screen propagators

Jérôme H. L. Le Rousseau

— Doctoral Thesis —
Geophysics

Defended October 26, 2001

Committee Chair:	Prof. James McNeil
Advisor:	Prof. Maarten V. de Hoop
Co-advisor:	Prof. John A. Scales
Committee members:	Prof. Gregory Beylkin
	Prof. Paul A. Martin
	Prof. Gary R. Olhoeft
	Prof. Roel Snieder

Center for Wave Phenomena
Colorado School of Mines
Golden, Colorado 80401
(1) 303 273-3557

Abstract

The imaging procedure of reflection seismic data can be generated by an extension of the 'double-square-root equation' to heterogeneous media, which yields the process of wave-equation imaging. We carry a high-frequency analysis of the wave-equation imaging operator and show that it is microlocally equivalent to asymptotic approaches (e.g., Maslov-Kirchhoff/GRT). In an imaging-inversion procedure we characterize the medium with a smooth and a singular part. The singular part essentially represents reflectivity, while the smooth part is used for the computation of wave propagation. For asymptotic schemes such as Maslov-GRT one can create angle common-image-point gathers (ACIG) that represent a redundancy in the data with two angles as parameters: azimuth and scattering angle at the image point. We show that with wave-equation based methods we can also extract those ACIGs via a stationary-phase analysis. It is then possible to exploit such a redundancy for velocity analysis, i.e., invert for the smooth part of the medium.

In wave-equation-based methods the propagator can be represented by a Hamiltonian path integral. Such a path integral accounts for the formation of caustics and coupling between modes. The main problem with path integrals is the computational complexity of their numerical evaluation. We have developed a method that reduces the computational complexity of such evaluation, at the cost of adjusting the shape of wave fronts. The result is an algorithm that, for each propagation step, is built from a multiplication, a forward Fourier transform, a multiplication, and an inverse Fourier transform, where the transform is in the horizontal directions and may be windowed. Since this algorithmic structure coincides with that of the classical phase-screen propagator, we denote our approximations as generalized screens (GS). We have designed a hierarchy of approximations of increasing accuracy. First developed for acoustic media we have extended the GS approach to elastic media, in which, the continuous coupling between P and S waves is honored. We show various modeling examples as well as imaging results for field data and illustrate the prediction of multipathing in complex structures. We compare the GS approach with other wave-equation and asymptotic schemes. Those results demonstrate the accuracy of the GS method for the modeling and imaging of seismic data in complex geologic structures.

Pour ma famille

Table of Contents

Acknowledgments

First, I would like to express my sincere gratitude to Prof. Maarten V. de Hoop who has advised my thesis research work at the Center for Wave Phenomena (CWP). His encouragement and interest has been a great source of motivation for me; I admire his mathematical and physical intuitions. Learning microlocal analysis was a long process; Martijn has always been very supportive even when I was not productive and would spend most of my time reading and learning. I also want to thank him for giving me opportunities to gain teaching experience, especially within the framework of our microlocal-group seminar.

I would like to express my sincere appreciation to Total Fina Elf for the partial financial support of this research. I want to especially thank Dr. Henri Calandra for providing this support, giving me access to the computation facilities of Total Fina Elf in Pau, France, for his help in processing the L7D data set, and for many suggestions and ideas on migration and inversion. He also provided the Kirchhoff results of Chapter 6.

I also want to thank CWP at the Colorado School of Mines (CSM) for partially supporting me. This work was also supported by the members of the Consortium Project on Seismic Inverse Methods for Complex Structures at CWP, CSM.

I want to extend my thanks to my thesis committee members for their valuable comments: Prof. John A. Scales, who also served as my co-advisor, Prof. Roel Snieder, and Prof. Gary R. Olhoeft, all of the Geophysics department at CSM; Prof. Paul A. Martin of the Mathematics department at CSM –in particular, for his valuable comments on Chapter 7; Prof. Gregory Beylkin of the Applied Mathematics department at the University of Colorado at Boulder; and Prof. James McNeil of the Physics department at CSM. I also want to thank Prof. Ilya Tsvankin for his comments on generalized screens in anisotropic media (Chapter 5) and Prof. Ken Larner for numerous discussions and comments –and for the (red) corrections that made the various chapters (and papers) of this thesis much more readable.

My very special thanks go to Dr. Günther Hörmann of the Institute for Mathematics at the University of Vienna, Austria. Günther visited CWP for an extensive period of time and co-led the microlocal group at CWP. As a collegue and a friend he has greatly influenced my learning of mathematics and has been a great source of inspiration for me.

I particularly wish to thank the student members of the microlocal group led by Martijn de Hoop: Alison Malcolm and Dr. Sverre Brandsberg-Dahl. Working with and around them has always been rewarding and stimulating. I want to thank all my fellow students at CWP for their support and friendship during these years at CSM, in particular Alexander Gret –for the running therapy also–, Petr Jílek, Matt Haney, Albena Mateeva, Kasper van Wijk –for all the non-academic new skills he's also taught me–, Alberto Villarreal –for teaching me parallel computing–, and Brian Zadler. I also want to thank Dr. Lydia H. Deng who was always available to help me when I first arrived in CWP, and Dr. Edward Jenner for

his help on processing my very first pre-stack dataset, the 2D Marmousi model. I want to thank John W. Stockwell, Jr. for his dedication to CWP students and his great help in writing 'SU-style' codes.

Thanks to Sara Summers and the staff members of CWP, Jo Ann Fink, Barbara McLenon, Michelle Szobody, and Lela Webber who have been very supportive and helpful.

Finally, I would like to thank Dr. Sverre Brandsberg-Dahl for letting me use his lens model and the dataset which was generated by Dr. Ketil Hokstad (Chapter 2); BP Amoco for letting me use their VTI Valhall model (Chapter 5); Alberto Villarreal (CWP, CSM) for the use of his elastic finite-difference code in anisotropic media; and Total Fina Elf for letting me use their L7D 3D marine dataset.

Chapter 1

Introduction

The key component in the modeling, imaging, and inversion of reflection seismic data is accurate computation of wave propagation, in particular, propagation between seismic sources, subsurface scattering points, and receivers. For asymptotic methods (e.g., Maslov-Kirchhoff) the handling of caustics has to be done explicitly (De Hoop & Brandsberg-Dahl, 2000). Difficulties arise if caustics and pseudocaustics (i.e., caustics in the slowness variables) are closely spaced. In addition the continuous coupling between P and S waves can not be honored. We propose alternative approaches to cure those shortcomings.

A scattering theory that follows the ray picture but accounts for full-wave behavior has been developed by De Hoop (1996). The method consists of three main steps: (i) *decomposition* of the field into two constituents, upward or downward *propagation* along a preferred direction (here vertical), (ii) computation of the interaction (*coupling*) of the counter-propagating constituents, and (iii) *re-composition* of the constituents into observables at the positions of interest. Such a method is based on an extension of the Bremmer coupling series to multi-dimensionally varying media. Bremmer's method decomposes the wavefield into a recursion of one-way propagations and up-down reflections-transmissions. The one-way operators propagate waves in the preferred vertical direction and account for scattering in the transverse direction while reflection-transmission operators account for scattering in the vertical direction. Thus, the method first generates a wavefield dominated by downward propagation, then generates a 'first' upward propagating wavefield, then a 'second' downward propagating field, etc. In this manner, multiple reflections are accounted for in a controlled manner. We therefore distinguish two classes of multiple scattering: one in which the multiples are identified with respect to the projection of their propagation paths onto the *vertical* direction (depth), and one where the multiples are identified with respect to the projection of their propagation paths onto the *horizontal* plane. In the asymptotic framework of wavefront analysis, paths are rays. The *first* class of multiple scattering is associated with 'turning rays' and 'internal multiples' as well as 'surface multiples', the *second*, possibly combined with the first class of multiple scattering, is associated with 'multipathing'.

The Bremmer series in acoustic media have already found application in Van Stralen *et al.* (1998), where the one-way wave operator is approximated with an accurate optimal finite-difference algorithm based on a rational expansion, as opposed to the generalized-screen expansion by Le Rousseau and De Hoop (2001b).

The propagator in the generation of this series is based on a Hamiltonian path-integral representation (De Witte-Morette *et al.*, 1979; Fishman & McCoy, 1984a; Fishman & Mc-

Coy, 1984b). By summing over all possible path such a representation accounts for not only the energy traveling along the stationary paths (rays) but also for the transport along non-stationary paths. These path integrals reveal any possible multipathing. The path integral generalizes Gazdag's phase-shift migration operator (Gazdag, 1978). In Gazdag's method, wavefield continuation is achieved through a phase multiplier (forward lateral Fourier transform - phase multiplication - inverse Fourier transform) that emphasizes vertical propagation. While this method is valid in laterally homogeneous background media, it has to be generalized if the medium is laterally heterogeneous. In particular, we replace it by our path integral. A realization of the Hamiltonian path integral is made possible by the Trotter product formula: Integrations in phase space are performed rather than on the space of all paths. They correspond to the extrapolation of the wavefield in depth. The Trotter representation is characterized by a limiting process with the number of extrapolation steps going to infinity and the step size going to zero. In this limiting process every path is taken into account. We describe the Trotter product formula by means of microlocal analysis[1], essentially with the aid of pseudodifferential and Fourier integral operators (Hörmander, 1985a; Hörmander, 1985b; Duistermaat, 1996). Asymptotic-ray description of propagating waves follows from the Trotter product formula by a stationary phase analysis. Such analysis yields a common ground for inversion and velocity analysis for asymptotic methods, e.g., 'Maslov-GRT' (De Hoop & Brandsberg-Dahl, 2000) and wave-based methods, 'Trotter-Bremmer'.

The problem with the path integrals is the computational complexity of their numerical evaluation. To propagate waves across a thin slab one has to perform a Fourier transform of the wavefield in the horizontal directions, a phase shift and an inverse Fourier transform. The phase shift is a function of both the space variables (input and output points) and phase variables (wavenumber). The sequence of operations has therefore to be performed for every output point at the next depth level (and every wavenumber if there is dependency on the input point) which yields a high computational complexity. De Hoop *et al.* (2000) (Chapter 3) and Le Rousseau and De Hoop (2001b) (Chapter 4) have developed a method that dramatically reduces the computational complexity of such evaluation, at the cost of departing from the exact shape of wavefronts. The result is an algorithm that, for each propagation step, is built from the sequence: (several) forward Fourier transform(s), multiplication, inverse Fourier transform, multiplication –where the transform is in the horizontal directions and may be windowed. Since this algorithmic structure coincides with that of the classical phase-screen propagator, we denote our approximations as generalized screens (GS). To achieve such a structure, the phase shift is expanded in a series that separates space and phase dependencies. The series expansion constitutes the GS expansion. Truncating the GS expansion at increasing orders yields a hierarchy of increasingly accurate approximations. The number of forward (fast) Fourier transforms in the algorithm depends on the number of terms used in the GS expansion but does *not* depend on the number of nodes in the horizontal direction for which the wavefield is computed. Underlying these

[1]For a review of the fundamental concepts and tools of microlocal analysis see Appendix A. In short, microlocal analysis is the study of the wave front sets of distributions.

approximations of the exact phase-shift is an expansion of the medium wave-speed model simultaneously into smoothness and magnitude of variation with respect to a background medium.

The original phase-screen method was designed for multiple forward scattering of waves. It included phenomena such as focusing and defocusing. The applicability of the phase-screen method generally requires that the screen interval satisfies the following criteria: small medium variations (weak scattering), laterally smooth medium variations (narrow-angle scattering), and even smoother variations in the preferred direction (negligible back-scattering). With the GS approach, we access the accuracy of the phase-screen method, and extend it to larger-contrast, wider-angle, and back-scattering. Our approach accounts for the multiple scattering through the generalized Bremmer series (De Hoop, 1996; Van Stralen *et al.*, 1998; Le Rousseau & De Hoop, 2001b), and accounts for multipathing through the GS propagation (De Hoop *et al.*, 2000; Le Rousseau & De Hoop, 2001b).

1.1 Microlocal analysis of the Trotter product formula

The framework of wave-equation imaging with the so-called double-square-root equation is presented in Chapter 2. With the aid of the Trotter product formula, one can generate a realization of the Hamiltonian-path integral representation of the Green's function associated with the one-way (or single-square root) wave equation. (Such a one-way wave equation is obtained by a directional wavefield decomposition that separates up- from down-going waves.) In this approach the wavefield is extrapolated from one depth to the next, in a number of steps increasing to infinity (and the size of the steps going to zero). This limiting process shows how every path between the input and output points is taken into account in the evaluation of the extrapolated wavefield. We interpret each extrapolation step as the action of a Fourier integral operator [see Hörmander (1985b) and Duistermaat (1996) and Appendix A] on the wavefield. The Trotter product formula representation is then the composition (i.e., the cascade) of those. Fourier integral operators can be used to solve wave equations. They offer the proper tools to follow the propagation of singularities of the data (initial/boundary conditions) into the wavefield (see Appendix A). This interpretation thus enables us to analyze the propagation of singularities. We show, via stationary-phase analysis, that the Trotter product formula representation and the asymptotic approach (e.g., Maslov canonical operator) coincide on the wave front set of the wavefield, i.e., that the first one yields a Fourier integral operator, and that its amplitude satisfies the proper transport equation. The stationary phase analysis also reveals a Hamiltonian-like system with depth rather than travel-time as a parameter. Away from so-called turning rays, we show the Hamiltonian flows associated with the Trotter product formula representation and with the asymptotic method to be equivalent.

The double-square-root equation (Claerbout, 1986) generates the wave-equation seismic imaging procedure. In particular, we show that the (Maslov-)Kirchhoff and the wave-equation imaging procedures are microlocally compatible and hence should yield the *same* result on the singular support of the image, i.e., the reflectors. We design a wave-equation imaging scheme honoring the redundancy in the data with two angles as parameters: az-

imuth and scattering angle at the image point [i.e., the characteristic strips in the wavefront set of seismic data (Stolk & De Hoop, 2000)]. Thus we can generate *scattering-angle/azimuth common image point gathers* (ACIGs) of the type introduced in Kirchhoff-style imaging procedures (Brandsberg-Dahl *et al.*, 2000). ACIGs are used for amplitude inversion as well as in tomography (De Hoop *et al.*, 2001b; Brandsberg-Dahl *et al.*, 2001). We show numerical examples of those common image-point gathers.

1.2 Generalized-screen propagator

In Chapter 3, we present the foundations of the GS approximation for scalar wave scattering. The scattering is first subjected to directional decomposition, which consists of three main steps: (i) decomposing the field into two constituents, those propagating upward and downward along the vertical direction, (ii) computing the interaction of the counter-propagating constituents, and (iii) re-composing the constituents into observable quantities at the positions of interest. Decomposition is beneficial because it leads to computationally efficient algorithms for the scattering of waves, and it can be used to separate different propagation phenomena, which is of importance, for example, in the interpretation and inversion of seismic data.

The directional wavefield-decomposition procedure generates a system of coupled one-way wave equations. The one-way wave equations account for transverse left-right scattering. The two one-way wave equations are coupled by the reflection/transmission operators that account for vertical up-down scattering. The solution of those one way wave equations can be represented with the Trotter product formula. The Hamiltonian in the phase of the propagator is the vertical wave slowness (vertical wavenumber divided by frequency) symbol[2] which depends both on (lateral) phase and (lateral) space coordinates. For laterally homogeneous media the space dependency vanishes, which yields a fast algorithm for the numerical evaluation [Gazdag phase-shift operator (Gazdag, 1978)]. However, in laterally heterogeneous media, such an approach yields a tremendously large computational complexity. For each depth extrapolation the computation of the wavefield at each output point requires a forward Fourier transform, a phase multiplication, and a inverse Fourier transform. Our aim is to significantly reduce the complexity to that of a small number of Fourier transforms and phase multiplications. Nonetheless, we want to preserve the shape of the wave front as much as we can, i.e., preserve the microlocal properties of the propagator.

To achieve such a simplification, we separate the phase and space dependencies of the *vertical slowness symbol*, which appear in the phase of the exact wave propagator. This is achieved by a (polyhomogeneous) expansion of the symbol with respect to a background and perturbation medium (the two combine to form the exact medium) which constitutes the GS expansion. The vertical slowness symbol is responsible for the transverse scattering. Subjecting the vertical slowness symbol to the separation of phase-space coordinates thus induces an adjustment of wave theory and scattering, yielding deformations of the wavefront

[2]See Appendix A for a definition of *symbols*.. A symbol represents the action of an operator in the Fourier domain.

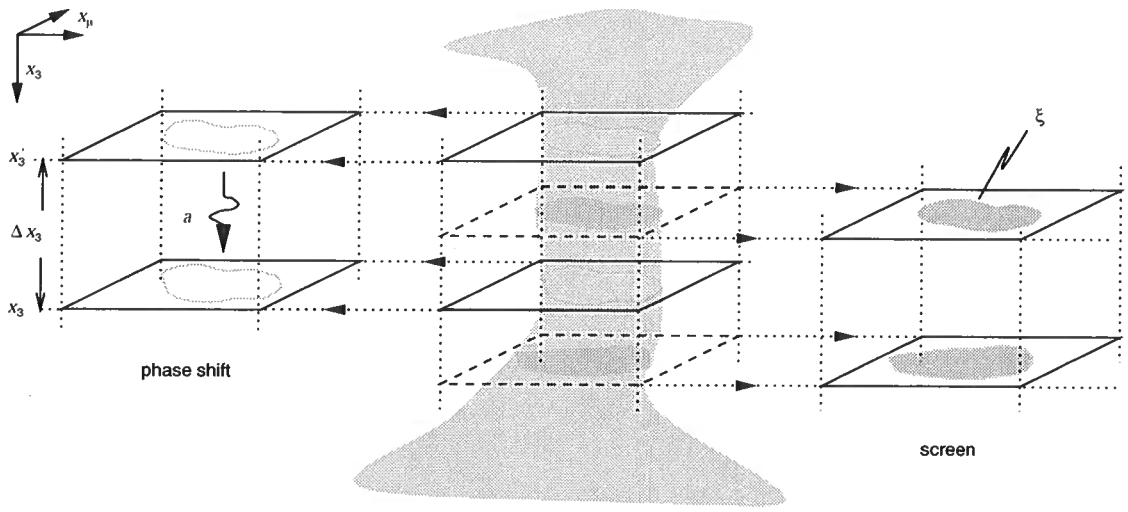

Figure 1.1. The screen representation for one-way propagation in a laterally heterogeneous medium. Δx_3 is the vertical extrapolation step, a is the generalized phase shift, i.e., the term that depends on the wave number in the GS expansion, while ξ is the generalized screen, i.e., the term that depends on the spatial coordinates in the GS expansion. The shaded area represents a high wave-speed zone, e.g., a salt structure.

shapes. In doing so we have designed a hierarchy of approximations of increasing accuracy. Here, the preferred direction of propagation is vertical. Hence, we impose maximum accuracy at vertical propagation while the errors at larger propagation angle decrease with the increasing number of terms used in the GS expansion. We can view the action of the screen propagator as a propagation in the background medium, first corrected for accuracy at vertical propagation (split-step Fourier) and then further corrected by passing the wavefield through the screens of the various order terms in the GS expansion representing the lateral variations in the wave speed (see Figure 1.1).

In Chapter 3, we also introduce the Bremmer coupling series, which allow coupling of the up-going and the down-going fields through the reflection and transmission operators. Again, to simplify their numerical evaluation we derive a GS-like approximation of those operators.

1.3 Algorithms based on scalar generalized screens

In Chapter 4, we first present the GS representation of the thin-slab propagator and cast that result into numerical algorithms that we apply to modeling and imaging.

In the GS framework, for each depth level we distinguish a constant background medium from a rapidly fluctuating contrast. The GS expansion of the vertical slowness

symbol yields a hierarchy of $\mathcal{O}(N \log N)$ algorithms. Here, N is the number of nodes in the horizontal directions, where the wavefield is measured and continued. A key issue in developing the algorithms is that of unitarity: By expanding the exponential of the phase function in the propagator, $\exp[\mathrm{i}\phi] \simeq 1 + \mathrm{i}\phi$, we destroy the unitarity of the exact propagator. The cascade of successive (depth) extrapolations then yields errors in the amplitudes by boosting some amplitudes, usually those associated with wide-angle propagation. We have to re-enforce unitarity of the propagator after having built a fast algorithm. Other issues such as the presence of branch points for the numerical evaluation of the GS propagator are addressed in Chapter 4.

Our accuracy analysis is carried out primarily by modeling. We analyze the migration operator before stacking, which is conventionally performed in the process of imaging. We focus on multipathing and 'second'-arrival energy. Because a proper treatment of such phenomena is the key to imaging in complex regions. We analyze the accuracy of the GS method in complex structures using synthetic models that exhibit significant multipathing: the IFP (Institut Français du Pétrole) two-dimensional (2D) Marmousi model and the SEG-EAGE 3D salt model. These two models represent two fundamentally different geological situations. In the Marmousi model, complexity arises from faulting and tectonic deformation in a sedimentary region. In the SEG-EAGE 3D salt model, it arises from the intrusion of a salt body the wave speed of which is significantly higher than that in the surrounding formations. These models commonly yield poor imaging below these complex structures. With the help of the GS propagator, which we prove to be accurate in these situations, we illustrate that the origin of this problem is possibly associated with multipathing. We illustrate the modeling capacity of the GS method both in 2D and 3D. We compare the GS method with some of its competitive algorithms. All these algorithms account up to a certain degree for multipathing: one-way (split-step Fourier, Phase-Shift-Plus-Interpolation method (PSPI)), two-way (finite differences). For completeness, we also show some prestack depth migration results in 2D for the Marmousi model. We apply the GS migration-imaging algorithms to field data in Chapter 6.

1.4 Extension of the scalar formulation of generalized-screen methods to TI media

In Chapter 5 we extend the scalar GS algorithm developed for P waves in isotropic fluid media (Le Rousseau & De Hoop, 2001b) (Chapter 4) to quasi-P (qP) waves in transversely isotropic (TI) media with a vertical axis of symmetry. In this way, S waves are ignored, but the wave front *shapes* are properly approximated. To preserve the structure of the isotropic GS algorithm, we employ the *rational* approximation of the dispersion relation for qP waves in TI media by Schoenberg and De Hoop (2000). In this approximation, we match the values, slopes and curvatures for the slowness at vertical and grazing incidence.

We carry out an accuracy analysis of our discretized approximations in the BP-Amoco Valhall model (Brandsberg-Dahl *et al.*, 1999; Thomsen *et al.*, 1997). We also investigate the impact of the approximation of Schoenberg and De Hoop (2000) on the polarization vector associated with the qP waves.

1.5 3D case study

To further test the GS approach to wave propagation we apply the associated imaging operator (cf., Chapter 2) to field data. We use TotalFinaElf's L7D data set and velocity model. The main feature of this 3D marine data set from the North Sea is the presence of an intrusive salt body in a surrounding sedimentary sequence. Subsequent tectonic events created faults at various depths that we hope to identify in the imaging process. The salt body yields large lateral wave-speed variations, which makes the imaging procedure challenging for Fourier-transform based wave-extrapolation methods (Stolt, 1978; Gazdag & Sguazzero, 1984; Stoffa *et al.*, 1990). Such a data set therefore seems adequate for the testing of the GS propagator for depth imaging. We first illustrate the post-stack migration performance, showing the extent to which such processing fails to account for multipathing. We illustrate this aspect further by exhibiting isochrones in a 2D section of the the SEG/EAGE salt model. Not taking multipathing into account in such complex regions usually yields poor imaging. We also illustrate the importance of multiple scattering. For 3D pre-stack imaging, we make use of a common-azimuth approximation (see Biondi and Palacharla (1996) and Appendix D) which is motivated by the marine acquisition geometry used for the L7D data set. We compare the accuracy of the GS propagator and a hybrid PSPI/split-step Fourier propagator. Those results confirm that pre-stack imaging in complex regions requires multipathing and that the GS approximations predict such a multipathing accurately. To illustrate that wave-equation imaging is microlocally equivalent to Kirchhoff/GRT imaging-inversion (De Hoop *et al.*, 2001a) (Chapter 2) we compare our GS results with those with a Kirchhoff approach.

1.6 Generalized-screen approximation for elastic waves

In actuality, the propagation of waves takes place in an elastic subsurface. In a strongly heterogeneous subsurface, the scattering leads not only to multipathing but also to *multi-mode* propagation along each path: the qP wave is continuously coupled to qS waves. In its simplest manifestation, the qP arrivals may have partly traveled through the subsurface as qS. It is not difficult to obtain such a path through a salt structure, with application to imaging below salt. In Chapter 7, I present the foundation of the GS approximation for *vector* wave scattering and the resulting algorithm for propagating elastic waves.

To arrive at an efficient screen algorithm that is multipathed and multi-mode, we need to find a *vectorial* vertical slowness (square-root Hamiltonian) to replace the scalar one. In a derivation of this kind, we have to keep in mind that, due to horizontal heterogeneity, in a full-wave formulation we cannot separate the different modes of propagation, though in the high-frequency approximation this separation is implied. We make use of the elastic wave-field decomposition procedure of De Hoop and De Hoop (1994) as a point of departure. With the one-way elastic wave equation at hand, we can represent the solution with a Hamiltonian path integral, and as in the acoustic case use the Trotter product formula to obtain a realization of the path integral. The path integral representation accounts for all possible paths and therefore accounts for multipathing and the continuous mode coupling.

To obtain a proper GS representation we make the choice of using the *right symbol* of the vertical slowness operator. Other possible choices are discussed.

To decrease the computational complexity of the propagator we expand the vertical slowness symbol in terms of a background and a perturbation medium, which yields a separation of the space phase dependencies of the symbol. Here we manipulate matrices of symbols rather than scalar symbols as was done in the acoustic case. Non-commutativity issues for symbol matrices yield a more involved analysis than in the scalar case. By diagonalizing the vertical slowness symbol, we exhibit the pseudodifferential operator that allows us to separate P and S waves. We discuss the possibility of expanding the phase-shift exponential with the vertical slowness symbol in either its non-diagonal or diagonal form. We show that the expansion in the diagonal form yields more accurate approximations. We also introduce the use of two different background media to prevent the introduction of artificial branch points in the propagating-wave regime. Those choices yield a particular structure for the elastic GS propagator that we describe extensively. The resulting propagator is an extension and generalization of Wu's complex screen method (Wu, 1994). As in the acoustic case, the GS method stays close to the path-integral representation for wave propagation, so multipathing and continuous mode coupling are naturally taken into account.

We show numerical results of the behavior of the elastic GS propagator and the continuous P-S mode coupling in particular.

1.7 Notice

This thesis is a collection of papers that were written to be published independently. They are collected here as chapters. At the beginning of each chapter, we indicate the journal to which it has been submitted or in which it has been published. Those articles are self-contained. For this reason, some sections are duplicated. The duplicated material throughout the thesis is as follows: The directional wavefield decomposition procedure can be found in Sections 2.3 and 3.3 in the acoustic case; the Trotter-product representation of the one-way wave propagator can be found in Sections 2.4, 3.4, and 7.4; Sections 3.6 also has much in common with Sections 7.5 and 7.6.

Those journal articles (De Hoop *et al.*, 2001a; De Hoop *et al.*, 2000; Le Rousseau & De Hoop, 2001b; Le Rousseau & De Hoop, 2001c; Le Rousseau & De Hoop, 2001a) have various coauthors. While the author has made major contributions to those articles, he acknowledges their contributions here.

Chapter 2

Symplectic structure of wave-equation imaging: A path-integral approach based on the double-square-root equation[1]

2.1 Summary

We carry out high-frequency analyses of Claerbout's double-square-root equation and its (numerical) solution procedures in *heterogeneous* media. We show that the double-square-root equation generates the adjoint of the single-scattering modeling operator upon substituting the leading term of the generalized Bremmer series for the background Green's function. This adjoint operator yields the process of 'wave-equation' imaging. We finally decompose the wave-equation imaging process into *common image point gathers* in accordance with the characteristic strips in the wavefront set of the data.

2.2 Introduction

Directional wavefield decomposition is a tool for analyzing and computing the propagation of waves in configurations with a certain global directionality, such as waveguiding structures. The method consists of three main steps: (i) *decomposing* the field into two constituents, and *propagating* them upward or downward along a principal or preferred direction, (ii) computing the interaction (*coupling*) of the counterpropagating constituents and (iii) *recomposing* the constituents into observables at the positions of interest. (The preferred direction is 'vertical' whereas the directions orthogonal to the preferred direction are referred to as the 'lateral' directions.) The method allows one to 'trace' wave constituents in a global coordinate system in a given medium, and thus distinguish constituents that have been scattered along the up/down direction a different number of times. It also allows the separation of head waves from body waves. The (generalized) Bremmer series superimposes all the constituents ('multiples') to recover the full, original wavefield (De Hoop, 1996).

In the framework of remote sensing and inverse scattering, tracing waves helps in the interpretation and separation of constituents prior to the inversion of the observed wavefield (De Hoop, 1998). Directional decomposition maps the 'two-way' wavefield into constituents that satisfy a coupled system of 'one-way' wave or 'single-square-root' equations. In large-scale configurations in which the coupling is weak, wavefield computations

[1]This chapter as been submitted to *Geophysical Journal International* with M.V. de Hoop and B. Biondi.

can be restricted to a single one-way constituent. In the fields of ocean acoustics (Tappert, 1977; Collins, 1989), seismics (Claerbout, 1970), and integrated optics (Hadley, 1992), this observation has been exploited extensively; for a more complete list of references in this matter, we refer the reader to Van Stralen *et al.* (1998). The decomposition procedure is applied in an assumed computational embedding.

The double-square-root equation (Claerbout, 1986) generates the wave-equation seismic imaging procedure. In particular, we show that (Maslov-)Kirchhoff and wave-equation imaging procedures are microlocally compatible and hence should yield the *same* result on the singular support of the image. We design a wave-equation imaging scheme honoring the characteristic strips in the wavefront set of seismic data (Stolk & De Hoop, 2000), i.e., the redundancy in the data with two angles as parameters: azimuth and scattering angle at the image point. Thus we can generate *scattering-angle/azimuth common image point gathers* (ACIGs) of the type introduced in Kirchhoff-style imaging procedures (Brandsberg-Dahl *et al.*, 2000). ACIGs are used for amplitude inversion as well as in tomography (De Hoop *et al.*, 2001b; Brandsberg-Dahl *et al.*, 2001).

The exact decomposition procedure is summarized in Section 2.3. In Section 2.4 we analyze the one-way wave ('single-square-root') equation. We introduce a sequence of approximate representations of the one-way propagator which in a certain limit converges to the 'true' one. Each member of the sequence corresponds to a finite cascade of thin-slab propagators. We investigate the propagation of singularities by individual members of the sequence and discover a condition for the proper treatment of caustics. We show that the limit of the sequence propagates singularities precisely in accordance with ray theory. The one-way theory is invoked to develop a (sequence of) imaging operator(s) (Section 2.5). Such an operator follows from an optimization approach to inverse scattering based on the reciprocity theorem of time-correlation type (De Hoop & De Hoop, 2000). The one-way propagator is applied to the source excitation and the measurement traces simultaneously. In fact, the imaging operator kernel solves Claerbout's (1986) 'double-square-root' equation in smoothly varying media [see also Clayton (1978) and Popovici (1996)] and hence extends the usual constant media analyses. We analyze the symplectic structure of the imaging kernel and extract a procedure to generate common-image-point angles gathers (ACIGs). To interpret such gathers, in Section 2.6, we develop a method based upon microlocalization to estimate the normal direction to the isochrones. A numerical example is shown in Section 2.7. ACIGs are the input to seismic amplitude inversion and (residual) velocity analysis. With the tools developed in the main text, we assess in Appendix D the extent to which the reduction to the computationally efficient 'common azimuth continuation' approach (Biondi & Palacharla, 1996) can be applied.

If the medium of the configuration were laterally homogeneous, the directional decomposition becomes an algebraic operation in the lateral Fourier or wavenumber domain [see, e.g., Kennett (1985)]. In such a medium, the phase-shift method (Gazdag & Sguazzero, 1984) is amongst the fastest (and accurate) one-way algorithms. In this method, in the lateral wavenumber domain, the phase shift is simply proportional to the vertical wavenumber; the vertical and lateral wavenumbers are connected through an algebraic dispersion relation. As soon as the medium becomes laterally heterogeneous, it still is advantageous to carry out

the analysis in the lateral wavenumber domain, but without leaving the lateral space domain – an observation well established in the field of microlocal analysis [see, e.g., Treves (1980a; 1980b)] and applied by Fishman and McCoy (1984a). The lateral space-wavenumber domain constitutes the (lateral) phase space. Through the Fourier transforms, the space and wavenumber domains are 'dual' to one another. In the directional (de)composition – and in the downward and upward propagation, and in the reflection and transmission due to variations in medium properties in the preferred direction – we now encounter pseudodifferential operators the symbols of which are defined on phase space, and lead to a calculus that generalizes the algebraic manipulations in the case of a laterally homogeneous medium [see De Hoop (1996) and Section 2].

Unfortunately, numerical evaluation and application of pseudodifferential operators arising from the wave scattering problem are, in general, involved. Hence, approximations to their symbols are sought for to improve computational efficiency. We mention the hierarchy of increasingly accurate approaches: one-way finite-difference, i.e., 15°, 45° (Claerbout, 1970; Claerbout, 1986) and optimal rational (De Hoop & De Hoop, 1992; Van Stralen *et al.*, 1998), Hale-McLellan filter (Hale, 1991a), Fourier split-step and phase and generalized screens (De Hoop *et al.*, 2000; Le Rousseau & De Hoop, 2001b; Le Rousseau & De Hoop, 2001c), Phase-Shift-Plus-Interpolation (Gazdag & Sguazzero, 1984), uniform asymptotic (De Hoop & Gautesen, 2000), and spectral projection (normal modes) (Fishman *et al.*, 2000). In this chapter, we treat the exact and approximate cases jointly.

The wave-equation approach to seismic imaging, analyzed here, is advantageous, in particular, if the Earth's properties' complexity is such that caustics (and pseudocaustics) develop. Its geometrical-ray counterpart, the high-frequency approach, has been discussed in Burridge *et al.* (1998). The approach is applicable, not only in exploration seismology but also in crustal seismology, imaging teleseismic body waves for detailed lithospheric profiling (Bostock & Rondenay, 1999). Examples of subsurface complexities are salt domes and (shallow) magma chambers.

2.3 One-way wave equations

For the details of the derivation of exact one-way wave equations, we refer the reader to De Hoop (1996). Here, we restrict ourselves to a summary. Let p = acoustic pressure [Pa], v_r = particle velocity [m/s], ρ = volume density of mass [kg/m^3], κ = compressibility [Pa^{-1}], q = volume source density of injection rate [s^{-1}], and f_k = volume source density of force [N/m^3]. We assume that the coefficients κ and ρ are smooth, and constant outside a compact domain. This provision enables us to formulate the acoustic wave propagation, when necessary, as a scattering problem in a homogeneous embedding. The smoothness entails that the singularities of the wavefield (in particular the ones in the neighborhood of the wave arrival) arise from the ones in the signatures of the source distributions. The formation of caustics, associated with scattering in the lateral directions ('multipathing'), is captured in the approach developed in this chapter.

To be able to make use of the standard calculus of pseudodifferential operators, we should carry out our analysis in the time-Laplace domain (Widder, 1946). To show the

notation, we give the expression for the acoustic pressure,

$$\hat{p}(\boldsymbol{x}, s) = \int_{t=0}^{\infty} \exp(-st) p(\boldsymbol{x}, t)\, \mathrm{d}t \,. \tag{2.1}$$

Under this transformation, assuming zero initial conditions, we have $\partial_t \to s$. In the Laplace domain, the acoustic wavefield satisfies the system of first-order equations

$$\partial_k \hat{p} + s\rho\, \hat{v}_k = \hat{f}_k \,, \tag{2.2}$$

$$s\kappa\, \hat{p} + \partial_r \hat{v}_r = \hat{q} \,. \tag{2.3}$$

However, for the purpose of the microlocal analysis to follow, we will invoke the Fourier (transform) limit, $s \to \mathrm{i}\omega$. (The condition $\mathrm{Re}\, s > 0$ allows to compute the square root Hamiltonian, i.e. the vertical slowness symbol. See below.) Since we allow the medium to vary with all coordinates and hence also with coordinate in the preferred direction, we are forced to carry out the wavefield decomposition from the system of first-order equations rather than the second-order scalar 'Helmholtz' equation.

The evolution of the wavefield in the direction of preference will now be expressed in terms of the changes of the wavefield in the directions transverse to it. The direction of preference is taken along the x_3-axis (or 'vertical' axis) pointing into the subsurface and the remaining ('lateral' or 'horizontal') coordinates are denoted by x_μ, $\mu = 1, 2$. Since we allow the medium to vary with all coordinates and hence also with the coordinate in the preferred direction, we are forced to carry out the wavefield decomposition from the system of first-order equations rather than the second-order scalar Helmholtz equation.

2.3.1 The reduced system of equations

The decomposition procedure requires a separate handling of the horizontal components of the particle velocity. From equations (2.2) and (2.3) we obtain

$$\hat{v}_\mu = \mathrm{i}\rho^{-1}\omega^{-1}(\partial_\mu \hat{p} - \hat{f}_\mu) \,, \tag{2.4}$$

leaving, upon substitution, the matrix differential equation

$$(\partial_3 \delta_{IJ} + \mathrm{i}\omega \hat{A}_{IJ})\hat{F}_J = \hat{N}_I \,, \quad \hat{A}_{IJ} = \hat{A}_{IJ}(x_\mu, D_\nu; x_3) \,, \quad D_\nu \equiv \frac{\mathrm{i}}{\omega}\partial_\nu \,, \tag{2.5}$$

in which δ_{IJ} is the Kronecker delta, and the elements of the acoustic field matrix are given by

$$\hat{F}_1 = \hat{p} \,, \quad \hat{F}_2 = \hat{v}_3 \,, \tag{2.6}$$

the elements of the acoustic system's operator matrix by

$$\hat{A}_{11} = \hat{A}_{22} = 0 \,, \tag{2.7}$$

$$\hat{A}_{12} = \rho \,, \tag{2.8}$$

$$\hat{A}_{21} = -D_\nu(\rho^{-1} D_\nu) + \kappa \,, \tag{2.9}$$

and the elements of the notional source matrix by

$$\hat{N}_1 = \hat{f}_3 \,, \quad \hat{N}_2 = D_\nu(\rho^{-1}\hat{f}_\nu) + \hat{q} \,. \tag{2.10}$$

It is observed that the right-hand side of equation (2.4) and $\hat{A}_{IJ}$ contain the spatial derivatives D_ν with respect to the horizontal coordinates only. D_ν has the interpretation of *horizontal slowness* operator. Further, it is noted that $\hat{A}_{12}$ is simply a multiplicative operator.

2.3.2 The coupled system of one-way wave equations

To distinguish up- and downgoing constituents in the wavefield, we shall construct an appropriate linear operator $\hat{L}_{IJ}$ with

$$\hat{F}_I = \hat{L}_{IJ}\hat{W}_J \,, \tag{2.11}$$

that, with the aid of the commutation relation

$$[\partial_3, \hat{L}_{IJ}](\cdot) = \partial_3(\hat{L}_{IJ}(\cdot)) - \hat{L}_{IJ}\partial_3(\cdot) = (\partial_3 \hat{L}_{IJ})(\cdot) \,,$$

(since the operator $\hat{L}_{IJ}$ depends on the x_3 variable, whereas it only acts on x_1 and x_2) transforms equation (2.5) into

$$\hat{L}_{IJ}\,(\partial_3 \delta_{JM} + \mathrm{i}\omega\hat{\Lambda}_{JM})\hat{W}_M = -(\partial_3 \hat{L}_{IJ})\,\hat{W}_J + \hat{N}_I \,, \tag{2.12}$$

as to make $\hat{\Lambda}_{JM}$, satisfying

$$\hat{A}_{IJ}\hat{L}_{JM} = \hat{L}_{IJ}\hat{\Lambda}_{JM} \,, \tag{2.13}$$

a diagonal matrix of operators. We denote $\hat{L}_{IJ}$ as the composition operator and $\hat{W}_M$ as the wave matrix. The matrix expression in parentheses on the left-hand side of equation (2.12) is diagonal and its diagonal entries are the two so-called *one-way* wave operators. The first term on the right-hand side of equation (2.12) is representative for the scattering due to variations of the medium properties in the vertical direction. The scattering due to variations of the medium properties in the horizontal directions is contained in $\hat{\Lambda}_{JM}$ and, implicitly, in $\hat{L}_{IJ}$ also.

To investigate whether solutions of equation (2.13) exist, we introduce the generalized

eigenvector operators $\hat{L}_I^{(\pm)}$ columnwise according to

$$\hat{L}_I^{(+)} = \hat{L}_{I1} \,, \quad \hat{L}_I^{(-)} = \hat{L}_{I2} \,. \tag{2.14}$$

Upon writing the diagonal entries of $\hat{\Lambda}_{JM}$, the generalized eigenvalue operators, as

$$\hat{\Lambda}_{11} = \hat{\Gamma}^{(+)} \,, \quad \hat{\Lambda}_{22} = \hat{\Gamma}^{(-)} \,, \tag{2.15}$$

equation (2.13) decomposes into the two systems of equations

$$\hat{A}_{IJ}\hat{L}_J^{(\pm)} = \hat{L}_I^{(\pm)}\hat{\Gamma}^{(\pm)} \,. \tag{2.16}$$

By analogy with the case where the medium is translationally invariant in the horizontal directions, we shall denote $\hat{\Gamma}^{(\pm)}$ as the *vertical slowness* operators. Notice that the operators $\hat{L}_1^{(\pm)}$ compose the acoustic pressure and that the operators $\hat{L}_2^{(\pm)}$ compose the vertical particle velocity from the elements of $\hat{W}_M$ associated with the up- and downgoing constituents.

In De Hoop (1996) an Ansatz procedure has been followed to solve the generalized eigenvalue-eigenvector problem (2.16) in operator sense: choosing the *acoustic-pressure normalization* analog, we satisfy the commutation rule

$$[\hat{A}_{12}\hat{L}_2^{(\pm)}, \hat{A}_{12}\hat{A}_{21}] = 0 \,. \tag{2.17}$$

In this normalization, we find the vertical slowness operator or generalized eigenvalues to be

$$\hat{\Gamma}^{(+)} = -\hat{\Gamma}^{(-)} = \hat{\Gamma} = \hat{\mathrm{A}}^{1/2} \,, \quad \hat{\mathrm{A}} \equiv \hat{A}_{12}\hat{A}_{21} \,; \quad \hat{\Gamma}^2 = \hat{\mathrm{A}} \tag{2.18}$$

is the *characteristic operator equation*, while the generalized eigenvectors constitute the *composition* operator

$$\hat{L} = \begin{pmatrix} I & I \\ \hat{Y} & -\hat{Y} \end{pmatrix} \,, \tag{2.19}$$

with $\hat{Y} = \hat{A}_{12}^{-1}\hat{\Gamma}$ denoting the vertical acoustic impedance operator. With respect to the normalization, note that we have decomposed the *pressure* viz. according to $\hat{F}_1 = \hat{W}_1 + \hat{W}_2$. In terms of the inverse vertical acoustic impedance operator, the *decomposition* operator then follows as

$$\hat{L}^{-1} = \tfrac{1}{2}\begin{pmatrix} I & \hat{Y}^{-1} \\ I & -\hat{Y}^{-1} \end{pmatrix} \,. \tag{2.20}$$

The (de)composition operators account for the radiation patterns of the different source mechanisms and receiver types.

Using the decomposition operator, equation (2.12) transforms into

$$(\partial_3\delta_{IM} + \mathrm{i}\omega\hat{\Lambda}_{IM})\hat{W}_M = -\underbrace{(\hat{L}^{-1})_{IM}(\partial_3\hat{L}_{MK})}_{\text{image} \Leftarrow \text{coupling}}\hat{W}_K + \underbrace{(\hat{L}^{-1})_{IM}\hat{N}_M}_{\text{initial values}}, \tag{2.21}$$

which can be interpreted as a coupled system of one-way wave equations. The coupling between the counter-propagating components, $\hat{W}_1$ and $\hat{W}_2$, is apparent in the first source-like term on the right-hand side, which can be written as

$$-\hat{L}^{-1}(\partial_3\hat{L}) = \begin{pmatrix} \hat{T} & \hat{R} \\ \hat{R} & \hat{T} \end{pmatrix}, \tag{2.22}$$

in which $\hat{T}$ and $\hat{R}$ represent the *transmission* and *reflection* operators, respectively. (The goal of the double-square-root propagation, to be explained in Section 2.5, is to image the kernel of the coupling operator.) In the acoustic-pressure normalization analog, we find

$$\hat{R} = -\hat{T} = \tfrac{1}{2}\hat{Y}^{-1}(\partial_3\hat{Y}) . \tag{2.23}$$

The second, primary, source term on the right-hand side of equation (2.21) is chosen in accordance with the Helmholtz Green's function: A volume injection point source will result in $\hat{N}_1 = 0$, $\hat{N}_2 = \delta(\boldsymbol{x} - \boldsymbol{x}')$ and hence the inhomogeneous term in equation (2.21) will reduce to a vector with components

$$(\hat{L}^{-1})_{12}\hat{N}_2 = -(\hat{L}^{-1})_{22}\hat{N}_2 = \tfrac{1}{2}(\hat{\mathcal{Y}}^{-1})(x_\mu, x'_\nu; x'_3) \otimes \delta(x_3 - x'_3) , \tag{2.24}$$

where $\hat{\mathcal{Y}}^{-1}$ indicates the Schwartz kernel of $\hat{Y}^{-1}$.

2.4 Trotter-product one-way wave propagator

To analyze the solutions of the system of one-way wave equations, we introduce the inverse of the one-way wave operator, $\hat{\mathrm{G}}^{(\pm)} = (\partial_3 + \mathrm{i}\omega\hat{\Gamma}^{(\pm)})^{-1}$. The one-sided elementary kernels $\hat{\mathcal{G}}^{(\pm)}(x_\mu, x_3; x'_\nu, x'_3)$ associated with these operators are the so-called one-way Green's functions. They satisfy the equations

$$(\partial_3 + \mathrm{i}\omega\hat{\Gamma}^{(\pm)})\hat{\mathcal{G}}^{(\pm)} = \delta(x_\nu - x'_\nu)\,\delta(x_3 - x'_3) , \tag{2.25}$$

together with the condition of causality enforcing that $\hat{\mathcal{G}}^{(\pm)}$ decays as $x_3 \to \pm\infty$. Now, consider the case $\hat{\mathrm{G}} = \hat{\mathrm{G}}^{(+)}$, $\hat{\mathcal{G}} = \hat{\mathcal{G}}^{(+)}$ and $\hat{\Gamma} = \hat{\Gamma}^{(+)}$. The operator $\hat{\mathrm{G}}$ acts on a test field $\hat{u}$ as

$$(\hat{\mathrm{G}}\hat{u})(x_\mu, x_3) = \int_{\zeta\in\mathbb{R}}\int_{x'_\nu\in\mathbb{R}} \hat{\mathcal{G}}(x_\mu, x_3; x'_\nu, \zeta)\,\hat{u}(x'_\nu, \zeta)\,\mathrm{d}x'_1\mathrm{d}x'_2\,\mathrm{d}\zeta . \tag{2.26}$$

Let us define the initial-value problem of determining the function $\hat{U}(x_\mu, x_3; \zeta)$:

$$(\partial_3 + \mathrm{i}\omega\hat{\Gamma})\,\hat{U} = 0 \text{ for } x_3 \geq \zeta, \quad \hat{U}(x_\mu, \zeta; \zeta) = \hat{u}(x_\mu, \zeta)\ . \tag{2.27}$$

Then it is observed that

$$(\hat{\mathrm{G}}\hat{u})(x_\mu, x_3) = \int_{\zeta=-\infty}^{x_3} \hat{U}(x_\mu, x_3; \zeta)\,\mathrm{d}\zeta\ . \tag{2.28}$$

2.4.1 The product integral

We note that the vertical slowness operators at different levels of x_3 do not necessarily commute with one another due to the heterogeneity of the medium. Thus we arrive at a 'time'-ordered product integral representation (De Witte-Morette *et al.*, 1979) of the one-sided propagators [cf., equation (2.27)] associated with the one-way wave equations (De Hoop, 1996; Fishman & McCoy, 1984a; Fishman & McCoy, 1984b) where 'time' here refers to the vertical coordinate x_3,

$$\hat{U}^{(\pm)}(., x_3; x_3') = \pm H(\mp[x_3' - x_3]) \left\{ \prod_{\zeta=x_3'}^{x_3} \exp[-\mathrm{i}\omega\hat{\Gamma}^{(\pm)}(., \zeta)\,\mathrm{d}\zeta] \right\} \hat{u}(., x_3')\ , \tag{2.29}$$

where H denotes the Heaviside function. Equation 2.29 expresses the 'accumulation' of infinitesimal solutions of the one-way wave equation 2.25: In this expression, the operator ordering is initiated by $\exp[-\mathrm{i}\omega\hat{\Gamma}(., x_3')\,\mathrm{d}\zeta]$ acting on $\hat{u}(., x_3')$ followed by applying $\exp[-\mathrm{i}\omega\hat{\Gamma}(., \zeta)\,\mathrm{d}\zeta]$ to the result, successively for increasing ζ.

2.4.2 The 'square-root' or vertical slowness operator symbol, the Trotter product

If the medium in the interval $[x_3', x_3]$ were weakly varying in the vertical direction, the Trotter product formula can be applied to the product integral in equation (2.29). This results in the Hamiltonian path integral representations (De Witte-Morette *et al.*, 1979) with 'measure' $\mathcal{D}$ for the Green's functions,

$$\hat{\mathcal{G}}^{(\pm)}(x_\mu, x_3; x_\nu', x_3') = \pm H(\mp[x_3' - x_3]) \int_P \mathcal{D}(x_\mu'', \alpha_\nu'') \tag{2.30}$$
$$\exp\left[-\mathrm{i}\omega \int_{\zeta=x_3'}^{x_3} \mathrm{d}\zeta\{\alpha_\sigma''(d_\zeta x_\sigma'') + \hat{\gamma}^{(\pm)}(x_\mu'', \zeta, \alpha_\nu'')\}\right]\ ,$$

P being a set of paths $(x_\mu''(\zeta),\ \alpha_\nu''(\zeta))$ in (horizontal) phase space satisfying $x_\mu''(\zeta = x_3') = x_\mu'$, $x_\mu''(\zeta = x_3) = x_\mu$; see also Schlottmann (1999). In equation (2.30), $\hat{\gamma}^{(\pm)}$ is the *left*

symbol[2] of $\hat{\Gamma}^{(\pm)}$, i.e.,

$$\hat{\Gamma}^{(\pm)}(x_\mu, D_\nu; \zeta)\, \exp(-\mathrm{i}\omega\alpha_\sigma x_\sigma) = \hat{\gamma}^{(\pm)}(x_\mu, \zeta, \alpha_\nu) \exp(-\mathrm{i}\omega\alpha_\sigma x_\sigma)\ , \tag{2.31}$$

where α_ν indicate the horizontal slownesses The path integral in equation (2.30) is to be interpreted as the lattice multi-variate integral

$$\hat{\mathcal{G}}^{(\pm)}(x_\mu, x_3; x'_\nu, x'_3) = \pm H(\mp[x'_3 - x_3]) \lim_{M\to\infty} \int \prod_{i=1}^{M} (\omega/2\pi)^2 \mathrm{d}\alpha_1^{(i)} \mathrm{d}\alpha_2^{(i)} \prod_{j=1}^{M-1} \mathrm{d}x_1^{(j)} \mathrm{d}x_2^{(j)}$$
$$\exp\left[-\mathrm{i}\omega \sum_{k=1}^{M} \{\alpha_\sigma^{(k)}(x_\sigma^{(k)} - x_\sigma^{(k-1)}) + \hat{\gamma}^{(\pm)}(x_\mu^{(k)}, \bar{\zeta}_k, \alpha_\nu^{(k)}) M^{-1}\Delta x_3\}\right]\ , \tag{2.32}$$

where

$$\bar{\zeta}_k = \zeta_k - \tfrac{1}{2} M^{-1}\Delta x_3 \tag{2.33}$$

with $x_\mu^{(0)} = x'_\mu$, $x_\mu^{(M)} = x_\mu$, and $\Delta x_3 = x_3 - x'_3$. All the integrations are taken over the interval $(-\infty, \infty)$, $M^{-1}\Delta x_3$ is the step size in ζ, and $(x_\mu^{(j)}, \alpha_\nu^{(j)})$ are the coordinates of a path at the discrete values ζ_j of ζ as $j = 1, \cdots, M$.

To account for the source-radiation pattern [cf., equation (2.24)], we invoke the Volterra composition

$$\hat{\mathcal{G}}^{(\pm)}(x_\mu, x_3; x'_\nu, x'_3) \to \int \hat{\mathcal{G}}^{(\pm)}(x_\mu, x_3; x''_\nu, x'_3)\, \tfrac{1}{2}(\hat{\mathcal{Y}}^{-1})(x''_\nu, x'_\nu; x'_3)\, \mathrm{d}x''_1 \mathrm{d}x''_2 = \tag{2.34}$$
$$\int \hat{\mathcal{G}}^{(\pm)}(x_\mu, x_3; x_\nu^{(0)}, x'_3)\, (\omega/2\pi)^2 \mathrm{d}\alpha_1^{(0)} \mathrm{d}\alpha_2^{(0)}$$
$$\times \underbrace{\tfrac{1}{2}\hat{y}^{-1}(x'_\nu, \alpha_\nu^{(0)}; x'_3) \exp[-\mathrm{i}\omega\alpha_\sigma^{(0)}(x_\sigma^{(0)} - x'_\sigma)]}_{\mathcal{R}(x_\nu^{(0)}, \alpha_\nu^{(0)}; \boldsymbol{x}')} \mathrm{d}x_1^{(0)} \mathrm{d}x_2^{(0)},$$

where $\hat{y}^{-1}$ is the dual (or right) symbol of $\hat{Y}^{-1}$. Then equation (2.32) changes to

$$\hat{\mathcal{G}}^{(\pm)}(x_\mu, x_3; x'_\nu, x'_3) = \tag{2.35}$$
$$\pm H(\mp[x'_3 - x_3]) \lim_{M\to\infty} \int \prod_{i=0}^{M} (\omega/2\pi)^2 \mathrm{d}\alpha_1^{(i)} \mathrm{d}\alpha_2^{(i)} \prod_{j=0}^{M-1} \mathrm{d}x_1^{(j)} \mathrm{d}x_2^{(j)} \mathcal{R}$$
$$\times \exp\left[-\mathrm{i}\omega \sum_{k=1}^{M} \{\alpha_\sigma^{(k)}(x_\sigma^{(k)} - x_\sigma^{(k-1)}) + \hat{\gamma}^{(\pm)}(x_\mu^{(k)}, \bar{\zeta}_k, \alpha_\nu^{(k)}) M^{-1}\Delta x_3\}\right]\ ,$$

In preparation of the microlocal analysis of the Green's functions, we now introduce the

[2] To highlight (medium) symmetries the Weyl symbol is the preferred choice, whereas the dual symbol has algorithmic advantages (Le Rousseau & De Hoop, 2001a).

wavevectors

$$K_\nu^{(k)} = \omega\alpha_\nu^{(k)} \ , \quad K_3^{(\pm)} = \omega\hat{\gamma}^{(\pm)} \ , \tag{2.36}$$

for $k = 1, \ldots, M$, which components together at $k = M$ will relate to the cotangent vectors appearing in the wavefront set of $\mathcal{G}^{(\pm)}$. Note that $K_3^{(\pm)} = K_3^{(\pm)}(x_\mu, \zeta, K_\nu; \omega)$. Then, in the time domain, the Trotter product formula can be written as the limit of a sequence of the form

$$\begin{aligned}
&\mathcal{G}^{(\pm);M}(x_\mu, x_3, t; x'_\nu, x'_3) = \\
&\quad \pm H(\mp[x'_3 - x_3]) \int_{\mathbb{R}} \frac{1}{2\pi} \mathrm{d}\omega \int \prod_{i=0}^{M} \left(\frac{1}{2\pi}\right)^2 \mathrm{d}K_1^{(i)} \mathrm{d}K_2^{(i)} \prod_{j=0}^{M-1} \mathrm{d}x_1^{(j)} \mathrm{d}x_2^{(j)} \mathcal{R} \\
&\quad \times \exp\left[-\mathrm{i} \sum_{k=1}^{M} \{K_\sigma^{(k)}(x_\sigma^{(k)} - x_\sigma^{(k-1)}) + K_3^{(\pm)}(x_\mu^{(k)}, \bar{\zeta}_k, K_\nu^{(k)}; \omega) M^{-1} \Delta x_3\}\right] \exp(\mathrm{i}\omega t) \ ,
\end{aligned} \tag{2.37}$$

and similarly without the radiation pattern $\mathcal{R}$. We have assumed that the source is operative at $t = 0$. In general, shifting this instance to t', yields

$$\begin{aligned}
&\mathcal{G}^{(\pm);M}(x_\mu, x_3, t; x'_\nu, x'_3, t') = \\
&\pm H(\mp[x'_3 - x_3]) \int_{\mathbb{R}} \frac{1}{2\pi} \mathrm{d}\omega \int \underbrace{\prod_{i=0}^{M} \left(\frac{1}{2\pi}\right)^2 \mathrm{d}K_1^{(i)} \mathrm{d}K_2^{(i)}}_{\text{distributions}} \underbrace{\prod_{j=0}^{M-1} \mathrm{d}x_1^{(j)} \mathrm{d}x_2^{(j)}}_{\text{compositions}} \mathcal{R} \\
&\times \exp\left[-\mathrm{i} \sum_{k=1}^{M} \{K_\sigma^{(k)}(x_\sigma^{(k)} - x_\sigma^{(k-1)}) + K_3^{(\pm)}(x_\mu^{(k)}, \bar{\zeta}_k, K_\nu^{(k)}; \omega) M^{-1} \Delta x_3\}\right] \exp(\mathrm{i}\omega(t - t')) \ .
\end{aligned} \tag{2.38}$$

As before, for simplicity of notation, we will restrict our analysis again to $\mathcal{G} = \mathcal{G}^{(+)}$, $K_3 = K_3^{(+)}$. Equation (2.38) is a simplified representation of the actual compositions of thin-slab propagators: Each composition is in horizontal space and time. However, the integrals over the successive times result in Dirac measures in the difference of successive frequencies. Those measures have been integrated out in Equations (2.37),(2.38), conveying the conservation of frequency.

2.4.3 The canonical relation

For operators with kernels of the form (2.38), the propagation of singularities is controlled by the phase function. This is described by the canonical relation. With the canonical relation we recover the geometrical (ray) aspect of wave propagation. The canonical relation is a Lagrangian manifold [see also (Kendall & Thomson, 1993)].

The phase function in equations (2.37), (2.38) is given by

$$\phi(\boldsymbol{x},t,\boldsymbol{s}',t',\langle x_\mu^{(l)}\rangle_{1\le l\le M-1},\langle K_\nu^{(k)}\rangle_{1\le k\le M},\omega) \tag{2.39}$$
$$= \omega(t-t') - \sum_{k=1}^{M}\left\{K_\sigma^{(k)}(x_\sigma^{(k)} - x_\sigma^{(k-1)}) + K_3^{\text{prin}}(x_\mu^{(k)},\bar{\zeta}_k,K_\nu^{(k)},\omega)M^{-1}\Delta x_3\right\} ,$$

with

$$K_3^{\text{prin}}(x_\mu^{(k)},\bar{\zeta}_k,K_\nu^{(k)},\omega) = \sqrt{\omega^2 c(x_\mu^{(k)},\bar{\zeta}_k)^{-2} - K_\sigma^{(k)}K_\sigma^{(k)}} , \tag{2.40}$$

in accordance with the eikonal equation, and where $\boldsymbol{x}' = (\boldsymbol{s}', s_3)$ with $s_3 = 0$ (corresponding with $k = 0$), $\boldsymbol{x}$ corresponds with $k = M$, and where $\mu = 1,2$ and $\nu = 1,2$. We have $\Delta x_3 = x_3 - s_3 = x_3$. We further introduced the principal part K_3^{prin} of K_3; the remaining exponentials

$$\exp\left[-\mathrm{i}\{K_3(x_\mu^{(k)},\bar{\zeta}_k,K_\nu^{(k)},\omega) - K_3^{\text{prin}}(x_\mu^{(k)},\bar{\zeta}_k,K_\nu^{(k)},\omega)\}M^{-1}\Delta x_3\right]$$

are contained in the 'amplitude' of $\mathcal{G}$ and account for phenomena not associated with the wavefront set. This remaining exponential factor is (a symbol) of order -1 and can therefore be considered as an amplitude.

Then the phase is homogeneous in $(\langle K_\nu^{(k)}\rangle_{1\le k\le M},\omega)$[3] [see also Duistermaat (1996)]. Note that the operator $\mathcal{R}$ in equation (2.38) is pseudodifferential and does not move the wavefront set. Let us collect the phase variables according to

$$\theta = (\langle x_\mu^{(l)}\rangle_{1\le l\le M-1},\langle K_\nu^{(k)}\rangle_{1\le k\le M},\omega) . \tag{2.41}$$

The stationary point set, Σ_ϕ, is defined as ('prime' indicates taking the gradient)

$$\Sigma_\phi = \{(\boldsymbol{x},t,\boldsymbol{s}',t',\theta) \mid (\phi')_\theta(\boldsymbol{x},t,\boldsymbol{s}',t',\theta) = 0\} . \tag{2.42}$$

Thus, the defining equations of the stationary point set, Σ_ϕ, are

$$\begin{aligned}
(\phi')_{x_\sigma^{(l)}} &= -K_\sigma^{(l)} + K_\sigma^{(l+1)} - M^{-1}\Delta x_3\,(K_3^{\text{prin}'})_{x_\sigma}(x_\mu^{(l)},\bar{\zeta}_l,K_\nu^{(l)},\omega) = 0 ,\\
(\phi')_{K_\sigma^{(k)}} &= -x_\sigma^{(k)} + x_\sigma^{(k-1)} - M^{-1}\Delta x_3\,(K_3^{\text{prin}'})_{K_\sigma}(x_\mu^{(k)},\bar{\zeta}_k,K_\nu^{(k)},\omega) = 0 ,\\
(\phi')_\omega &= (t-t') - M^{-1}\Delta x_3\textstyle\sum_{k=1}^{M}(K_3^{\text{prin}'})_\omega(x_\mu^{(k)},\bar{\zeta}_k,K_\nu^{(k)},\omega) = 0 ,
\end{aligned} \tag{2.43}$$

for $\sigma = 1,2$ and $l = 1,\cdots,M-1$, $k = 1,\cdots,M$.

[3]Note that the 'intermediate' space variables, $\langle x_\mu^{(l)}\rangle_{1\le l\le M-1}$, in equation (2.38) behave appropriately through the composition of Fourier integral operators (Hörmander, 1985a, p.295) and (Hörmander, 1985b, p.20).

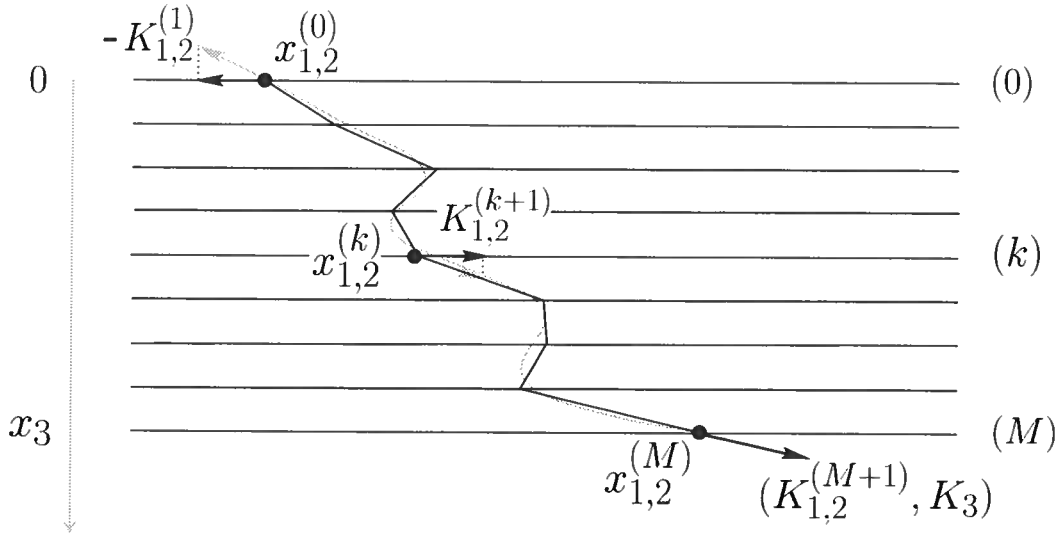

Figure 2.1. One-way scattering process: The true bicharacteristic is approached by a finite-difference square-root Hamiltonian system. To each depth level is associated a position vector $(x_1^{(k)}, x_2^{(k)})$ and a wave (cotangent) vector $(K_1^{(k+1)}, K_2^{(k+1)})$.

In Appendix B, it is shown that the phase is non-degenerate for M sufficiently large. Hence the phase is clean with excess 0, and the mapping

$$\begin{aligned} \Sigma_\phi \to &\quad \Lambda_\phi \,, \\ (\boldsymbol{x}, t, \boldsymbol{s}', t', \theta) \mapsto &\quad (\boldsymbol{x}, t, -K_{1,2}^{(M+1)}, -K_3, \omega; \boldsymbol{s}', t', K_{1,2}^{(1)}, -\omega) \\ &\quad = (\boldsymbol{x}, t, (\phi')_{\boldsymbol{x}}, (\phi')_t; \boldsymbol{s}', t', (\phi')_{\boldsymbol{s}'}, (\phi')_{t'}), \end{aligned} \tag{2.44}$$

is a diffeomorphism. The stationary point set, Σ_ϕ, is a submanifold of the manifold $\{(\boldsymbol{x}, t, \boldsymbol{s}', t', \theta)\}$. Λ_ϕ is the associated Lagrangian submanifold in the cotangent bundle associated with the manifold of points $\{(\boldsymbol{x}, t, \boldsymbol{s}', t')\}$. In the mapping above, $K_{1,2}^{(M+1)}$ is given by

$$K_{1,2}^{(M+1)} = K_{1,2}^{(M)} + M^{-1}\Delta x_3 \, (K_3^{\text{prin}'})_{x_{1,2}}(x_\mu^{(M)}, \bar{\zeta}_M, K_\nu^{(M)}, \omega) \,, \tag{2.45}$$

following equations (2.43) while for M large enough,

$$(\phi')_{x_3} \simeq -K_3 \equiv -K_3^{\text{prin}}(x_\mu^{(M)}, \bar{\zeta}_M, K_\nu^{(M+1)}, \omega) \tag{2.46}$$

(cf., Appendix C) on the stationary point set.

Observe that the (finite) system of equations defining the stationary point set, Σ_ϕ, is derived from a complex-analytic square-root Hamiltonian, K_3^{prin}, see Section 2.4.5 below. The solution of this system can be interpreted as a set of bicharacteristics on a lattice

as illustrated in Figure 2.1. Omitting so-called turning rays, through a finite-difference approximation in the vertical (x_3) coordinate, this system yields in the limit $M \to \infty$ the Hamilton system that defines the geometry of asymptotic ray and Maslov high-frequency solutions (Kendall & Thomson, 1993; De Hoop & Brandsberg-Dahl, 2000) to the wave equation.

The canonical relation, C_ϕ, is then obtained by twisting the Lagrangian submanifold Λ_ϕ

$$C_\phi = \left\{ (\boldsymbol{x}, t, -K_{1,2}^{(M+1)}, -K_3, \omega; \boldsymbol{s}', t', -K_{1,2}^{(1)}, \omega) \;\middle|\; (\boldsymbol{x}, t, -K_{1,2}^{(M+1)}, -K_3, \omega; \boldsymbol{s}', t', K_{1,2}^{(1)}, -\omega) \in \Lambda_\phi \right\}, \quad K_3 = K_3^{\text{prin}}(\boldsymbol{x}, K_{1,2}^{(M+1)}, \omega).$$

2.4.4 Propagation of singularities

Let G denote the time-domain counterpart of the previously defined $\hat{\mathrm{G}}$ [cf., equation (2.26)]. Then $\mathcal{G}(.,.,.;\boldsymbol{s}_0', 0, t_0') = \mathrm{G}(\delta(\boldsymbol{s}' - \boldsymbol{s}_0') \otimes \delta(t' - t_0'))$. We denote the wavefront set of this Green's function as $\mathrm{WF}(\mathcal{G})$. With the aid of the canonical relation C_ϕ, we find that

$$\mathrm{WF}(\mathcal{G}) = C_\phi \circ \mathrm{WF}(\delta(\boldsymbol{s}' - \boldsymbol{s}_0') \otimes \delta(t' - t_0')) \tag{2.47}$$

so that

$$\mathrm{WF}(\mathcal{G}) = \left\{ (\boldsymbol{x}, t, \boldsymbol{\xi}, -\omega) \;\middle|\; \exists \boldsymbol{s}_0', t_0', K_{1,2}^{(1)}, \; (\boldsymbol{x}, t, \boldsymbol{\xi}, -\omega; \boldsymbol{s}_0', t_0', K_{1,2}^{(1)}, -\omega) \in C_\phi \right\}, \tag{2.48}$$

which means that the cotangent vector, $\boldsymbol{\xi}$, is the cotangent vector at $\boldsymbol{x}$ associated with the bicharacteristic joining the source, $\boldsymbol{s}_0'$, and the point $\boldsymbol{x}$, with initial 'slope' or 'slant' given by $\omega^{-1} K_\nu^{(1)}$, and 'one-way' travel time $(t - t_0')$.

2.4.5 Square-root Hamiltonian system

Let H be the Hamiltonian associated with the (original wave equation's) propagation process: $H = H(\boldsymbol{x}, \boldsymbol{K}, \omega)$. By the implicit function theorem, if $(H')_{K_3} \neq 0$ at $(\boldsymbol{x}_0, \boldsymbol{K}_0, \omega_0)$, there exist a neighborhood $\mathcal{U}$ of $(\boldsymbol{x}_0, \boldsymbol{K}_0, \omega_0)$ and a *unique* function, H_3, such that $H(\boldsymbol{x}, \boldsymbol{K}, \omega) = 0$ is equivalent to $K_3 - H_3(\boldsymbol{x}, K_{1,2}, \omega) = 0$ and $H_3(\boldsymbol{x}, K_{1,2}, \omega)$ has the same degree of smoothness as $H(\boldsymbol{x}, \boldsymbol{K}, \omega)$. Also, the implicit function theorem states that

$$(H_3')_{x_i} = -(H')_{x_i}/(H')_{K_3}, \quad i = 1,2,3, \tag{2.49}$$

$$(H_3')_{K_i} = -(H')_{K_i}/(H')_{K_3}, \quad i = 1,2, \tag{2.50}$$

$$(H_3')_t = 0, \tag{2.51}$$

$$(H_3')_\omega = -(H')_\omega/(H')_{K_3}. \tag{2.52}$$

We set

$$F(\boldsymbol{x}, \boldsymbol{K}, \omega) = K_3 - H_3(\boldsymbol{x}, K_{1,2}, \omega) \; .$$

Then, in the considered neighborhood $\mathcal{U}$, F and H have the same Hamiltonian flow:

$$\frac{\mathrm{d}x_i}{\mathrm{d}\zeta} = (F')_{K_i} = -({H_3}')_{K_i} = (H')_{K_i}/(H')_{K_3} \; , \quad i = 1, 2 \; , \tag{2.53}$$

$$\frac{\mathrm{d}x_3}{\mathrm{d}\zeta} = (F')_{K_3} = 1 \; , \tag{2.54}$$

$$\frac{\mathrm{d}K_i}{\mathrm{d}\zeta} = -(F')_{x_i} = ({H_3}')_{x_i} = -(H')_{x_i}/(H')_{K_3} \; , \quad i = 1, 2, 3 \; , \tag{2.55}$$

$$\frac{\mathrm{d}t}{\mathrm{d}\zeta} = (F')_{\omega} = -({H_3}')_{\omega} = (H')_{\omega}/(H')_{K_3} \; , \tag{2.56}$$

$$\frac{\mathrm{d}\omega}{\mathrm{d}\zeta} = -(F')_t = 0 \; . \tag{2.57}$$

Because of equation (2.54), the flow of F is parametrized by $\zeta = x_3$. Now, if τ is the parameter for the Hamiltonian flow associated with H, we have

$$\frac{\mathrm{d}x_3}{\mathrm{d}\tau} = +(H')_{K_3} \; , \tag{2.58}$$

which implies

$$\mathrm{d}\zeta = +(H')_{K_3}\mathrm{d}\tau \; , \tag{2.59}$$

which relates evolution in depth to evolution in time. (This relation is at the basis of the theory of one-way wave propagation.) Hence the equivalence of the two Hamilton systems and their solutions.

In the present case,

$$H(\boldsymbol{x}, \boldsymbol{K}, \omega) = -\omega + c(\boldsymbol{x})|\boldsymbol{K}| \tag{2.60}$$

and $(H')_{K_3} = 0$ implies that $K_3 = 0$. In view of equations (2.49)-(2.52), for the equivalence of Hamiltonian flows to apply, any bicharacteristic for which K_3 vanishes at some point, a so-called turning ray, must be excluded (see also Appendix B). In an open set $\mathcal{U} \subset \mathbb{R}^3 \times \mathbb{R}^3$ which closure is away from these bicharacteristics, F is then simply defined as

$$F(\boldsymbol{x}, \boldsymbol{K}, \omega) = K_3 - \sqrt{\omega^2 c(\boldsymbol{x})^{-2} - K_\nu K_\nu} \; . \tag{2.61}$$

In the present case, we therefore have $H_3 = K_3^{\mathrm{prin}}$.

In the process of discretizing system (2.53)-(2.56) we take $\Delta\zeta = M^{-1}\Delta x_3$ and subdivide the depth or vertical range into M steps. We recover system (2.43), hence the earlier interpretation of flow in terms of bicharacteristics on a lattice.

2.4.6 Amplitude of the propagator kernel

To analyze the amplitude behavior of the Trotter product representation for the one-way Green's function, we consider equation (2.38) to be the composition of M Fourier integral operators [see Le Rousseau *et al.* (2001)]. The kernel of each constituent operator is a distribution with an oscillatory integral representation. The phase of each such representation is of the form [cf., equation (2.39)]

$$\begin{aligned}\phi^{(k)} &= -K_\sigma^{(k)}(x_\sigma^{(k)} - x_\sigma^{(k-1)}) - K_3^{\text{prin}}(x_\mu^{(k)}, \bar{\zeta}_k, K_\nu^{(k)}; \omega^{(k)})\, M^{-1}\Delta x_3 \\ &\quad + \omega^{(k)}(t^{(k)} - t^{(k-1)})\,.\end{aligned} \tag{2.62}$$

In the composition it follows that all $\omega^{(k)} = \omega$; we have $t^{(M)} = t$ and $t^{(0)} = 0$.

We will first establish that, in the stationary phase approximation, the oscillatory integral representation of each constituent distribution yields a change of coordinates on the Lagrangian manifold $\Lambda_{\phi^{(k)}}$. The stationary point set, $\Sigma_{\phi^{(k)}}$, follows from

$$(\phi^{(k)})'_{K_\sigma^{(k)}} = -(x_\sigma^{(k)} - x_\sigma^{(k-1)}) + \frac{K_\sigma^{(k)}}{K_3^{\text{prin}}(x_\mu^{(k)}, \bar{\zeta}_k, K_\nu^{(k)}; \omega^{(k)})}\, M^{-1}\Delta x_3 = 0\,,$$

and a likewise equation for $(\phi^{(k)})'_{\omega^{(k)}} = 0$ determining the travel time. The equation above can be solved for $x_\sigma^{(k)}$ as a function of $K_\sigma^{(k)}$ if the Hessian,

$$\begin{aligned}(\phi^{(k)})''_{K_\mu^{(k)} x_\nu^{(k)}} &= -\delta_{\mu\nu} - \frac{K_\mu^{(k)}}{(K_3^{\text{prin}})^2}\frac{\partial K_3^{\text{prin}}}{\partial x_\nu^{(k)}}\, M^{-1}\Delta x_3 \\ &= -\delta_{\mu\nu} - \frac{K_\mu^{(k)}(\omega^{(k)})^2}{(K_3^{\text{prin}})^3} c^{-1}\frac{\partial c^{-1}}{\partial x_\nu^{(k)}}\, M^{-1}\Delta x_3,\end{aligned} \tag{2.63}$$

is non-singular [by virtue of the implicit function theorem (Dieudonné, 1969)]. Here, the speed c is evaluated at $(x_{1,2}^{(k)}, \bar{\zeta}_k)$. Having the functions $x_\sigma^{(k)}$ implicitly defined, we apply the chain rule to arrive at

$$\begin{pmatrix} \partial_{K_1^{(k)}} x_1^{(k)} & \partial_{K_2^{(k)}} x_1^{(k)} \\ \partial_{K_1^{(k)}} x_2^{(k)} & \partial_{K_2^{(k)}} x_2^{(k)} \end{pmatrix} =$$

$$-\begin{pmatrix} (\phi^{(k)})''_{K_1^{(k)} x_1^{(k)}} & (\phi^{(k)})''_{K_1^{(k)} x_2^{(k)}} \\ (\phi^{(k)})''_{K_2^{(k)} x_1^{(k)}} & (\phi^{(k)})''_{K_2^{(k)} x_2^{(k)}} \end{pmatrix}^{-1} \begin{pmatrix} (\phi^{(k)})''_{K_1^{(k)} K_1^{(k)}} & (\phi^{(k)})''_{K_1^{(k)} K_2^{(k)}} \\ (\phi^{(k)})''_{K_2^{(k)} K_1^{(k)}} & (\phi^{(k)})''_{K_2^{(k)} K_2^{(k)}} \end{pmatrix}. \tag{2.64}$$

Since

$$\lim_{M\to\infty} \det \begin{bmatrix} (\phi^{(k)})''_{K_1^{(k)}x_1^{(k)}} & (\phi^{(k)})''_{K_1^{(k)}x_2^{(k)}} \\ (\phi^{(k)})''_{K_2^{(k)}x_1^{(k)}} & (\phi^{(k)})''_{K_2^{(k)}x_2^{(k)}} \end{bmatrix} = 1 \,,$$

we conclude that as $M \to \infty$,

$$\det \begin{bmatrix} \partial_{K_1^{(k)}} x_1^{(k)} & \partial_{K_2^{(k)}} x_1^{(k)} \\ \partial_{K_1^{(k)}} x_2^{(k)} & \partial_{K_2^{(k)}} x_2^{(k)} \end{bmatrix} \to \det \begin{bmatrix} (\phi^{(k)})''_{K_1^{(k)}K_1^{(k)}} & (\phi^{(k)})''_{K_1^{(k)}K_2^{(k)}} \\ (\phi^{(k)})''_{K_2^{(k)}K_1^{(k)}} & (\phi^{(k)})''_{K_2^{(k)}K_2^{(k)}} \end{bmatrix} ,$$

which confirms that in the stationary phase approximation (generating the determinant on the right-hand side) we retain a coordinate transformation (generating the determinant on the left-hand side) in accordance with the Maslov representation of the Green's function. The *condition* of non-singularity is satisfied if we enforce [cf., equation (2.63)]

$$M^{-1}\Delta x_3 < \frac{(K_3^{\text{prin}})^3}{\|K_{1,2}^{(k)}\|(\omega^{(k)})^2} \left\| c^{-1}\partial_{x_{1,2}^{(k)}} c^{-1} \right\|^{-1} , \tag{2.65}$$

where the first factor on the right-hand side is bounded in view of its homogeneity property (degree 0). Observe that if the medium were laterally homogeneous, M could simply be chosen equal to 1. The same condition appears in the proof that the compositions in equation (2.38) preserve the geometrical aspects of the propagation of the singularities (Le Rousseau *et al.*, 2001). Note that the *vertical* stepsize is bounded in terms of a norm of *horizontal* medium derivatives.

Second, we establish that the stationary phase approximation of each constituent oscillatory integral representation, in particular the initial one ($k = 1$), reproduces the geometrical spreading i.e., the solution of the transport equation. Using equation (2.62), we find that

$$\det \begin{bmatrix} (\phi^{(k)})''_{K_1^{(k)}K_1^{(k)}} & (\phi^{(k)})''_{K_1^{(k)}K_2^{(k)}} \\ (\phi^{(k)})''_{K_2^{(k)}K_1^{(k)}} & (\phi^{(k)})''_{K_2^{(k)}K_2^{(k)}} \end{bmatrix} = \frac{(\omega^{(k)})^2}{c^2(K_3^{\text{prin}})^4} \left(\frac{\Delta x_3}{M}\right)^2 . \tag{2.66}$$

The equation $(\phi^{(k)})'_{\omega^{(k)}} = 0$ leads to the relation

$$t^{(k)} - t^{(k-1)} = \frac{\omega^{(k)}}{c^2 K_3^{\text{prin}}} \frac{\Delta x_3}{M}$$

so that

$$\frac{\Delta x_3}{M} = \frac{(t^{(k)} - t^{(k-1)})\, c^2 K_3^{\text{prin}}}{\omega^{(k)}} . \tag{2.67}$$

Substituting this equation into equation (2.66) then yields

$$\left|\det\begin{bmatrix} (\phi^{(k)})''_{K_1^{(k)}K_1^{(k)}} & (\phi^{(k)})''_{K_1^{(k)}K_2^{(k)}} \\ (\phi^{(k)})''_{K_2^{(k)}K_1^{(k)}} & (\phi^{(k)})''_{K_2^{(k)}K_2^{(k)}} \end{bmatrix}\right|^{-1/2} = \frac{c(K_3^{\text{prin}})^2}{\omega^{(k)}}\frac{M}{\Delta x_3} = \frac{K_3^{\text{prin}}}{c\,(t^{(k)}-t^{(k-1)})}\,, \quad (2.68)$$

in which $t^{(k)} - t^{(k-1)}$ represents the travel time to cross the k^{th} slab. We recognize the geometrical spreading – for $x^{(k-1)}, \omega^{(k)}$ fixed – as well as the radiation pattern of a vertical force ($\omega^{-1}K_3^{\text{prin}}$) which is removed by the initial decomposition introduced in equations (2.24) and (2.35) – the factor ω^{-1} accounts for the fact that we employ the particle velocity rather than displacement.

2.5 Trotter-product double-square-root propagator

In the remote sensing problem one places sources and receivers at the surface ($x_3 = 0$). Sources (at $s_{1,2}$) generate acoustic waves, which scatter at points $\boldsymbol{x} = (x_{1,2}, z)$ in the subsurface and are observed at $r_{1,2}$ as a function of time t. (The 3^{rd} axis points into the subsurface.) To image the observations, the sources and receivers' measurements are propagated into the subsurface in a presumed background medium back to the time when the scattering took place (Claerbout, 1986). The thus obtained operator is composed of a propagator of the previous type associated with the source and a propagator of the previous type associated with the receiver.

2.5.1 The imaging kernel

Using, for example, arguments based on reciprocity (De Hoop & De Hoop, 2000), it follows that the process of seismic imaging can be written in the operator form[4]

$$(\mathrm{I}W_2)(x_{1,2}, z) = (1/2\pi)\int\int\int \mathcal{I}(x_{1,2}, z; s_{1,2}, r_{1,2}, t)\, W_2(s_{1,2}, r_{1,2}, t)\,\mathrm{d}t\,\mathrm{d}s_1\mathrm{d}s_2\mathrm{d}r_1\mathrm{d}r_2\,, \quad (2.69)$$

[4] i.e., the adjoint of the operator generated by the first-order (single-backscattering) term of the generalized Bremmer series

where W_2 represents the (upgoing component of the) data. Here, $\mathcal{I}$ denotes the distributional imaging kernel which can be written as the Trotter-product representation

$$\mathcal{I}^M(x_{1,2},z;s_{1,2},r_{1,2},t) = \int_{\mathbb{R}}(1/2\pi)\mathrm{d}\omega \tag{2.70}$$
$$\int_{\mathbb{R}^{4(M+1)}}\int_{\mathbb{R}^{4M}}\prod_{i=0}^{M}(1/2\pi)^2\mathrm{d}\widetilde{K}_1^{(i)}\mathrm{d}\widetilde{K}_2^{(i)}(1/2\pi)^2\mathrm{d}\widehat{K}_1^{(i)}\mathrm{d}\widehat{K}_2^{(i)}\prod_{j=0}^{M-1}\mathrm{d}s_1^{(j)}\mathrm{d}s_2^{(j)}\mathrm{d}r_1^{(j)}\mathrm{d}r_2^{(j)}\widetilde{\mathcal{R}}\widehat{\mathcal{R}}$$
$$\times\exp\Bigg[-\mathrm{i}\sum_{k=1}^{M}\{\widetilde{K}_\sigma^{(k)}(s_\sigma^{(k)}-s_\sigma^{(k-1)})+\widehat{K}_\sigma^{(k)}(r_\sigma^{(k)}-r_\sigma^{(k-1)})$$
$$+\Big[K_3(s_\mu^{(k)},\bar{\zeta}_k,\widetilde{K}_\nu^{(k)},\omega)+K_3(r_\mu^{(k)},\bar{\zeta}_k,\widehat{K}_\nu^{(k)},\omega)\Big]M^{-1}\Delta x_3\}\Bigg]\exp(\mathrm{i}\omega t)\ ,$$

forming a sequence, with $\Delta x_3 = z$ and

$$s_{1,2}^{(0)} = \underbrace{s_{1,2}}_{s'}\ ,\ r_{1,2}^{(0)} = \underbrace{r_{1,2}}_{r'}\ ,\ s_{1,2}^{(M)} = r_{1,2}^{(M)} = x_{1,2}\ ,\ \zeta_0 = 0\ ,\ \zeta_M = z\ . \tag{2.71}$$

The imaging kernel follows the simultaneous downward continuation of sources (variables with $\widetilde{\ }$) and receivers (variables with $\widehat{\ }$) in accordance with the one-way Trotter product represented by equation (2.37). In the absence of turning rays, in the high-frequency approximation, the kernel will approach $\delta(t - T((r_{1,2},0),(x_{1,2},z),(s_{1,2},0)))$ with T denoting two-way travel time. (This expression has the form of a pull-back within the distributions in $\boldsymbol{x}$.)

Let us now rotate coordinates at each level to (intermediate) 'midpoint' and 'offset', i.e.,

$$\begin{array}{rclcrcl} y_{1,2}^{(k)} & = & \frac{1}{2}(r_{1,2}^{(k)}+s_{1,2}^{(k)}) & , & h_{1,2}^{(k)} & = & \frac{1}{2}(r_{1,2}^{(k)}-s_{1,2}^{(k)})\ , \\ K_{1,2}^{(k)} & = & \widehat{K}_{1,2}^{(k)}+\widetilde{K}_{1,2}^{(k)} & , & k_{1,2}^{(k)} & = & \widehat{K}_{1,2}^{(k)}-\widetilde{K}_{1,2}^{(k)}\ . \end{array} \tag{2.72}$$

Such change anticipates the estimation of the wavefront set of the imaging kernel. We have

$$\mathrm{d}s_1^{(j)}\mathrm{d}s_2^{(j)}\mathrm{d}r_1^{(j)}\mathrm{d}r_2^{(j)} = 16\,\mathrm{d}y_1^{(j)}\mathrm{d}y_2^{(j)}\mathrm{d}h_1^{(j)}\mathrm{d}h_2^{(j)}\ ,$$
$$\mathrm{d}\widetilde{K}_1^{(i)}\mathrm{d}\widetilde{K}_2^{(i)}\mathrm{d}\widehat{K}_1^{(i)}\mathrm{d}\widehat{K}_2^{(i)} = \tfrac{1}{16}\,\mathrm{d}K_1^{(i)}\mathrm{d}K_2^{(i)}\mathrm{d}k_1^{(i)}\mathrm{d}k_2^{(i)}$$

and we write the distribution kernel of the double-square-root propagator, J, as the sequence

$$\mathcal{J}^M(x_{1,2},z;y_{1,2},h_{1,2},t;h^{\text{im}}_{1,2}) = \int_{\mathbb{R}}(1/2\pi)\mathrm{d}\omega \tag{2.73}$$
$$\tfrac{1}{16}\int_{\mathbb{R}^{4(M+1)}}\int_{\mathbb{R}^{4M}}\prod_{i=0}^{M}(1/2\pi)^2\mathrm{d}K_1^{(i)}\mathrm{d}K_2^{(i)}(1/2\pi)^2\mathrm{d}k_1^{(i)}\mathrm{d}k_2^{(i)}\prod_{j=0}^{M-1}\mathrm{d}y_1^{(j)}\mathrm{d}y_2^{(j)}\mathrm{d}h_1^{(j)}\mathrm{d}h_2^{(j)}\widetilde{\mathcal{R}}\widehat{\mathcal{R}}$$
$$\times\exp(\mathrm{i}\omega t)\exp\Bigg[-\mathrm{i}\sum_{k=1}^{M}\{K_\sigma^{(k)}y_\sigma^{(k)}-K_\sigma^{(k)}y_\sigma^{(k-1)}+k_\sigma^{(k)}h_\sigma^{(k)}-k_\sigma^{(k)}h_\sigma^{(k-1)}+$$
$$\Big[K_3(y_\mu^{(k)}-h_\mu^{(k)},\bar{\zeta}_k,\tfrac{1}{2}(K_\nu^{(k)}-k_\nu^{(k)}),\omega)$$
$$+K_3(y_\mu^{(k)}+h_\mu^{(k)},\bar{\zeta}_k,\tfrac{1}{2}(K_\nu^{(k)}+k_\nu^{(k)}),\omega)\Big]M^{-1}\Delta x_3\}\Bigg]\ ,$$

subject to

$$y_{1,2}^{(0)}=\underbrace{y_{1,2}}_{\boldsymbol{y}'}\ (\text{midpoint})\ ,\ y_{1,2}^{(M)}=x_{1,2}\ ,\ h_{1,2}^{(0)}=\underbrace{h_{1,2}}_{\boldsymbol{h}'}\ (\text{offset})\ ,\ h_{1,2}^{(M)}=h^{\text{im}}_{1,2}\ . \tag{2.74}$$

In the limit $M\to\infty$, we write

$$(\mathrm{J}W_2)(x_{1,2},z;h^{\text{im}}_{1,2}) = (1/2\pi)\,16\int\!\!\int\!\!\int\mathcal{J}(x_{1,2},z;y_{1,2},h_{1,2},t;h^{\text{im}}_{1,2})$$
$$\times W_2(y_{1,2}-h_{1,2},y_{1,2}+h_{1,2},t)\,\mathrm{d}y_1\mathrm{d}y_2\mathrm{d}h_1\mathrm{d}h_2\ \mathrm{d}t\ , \tag{2.75}$$

and the image with the sequence in equation (2.70) is obtained at $h^{\text{im}}_{1,2}=0$. ($\mathcal{J}|_{h^{\text{im}}_{1,2}=0}=\mathcal{I}$.)

2.5.2 The canonical relation of the imaging operator ($h^{\text{im}}_{1,2}=0$)

The phase function associated with distribution (2.73) is given by

$$\Phi(\boldsymbol{x},y_{1,2},h_{1,2},t,\langle y_\mu^{(l)}\rangle_{1\le l\le M-1},\langle K_\nu^{(k)}\rangle_{1\le k\le M},\langle h_\mu^{(l)}\rangle_{1\le l\le M-1},\langle k_\nu^{(k)}\rangle_{1\le k\le M},\omega)$$
$$=\omega t-\sum_{k=1}^{M}\Bigg\{K_\sigma^{(k)}(y_\sigma^{(k)}-y_\sigma^{(k-1)})+k_\sigma^{(k)}(h_\sigma^{(k)}-h_\sigma^{(k-1)})$$
$$+M^{-1}\Delta x_3\Big[K_3^{\text{prin}}(y_\mu^{(k)}-h_\mu^{(k)},\bar{\zeta}_k,\tfrac{1}{2}(K_\nu^{(k)}-k_\nu^{(k)}),\omega)$$
$$+K_3^{\text{prin}}(y_\mu^{(k)}+h_\mu^{(k)},\bar{\zeta}_k,\tfrac{1}{2}(K_\nu^{(k)}+k_\nu^{(k)}),\omega)\Big]\Bigg\}\ , \tag{2.76}$$

where $\mu=1,2$ and $\nu=1,2$ and $\boldsymbol{x}=(y_{1,2}^{(M)},z)$. If we collect the phase variables,

$$\theta=(\langle y_\mu^{(l)}\rangle_{1\le l\le M-1},\langle K_\nu^{(k)}\rangle_{1\le k\le M},\langle h_\mu^{(l)}\rangle_{1\le l\le M-1},\langle k_\nu^{(k)}\rangle_{1\le k\le M},\omega)\ , \tag{2.77}$$

the stationary point set, Σ_Φ, is defined as

$$\Sigma_\Phi = \{(\boldsymbol{x}, y_{1,2}, h_{1,2}, t, \theta) \mid (\phi')_\theta(\boldsymbol{x}, y_{1,2}, h_{1,2}, t, \theta) = 0\} \ . \tag{2.78}$$

The defining equations of the stationary point set, Σ_Φ, are then

$$\begin{aligned}(\Phi')_{y_\sigma^{(l)}} &= -K_\sigma^{(l)} + K_\sigma^{(l+1)} - \Big\{ (K_3^{\text{prin}'})_{x_\sigma}(y_\mu^{(l)} - h_\mu^{(l)}, \bar{\zeta}_l, \tfrac{1}{2}(K_\nu^{(l)} - k_\nu^{(l)}), \omega) \\ &\quad + (K_3^{\text{prin}'})_{x_\sigma}(y_\mu^{(l)} + h_\mu^{(l)}, \bar{\zeta}_l, \tfrac{1}{2}(K_\nu^{(l)} + k_\nu^{(l)}), \omega) \Big\} M^{-1}\Delta x_3 = 0 \ , \end{aligned} \tag{2.79}$$

$$\begin{aligned}(\Phi')_{K_\sigma^{(k)}} &= -y_\sigma^{(k)} + y_\sigma^{(k-1)} - \Big\{ (K_3^{\text{prin}'})_{K_\sigma}(y_\mu^{(k)} - h_\mu^{(k)}, \bar{\zeta}_k, \tfrac{1}{2}(K_\nu^{(k)} - k_\nu^{(k)}), \omega) \\ &\quad + (K_3^{\text{prin}'})_{K_\sigma}(y_\mu^{(k)} + h_\mu^{(k)}, \bar{\zeta}_k, \tfrac{1}{2}(K_\nu^{(k)} + k_\nu^{(k)}), \omega) \Big\} \tfrac{1}{2} M^{-1}\Delta x_3 = 0 \ , \end{aligned} \tag{2.80}$$

$$\begin{aligned}(\Phi')_{h_\sigma^{(l)}} &= -k_\sigma^{(l)} + k_\sigma^{(l+1)} - \Big\{ -(K_3^{\text{prin}'})_{x_\sigma}(y_\mu^{(l)} - h_\mu^{(l)}, \bar{\zeta}_l, \tfrac{1}{2}(K_\nu^{(l)} - k_\nu^{(l)}), \omega) \\ &\quad + (K_3^{\text{prin}'})_{x_\sigma}(y_\mu^{(l)} + h_\mu^{(l)}, \bar{\zeta}_l, \tfrac{1}{2}(K_\nu^{(l)} + k_\nu^{(l)}), \omega) \Big\} M^{-1}\Delta x_3 = 0 \ , \end{aligned} \tag{2.81}$$

$$\begin{aligned}(\Phi')_{k_\sigma^{(k)}} &= -h_\sigma^{(k)} + h_\sigma^{(k-1)} - \Big\{ -(K_3^{\text{prin}'})_{K_\sigma}(y_\mu^{(k)} - h_\mu^{(k)}, \bar{\zeta}_k, \tfrac{1}{2}(K_\nu^{(k)} - k_\nu^{(k)}), \omega) \\ &\quad + (K_3^{\text{prin}'})_{K_\sigma}(y_\mu^{(k)} + h_\mu^{(k)}, \bar{\zeta}_k, \tfrac{1}{2}(K_\nu^{(k)} + k_\nu^{(k)}), \omega) \Big\} \tfrac{1}{2} M^{-1}\Delta x_3 = 0 \ , \end{aligned} \tag{2.82}$$

$$\begin{aligned}(\Phi')_\omega &= t - M^{-1}\Delta x_3 \sum_{k=1}^{M} \Big\{ (K_3^{\text{prin}'})_\omega(y_\mu^{(k)} - h_\mu^{(k)}, \bar{\zeta}_k, \tfrac{1}{2}(K_\nu^{(k)} - k_\nu^{(k)}), \omega) \\ &\quad + (K_3^{\text{prin}'})_\omega(y_\mu^{(k)} + h_\mu^{(k)}, \bar{\zeta}_k, \tfrac{1}{2}(K_\nu^{(k)} + k_\nu^{(k)}), \omega) \Big\} = 0 \ , \end{aligned} \tag{2.83}$$

for $\sigma = 1, 2$ and $l = 1, \cdots, M-1$, $k = 1, \cdots, M$. In analogy with the analysis of the one-way wave propagator, one can view the solution of the system of equations (2.79)-(2.83) as an approximation on a lattice of the geometry of the Maslov high-frequency solution of the two-way scattering process, as represented in Figure 2.2.

An extension of the proof of Appendix B shows that the phase Φ is non-degenerate. The associated Lagrangian submanifold of the cotangent bundle associated with the manifold of

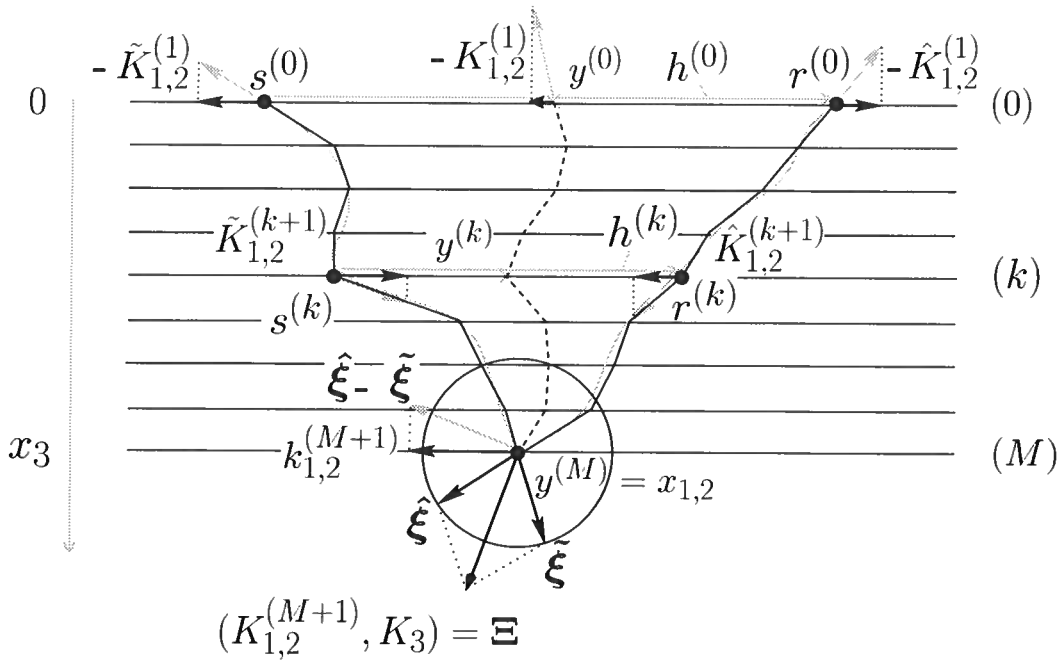

Figure 2.2. Bicharacteristics and wave vectors in the two-way scattering process.

points $\{(\boldsymbol{x}, y_{1,2}, h_{1,2}, t)\}$, is now given by

$$\begin{aligned} \Sigma_\Phi \quad &\to \Lambda_\Phi \\ (\boldsymbol{x}, y_{1,2}, h_{1,2}, t, \theta) \quad &\mapsto \quad (\boldsymbol{x}, -K_{1,2}^{(M+1)}, -K_3; y_{1,2}, h_{1,2}, t, K_{1,2}^{(1)}, k_{1,2}^{(1)}, \omega) \\ &\qquad = (\boldsymbol{x}, (\Phi')_{\boldsymbol{x}}; y_{1,2}, h_{1,2}, t, (\Phi')_{y_{1,2}}, (\Phi')_{h_{1,2}}, (\Phi')_t) \ , \end{aligned} \tag{2.84}$$

following equations (2.45)-(2.46) for the source and receiver contributions:

$$-K_\nu^{(M+1)} = -(\tilde{K}_\nu^{(M+1)} + \hat{K}_\nu^{(M+1)}) \ ,$$

in accordance with the transformation to midpoint; K_3 is given by

$$K_3^{\text{prin}}(x_{1,2}, z, \tfrac{1}{2}(K_\nu^{(M+1)} - k_\nu^{(M+1)}), \omega) + K_3^{\text{prin}}(x_{1,2}, z, \tfrac{1}{2}(K_\nu^{(M+1)} + k_\nu^{(M+1)}), \omega) \ .$$

As before, the canonical relation, C_Φ, is obtained by twisting the Lagrangian submanifold Λ_Φ,

$$C_\Phi = \left\{ (\boldsymbol{x}, -K_{1,2}^{(M+1)}, -K_3; y_{1,2}, h_{1,2}, t, -K_{1,2}^{(1)}, -k_{1,2}^{(1)}, -\omega) \;\middle|\; (\boldsymbol{x}, -K_{1,2}^{(M+1)}, -K_3; y_{1,2}, h_{1,2}, t, K_{1,2}^{(1)}, k_{1,2}^{(1)}, \omega) \in \Lambda_\Phi \right\} .$$

The so-called isochrone, the projection of the canonical relation onto the subsurface for

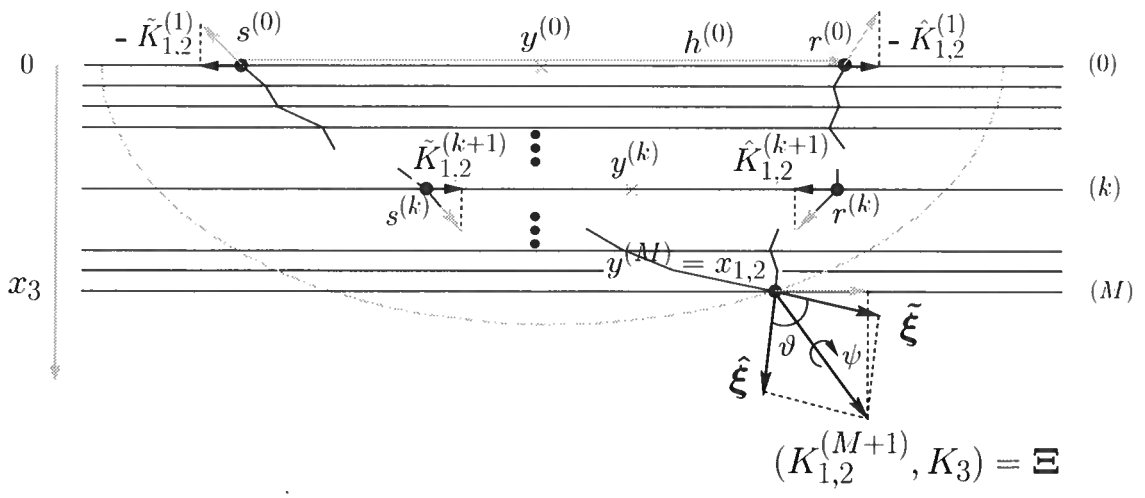

Figure 2.3. Isochrone: illustration of a subsurface section of the canonical relation in the two-way scattering process.

fixed two-way travel time t and source and receiver, i.e., fixed $h_{1,2}$ and $y_{1,2}$, is shown in Figure 2.3.

2.5.3 The isochrone and its cotangent directions

The *isochrone* is given as the singular support of $\mathcal{I}_0 = \mathrm{I}(\delta(\boldsymbol{s}'-\boldsymbol{s}'_0)\otimes\delta(\boldsymbol{r}'-\boldsymbol{r}'_0)\otimes\delta(t-t_0))$ [cf., equation (2.69)], which is distributional in $(x_{1,2}, z)$ for given $\boldsymbol{s}'_0$, $\boldsymbol{r}'_0$ and t_0. Here, we are not just interested in the singular support but rather in its wavefront set: $\mathrm{WF}(\mathcal{I}_0)$. With the aid of the canonical relation previously defined, we have

$$\mathrm{WF}(\mathcal{I}_0) = C_\Phi \circ \mathrm{WF}(\delta(\boldsymbol{s}' - \boldsymbol{s}'_0) \otimes \delta(\boldsymbol{r}' - \boldsymbol{r}'_0) \otimes \delta(t - t_0)) \tag{2.85}$$

so that

$$\mathrm{WF}(\mathcal{I}_0) = \Big\{ (\boldsymbol{x}, \boldsymbol{\Xi}) \;\Big|\; \exists\, \boldsymbol{y}'_0, \boldsymbol{h}'_0, t_0, K_{1,2}^{(1)}, k_{1,2}^{(1)}, \omega : (\boldsymbol{x}, \boldsymbol{\Xi}; \boldsymbol{y}'_0, \boldsymbol{h}'_0, t_0, K_{1,2}^{(1)}, k_{1,2}^{(1)}, -\omega) \in C_\Phi \Big\}, \tag{2.86}$$

which means that the cotangent vector, $\boldsymbol{\Xi}$, is the sum of the two cotangent vectors at $\boldsymbol{x}$ associated with the two bicharacteristics joining the source, $\boldsymbol{s}'_0$, the scattering point, $\boldsymbol{x}$, and the receiver, $\boldsymbol{r}'_0$ with initial 'slopes' given by $\omega^{-1}\tilde{K}_\nu^{(1)}, \omega^{-1}\hat{K}_\nu^{(1)}$, and 'two-way' travel time t_0 as illustrated in Figure 2.3. The limit $M \to \infty$ can be understood with the use of Appendix C.

To find a parameterization for the canonical relation and an expression for the cotan-

gent vectors Ξ, we reconsider the wave vectors $(k = 1)$

$$\widetilde{K}^{(1)}_{1,2} = \omega \boldsymbol{p}_{s_{1,2}} , \quad \widehat{K}^{(1)}_{1,2} = \omega \boldsymbol{p}_{r_{1,2}} , \quad \omega,$$

dual to $(s_{1,2}, r_{1,2}, t)$, as well as $(k = M)$

$$(\widetilde{K}^{(M+1)}_{1,2}, K^{\text{prin}}_3(s^{(M)}_{1,2}, \bar{\zeta}_M, \widetilde{K}^{(M+1)}_{1,2})) = \widetilde{\boldsymbol{\xi}} \quad \text{at } (x_{1,2}, z) ,$$

$$(\widehat{K}^{(M+1)}_{1,2}, K^{\text{prin}}_3(r^{(M)}_{1,2}, \bar{\zeta}_M, \widehat{K}^{(M+1)}_{1,2})) = \widehat{\boldsymbol{\xi}} \quad \text{at } (x_{1,2}, z) ,$$

defining, through the canonical relation,

$$\Xi = \widetilde{\boldsymbol{\xi}} + \widehat{\boldsymbol{\xi}} ,$$

dual to $(x_{1,2}, z)$.

The polar angles associated with the covector Ξ are denoted by (θ_Ξ, ψ_Ξ). We now introduce the parameters scattering angle and azimuth $\{\vartheta, \psi\}$ at $(x_{1,2}, z)$ according to

$$\begin{aligned} \cos\vartheta &= \|\widetilde{\boldsymbol{\xi}}\|^{-1}\widetilde{\boldsymbol{\xi}} \cdot \|\widehat{\boldsymbol{\xi}}\|^{-1}\widehat{\boldsymbol{\xi}} , \\ \cos\psi &= \boldsymbol{r}_0 \cdot \boldsymbol{r}_\psi , \end{aligned}$$

where

$$\boldsymbol{r}_\psi = [\sin\vartheta]^{-1}\|\Xi\|^{-1}\Xi \wedge \|\widetilde{\boldsymbol{\xi}}\|^{-1}\widetilde{\boldsymbol{\xi}} \wedge \|\widehat{\boldsymbol{\xi}}\|^{-1}\widehat{\boldsymbol{\xi}} , \tag{2.87}$$

and $\boldsymbol{r}_0$ is given as the vertical vector pointing up (negative x_3 direction) in the plane orthogonal to Ξ as illustrated in Figure 2.4.

By analyzing Figure 2.4, we find that through the canonical relation

$$\begin{aligned} k^{(M+1)}_1 &\overset{\text{WF}}{=} \widehat{\xi}_1 - \widetilde{\xi}_1 \qquad (2.88) \\ &= -\frac{2\omega}{c(x_{1,2}, z)} \sin\left(\tfrac{1}{2}\vartheta\right) [\sin(\psi_\Xi)\sin(\psi) + \cos(\theta_\Xi)\cos(\psi_\Xi)\cos(\psi)] , \\ k^{(M+1)}_2 &\overset{\text{WF}}{=} \widehat{\xi}_2 - \widetilde{\xi}_2 \qquad (2.89) \\ &= \frac{2\omega}{c(x_{1,2}, z)} \sin\left(\tfrac{1}{2}\vartheta\right) [\cos(\psi_\Xi)\sin(\psi) - \cos(\theta_\Xi)\sin(\psi_\Xi)\cos(\psi)] , \end{aligned}$$

which define, given (θ_Ξ, ψ_Ξ), a mapping $(\vartheta, \psi) \mapsto (k^{(M+1)}_1, k^{(M+1)}_2)$. On the other hand, we have

$$K^{(M+1)}_1 \overset{\text{WF}}{=} \Xi_1 = \frac{2\omega}{c(x_{1,2}, z)} \cos\left(\tfrac{1}{2}\vartheta\right) \cos(\psi_\Xi)\sin(\theta_\Xi) , \tag{2.90}$$

$$K^{(M+1)}_2 \overset{\text{WF}}{=} \Xi_2 = \frac{2\omega}{c(x_{1,2}, z)} \cos\left(\tfrac{1}{2}\vartheta\right) \sin(\psi_\Xi)\sin(\theta_\Xi) , \tag{2.91}$$

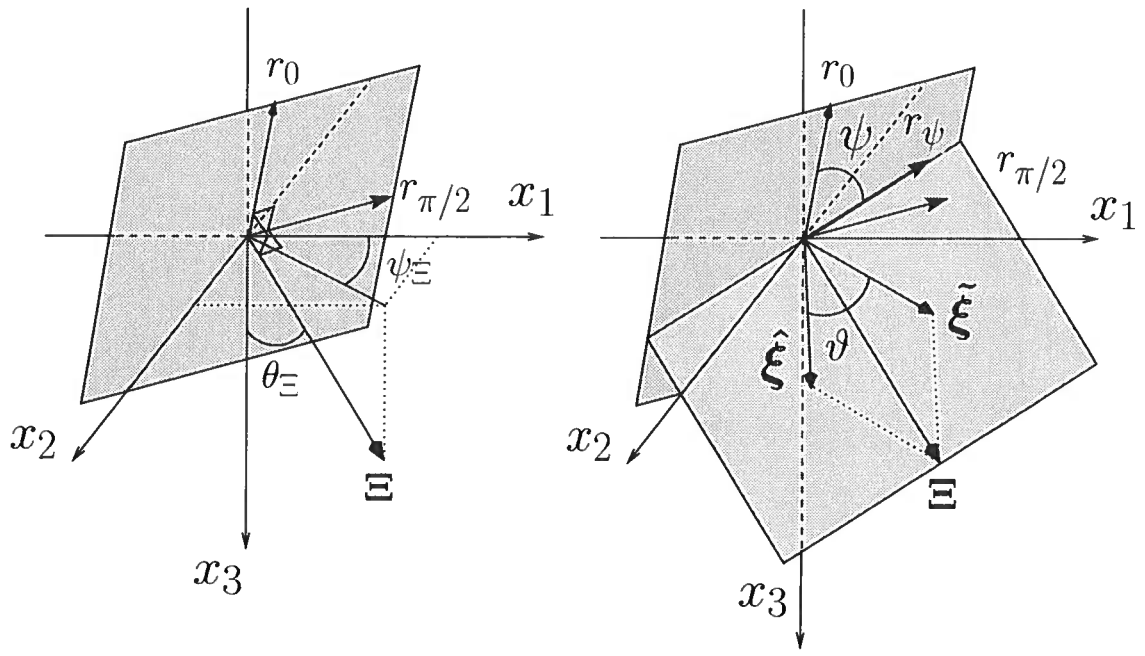

Figure 2.4. Euler angles associated with the two-way scattering process. Left: The unit vector-with positive first component along the intersection of the vertical plane containing Ξ and the horizontal plane is denoted $\boldsymbol{r}_{\pi/2}$. We then denote $\boldsymbol{r}_0 = \Xi \times \boldsymbol{r}_{\pi/2}$. Right: call $\boldsymbol{r}_\psi$ the unit vector in the direction $\widetilde{\boldsymbol{\xi}} - \widehat{\boldsymbol{\xi}}$. It lies along the intersection of the scattering plane $(\widetilde{\boldsymbol{\xi}},\widehat{\boldsymbol{\xi}})$ with the plane orthogonal to Ξ, i.e., $(\boldsymbol{r}_0, \boldsymbol{r}_{\pi/2})$. The azimuth angle is defined as the angle between $\boldsymbol{r}_\psi$ and $\boldsymbol{r}_0$, while the scattering angle ϑ is defined as the angle between $\widetilde{\boldsymbol{\xi}}$ and $\widehat{\boldsymbol{\xi}}$.

while

$$K_3(y_{1,2}^{(M)}, \bar{\zeta}_M, \tfrac{1}{2}(K_{1,2}^{(M+1)} - k_{1,2}^{(M+1)})) + K_3(y_{1,2}^{(M)}, \bar{\zeta}_M, \tfrac{1}{2}(K_{1,2}^{(M+1)} + k_{1,2}^{(M+1)}))$$
$$\overset{\text{WF}}{=} \Xi_3 = \frac{2\omega}{c(x_{1,2}, z)} \cos\left(\tfrac{1}{2}\vartheta\right) \cos(\theta_\Xi) \,. \tag{2.92}$$

We observe that the construction of Ξ_3 out of $\widetilde{\boldsymbol{\xi}}, \widehat{\boldsymbol{\xi}}$ is independent of azimuth in view of the isotropy of the medium here.

In general, we will have four unknown angles $(\vartheta, \psi), (\theta_\Xi, \psi_\Xi)$ and four accessible spectral variables, $(k_{1,2}^{(M+1)}, K_{1,2}^{(M+1)})$. They are a manifestation of offset and midpoint in the subsurface. The mentioned scattering angle and azimuth together form the set of parameters along the characteristic strips in the wavefront set of the single-scattered seismic data [see Stolk and de Hoop (2000)]. It is along these characteristic strips that we can verify the velocity model by differential semblance.

2.5.4 Angle-gather imaging condition

The process of imaging, through the path integral, induces a composite mapping

$$h_{1,2} \overset{\mathcal{J}}{\mapsto} h_{1,2}^{\text{im}} \overset{\text{dual}}{\mapsto} k_{1,2}^{(M+1)} \overset{\text{WF}}{\mapsto} (\vartheta, \psi) \ .$$

To highlight the redundancy in the data, the redundancy being parameterized by (ϑ, ψ), we will create images as a function of (ϑ, ψ). To this end, we carry out a final Fourier transform of the kernel of the double-square-root propagator, $\mathcal{J}^M$, with respect to $(h_1^{(M)}, h_2^{(M)})$, viz.

$$\bar{\mathcal{J}}^M(x_{1,2}, z; y_{1,2}, h_{1,2}, t; (\vartheta, \psi)) = \int_{\mathbb{R}} (1/2\pi) \mathrm{d}\omega \int_{\mathbb{R}^2} \mathrm{d}h_1^{(M)} \mathrm{d}h_2^{(M)} \tag{2.93}$$

$$\tfrac{1}{16} \int_{\mathbb{R}^{4(M+1)}} \int_{\mathbb{R}^{4M}} \prod_{i=0}^{M} (1/2\pi)^2 \mathrm{d}K_1^{(i)} \mathrm{d}K_2^{(i)} (1/2\pi)^2 \mathrm{d}k_1^{(i)} \mathrm{d}k_2^{(i)} \prod_{j=0}^{M-1} \mathrm{d}y_1^{(j)} \mathrm{d}y_2^{(j)} \mathrm{d}h_1^{(j)} \mathrm{d}h_2^{(j)} \widetilde{\mathcal{R}} \widehat{\mathcal{R}}$$

$$\times \exp(\mathrm{i} k_\sigma^{(M+1)} h_\sigma^{(M)}) \exp(\mathrm{i}\omega t) \exp\Bigg[-\mathrm{i} \sum_{k=1}^{M} \{ K_\sigma^{(k)} y_\sigma^{(k)} - K_\sigma^{(k)} y_\sigma^{(k-1)} + k_\sigma^{(k)} h_\sigma^{(k)} - k_\sigma^{(k)} h_\sigma^{(k-1)}$$

$$+ \Big[K_3(y_\mu^{(k)} - h_\mu^{(k)}, \bar{\zeta}_k, \tfrac{1}{2}(K_\nu^{(k)} - k_\nu^{(k)})) + K_3(y_\mu^{(k)} + h_\mu^{(k)}, \bar{\zeta}_k, \tfrac{1}{2}(K_\nu^{(k)} + k_\nu^{(k)})) \Big] M^{-1} \Delta x_3 \} \Bigg]$$

subject to the substitution

$$k_1^{(M+1)} = -\frac{2\omega}{c(x_{1,2}, z)} \sin\left(\tfrac{1}{2}\vartheta\right) \left[\sin(\psi_{\Xi}) \sin(\psi) + \cos(\theta_{\Xi}) \cos(\psi_{\Xi}) \cos(\psi) \right] \ ,$$

$$k_2^{(M+1)} = \frac{2\omega}{c(x_{1,2}, z)} \sin\left(\tfrac{1}{2}\vartheta\right) \left[\cos(\psi_{\Xi}) \sin(\psi) - \cos(\theta_{\Xi}) \sin(\psi_{\Xi}) \cos(\psi) \right] \ .$$

We consider the outcome at $y_{1,2}^{(M)} = x_{1,2}$ as a function of (ϑ, ψ), which defines the *angle common image point gather* at depth z. Such angle gathers are controlled by dip $(\theta_{\Xi}, \psi_{\Xi},)$. To create these gathers we therefore need to determine the direction of the isochrone cotangent vector, which is the subject of the next section.

2.6 Multiresolution approach to determining the migration dip (isochrone cotangent direction)

In the simplest situation, let $\psi = \psi_{\Xi} = 0$ ('in-line' scattering). Then we obtain the angle ϑ out of the ratio

$$\tan\left(\tfrac{1}{2}\vartheta\right) = \frac{k_1^{(M)}}{\Xi_3} \tag{2.94}$$

and we just have to determine Ξ_3. In general, we will have to determine both $(\theta_{\Xi}, \psi_{\Xi})$. We will do so by a careful windowed Fourier analysis.

The estimation of the isochrone cotangent direction, known in seismology as the migration dip, can be carried out with the aid of a continuous wavelet transform. Let

$$\phi^\tau(\boldsymbol{x}) = \tau^{3/4}\phi(\tau^{1/2}\boldsymbol{x}) \tag{2.95}$$

be a symmetric, smooth function (Gaussian for example), and define the spatial Fourier transform (indicated by $\tilde{\cdot}$) P^τ_ϕ combined with a cut-off ϕ as

$$P^\tau_\phi f(\boldsymbol{\xi}, \boldsymbol{x}) = \exp\left(\tfrac{1}{2}\mathrm{i}\xi_j x_j\right)\, \tilde{f} * \tilde{\psi}_{\boldsymbol{x},\tau}(\boldsymbol{\xi}) \tag{2.96}$$

with

$$\psi_{\boldsymbol{x},\tau}(\boldsymbol{y}) = \overline{\phi^\tau(\boldsymbol{y} - \boldsymbol{x})}\,. \tag{2.97}$$

If ϕ is Gaussian, its Fourier transform $\tilde{\psi}_{\boldsymbol{x},t}$ is Gaussian also.

For f we now substitute the distribution imaging kernel $\mathcal{I}$, and employ the Fourier transform $\boldsymbol{x}_0 = (y^{(M)}_{1,2}, z) \mapsto (K^{(M+1)}_{1,2}, K_3) = \Xi_0$. Then $(\boldsymbol{x}_0, \Xi_0)$ does *not* belong to the wavefront set of $\mathcal{I}$ if there is a conic neighborhood of $(\boldsymbol{x}_0, \Xi_0)$ such that on this neighborhood for all $a, N \geq 1$,

$$|P^\tau_\phi \mathcal{I}(\boldsymbol{x}, \tau\Xi)| \leq C_{a,N}\tau^{-N} \quad \text{for} \quad \tau \geq 1\,,\ a^{-1} \leq |\Xi| \leq a\,,$$

a result due to Folland, and Córdoba and Fefferman (Folland, 1989). Taking the complement of such conic neighborhoods yields the singular direction associated with the isochrone.

2.7 Numerical example

We will briefly discuss an example of applying the method to synthetic data in the presence of caustics. The model (Brandsberg-Dahl *et al.*, 2000) (two-dimensional) contains a low-velocity lens (Figure 2.5). It further consists of two layers separated by a ramp-like interface that represent a target reflector with an adjacent fault.

The upper layer has constant gradients. The seismic data were generated by a time-domain finite-difference approach (the dominant frequency of the source signature was 35Hz). The vertical component of a typical shot gather over the lens is shown in Figure 2.6 (the direct arrival has been removed from the shot gathers by remodelling without the reflector present).

For the imaging we invoked the generalized screen approximation for the Trotter product (De Hoop *et al.*, 2000; Le Rousseau & De Hoop, 2001b). First we focus on a horizontal location to the right of the lens where small scattering angles correspond with single-pathing. The ACIG is shown in Figure 2.7(a). The perfect alignment of events confirms the redundancy in the data. Second, we generate an ACIG at a location where multipathing dominates [Figure 2.7(b)]. Still the seismic event is unfolded. Since we used the true model in our imaging, the events in the ACIGs are 'flat' so that the differential semblance with angle vanishes. An incorrect model would have resulted in 'non-flat' events in the ACIGs, whence

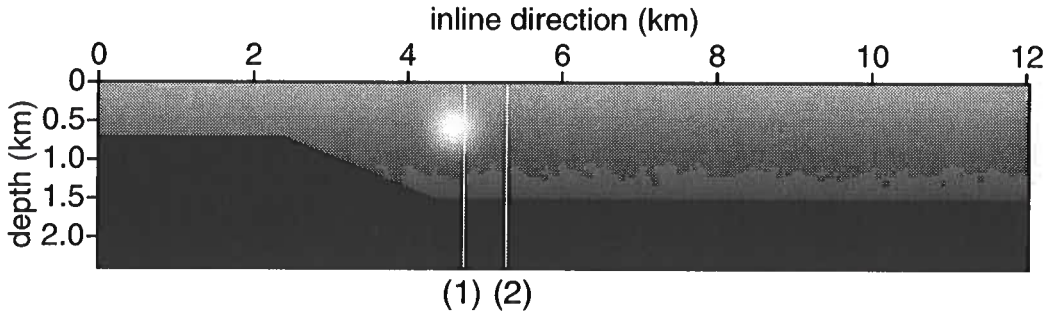

Figure 2.5. Lens model: wave-speed model for P waves with a low wave-speed zone. The maximum wave speed is 2400 m/s (black). The minimum wave speed is 1060 m/s (white).

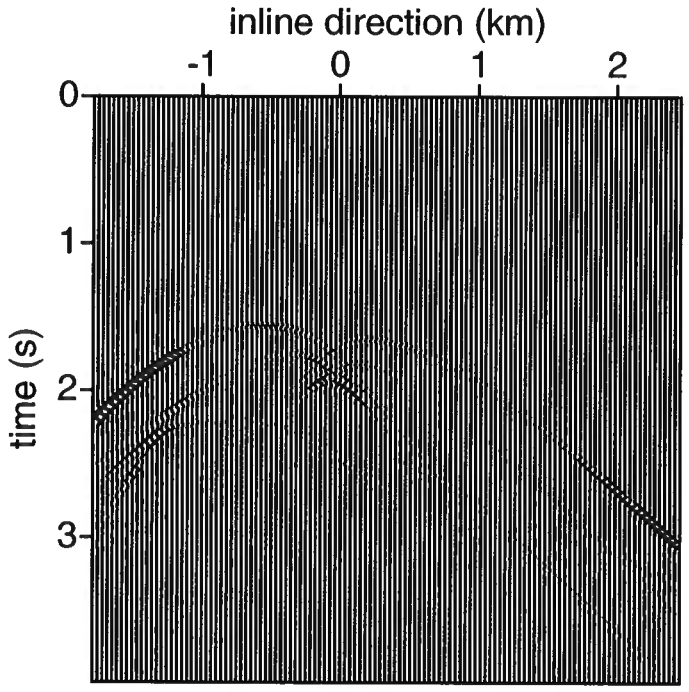

Figure 2.6. Typical shot record. source location is at location (1) of Figure 2.5.

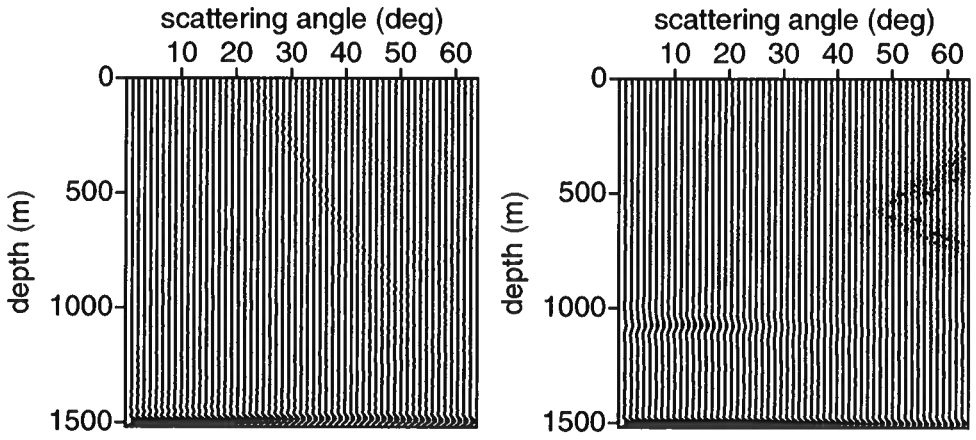

(a) (b)

Figure 2.7. ACIGs for a) location (2) and b) location (1) of Figure 2.5. No boundary condition were used for this computation which resulted in the artifacts close to 1000 m depth in a).

the differential semblance can be used as a mismatch criterion for tomographic inversion (De Hoop *et al.*, 2001b; Brandsberg-Dahl *et al.*, 2001).

2.8 Discussion

In this chapter, we have presented a microlocal (high-frequency) analysis of the double-square-root equation and its possible solution schemes. The double-square-root equation generates the wave-equation seismic imaging procedure. In particular, we found that (Maslov-)Kirchhoff and wave-equation imaging procedures are microlocally compatible and hence should yield the *same* result on the singular support of the image. More precisely they are equivalent if *all* the data are used (and the dataset is complete, i.e., 5D). However, high-frequency methods (Brandsberg-Dahl *et al.*, 2000; Brandsberg-Dahl *et al.*, 2001) show artifacts in ACIGs with a moveout (with angle) that are not visible in the results of Section 2.7. Such differences suggest that in the angle domain the two methods are not fully microlocally equivalent and call for further studies.

As far as the solution schemes of the double-square-root equation are concerned, we found a *fundamental condition* for the step size in depth that plays an important role in complex (strongly heterogeneous) velocity models. Finally, we designed a wave-equation imaging scheme honoring the characteristic strips in the wavefront set of seismic data, thus generating *scattering-angle/azimuth common image point gathers* (ACIGs) of the type introduced in Kirchhoff-style imaging procedures. ACIGs are used for amplitude inversion as well as in tomography.

With our approach, 'true-amplitude' aspects of the imaging procedure in *inhomogeneous* media can be addressed also, viz. via the composition of the adjoint (solution of the double-square-root equation) and the forward scattering operator (first term of the generalized Bremmer coupling series). In the case of laterally *homogeneous* media such analysis has been carried out (Deregowski & Rocca, 1981; Dubrulle, 1983; Ekren & Ursin, 1999).

We analyzed the case of acoustic waves. The tools needed to extend the current theory to mode-coupled elastic waves my be found in Le Rousseau and De Hoop (2001a).

Chapter 3

Generalization of the phase-screen approximation for the scattering of acoustic waves[1]

3.1 Summary

With the use of Fourier analysis, we describe the propagation and scattering of acoustics waves in smoothly varying, heterogeneous, media. The starting point is the generalized Bremmer coupling series solution – distinguishing multiple up/down scattered constituents – to the wave equation, which requires the introduction of pseudo-differential operators. Then, we introduce a class of approximations to these pseudo-differential operators with the structure of the classical phase-screen method for one-way wave propagation. These approximations induce a fast, iterated, marching algorithm for the evaluation of the Bremmer series. The algorithm consists of multiplications by multiple 'screen' functions in the lateral space domain and generalized 'phase shifts' in the lateral wavenumber domain; the shuttling between the two domains is accomplished by the fast Fourier transform. Our scheme extends the use of the classical phase-screen method in the following ways: we consider larger medium variations; we enhance the accuracy for wider scattering angles; we introduce (de)composition operators to incorporate any desired source- or receiver-type with the appropriate radiation characteristics; we include the backscattered field with the aid of the generalized Bremmer coupling series.

3.2 Introduction

Directional wavefield decomposition is a tool for analyzing and computing the propagation of waves in configurations with a certain directionality, such as waveguiding structures. The method consists of three main steps: (i) *decomposing* the field into two constituents, *propagating* upward or downward along a preferred direction, (ii) computing the interaction (*coupling*) of the counterpropagating constituents and (iii) *recomposing* the constituents into observables at the positions of interest. (The preferred direction is 'vertical' whereas the directions orthogonal to the preferred direction are referred to as the 'lateral' directions.) The method allows one to 'trace' wave constituents in a given medium, and thus distinguish constituents that have been scattered along the up/down direction a different number of times. It allows the separation of head waves from body waves also. The (generalized)

[1]This chapter was published in *Wave Motion*, **31**, (2000) pp.43-70, with M.V. de Hoop and R.-S. Wu.

Bremmer series superimposes all the constituents ('multiples') to recover the full, original wavefield (De Hoop, 1996).

In the framework of remote sensing and inverse scattering, tracing waves helps in the interpretation and separation of constituents prior to the inversion of the observed wavefield (De Hoop, 1998). Directional decomposition maps the 'two-way' wavefield into constituents that satisfy a coupled system of 'one-way' wave equations. In large-scale configurations in which the coupling is weak, wavefield computations can be restricted to a single one-way constituent. In the fields of ocean acoustics (Tappert, 1977; Collins, 1989), seismics (Claerbout, 1970), and integrated optics (Hadley, 1992), this observation has been exploited extensively; for a more complete list of references in this matter, we refer the reader to Van Stralen *et al.* (1998). However, to arrive at 'fast' one-way algorithms in the mentioned applications, various approximations to the decomposition underly their designs.

If the medium of the configuration were laterally homogeneous, the directional decomposition becomes an algebraic operation in the lateral Fourier or wavenumber domain [see, e.g., Kennett (1985)]. In such a medium, the phase-shift method (Gazdag, 1978) is amongst the fastest (and accurate) one-way algorithms. In this method, in the lateral wavenumber domain, the phase shift is simply proportional to the vertical wavenumber; the vertical and lateral wavenumbers are connected through an algebraic dispersion relation. As soon as the medium becomes laterally heterogenous, it still advantageous to carry out the analysis in the lateral wavenumber domain, but without leaving the lateral space domain – an observation well established in the field of micro-local analysis [see, e.g., Treves (1980a)] and applied by Fishman and McCoy (1984a). The lateral space-wavenumber domain constitutes the (lateral) phase space. Through the Fourier transforms, the space and wavenumber domains are 'dual' to one another. In the directional (de)composition – and in the downward and upward propagation, and in the reflection and transmission due to variations in medium properties in the preferred direction – we now encounter pseudo-differential operators the symbols of which are defined on phase space, and lead to a calculus that generalizes the algebraic manipulations in the case of a laterally homogeneous medium [(De Hoop, 1996) and Section 3.3]. Unfortunately, numerical evaluation and application of pseudo-differential operators arising from the wave scattering problem are, in general, involved. Hence, approximations to their symbols are sought for to improve computational efficiency. The phase-screen method (Stoffa *et al.*, 1990; Wu & Huang, 1992) provides one such approximation and leads to an algorithm with computational complexity comparable to the one of the phase-shift method in laterally homogeneous media. A competing approximation is the rational one, analyzed in detail by De Hoop and De Hoop (1992) and Van Stralen *et al.* (1998).

The reason why the phase-screen approximation leads to an efficient algorithm is, that its associated symbols reveal a separation of phase-space coordinates. We will use this observation as the starting point for developing a general class of approximations: the *generalized screen* approximations. It comprises *enforcing* a *separation* of phase-space coordinates in the symbols of the pseudo-differential operators that generate the generalized Bremmer series. The one-way algorithm, inside the Bremmer series, yields an approximate realization of the phase-space path-integral representation for one-way propagation (Fishman &

McCoy, 1984b; De Hoop, 1996); the Hamiltonian of this path integral is the vertical wave slowness (vertical wavenumber divided by frequency) symbol subjected to the separation of phase-space coordinates (Section 3.4). Now, the vertical wave slowness and the lateral wave slownesses are connected through a symbol composition equation. The path integral extends the phase-shift operation to laterally heterogeneous media; its generalized screen realization is founded upon a continuous shuttling between the lateral space and lateral wavenumber domains using the fast Fourier transform (Section 3.6).

Subjecting the symbols, in particular the vertical wave slowness symbol, to the separation of phase-space coordinates, induces an 'adjustment' of wave theory and deformations of the wavefront shapes. The accuracy of the generalized screen approximations is most accessible in phase space by analyzing the (approximate) vertical wave slowness symbols as functions of the lateral wave slownesses (lateral wavenumbers) pointwise in lateral space. In the high-frequency approximation, i.e., up to principal symbols, these functions generate the slowness surface, the polar reciprocal of which creates the Huygens wavefront (Section 3.6). In Section 3.7 we discuss the generalized screen representations of (de)composition; in Section 3.8 we introduce the generalized screen representations of reflection and transmission. The marching algorithm associated with the generalized Bremmer series and leading to the wavefield solution is summarized in Section 3.5; in this algorithm, the thin-slab propagator of Section 3.6, the reflection and transmission operators of Section 3.8, and the (de)composition operators of Section 3.7 are to be substituted.

A framework of marching algorithms and path integrals for wave propagation has been established by McCoy and Frazer (1987). The method of phase screens has been widely used for one-way wave propagation in *smoothly* varying, heterogeneous media. In particular, the method has been applied to light transmission through the atmosphere (Ratcliffe, 1956; Mercier, 1962; Martin & Flatté, 1988), propagation of light in optical fibers (Feit & Fleck, 1978), propagation of radio signals through the ionosphere (Buckley, 1975; Bramley, 1977; Knepp, 1983), propagation of acoustic waves in the ocean (Flatté *et al.*, 1979; Thomson & Chapman, 1983), and propagation of seismic waves in the earth (Stoffa *et al.*, 1990). More recently, the screen method has been introduced for elastic waves (Fisk & McCartor, 1991; Fisk *et al.*, 1992; Wu, 1994). The phase-screen approach has also been applied in media that are not smoothly varying at all: Berry (1979) analyzed the intensity fluctuations of an incident plane wave scattered in a *fractal* medium.

Classically, the phase-screen method was designed for multiple downward scattering of waves, the downward direction being the preferred direction of propagation. Thus it included phenomena like focussing and defocussing, i.e., 'multipathing' of the characteristic set. The applicability of the phase-screen method generally requires that the screen interval satisfies the following criteria: small[2] medium variations (weak scattering), laterally smooth medium variations (narrow angle scattering), and even smoother variations in the preferred direction (negligible backscattering). In this chapter, we access the accuracy of the screen method, and generalize it to larger-contrast (larger range of medium variations within a screen interval), wider-angle, and back scattering. The higher the order of the generalized

[2]By small it is meant small enough for the Born approximation to be valid.

screen approximation, the more parameters occur that shape the wavefront. The order controls the accuracy.

Given the order of the generalized screen approximation, its accuracy can still be enhanced by replacing the (fast) lateral Fourier transform by a *windowed* lateral Fourier transform, the windows following an imprint of the major lateral changes in medium properties (Section 3.6). One may wonder whether the underlying windowed, lateral Fourier basis could be even further improved upon. De Hoop and Gautesen (2000) have accomplished such an improvement, incorporating all one-way wave phenemona, at the cost of computational efficiency.

3.3 Directional wavefield decomposition

For the details on the derivation of the Bremmer coupling series solution of the acoustic wave equation, we refer the reader to De Hoop (1996). Here, we restrict ourselves to a summary of the method. Our configuration is three-dimensional.

Let p = acoustic pressure [Pa], v_r = particle velocity [m/s], ρ = volume density of mass [kg/m^3], κ = compressibility [Pa^{-1}], q = volume source density of injection rate [s^{-1}], and f_k = volume source density of force [N/m^3]. We assume that the coefficients κ and ρ are smooth, and constant outside a compact domain. This provision enables us to formulate the acoustic wave propagation, when necessary, as a scattering problem in a homogeneous embedding. The smoothness entails that the singularities of the wavefield (in particular the ones in the neighborhood of the wave arrival) arise from the ones in the signatures of the source distributions. The formation of caustics, associated with scattering in the lateral directions ('multipathing'), is captured in the approximation procedure developed in this chapter.

We carry out our analysis in the time-Laplace domain. To show the notation, we give the expression for the acoustic pressure,

$$\hat{p}(x_m, s) = \int_{t=0}^{\infty} \exp(-st) p(x_m, t)\, \mathrm{d}t \; . \tag{3.1}$$

Under this transformation, assuming zero initial conditions, we have $\partial_t \to s$. In the Laplace domain, the acoustic wavefield satisfies the system of first-order equations

$$\partial_k \hat{p} + s\rho\, \hat{v}_k = \hat{f}_k \; , \tag{3.2}$$

$$s\kappa\, \hat{p} + \partial_r \hat{v}_r = \hat{q} \; . \tag{3.3}$$

The evolution of the wavefield in the direction of preference can now be expressed in terms of the changes of the wavefield in the direction transverse to it. The direction of preference is taken along the x_3-axis (or 'vertical' axis) and the remaining ('lateral' or 'horizontal') coordinates are denoted by x_μ, $\mu = 1, 2$.

Since we allow the medium to vary with all coordinates and hence also with coordinate in the preferred direction, we are forced to carry out the wavefield decomposition from the system of first-order equations rather than the second-order scalar 'Helmholtz' equation.

3.3.1 The reduced system of equations

The decomposition procedure requires a separate handling of the horizontal components of the particle velocity. From equations (3.2) and (3.3) we obtain

$$\hat{v}_\mu = -\rho^{-1}s^{-1}(\partial_\mu \hat{p} - \hat{f}_\mu) \,, \tag{3.4}$$

leaving, upon substitution, the matrix differential equation

$$(\partial_3 \delta_{I,J} + s\hat{A}_{I,J})\hat{F}_J = \hat{N}_I \,, \quad \hat{A}_{I,J} = \hat{A}_{I,J}(x_\mu, D_\nu; x_3) \,, \quad D_\nu \equiv -\frac{1}{s}\partial_\nu \,, \tag{3.5}$$

in which $\delta_{I,J}$ is the Kronecker delta, and the elements of the acoustic field matrix are given by

$$\hat{F}_1 = \hat{p} \,, \quad \hat{F}_2 = \hat{v}_3 \,, \tag{3.6}$$

the elements of the acoustic system's operator matrix by

$$\hat{A}_{1,1} = \hat{A}_{2,2} = 0 \,, \tag{3.7}$$

$$\hat{A}_{1,2} = \rho \,, \tag{3.8}$$

$$\hat{A}_{2,1} = -D_\nu(\rho^{-1}D_\nu) + \kappa \,, \tag{3.9}$$

and the elements of the notional source matrix by

$$\hat{N}_1 = \hat{f}_3 \,, \quad \hat{N}_2 = D_\nu(\rho^{-1}\hat{f}_\nu) + \hat{q} \,. \tag{3.10}$$

It is observed that the right-hand side of equation (3.4) and $\hat{A}_{I,J}$ contain the spatial derivatives D_ν with respect to the horizontal coordinates only. D_ν has the interpretation of *horizontal slowness* operator. Further, it is noted that $\hat{A}_{1,2}$ is simply a multiplicative operator.

3.3.2 The coupled system of one-way wave equations

To distinguish up- and downgoing constituents in the wavefield, we shall construct an appropriate linear operator $\hat{L}_{I,J}$, pseudodifferential in lateral variables, x_1 and x_2, with

$$\hat{F}_I = \hat{L}_{I,J}\hat{W}_J \,, \tag{3.11}$$

that, with the aid of the commutation relation $(\partial_3 \hat{L}_{I,J}) = [\partial_3, \hat{L}_{I,J}]$, (since the symbol of $L_{I,J}$ depends on the x_3 variable, whereas $L_{I,J}$ only acts on x_1 and x_2) transforms equation (3.5) into

$$\hat{L}_{I,J}\,(\partial_3 \delta_{J,M} + s\hat{\Lambda}_{J,M})\hat{W}_M = -(\partial_3 \hat{L}_{I,J})\,\hat{W}_J + \hat{N}_I \,, \tag{3.12}$$

as to make $\hat{\Lambda}_{J,M}$, satisfying

$$\hat{A}_{I,J}\hat{L}_{J,M} = \hat{L}_{I,J}\hat{\Lambda}_{J,M} , \tag{3.13}$$

a diagonal matrix of operators. We denote $\hat{L}_{I,J}$ as the composition operator and $\hat{W}_M$ as the wave matrix. The matrix expression in parentheses on the left-hand side of equation (3.12) is diagonal and its diagonal entries are the two so-called *one-way* wave operators. The first term on the right-hand side of equation (3.12) is representative for the scattering due to variations of the medium properties in the vertical direction. The scattering due to variations of the medium properties in the horizontal directions is contained in $\hat{\Lambda}_{J,M}$ and, implicitly, in $\hat{L}_{I,J}$ also.

To investigate whether solutions of equation (3.13) exist, we introduce the column matrix operators $\hat{L}_I^{(\pm)}$ according to

$$\hat{L}_I^{(+)} = \hat{L}_{I,1} , \quad \hat{L}_I^{(-)} = \hat{L}_{I,2} . \tag{3.14}$$

Upon writing the diagonal entries of $\hat{\Lambda}_{J,M}$ as

$$\hat{\Lambda}_{1,1} = \hat{\Gamma}^{(+)} , \quad \hat{\Lambda}_{2,2} = \hat{\Gamma}^{(-)} , \tag{3.15}$$

equation (3.13) decomposes into the two systems of equations

$$\hat{A}_{I,J}\hat{L}_J^{(\pm)} = \hat{L}_I^{(\pm)}\hat{\Gamma}^{(\pm)} . \tag{3.16}$$

By analogy with the case where the medium is translationally invariant in the horizontal directions, we shall denote $\hat{\Gamma}^{(\pm)}$ as the *vertical slowness* operators. Notice that the operators $\hat{L}_1^{(\pm)}$ compose the acoustic pressure and that the operators $\hat{L}_2^{(\pm)}$ compose the vertical particle velocity from the elements of $\hat{W}_M$ associated with the up- and downgoing constituents.

In De Hoop (1996) an Ansatz procedure has been followed to solve the generalized eigenvalue-eigenvector problem (3.16) in operator sense: choosing the *acoustic-pressure normalization* analog, we satisfy the commutation rule

$$[\hat{L}_2^{(\pm)}, \hat{A}_{2,1}\hat{A}_{1,2}] = 0 . \tag{3.17}$$

In this normalization, we find the vertical slowness operator or generalized eigenvalues to be

$$\hat{\Gamma}^{(+)} = -\hat{\Gamma}^{(-)} = \hat{\Gamma} = \hat{\mathrm{A}}^{1/2} , \quad \hat{\mathrm{A}} \equiv \hat{A}_{2,1}\hat{A}_{1,2} ; \quad \hat{\Gamma}^2 = \hat{\mathrm{A}} \tag{3.18}$$

is the characteristic operator equation, while the generalized eigenvectors constitute the *composition* operator

$$\hat{L} = \begin{pmatrix} \hat{A}_{1,2} & \hat{A}_{1,2} \\ \hat{\Gamma} & -\hat{\Gamma} \end{pmatrix} . \tag{3.19}$$

With respect to the normalization, note that we have decomposed the *pressure* (up to a multiplication by density) viz. according to $\hat{F}_1 = \hat{F}_1^+ + \hat{F}_1^-$, $\hat{F}_1^+ = \hat{A}_{1,2}\hat{W}_1$ and $\hat{F}_1^- = \hat{A}_{1,2}\hat{W}_2$.

In terms of the inverse vertical slowness operator, $\hat{\Gamma}^{-1} = \hat{\mathrm{A}}^{-1/2}$, the *decomposition* operator then follows as

$$\hat{L}^{-1} = \tfrac{1}{2}\begin{pmatrix} \hat{A}_{1,2}^{-1} & \hat{\Gamma}^{-1} \\ \hat{A}_{1,2}^{-1} & -\hat{\Gamma}^{-1} \end{pmatrix} . \tag{3.20}$$

The (de)composition operators account for the radiation patterns of the different source and receiver types.

Using the decomposition operator, equation (3.12) transforms into

$$(\partial_3 \delta_{I,M} + s\hat{\Lambda}_{I,M})\hat{W}_M = -(\hat{L}^{-1})_{I,M}(\partial_3 \hat{L}_{M,K})\hat{W}_K + (\hat{L}^{-1})_{I,M}\hat{N}_M , \tag{3.21}$$

which can be interpreted as a coupled system of one-way wave equations. The coupling between the counter-propagating components, $\hat{W}_1$ and $\hat{W}_2$, is apparent in the first source-like term on the right-hand side, which can be written as

$$-\hat{L}^{-1}(\partial_3 \hat{L}) = \begin{pmatrix} \hat{T} & \hat{R} \\ \hat{R} & \hat{T} \end{pmatrix} , \tag{3.22}$$

in which $\hat{T}$ and $\hat{R}$ represent the *transmission* and *reflection* operators, respectively. In the acoustic-pressure normalization analog, we find

$$-\hat{T} = \tfrac{1}{2}\hat{A}_{1,2}^{-1}(\partial_3 \hat{A}_{1,2}) + \tfrac{1}{2}\hat{\Gamma}^{-1}(\partial_3 \hat{\Gamma}) , \quad \hat{R} = -\tfrac{1}{2}\hat{A}_{1,2}^{-1}(\partial_3 \hat{A}_{1,2}) + \tfrac{1}{2}\hat{\Gamma}^{-1}(\partial_3 \hat{\Gamma}) . \tag{3.23}$$

3.4 The one-way wave propagator

To arrive at a coupled system of integral equations that is equivalent to equation (3.21) and that can be solved in terms of a Neumann expansion, we have to invert the operator occurring on the left-hand side. We set $\hat{\mathrm{G}}^{(\pm)} = (\partial_3 + s\hat{\Gamma}^{(\pm)})^{-1}$. The one-sided elementary kernels $\hat{\mathcal{G}}^{(\pm)}(x_\mu, x_3; x'_\nu, x'_3)$ associated with these operators are the so-called one-way Green's functions. They satisfy the equations

$$(\partial_3 + s\hat{\Gamma}^{(\pm)})\hat{\mathcal{G}}^{(\pm)} = \delta(x_\nu - x'_\nu)\,\delta(x_3 - x'_3) , \tag{3.24}$$

together with the condition of causality enforcing that $\hat{\mathcal{G}}^{(\pm)}$ decays as $x_3 \to \pm\infty$.

Now, consider the case $\hat{\mathrm{G}} = \hat{\mathrm{G}}^{(+)}$, $\hat{\mathcal{G}} = \hat{\mathcal{G}}^{(+)}$ and $\hat{\Gamma} = \hat{\Gamma}^{(+)}$. The operator $\hat{\mathrm{G}}$ acts on a test field $\hat{u}$ as

$$(\hat{\mathrm{G}}\hat{u})(x_\mu, x_3) = \int_{\zeta\in\mathbb{R}} \int_{x'_\nu\in\mathbb{R}} \hat{\mathcal{G}}(x_\mu, x_3; x'_\nu, \zeta)\,\hat{u}(x'_\nu, \zeta)\,\mathrm{d}x'_1\mathrm{d}x'_2\,\mathrm{d}\zeta . \tag{3.25}$$

Let us define the initial-value problem of determining the function $\hat{U}(x_\mu, x_3; \zeta)$ satisfying

$$(\partial_3 + s\hat{\Gamma})\,\hat{U} = 0 \text{ for } x_3 \geq \zeta, \quad \hat{U}(x_\mu, \zeta; \zeta) = \hat{u}(x_\mu, \zeta)\ . \tag{3.26}$$

Then it is observed that

$$(\hat{\mathrm{G}}\hat{u})(x_\mu, x_3) = \int_{\zeta=-\infty}^{x_3} \hat{U}(x_\mu, x_3; \zeta)\,\mathrm{d}\zeta\ . \tag{3.27}$$

3.4.1 The product integral

We note that the vertical slowness operators at different levels of x_3 do not necessarily commute with one another due to the heterogeneity of the medium. Thus we arrive at a 'time'-ordered product integral representation (De Witte-Morette *et al.*, 1979) of the one-sided propagators [cf., equation (3.26)] associated with the one-way wave equations (De Hoop, 1996; Fishman & McCoy, 1984a; Fishman & McCoy, 1984b) where 'time' refers to the vertical coordinate x_3,

$$\hat{U}^{(\pm)}(., x_3; x_3') = \pm H(\mp[x_3' - x_3]) \left\{ \prod_{\zeta=x_3'}^{x_3} \exp[-s\hat{\Gamma}^{(\pm)}(., \zeta)\,\mathrm{d}\zeta] \right\} \hat{u}(., x_3')\ , \tag{3.28}$$

where H denotes the Heaviside function. In this expression, the operator ordering is initiated by $\exp[-s\hat{\Gamma}(., x_3')\,\mathrm{d}\zeta]$ acting on $\hat{u}(., x_3')$ followed by applying $\exp[-s\hat{\Gamma}(., \zeta)\,\mathrm{d}\zeta]$ to the result, successively for increasing ζ.

If the medium in the interval $[x_3', x_3]$ were weakly varying in the vertical direction, the Trotter product formula can be applied to the product integral in equation (3.28). This results in the Hamiltonian path integral representations (De Witte-Morette *et al.*, 1979) with measure $\mathcal{D}$ for the Green's functions,

$$\hat{\mathcal{G}}^{(\pm)}(x_\mu, x_3; x_\nu', x_3') = \pm H(\mp[x_3' - x_3]) \int_P \mathcal{D}(x_\mu'', \alpha_\nu'') \tag{3.29}$$

$$\exp\left[-s \int_{\zeta=x_3'}^{x_3} \mathrm{d}\zeta \{\mathrm{i}\alpha_\sigma''(d_\zeta x_\sigma'') + \hat{\gamma}^{(\pm)}(x_\mu'', \zeta, \alpha_\nu'')\}\right] = \pm H(\mp[x_3' - x_3])\,\hat{g}^{(\pm)}(x_\mu, x_3; x_\nu', x_3')\ ,$$

P being a set of paths $(x_\mu''(\zeta),\ \alpha_\nu''(\zeta))$ in (horizontal) phase space satisfying $x_\mu''(\zeta = x_3') = x_\mu'$, $x_\mu''(\zeta = x_3) = x_\mu$. In equation (3.29), $\hat{\gamma}^{(\pm)}$ is the left symbol of $\Gamma^{(\pm)}$, i.e.,

$$\hat{\Gamma}^{(\pm)}(x_\mu, D_\nu; \zeta)\ \exp(-\mathrm{i}s\alpha_\sigma x_\sigma) = \hat{\gamma}^{(\pm)}(x_\mu, \zeta, \alpha_\nu) \exp(-\mathrm{i}s\alpha_\sigma x_\sigma)\ . \tag{3.30}$$

The path integral in equation (3.29) is to be interpreted as the lattice multi-variate integral

$$\hat{\mathcal{G}}^{(\pm)}(x_\mu, x_3; x'_\nu, x'_3) = \pm H(\mp[x'_3 - x_3]) \lim_{M\to\infty} \int \prod_{i=1}^{M} (s/2\pi)^2 \mathrm{d}\alpha_1^{(i)} \mathrm{d}\alpha_2^{(i)} \prod_{j=1}^{M-1} \mathrm{d}x_1^{(j)} \mathrm{d}x_2^{(j)}$$

$$\exp\left[-s \sum_{k=1}^{M} \{\mathrm{i}\alpha_\sigma^{(k)}(x_\sigma^{(k)} - x_\sigma^{(k-1)}) + \hat{\gamma}^{(\pm)}(x_\mu^{(k)}, \zeta_k - \tfrac{1}{2}M^{-1}\Delta x_3, \alpha_\nu^{(k)})M^{-1}\Delta x_3\}\right] \tag{3.31}$$

with $x_\mu^{(0)} = x'_\mu$, $x_\mu^{(M)} = x_\mu$, and $\Delta x_3 = x_3 - x'_3$. All the integrations are taken over the interval $(-\infty, \infty)$, $M^{-1}\Delta x_3$ is the step size in ζ, and $(x_\mu^{(j)}, \alpha_\nu^{(j)})$ are the coordinates of a path at the discrete values ζ_j of ζ as $j = 1, \cdots, M$.

3.4.2 The thin-slab propagator

If Δx_3 is sufficiently small (thin slab), the lattice multi-variate integral reduces to $(M = 1)$

$$\hat{g}^{(\pm)}(x_\mu, x_3; x'_\nu, x'_3) \simeq \int (s/2\pi)^2 \mathrm{d}\alpha''_1 \mathrm{d}\alpha''_2$$
$$\exp[-\mathrm{i}s\,\alpha''_\sigma(x_\sigma - x'_\sigma)] \exp[-s\,\hat{\gamma}^{(\pm)}(x_\mu, x_3 - \tfrac{1}{2}\Delta x_3, \alpha''_\nu)\Delta x_3] \,. \tag{3.32}$$

Thus, thin-slab propagation is composed of a forward Fourier transform, a multiplication by a phase factor (the phase is the vertical slowness left symbol) and an inverse Fourier transform. Switching from left to right symbols[3] yields

$$\hat{g}^{(\pm)}(x_\mu, x_3; x'_\nu, x'_3) \simeq \int (s/2\pi)^2 \mathrm{d}\alpha''_1 \mathrm{d}\alpha''_2$$
$$\exp[-\mathrm{i}s\,\alpha''_\sigma(x_\sigma - x'_\sigma)] \exp[-s\,\hat{\gamma}^{(\pm)}(x'_\nu, x_3 - \tfrac{1}{2}\Delta x_3, \alpha''_\nu)\Delta x_3] \,. \tag{3.33}$$

With the vertical slowness left symbol is associated a cokernel

$$\tilde{\gamma}(\alpha_\mu, \zeta, \alpha'_\nu) = \int_{x_\mu \in \mathbb{R}} \exp(\mathrm{i}s\alpha_\mu x_\mu)\, \hat{\gamma}(x_\mu, \zeta, \alpha'_\nu)\, \mathrm{d}x_1 \mathrm{d}x_2 \,. \tag{3.34}$$

Thus, in the Fourier domain, the thin slab propagator can written in the form [cf., equation (3.32)],

$$\tilde{g}^{(\pm)}(\alpha_\mu, x_3; \alpha''_\nu, x'_3) \simeq \int \mathrm{d}x_1 \mathrm{d}x_2$$
$$\exp[\mathrm{i}s\,(\alpha_\sigma - \alpha''_\sigma)\, x_\sigma] \exp[-s\,\hat{\gamma}^{(\pm)}(x_\mu, x_3 - \tfrac{1}{2}\Delta x_3, \alpha''_\nu, s)\Delta x_3] \,, \tag{3.35}$$

[3]The right or *dual* symbol $\hat{\gamma}_{\mathrm{R}}$ is related to the *left* symbol $\hat{\gamma}$ according to $\hat{\gamma}_{\mathrm{R}}(x_\mu, \zeta, \alpha_\nu) \sim \exp[\mathrm{i}\,\partial_{\alpha_\sigma} D_{x_\sigma}]\, \hat{\gamma}(x_\mu, \zeta, \alpha_\nu)$. We will omit the subscript $_{\mathrm{R}}$ whenever it is clear from the context which symbol is meant.

and may, for small Δx_3, be approximated by

$$\tilde{g}^{(\pm)}(\alpha_\mu, x_3; \alpha''_\nu, x'_3) \simeq \delta(\alpha_\mu - \alpha''_\mu) - s\,\tilde{\gamma}^{(\pm)}(\alpha_\mu - \alpha''_\mu, x_3 - \tfrac{1}{2}\Delta x_3, \alpha''_\nu, s)\Delta x_3 + \cdots . \quad (3.36)$$

This representation shows the interaction of Fourier constituents $\exp(-is\alpha_\sigma x_\sigma)$ explicitly.

3.5 The generalized Bremmer coupling series

3.5.1 The coupled system of integral equations

Applying the operators with kernels equation (3.29) to equation (3.21) we obtain a coupled system of integral equations (De Hoop, 1996). In operator form, they are given by

$$(\delta_{I,J} - \hat{\mathrm{K}}_{I,J})\hat{W}_J = \hat{W}_I^{(0)} , \quad (3.37)$$

in which $\hat{W}^{(0)}$ denotes the incident field. In our configuration the domain of heterogeneity will be restricted to the slab $(0, x_3^{\mathrm{exit}}]$, and the excitation of the waves will be specified through an initial condition at the level $x_3 = 0$, viz.

$$\hat{W}_1^{(0)}(x_\mu, x_3) = \int_{x'_\nu \in \mathbb{R}} \hat{\mathcal{G}}^{(+)}(x_\mu, x_3; x'_\nu, 0)\, \hat{W}_1(x'_\nu, 0)\, \mathrm{d}x'_1\, \mathrm{d}x'_2 , \quad (3.38)$$

$$\hat{W}_2^{(0)}(x_\mu, x_3) = 0 , \quad (3.39)$$

in the range of interest, $x_3 \in [0, x_3^{\mathrm{exit}}]$; the second equation reflects the assumption that there is no excitation below the heterogeneous slab. The integral operators in equation (3.37) are given by

$$(\hat{\mathrm{K}}_{1,1}\hat{W}_1)(x_\mu, x_3) = \int_{\zeta=0}^{x_3} \int_{x'_\nu \in \mathbb{R}} \hat{\mathcal{G}}^{(+)}(x_\mu, x_3; x'_\nu, \zeta)(\hat{T}\hat{W}_1)(x'_\nu, \zeta)\, \mathrm{d}x'_1\, \mathrm{d}x'_2\, \mathrm{d}\zeta , \quad (3.40)$$

$$(\hat{\mathrm{K}}_{1,2}\hat{W}_2)(x_\mu, x_3) = \int_{\zeta=0}^{x_3} \int_{x'_\nu \in \mathbb{R}} \hat{\mathcal{G}}^{(+)}(x_\mu, x_3; x'_\nu, \zeta)(\hat{R}\hat{W}_2)(x'_\nu, \zeta)\, \mathrm{d}x'_1\, \mathrm{d}x'_2\, \mathrm{d}\zeta , \quad (3.41)$$

$$(\hat{\mathrm{K}}_{2,1}\hat{W}_1)(x_\mu, x_3) = \int_{\zeta=x_3}^{x_3^{\mathrm{exit}}} \int_{x'_\nu \in \mathbb{R}} \hat{\mathcal{G}}^{(-)}(x_\mu, x_3; x'_\nu, \zeta)(\hat{R}\hat{W}_1)(x'_\nu, \zeta)\, \mathrm{d}x'_1\, \mathrm{d}x'_2\, \mathrm{d}\zeta , \quad (3.42)$$

$$(\hat{\mathrm{K}}_{2,2}\hat{W}_2)(x_\mu, x_3) = \int_{\zeta=x_3}^{x_3^{\mathrm{exit}}} \int_{x'_\nu \in \mathbb{R}} \hat{\mathcal{G}}^{(-)}(x_\mu, x_3; x'_\nu, \zeta)(\hat{T}\hat{W}_2)(x'_\nu, \zeta)\, \mathrm{d}x'_1\, \mathrm{d}x'_2\, \mathrm{d}\zeta . \quad (3.43)$$

They describe the interaction between the counter-propagating constituent waves.

We can represent the action of the one-sided Green's kernels by product integrals, viz.,

$$\hat{W}_1^{(0)}(., x_3) = \left\{ \prod_{\zeta'=0}^{x_3} \exp[-s\hat{\Gamma}^{(+)}(., \zeta')\, \mathrm{d}\zeta'] \right\} \hat{W}_1(., 0) , \quad (3.44)$$

while

$$(\hat{\mathrm{K}}_{1,1}\hat{W}_1)(.,x_3) = \int_{\zeta=0}^{x_3} \left\{ \prod_{\zeta'=\zeta}^{x_3} \exp[-s\hat{\Gamma}^{(+)}(.,\zeta')\,\mathrm{d}\zeta'] \right\} (\hat{T}\hat{W}_1)(.,\zeta)\,\mathrm{d}\zeta\ , \tag{3.45}$$

and so on.

3.5.2 Bremmer series

If s is real and sufficiently large, the Neumann expansion can be employed to invert $(\delta_{I,J} - \hat{\mathrm{K}}_{I,J})$ in equation (3.37). Such a procedure leads to the Bremmer coupling series,

$$\hat{W}_I = \sum_{j=0}^{\infty} \hat{W}_I^{(j)}\ , \qquad \text{in which } \hat{W}_I^{(j)} = \hat{\mathrm{K}}_{I,J}\hat{W}_J^{(j-1)} \text{ for } j \geq 1\ , \tag{3.46}$$

can be interpreted as the j-times reflected or scattered wave. This equation indicates that the solution of equation (3.37) can be found with the aid of an iterative scheme. This iterative scheme and its computational aspects are discussed in detail by Van Stralen *et al.* (Van Stralen *et al.*, 1998, III.C). On the basis of Lerch's theorem (Widder, 1946), we only need the individual terms for s on some real half line to get back to the time domain; the earlier condition 'sufficiently large' does not play any role in this respect.

3.5.3 An iterated marching algorithm

To arrive at a marching algorithm nested in an iterative scheme, consider the j-times reflected constituent wave. We split the interval $[0, x_3^{\text{exit}}]$ into M thin slabs with thickness Δx_3. Set

$$\hat{W}_I^{(j)}(.,k\Delta x_3) = \hat{I}_{I,1}^{(j)}(.,k) + \hat{I}_{I,2}^{(j)}(.,k)\ , \tag{3.47}$$

$j = 1, 2, \cdots$ and $k = 0, 1, \cdots, M$, where [cf., equation (3.46)]

$$\hat{I}_{I,1}^{(j)}(.,k) = (\hat{\mathrm{K}}_{I,1}\hat{W}_1^{(j-1)})(.,k\Delta x_3)\ , \tag{3.48}$$

$$\hat{I}_{I,2}^{(j)}(.,k) = (\hat{\mathrm{K}}_{I,2}\hat{W}_2^{(j-1)})(.,k\Delta x_3)\ . \tag{3.49}$$

Upon comparison with equation (3.45) we find that

$$\hat{I}_{1,1}^{(j)}(.,k) = \int_{\zeta=0}^{k\Delta x_3} \left\{ \prod_{\zeta'=\zeta}^{k\Delta x_3} \exp[-s\hat{\Gamma}^{(+)}(.,\zeta')\,\mathrm{d}\zeta'] \right\} \hat{X}_{1,1}^{(j)}(.,\zeta)\,\mathrm{d}\zeta\ , \tag{3.50}$$

with

$$\hat{X}_{1,1}^{(j)}(.,\zeta) = (\hat{T}\hat{W}_1^{(j-1)})(.,\zeta)\ . \tag{3.51}$$

Similarly,

$$\hat{I}^{(j)}_{1,2}(.,k) = \int_{\zeta=0}^{k\Delta x_3} \left\{ \prod_{\zeta'=\zeta}^{k\Delta x_3} \exp[-s\hat{\Gamma}^{(+)}(.,\zeta')\,\mathrm{d}\zeta'] \right\} \hat{X}^{(j)}_{1,2}(.,\zeta)\,\mathrm{d}\zeta\ , \tag{3.52}$$

$$\hat{I}^{(j)}_{2,J}(.,k) = -\int_{\zeta=k\Delta x_3}^{x_3^{\mathrm{exit}}} \left\{ \prod_{\zeta'=\zeta}^{k\Delta x_3} \exp[-s\hat{\Gamma}^{(-)}(.,\zeta')\,\mathrm{d}\zeta'] \right\} \hat{X}^{(j)}_{2,J}(.,\zeta)\,\mathrm{d}\zeta\ , \tag{3.53}$$

with

$$\hat{X}^{(j)}_{1,2}(.,\zeta) = (\hat{R}\hat{W}^{(j-1)}_2)(.,\zeta)\ , \tag{3.54}$$

$$\hat{X}^{(j)}_{2,1}(.,\zeta) = (\hat{R}\hat{W}^{(j-1)}_1)(.,\zeta)\ , \tag{3.55}$$

$$\hat{X}^{(j)}_{2,2}(.,\zeta) = (\hat{T}\hat{W}^{(j-1)}_2)(.,\zeta)\ . \tag{3.56}$$

To construct the iteration scheme, we carry out the following steps. Let $\hat{P}$ denote the *thin-slab propagator*

$$\hat{P}(.,k) = \left\{ \prod_{\zeta'=(k-1)\Delta x_3}^{k\Delta x_3} \exp[-s\hat{\Gamma}^{(+)}(.,\zeta')\,\mathrm{d}\zeta'] \right\}\ . \tag{3.57}$$

We approximate the kernel of this propagator by equation (3.32) with $x'_3 = (k-1)\Delta x_3$ and $x_3 = k\Delta x_3$. Then, using the semi-group property for the product integral,

$$\begin{aligned}\hat{I}^{(j)}_{1,1}(.,k) = {} & \left\{ \prod_{\zeta'=(k-1)\Delta x_3}^{k\Delta x_3} \exp[-s\hat{\Gamma}^{(+)}(.,\zeta')\,\mathrm{d}\zeta'] \right\} \\ & \int_{\zeta=0}^{(k-1)\Delta x_3} \left\{ \prod_{\zeta'=\zeta}^{(k-1)\Delta x_3} \exp[-s\hat{\Gamma}^{(+)}(.,\zeta')\,\mathrm{d}\zeta'] \right\} \hat{X}^{(j)}_{1,1}(.,\zeta)\,\mathrm{d}\zeta \\ & + \int_{\zeta=(k-1)\Delta x_3}^{k\Delta x_3} \left\{ \prod_{\zeta'=\zeta}^{k\Delta x_3} \exp[-s\hat{\Gamma}^{(+)}(.,\zeta')\,\mathrm{d}\zeta'] \right\} \hat{X}^{(j)}_{1,1}(.,\zeta)\,\mathrm{d}\zeta\ ,\end{aligned} \tag{3.58}$$

which can be written as

$$\hat{I}^{(j)}_{1,1}(.,k) = \hat{P}(.,k)\,\hat{I}^{(j)}_{1,1}(.,k-1) + \hat{Q}^{(j)}_{1,1}(.,k)\ , \tag{3.59}$$

where

$$\hat{Q}^{(j)}_{1,1}(.,k) = \int_{\zeta=(k-1)\Delta x_3}^{k\Delta x_3} \left\{ \prod_{\zeta'=\zeta}^{k\Delta x_3} \exp[-s\hat{\Gamma}^{(+)}(.,\zeta')\,\mathrm{d}\zeta'] \right\} \hat{X}^{(j)}_{1,1}(.,\zeta)\,\mathrm{d}\zeta\ . \tag{3.60}$$

Recursion relations similar to the one in equation (3.59) can be found for the other elements of $\hat{I}$, viz.,

$$\begin{aligned}\hat{I}^{(j)}_{1,J}(.,k) &= \hat{P}(.,k)\,\hat{I}^{(j)}_{1,J}(.,k-1) + \hat{Q}^{(j)}_{1,J}(.,k) \quad \text{for} \quad k = 1,2,\cdots,M\,,\\ \hat{I}^{(j)}_{2,J}(.,k) &= \hat{P}(.,k+1)\,\hat{I}^{(j)}_{2,J}(.,k+1) + \hat{Q}^{(j)}_{2,J}(.,k)\\ &\qquad\qquad \text{for} \quad k = M-1, M-2,\cdots,0\,. \end{aligned} \tag{3.61}$$

Here

$$\hat{Q}^{(j)}_{1,J}(.,k) = \int_{\zeta=(k-1)\Delta x_3}^{k\Delta x_3} \left\{ \prod_{\zeta'=\zeta}^{k\Delta x_3} \exp[-s\hat{\Gamma}^{(+)}(.,\zeta')\,\mathrm{d}\zeta'] \right\} \hat{X}^{(j)}_{1,J}(.,\zeta)\,\mathrm{d}\zeta\,, \tag{3.62}$$

$$\hat{Q}^{(j)}_{2,J}(.,k) = \int_{\zeta=(k+1)\Delta x_3}^{k\Delta x_3} \left\{ \prod_{\zeta'=k\Delta x_3}^{\zeta} \exp[s\hat{\Gamma}^{(-)}(.,\zeta')\,\mathrm{d}\zeta'] \right\} \hat{X}^{(j)}_{2,J}(.,\zeta)\,\mathrm{d}\zeta\,. \tag{3.63}$$

Equations (3.61) describe a *marching* algorithm, the top one going forward and the bottom one going backward.

The initial values for the recursion scheme (3.61) are given by

$$\hat{I}^{(j)}_{1,J}(x_\mu, 0) = 0\,, \tag{3.64}$$

$$\hat{I}^{(j)}_{2,J}(x_\mu, M) = 0\,, \tag{3.65}$$

again, for $j = 1,2,\cdots$.

3.5.4 Numerical issues

The implementation of the iterative scheme is as follows. It is initiated by the calculation of the incident field, $\hat{W}^{(0)}_1$, according to

$$\hat{W}^{(0)}_1(.,k\Delta x_3) = \hat{P}(.,k)\,\hat{W}^{(0)}_1(.,(k-1)\Delta x_3) \quad \text{for} \quad k = 1,2,\cdots,M\,, \tag{3.66}$$

with initial condition

$$\hat{W}^{(0)}_1(.,0) = \hat{W}_1(.,0)\,, \tag{3.67}$$

according to equation (3.38). During the forward marching, at each of the discrete levels, $\hat{X}^{(1)}_{J,1}$ are computed and stored; $\hat{X}^{(1)}_{J,2}$ are set to zero. The procedure is continued by the backward propagation defined by the second iteration in equation (3.61). At each of the discrete levels, $\hat{W}^{(1)}_2$ is computed [equation (3.47)] and used to calculate $\hat{X}^{(2)}_{J,2}$; the latter quantity is stored as before. The scheme continues to switch from backward to forward propagation based on the first iteration in equation (3.61), and so on.

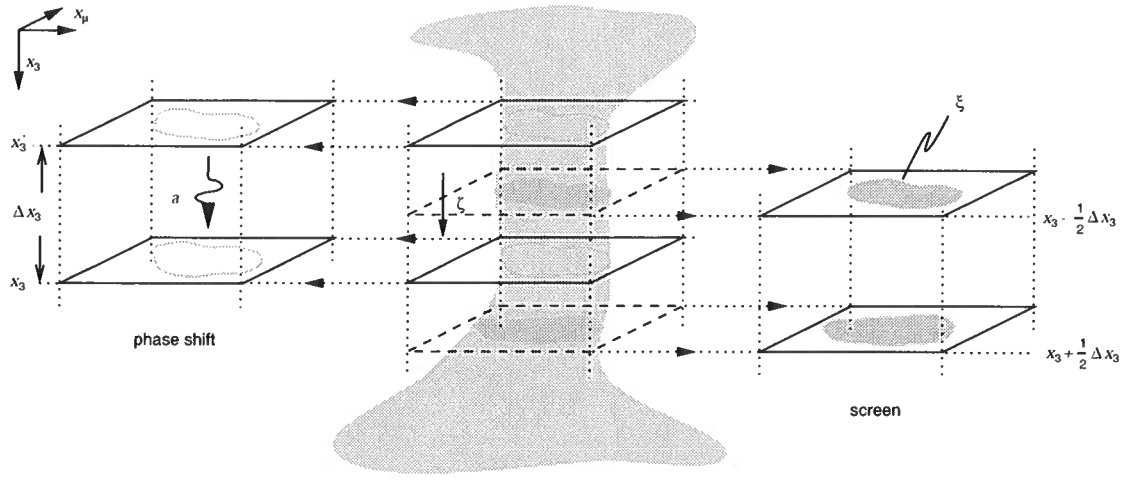

Figure 3.1. The screen representation for one-way propagation.

To evaluate the elements of $\hat{Q}^{(j)}$, we apply the trapezoidal rule. Then

$$\hat{Q}^{(j)}_{1,J}(.,k) \simeq \tfrac{1}{2}\Delta x_3 \left[\hat{X}^{(j)}_{1,J}(.,k\Delta x_3) + \hat{P}(.,k)\,\hat{X}^{(j)}_{1,J}(.,(k-1)\Delta x_3)\right] , \tag{3.68}$$

$$\hat{Q}^{(j)}_{2,J}(.,k) \simeq -\tfrac{1}{2}\Delta x_3 \left[\hat{X}^{(j)}_{2,J}(.,k\Delta x_3) + \hat{P}(.,k+1)\,\hat{X}^{(j)}_{2,J}(.,(k+1)\Delta x_3)\right] . \tag{3.69}$$

which formulas are accurate $\mathcal{O}((\Delta x_3)^2)$.

In the remainder of this chapter, we will derive approximate, screen representations for $\hat{\Gamma}$, $\hat{P}$, $\hat{\Gamma}^{-1}$ and $\hat{R}$. This will lead to an overal multiple screen representation of the full solution of the acoustic wave equation.

3.6 Screen representation of the propagator

There exists a wide variety of techniques to approximate the vertical slowness symbol to speed up the computation of the one-sided propagator equation (3.31) generated by equation (3.32). Here, we pursue the perturbative, split-step Fourier approach (Stoffa *et al.*, 1990) to arrive at a generalized-screen expansion of the propagator. A schematic view of this expansion is shown in Figure 3.1 (the symbols will be explained in the later analysis). Underlying the generalized-screen approach is an embedding procedure.

To introduce the embedding, consider a thin slab, $[x_3', x_3]$, with thickness $\Delta x_3 = x_3 - x_3'$. We introduce a *background* medium in the slab, with parameters ρ^0, κ^0. The background medium, or embedding, is constant in the slab, but may vary from one slab to another:

$$\rho^0(\zeta) = \rho^0(x_3) , \quad \kappa^0(\zeta) = \kappa^0(x_3) , \quad \zeta \in [x_3', x_3] .$$

3.6.1 The vertical slowness left symbol, contrast formulation

In the acoustic pressure normalization analog, the characteristic differential operator in equation (3.18) is given by

$$\hat{\mathrm{A}} = -D_\nu D_\nu + \kappa\rho - \rho^{-1}(D_\nu\rho)\, D_\nu - \rho^{-1}(D_\nu^2\rho) + \rho^{-2}(D_\nu\rho)^2 \,, \tag{3.70}$$

with left symbol $\hat{\mathrm{a}} = \hat{\mathrm{a}}(x_\mu, \zeta, \alpha_\nu)$. For the further analysis, we will employ a *contrast* formulation. Having introduced in the interval $[x_3', x_3]$ a background medium with parameters ρ^0, κ^0, the medium perturbation is given by

$$\epsilon_\kappa(x_\mu,\zeta) = \frac{\kappa^0(x_3)}{\kappa(x_\mu,\zeta)} - 1 \quad , \quad \epsilon_\rho(x_\mu,\zeta) = \frac{\rho(x_\mu,\zeta)}{\rho^0(x_3)} - 1 \,; \tag{3.71}$$

$$c = (\kappa\rho)^{-1/2} \quad , \quad c^0 = (\kappa^0\rho^0)^{-1/2} \,, \tag{3.72}$$

for $\zeta \in [x_3', x_3]$.

We will now expand the left symbol $\hat{\mathrm{a}}$ of $\hat{\mathrm{A}}$ simultaneously in medium contrast (the order is indicated by a superscript) and in symbol (or operator) order (this order is indicated by a subscript). Thus, expanding $\hat{\mathrm{a}}$ in medium contrast, yields the decomposition $\hat{\mathrm{a}} = \hat{\mathrm{a}}^0 + \hat{\mathrm{a}}^1 + \hat{\mathrm{a}}^2$, while expanding the individual terms appearing in the decomposition further into symbol order, leads to

$$\hat{\mathrm{a}}^0 \;=\; \hat{\mathrm{a}}^0_2 = \alpha_\nu^2 + (c^0)^{-2} \tag{3.73}$$

for the background, and

$$\hat{\mathrm{a}}^1 \;=\; \hat{\mathrm{a}}^1_2 + \hat{\mathrm{a}}^1_1 + \hat{\mathrm{a}}^1_0 \,, \tag{3.74}$$

and

$$\hat{\mathrm{a}}^2 \;=\; \hat{\mathrm{a}}^2_0 = (\rho^0)^2\rho^{-2}(D_\nu\epsilon_\rho)^2 \tag{3.75}$$

for the contrast. Here,

$$\hat{\mathrm{a}}^1_2 \;=\; (c^0)^{-2}\epsilon_\rho - c^{-2}\epsilon_\kappa \,, \tag{3.76}$$

$$\hat{\mathrm{a}}^1_1 \;=\; -\rho^0\rho^{-1}(D_\nu\epsilon_\rho)\,\mathrm{i}\alpha_\nu \,, \tag{3.77}$$

$$\hat{\mathrm{a}}^1_0 \;=\; -\rho^0\rho^{-1}(D_\nu^2\epsilon_\rho) \,. \tag{3.78}$$

Given the symbol $\hat{\mathrm{a}}$, we now have to construct the vertical slowness left symbol $\hat{\gamma}^{(\pm)}$ defined in equation (3.30). This symbol satisfies a characteristic equation following the composition of operators in equation (3.18) (De Hoop, 1996):

$$\exp\left[-\mathrm{i}\,\partial_{\alpha_\sigma'} D_{x_\sigma'}\right]\, \hat{\gamma}(x_\mu,\zeta,\alpha_\sigma')\hat{\gamma}(x_\sigma',\zeta,\alpha_\nu)\Big|_{(x_\mu',\alpha_\nu')=(x_\mu,\alpha_\nu)} = \hat{\mathrm{a}}(x_\mu,\zeta,\alpha_\nu) \,. \tag{3.79}$$

(The composition equation for the associated Weyl symbols follows from the work of Fishman and McCoy (1984a)). This equation defines the generalized slowness surface and has solutions $\hat{\gamma}^{(\pm)}$. The two branches are $\hat{\gamma}^{(\pm)}(x_\mu, \zeta, \alpha_\nu)$ such that $\mathrm{Re}\{\hat{\gamma}^{(+)}\} \geq 0$ and $\mathrm{Re}\{\hat{\gamma}^{(-)}\} \leq 0$. Due to the local up/down symmetry of the medium we have $\hat{\gamma}^{(+)} = -\hat{\gamma}^{(-)}$. Note that as $s \to \infty$ the composition of symbols tends to an ordinary multiplication, and the solution of equation (3.79) reduces to the principal parts of the symbols. The principal part of the vertical slowness symbol corresponds to the vertical gradient of travel time, in accordance with the eikonal equation (which can be obtained from the high-frequency approximation of the path integral (De Hoop, 1996).

3.6.2 Scaling

The solution, $\hat{\gamma}$, to equation (3.79) will be constructed by means of a (polyhomogeneous) series expansion following the expansion of $\hat{\mathrm{a}}$ introduced above. To ease the identification of medium-contrast and symbol orders in the construction, we introduce two dimensionless parameters, ε associated with the medium constrast and Ω associated with the symbol order. With these parameters, we control the *magnitude* of our medium contrast (ε) and the *smoothness* (Ω) also, i.e.

$$\epsilon_\kappa(x_\mu, \zeta) = \varepsilon\, \mathsf{e}_\kappa(\Omega x_\mu, \zeta)\,, \qquad \epsilon_\rho(x_\mu, \zeta) = \varepsilon\, \mathsf{e}_\rho(\Omega x_\mu, \zeta)\,. \tag{3.80}$$

With

$$\begin{aligned}
\rho^0\rho^{-1} &= 1 - \varepsilon\, \mathsf{e}_\rho + \varepsilon^2\, \mathsf{e}_\rho^2\,, \\
(\rho^0)^2\rho^{-2} &= 1 - 2\varepsilon\, \mathsf{e}_\rho + 3\varepsilon^2\, \mathsf{e}_\rho^2\,, \\
(\kappa^0)^{-1}\kappa &= 1 - \varepsilon\, \mathsf{e}_\kappa + \varepsilon^2\, \mathsf{e}_\kappa^2\,, \\
(c^0)^2c^{-2} &= 1 + \varepsilon\,(\mathsf{e}_\rho - \mathsf{e}_\kappa) - \varepsilon^2\, \mathsf{e}_\kappa\,(\mathsf{e}_\rho - \mathsf{e}_\kappa)\,,
\end{aligned}$$

up to $\mathcal{O}(\varepsilon^2)$, we rewrite the expansion of the symbol $\hat{\mathrm{a}}$ associated with the characteristic operator as [cf., equations (3.76)-(3.78)]

$$\hat{\mathrm{a}}_2^1 = \varepsilon(c^0)^{-2}\{\mathsf{e}_\rho - \mathsf{e}_\kappa[1 + \varepsilon\,(\mathsf{e}_\rho - \mathsf{e}_\kappa) - \varepsilon^2\, \mathsf{e}_\kappa(\mathsf{e}_\rho - \mathsf{e}_\kappa) + \cdots]\};, \tag{3.81}$$

$$\hat{\mathrm{a}}_1^1 = -\varepsilon\Omega\ \{1 - \varepsilon\, \mathsf{e}_\rho + \varepsilon^2\, \mathsf{e}_\rho^2 + \cdots\}\ (\mathsf{D}_\nu \mathsf{e}_\rho)\, \mathrm{i}\alpha_\nu\,, \tag{3.82}$$

$$\hat{\mathrm{a}}_0^1 = -\varepsilon\Omega^2\{1 - \varepsilon\, \mathsf{e}_\rho + \varepsilon^2\, \mathsf{e}_\rho^2 + \cdots\}\ (\mathsf{D}_\nu^2 \mathsf{e}_\rho)\,, \tag{3.83}$$

while [cf., equation (3.75)]

$$\hat{\mathrm{a}}_0^2 = \varepsilon^2\Omega^2\,\{1 - 2\varepsilon\, \mathsf{e}_\rho + \cdots\}\ (\mathsf{D}_\nu \mathsf{e}_\rho)^2\,. \tag{3.84}$$

We have introduced the scaled horizontal slowness operators D_ν which differentiates with respect to Ωx_ν: $\mathsf{D}_\nu = \Omega^{-1} D_\nu$. The expansions shown above appear in the Born series also (see Appendix E), which occurs naturally in the parameters ρ and κ. Here, we will treat the expansions in equations (3.81)-(3.84) between braces as single expressions and thus reparametrize the series for the characteristic symbol.

The symbol $\hat{a}_2^1$ is directly related to the *screen* function $S_{c^{-1}}$ (Wu & Huang, 1992) which we will encounter in the later analysis. Let $\epsilon_{c^{-1}}(x_\mu, \zeta)$ denote the relative medium slowness perturbation for $\zeta \in [x_3', x_3]$, then

$$\tfrac{1}{2}\hat{a}_2^1 \simeq (c^0)^{-2}\, \epsilon_{c^{-1}} \;, \quad \epsilon_{c^{-1}} \simeq \tfrac{1}{2}(\mathsf{e}_\rho - \mathsf{e}_\kappa) \;, \quad \text{while} \quad S_{c^{-1}} = \frac{1}{\Delta x_3}\int_{x_3'}^{x_3} \epsilon_{c^{-1}}\, \mathrm{d}\zeta \;. \tag{3.85}$$

These approximations are $\mathcal{O}(\varepsilon^2)$.

3.6.3 Perturbation expansion of the vertical slowness left symbol

We will solve equation (3.79) by method of expansion. In view of the contrast formulation, the vertical slowness in the laterally homogeneous embedding is introduced [cf., equation (3.73)]

$$\gamma^0(\zeta, \alpha_\nu, s) = \sqrt{\hat{a}_2^0(x_3, \alpha_\nu)} = \sqrt{\alpha_\nu^2 + [c^0(x_3)]^{-2}} = \gamma^0(x_3, \alpha_\nu) \;\text{ if }\; \zeta \in [x_3', x_3] \;. \tag{3.86}$$

We suppose that the vertical slowness symbol can be appoximated by a perturbation, $\hat{\gamma}^1$ say, superimposed on the vertical slowness in the laterally homogeneous embedding,

$$\hat{\gamma}(x_\mu, \zeta, \alpha_\nu, s) = \gamma^0(x_3, \alpha_\nu) + \hat{\gamma}^1(x_\mu, \zeta, \alpha_\nu, s) \;\text{ if }\; \zeta \in [x_3', x_3] \;. \tag{3.87}$$

First, let us expand the vertical slowness perturbation, asymptotically into the magnitude of the medium perturbation, i.e.

$$\hat{\gamma}^1(x_\mu, \zeta, \alpha_\nu, s) \sim \sum_{n=1}^{\infty} \varepsilon^n\, \eta^{[n]}(x_\mu, \zeta, \alpha_\nu, s) \;; \tag{3.88}$$

this expansion, though carried out in the space of symbols, has similarities with the Born series expansion [see, e.g., A.T. de Hoop (1991)]. Associated with the Born approximation is the condition

$$c(x_\mu, \zeta) \geq c^0(x_3) \;, \tag{3.89}$$

which for the symbols guarantees that no artificial branch point will enter the propagating-wave domain. Also, note that this expansion breaks down where the exact symbol fails to be analytic.

Second, we expand the series (3.88) further in terms of the smoothness of the medium perturbation,

$$\eta^{[n]}(x_\mu, \zeta, \alpha_\nu, s) \sim \sum_{m=0}^{\infty} \Omega^m\, \eta^{[n]}_{[1-m]}(x_\mu, \zeta, \alpha_\nu, s) \;. \tag{3.90}$$

The leading term of this expansion represents the high-frequency approximation or the principal part. We will suppress the dependencies on ζ and s in our notation.

While substituting these expansions into equation (3.79), we observe that for $k \geq 1$,

$$(-\mathrm{i}\partial_{\alpha'_\sigma} D_{x'_\sigma})^k \hat{\gamma}(x_\mu, \alpha'_\sigma)\hat{\gamma}(x'_\sigma, \alpha_\nu)\Big|_{(x'_\mu,\alpha'_\nu)=(x_\mu,\alpha_\nu)} = \tag{3.91}$$
$$\sum_{\ell=0}^{k} \binom{k}{l} (-\mathrm{i})^k \left[(\partial_{\alpha_1}^{k-\ell}\partial_{\alpha_2}^{\ell}\gamma^0)(x_\mu,\alpha_\nu) + (\partial_{\alpha_1}^{k-\ell}\partial_{\alpha_2}^{\ell}\hat{\gamma}^1)(x_\mu,\alpha_\nu)\right] (D_{x_1}^{k-\ell} D_{x_2}^{\ell}\hat{\gamma}^1)(x_\mu,\alpha_\nu)\,,$$

hence

$$(-\mathrm{i}\partial_{\alpha'_\sigma} D_{x'_\sigma})^k \hat{\gamma}(x_\mu, \alpha'_\sigma)\hat{\gamma}(x'_\sigma, \alpha_\nu)\Big|_{(x'_\mu,\alpha'_\nu)=(x_\mu,\alpha_\nu)} = \tag{3.92}$$
$$\sum_{\ell=0}^{k} \binom{k}{l} (-\mathrm{i})^k \Omega^k \sum_{n'=1}^{\infty} \varepsilon^{n'} \sum_{m'=0}^{\infty} \Omega^{m'} (\mathsf{D}_{x_1}^{k-\ell}\mathsf{D}_{x_2}^{\ell}\eta_{[1-m']}^{[n']})(x_\mu,\alpha_\nu)$$
$$\times \left[(\partial_{\alpha_1}^{k-\ell}\partial_{\alpha_2}^{\ell}\gamma^0)(x_\mu,\alpha_\nu) + \sum_{n=1}^{\infty}\varepsilon^n \sum_{m=0}^{\infty} \Omega^m (\partial_{\alpha_1}^{k-\ell}\partial_{\alpha_2}^{\ell}\eta_{[1-m]}^{[n]})(x_\mu,\alpha_\nu)\right] .$$

Upon substituting the expansions (3.88)-(3.90) into equation (3.79), we will collect terms of equal order in ε. These terms are then separated in orders of Ω. We will carry out our analysis up to $\mathcal{O}(\Omega^2)$.

The terms $\mathcal{O}(\varepsilon^0)$ yield equation (3.86), viz.

$$(\gamma^0)^2 = \hat{\mathrm{a}}_2^0 \qquad [k=0]\ (3.93)$$

which is $\mathcal{O}(\Omega^0)$. The terms $\mathcal{O}(\varepsilon)$ decompose into

$$2\gamma^0\ \eta_{[1]}^{[1]} = \hat{\mathrm{a}}_2^1 \qquad [k=0]\ (3.94)$$

which is $\mathcal{O}(\Omega^0)$, and

$$\begin{aligned}
&2\gamma^0\ \eta_{[0]}^{[1]} - \mathrm{i}\,(\partial_{\alpha_\sigma}\gamma^0)\,(\mathsf{D}_{x_\sigma}\eta_{[1]}^{[1]}) = \hat{\mathrm{a}}_1^1\,, && [k=0,1]\\
&2\gamma^0\ \eta_{[-1]}^{[1]} - \mathrm{i}\,(\partial_{\alpha_\sigma}\gamma^0)\,(\mathsf{D}_{x_\sigma}\eta_{[0]}^{[1]}) && [k=0,1]\ (3.95)\\
&-\tfrac{1}{2}[(\partial_{\alpha_1}^2\gamma^0)(\mathsf{D}_{x_1}^2\eta_{[1]}^{[1]}) + 2(\partial_{\alpha_1}\partial_{\alpha_2}\gamma^0)(\mathsf{D}_{x_1}\mathsf{D}_{x_2}\eta_{[1]}^{[1]}) + (\partial_{\alpha_2}^2\gamma^0)(\mathsf{D}_{x_2}^2\eta_{[1]}^{[1]})] = \hat{\mathrm{a}}_0^1 && [k=2]
\end{aligned}$$

which are $\mathcal{O}(\Omega^1)$ and $\mathcal{O}(\Omega^2)$, respectively. The terms $\mathcal{O}(\varepsilon^2)$ decompose into

$$(\eta_{[1]}^{[1]})^2 + 2\gamma^0\ \eta_{[1]}^{[2]} = 0 \qquad [k=0]\ (3.96)$$

which is $\mathcal{O}(\Omega^0)$,

$$2\eta_{[1]}^{[1]}\eta_{[0]}^{[1]} + 2\gamma^0\ \eta_{[0]}^{[2]} - \mathrm{i}\,(\partial_{\alpha_\sigma}\gamma^0)\,(\mathsf{D}_{x_\sigma}\eta_{[1]}^{[2]}) - \mathrm{i}\,(\partial_{\alpha_\sigma}\eta_{[1]}^{[1]})\,(\mathsf{D}_{x_\sigma}\eta_{[1]}^{[1]}) = 0 \qquad [k=0,1]\ (3.97)$$

which is $\mathcal{O}(\Omega)$, and

$$
\begin{aligned}
&2\gamma^0\,\eta^{[2]}_{[-1]} + (\eta^{[1]}_{[0]})^2 + 2\eta^{[1]}_{[1]}\eta^{[1]}_{[-1]} && [k=0]\\
&-\mathrm{i}\,[(\partial_{\alpha_\sigma}\gamma^0)\,(\mathsf{D}_{x_\sigma}\eta^{[2]}_{[0]}) + (\partial_{\alpha_\sigma}\eta^{[1]}_{[1]})\,(\mathsf{D}_{x_\sigma}\eta^{[1]}_{[0]}) + (\partial_{\alpha_\sigma}\eta^{[1]}_{[0]})\,(\mathsf{D}_{x_\sigma}\eta^{[1]}_{[1]})] && [k=1]\\
&-\tfrac{1}{2}[(\partial^2_{\alpha_1}\gamma^0)(\mathsf{D}^2_{x_1}\eta^{[2]}_{[1]}) + 2(\partial_{\alpha_1}\partial_{\alpha_2}\gamma^0)(\mathsf{D}_{x_1}\mathsf{D}_{x_2}\eta^{[2]}_{[1]}) + (\partial^2_{\alpha_2}\gamma^0)(\mathsf{D}^2_{x_2}\eta^{[2]}_{[1]}) && [k=2]\\
&+(\partial^2_{\alpha_1}\eta^{[1]}_{[1]})(\mathsf{D}^2_{x_1}\eta^{[1]}_{[1]}) + 2(\partial_{\alpha_1}\partial_{\alpha_2}\eta^{[1]}_{[1]})(\mathsf{D}_{x_1}\mathsf{D}_{x_2}\eta^{[1]}_{[1]}) + (\partial^2_{\alpha_2}\eta^{[1]}_{[1]})(\mathsf{D}^2_{x_2}\eta^{[1]}_{[1]})] && [k=2]\\
&=\hat{\mathrm{a}}^2_0
\end{aligned}
\tag{3.98}
$$

which is $\mathcal{O}(\Omega^2)$. Etc.

Solving the equations $\mathcal{O}(\Omega^0)$, i.e. for $\eta^{[n]}_{[1]}$, we observe that the constituent symbols generate an expansion of the type

$$
\hat{\gamma}_1 = \sqrt{\hat{\mathrm{a}}^0_2 + \hat{\mathrm{a}}^1_2} = \gamma^0\sqrt{1 + (\hat{\mathrm{a}}^1_2/\hat{\mathrm{a}}^0_2)} \sim \gamma^0 + \sum_{n=1}^{\infty}\varepsilon^n\,\eta^{[n]}_{[1]}\,, \tag{3.99}
$$

which could also be rewritten as

$$
\sqrt{\hat{\mathrm{a}}^0_2 + \hat{\mathrm{a}}^1_2} = \sqrt{\hat{\mathrm{a}}^1_2}\,\sqrt{1 + (\hat{\mathrm{a}}^0_2/\hat{\mathrm{a}}^1_2)}
$$

and expanded in a Taylor series accordingly. The first three terms of expansion (3.99) are illustrated in Figure 3.2. In this figure, we have carried out the rotations in the frequency and slowness domains

$$
s = \mathrm{i}\omega\,, \quad \alpha_\nu = -\mathrm{i}p_\nu\,.
$$

Solving the equations $\mathcal{O}(\Omega)$, i.e. for $\eta^{[n]}_{[0]}$, we find that the constituent symbols represent an expansion of the type (De Hoop, 1996, Section VIII)

$$
\begin{aligned}
&\frac{1}{2\,[\hat{\mathrm{a}}^0_2 + \hat{\mathrm{a}}^1_2]^{3/2}}\left[\hat{\mathrm{a}}^1_1\,[\hat{\mathrm{a}}^0_2 + \hat{\mathrm{a}}^1_2] + \tfrac{1}{2}\mathrm{i}\alpha_\sigma(D_{x_\sigma}\hat{\mathrm{a}}^1_2)\right] \qquad (3.100)\\
&= \frac{1}{2(\gamma^0)^3\,[1 + (\hat{\mathrm{a}}^1_2/\hat{\mathrm{a}}^0_2)]^{3/2}}\left[(\gamma^0)^2\hat{\mathrm{a}}^1_1\,[1 + (\hat{\mathrm{a}}^1_2/\hat{\mathrm{a}}^0_2)] + \tfrac{1}{2}\mathrm{i}\alpha_\sigma(D_{x_\sigma}\hat{\mathrm{a}}^1_2)\right] \sim \sum_{n=1}^{\infty}\varepsilon^n\,\eta^{[n]}_{[0]}\,,
\end{aligned}
$$

which takes into account the rate of change (gradient) of the medium properties in the lateral directions.

3.6.4 Screen reduction

The recursion for the solution of the vertical slowness left symbol described by equations (3.93)-(3.98) reveals that the expansion in ε implies a separation in the phase space

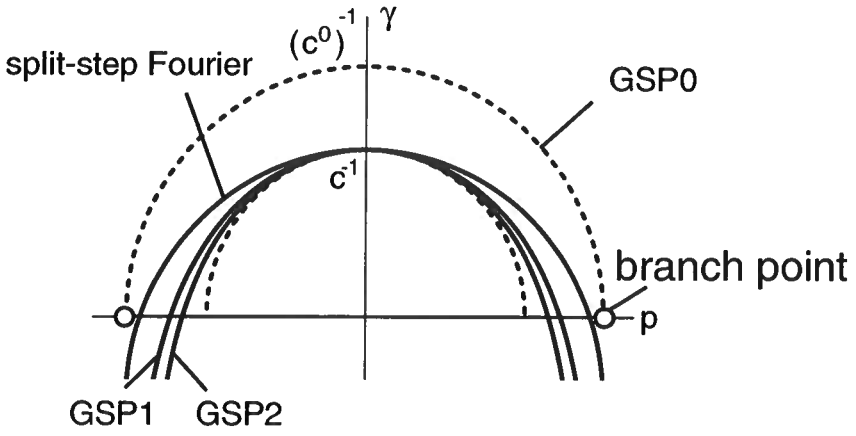

Figure 3.2. Principal parts of the generalized screen vertical slowness left symbols: zero order (GSP0), first order (GSP1) and second order (GSP2). 'Split-step' refers to the phase screen.

coordinates, x_μ and α_ν, of the constituent symbols in equation (3.90):

$$\eta^{[n]}_{[1-m]}(x_\mu, \alpha_\nu) = \sum_\lambda \overset{\lambda}{\xi}{}^{[n]}_{[1-m]}\,(x_\mu)\ \overset{\lambda}{a}{}^{[n]}_{[1-m]}\,(\alpha_\nu)\ , \qquad m = 0, 1, \cdots \tag{3.101}$$

We will illustrate the implications of this expansion for the case $n = 1$ and $m = 0$, when we have one term only. To simplify the notation, in this case, we omit the counter λ. Representation (3.101) is depicted in Figure 3.1.

The separation of variables is why our lattice integral equation (3.31) will reduce to a screen propagator (Wu & Huang, 1992). Equation (3.101) implies the following structure for the *cokernel* [cf., equation (3.36)] of the vertical slowness operator,

$$\widetilde{\eta^{[n]}_{[1-m]}}(\alpha_\mu - \alpha''_\mu, \alpha''_\nu) = \widetilde{\xi^{[n]}_{[1-m]}}(\alpha_\mu - \alpha''_\mu)\, a^{[n]}_{[1-m]}(\alpha''_\nu)\ , \qquad m = 0, 1, \cdots \tag{3.102}$$

which reveals how Fourier constituents ('plane' waves) interact. Asymptotically, we have

$$\widetilde{\xi^{[n]}_{[1-m]}}(\alpha_\mu - \alpha''_\mu) \sim s^{-2}\ \Big\{\xi^{[n]}_{[1-m]}(0)\,\delta(\alpha_\mu - \alpha''_\mu) + \mathrm{i}\Omega\,(\mathsf{D}_{x_\sigma}\xi^{[n]}_{[1-m]})(0)\,(\partial_{\alpha_\sigma}\delta)(\alpha_\mu - \alpha''_\mu) + \cdots\Big\}\ .$$

Let us consider the expansion for the vertical slowness left symbol up to $\mathcal{O}(\varepsilon)$ and $\mathcal{O}(\Omega^0)$. Using equation (3.99), we arrive at

$$\eta^{[1]}_{[1]}(x_\mu, \alpha_\nu) = \xi^{[1]}_{[1]}(x_\mu)\, a^{[1]}_{[1]}(\alpha_\nu)\ , \qquad \xi^{[1]}_{[1]} = \tfrac{1}{2}\hat{\mathrm{a}}^1_2\ , \qquad a^{[1]}_{[1]} = \frac{1}{\gamma^0}\ . \tag{3.103}$$

We denote this first-order expansion as the *wide-angle screen* approximation. (How the wide-angle screen approximation relates to the local-Born approximation is discussed in Appendix E.) Observe the occurrence of the branch point associated with the background medium, which is artificial. Ignoring the artifical branch point, we now Taylor expand the factor $a^{[1]}_{[1]}$ about $\alpha_\nu = 0$ (limiting to narrow angles). Up to zero-order,

$$a^{[1]}_{[1]}(\alpha_\nu) \simeq a^{[1]}_{[1]}(0) = c^0 \,, \tag{3.104}$$

which leads to the *phase-screen* or split-step approximation, which is also shown in Figure 3.2. For various applications, the second-order expansion in α_ν^2 is sufficiently accurate,

$$a^{[1]}_{[1]}(\alpha_\nu) \simeq c^0 - \tfrac{1}{2}(c^0)^3 \; \alpha_\nu^2 + \tfrac{3}{8}(c^0)^5 \; (\alpha_\nu^2)^2 \,. \tag{3.105}$$

These expansions are illustrated in Figure 3.3. Note that, upon carrying out the Taylor expansion of $a^{[1]}_{[1]}$ in α_ν, we can replace the background from *minimum* value in the thin slab to *average* value, thus enhancing the accuracy (Stoffa *et al.*, 1990). This replacement also represents the transition from the phase-screen to the split-step Fourier approach. Some wavefronts associated with Figures 3.2 and 3.3 are shown in Figure 3.4. Using Huygens principle, we can now anticipate the evolution of a wavefront in a heterogeneous medium. In all the approximations, independent of order, the propagation speed in the horizontal directions is c^0, which causes any of our approximate instantaneous wavefronts to fold inwards away from the true instantaneous wavefront. As such, the generalized-screen approximation differs, for example, from the paraxial approximation where the accuracy with propagation angle is *independent* of the medium (Claerbout, 1970; Van Stralen *et al.*, 1998). But, like in the paraxial approximation, *critical-angle* phenomena are *not* modelled properly within the generalized-screen approximation.

The contribution to the left symbol $\mathcal{O}(\varepsilon)$ and $\mathcal{O}(\Omega)$ follows directly from equation (3.95) as

$$\eta^{[1]}_{[0]} = \tfrac{1}{2}\hat{\mathrm{a}}^1_1 \frac{1}{\gamma^0} + \tfrac{1}{4}(D_{x_\sigma}\hat{\mathrm{a}}^1_2)\,\frac{\mathrm{i}\alpha_\sigma}{(\gamma^0)^3} \,, \tag{3.106}$$

which extends the wide-angle approximation equation (3.103).

3.6.5 Optimization

Rather than accepting a given order of expansion, we will discuss a way – introducing intermediate parameters – to smear out the error of our approximation in phase space. In particular, we will be concerned about the errors in travel times along the wave-constituent characteristics, and try to minimize those. Such errors are associated with the principal parts of the symbols.

As an example, consider the wide-angle approximation (3.103). By shifting the background medium branch points in this expression, we can 'bend' the principal part of the slowness curve. We will exploit this bending in an optimization procedure. In equations

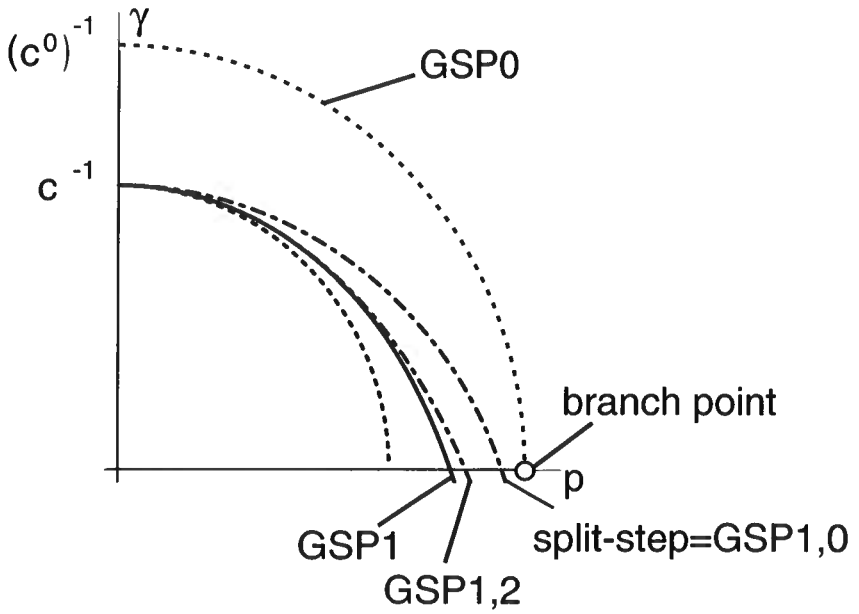

Figure 3.3. Taylor expansions of the principal part of the first-order generalized screen (GSP1) vertical slowness left symbol: zero order (GSP1,0) and second order (GSP1,2).

(3.87) and (3.103), we introduce parameters β_0, β_1 according to

$$\gamma^0(x_3, \alpha_\nu) \to \sqrt{\beta_0 \alpha_\nu^2 + [c^0(x_3)]^{-2}}\,, \quad a_{[1]}^{[1]}(\alpha_\nu) \to \frac{1}{\sqrt{\beta_1 \alpha_\nu^2 + [c^0(x_3)]^{-2}}}\,. \tag{3.107}$$

If the range of scattering angles is limited, by adjusting β_0, β_1, indeed the branch points can be moved inwards. However, upon applying the Taylor series expansion (3.105), the troublesome branch point in $a_{[1]}^{[1]}$ is removed; then we set

$$\gamma^0(x_3, \alpha_\nu) \to \gamma^0(x_3, \alpha_\nu)\,, \quad a_{[1]}^{[1]}(\alpha_\nu) \to c^0 - \tfrac{1}{2}(c^0)^3\, \beta_0 \alpha_\nu^2 + \tfrac{3}{8}(c^0)^5\, \beta_1 (\alpha_\nu^2)^2 \tag{3.108}$$

instead.

For the purpose of optimization, we will turn the composition equation (3.79) into a weak form, viz., we introduce the error function

$$\mathrm{err}(x_\mu, \zeta, s) = (s/2\pi)^2 \int \mathrm{d}\alpha_1 \mathrm{d}\alpha_2 \tag{3.109}$$

$$\left| \exp\left[-\mathrm{i}\, \partial_{\alpha'_\sigma} D_{x'_\sigma}\right]\, \hat{\gamma}(x_\mu, \zeta, \alpha'_\sigma, s) \hat{\gamma}(x'_\sigma, \zeta, \alpha_\nu, s) \Big|_{(x'_\mu, \alpha'_\nu) = (x_\mu, \alpha_\nu)} - \hat{\mathrm{a}}(x_\mu, \zeta, \alpha_\nu, s) \right|^2 ,$$

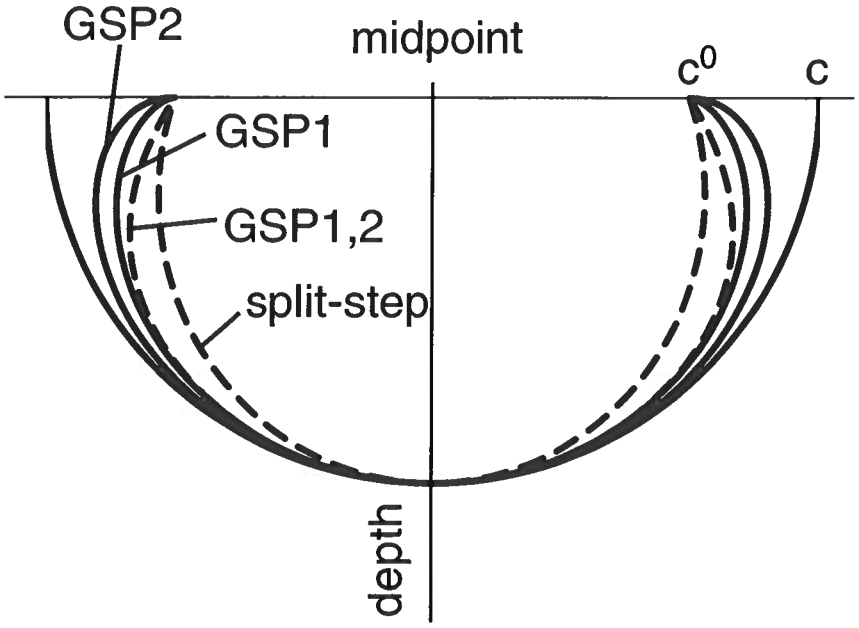

Figure 3.4. Wavefronts associated with the various generalized-screen approximations.

measuring an L^2 average over the horizontal slownesses up to the branch points (i.e., over the 'propagating' slowness surface). Restricting the error function to $\mathcal{O}(\Omega^0)$, i.e. the vertical gradients of travel time, yields

$$\mathrm{err}_{[1]}^{[N]}(x_\mu,\zeta;\beta) = (s/2\pi)^2 \int \left| \left[\gamma^0(x_3,\alpha_\nu) + \sum_{n=1}^{N} \varepsilon^n \, \eta_{[1]}^{[n]}(x_\mu,\zeta,\alpha_\nu) \right]^2 - \hat{a}_2^0(x_\mu,\zeta,\alpha_\nu) \right|^2 \mathrm{d}\alpha_1 \mathrm{d}\alpha_2 \, . \tag{3.110}$$

The misfit in the optimization for parameters β_0, β_1 is then simply the integral of the error function over horizontal space. This integration reflects the variation of the medium in the horizontal directions. Thus, for the $\mathcal{O}(\Omega^0)$ optimization problem, we might integrate over the associated range of medium slownesses instead.

Enforcing the parameters β_0, β_1 to be equal ensures that the approximate expression (3.107) contains a single branch point only. To ensure that the approximate expression reduces to a screen representation, the parameters should be independent of x_μ.

3.6.6 The screen propagator

We will now return to the basic symbol structure equations (3.87),(3.103) and analyze what this structure implies for the thin-slab propagator given in equation (3.32). In general,

with equation (3.87) we get

$$\hat{g}^{(+)}(x_\mu, x_3; x'_\nu, x_3 - \Delta x_3) \simeq \int (s/2\pi)^2 \mathrm{d}\alpha''_1 \mathrm{d}\alpha''_2 \exp[-\mathrm{i}s\,\alpha''_\sigma (x_\sigma - x'_\sigma)] \qquad (3.111)$$
$$\exp[-s\,\{\gamma^0(x_3 - \Delta x_3, \alpha''_\nu) + \hat{\gamma}^1(x_\mu, x_3 - \tfrac{1}{2}\Delta x_3, \alpha''_\nu)\}\,\Delta x_3]\ .$$

Invoking the first-order generalized-screen approximation (3.103) yields

$$\begin{aligned}
&\exp[-s\,\{\gamma^0(x_3 - \Delta x_3, \alpha''_\nu) + \hat{\gamma}^1(x_\mu, x_3 - \tfrac{1}{2}\Delta x_3, \alpha''_\nu)\}\,\Delta x_3] \qquad (3.112)\\
&\quad \simeq \exp[-s\varepsilon\,\xi^{[1]}_{[1]}(x_\mu, x_3 - \tfrac{1}{2}\Delta x_3) a^{[1]}_{[1]}(x_3 - \tfrac{1}{2}\Delta x_3, 0)\ \Delta x_3]\\
&\qquad \exp[-s\varepsilon\,\xi^{[1]}_{[1]}(x_\mu, x_3 - \tfrac{1}{2}\Delta x_3)\,[a^{[1]}_{[1]}(x_3 - \tfrac{1}{2}\Delta x_3, \alpha''_\nu) - a^{[1]}_{[1]}(x_3 - \tfrac{1}{2}\Delta x_3, 0)]\ \Delta x_3]\\
&\qquad\quad \exp[-s\,\gamma^0(x_3 - \Delta x_3, \alpha''_\nu)\,\Delta x_3]\\
&\quad \simeq \exp[-s\varepsilon\,\xi^{[1]}_{[1]}(x_\mu, x_3 - \tfrac{1}{2}\Delta x_3) a^{[1]}_{[1]}(x_3 - \tfrac{1}{2}\Delta x_3, 0)\ \Delta x_3]\\
&\qquad \left\{1 - s\varepsilon\,\xi^{[1]}_{[1]}(x_\mu, x_3 - \tfrac{1}{2}\Delta x_3)\,[a^{[1]}_{[1]}(x_3 - \tfrac{1}{2}\Delta x_3, \alpha''_\nu) - a^{[1]}_{[1]}(x_3 - \tfrac{1}{2}\Delta x_3, 0)]\ \Delta x_3\right\}\\
&\qquad\quad \exp[-s\,\gamma^0(x_3 - \Delta x_3, \alpha''_\nu)\,\Delta x_3]
\end{aligned}$$

if

$$\frac{s\,\Delta x_3}{c^0}\ \left|\varepsilon\, c^0 \xi^{[1]}_{[1]}(x_\mu, .)\,[a^{[1]}_{[1]}(., \alpha''_\nu) - a^{[1]}_{[1]}(., 0)]\right| \ll 1\ .$$

Note that $\varepsilon\, c^0 \xi^{[1]}_{[1]} = (c^0)^{-1} S_{c^{-1}}$ represents the absolute medium slowness perturbation, while $[a^{[1]}_{[1]}(., \alpha''_\nu) - a^{[1]}_{[1]}(., 0)]$ vanishes at normal incidence ($\alpha''_\nu = 0$) and is bounded by c^0 as $\alpha''_\nu \alpha''_\nu \to \infty$.

Substituting equation (3.112) into equation (3.111) results in

$$\begin{aligned}
&\hat{g}^{(+)}(x_\mu, x_3; x'_\nu, x_3 - \Delta x_3) \simeq \exp[-s\varepsilon\,\xi^{[1]}_{[1]}(x_\mu, x_3 - \tfrac{1}{2}\Delta x_3) a^{[1]}_{[1]}(x_3 - \tfrac{1}{2}\Delta x_3, 0)\ \Delta x_3]\\
&\quad \left\{ \int (s/2\pi)^2 \mathrm{d}\alpha''_1 \mathrm{d}\alpha''_2 \exp[-\mathrm{i}s\,\alpha''_\sigma x_\sigma]\ \exp[-s\,\gamma^0(x_3 - \Delta x_3, \alpha''_\nu)\,\Delta x_3]\ \exp[\mathrm{i}s\,\alpha''_\sigma x'_\sigma]\right.\\
&\qquad -s\varepsilon\,\xi^{[1]}_{[1]}(x_\mu, x_3 - \tfrac{1}{2}\Delta x_3)\,\Delta x_3 \int (s/2\pi)^2 \mathrm{d}\alpha''_1 \mathrm{d}\alpha''_2 \exp[-\mathrm{i}s\,\alpha''_\sigma x_\sigma] \qquad (3.113)\\
&\qquad\quad [a^{[1]}_{[1]}(x_3 - \tfrac{1}{2}\Delta x_3, \alpha''_\nu) - a^{[1]}_{[1]}(x_3 - \tfrac{1}{2}\Delta x_3, 0)]\ \exp[\mathrm{i}s\,\alpha''_\sigma x'_\sigma]\\
&\qquad\quad \left. \exp[-s\,\gamma^0(x_3 - \Delta x_3, \alpha''_\nu)\,\Delta x_3]\ \right\}
\end{aligned}$$

which, switching from left to right symbols [cf., equation (3.33)], can also be written as

$$\int \mathrm{d}x_1'\mathrm{d}x_2'\hat{g}^{(+)}(x_\mu, x_3; x_\nu', x_3 - \Delta x_3)(\cdot) \simeq \int (s/2\pi)^2 \mathrm{d}\alpha_1''\mathrm{d}\alpha_2'' \tag{3.114}$$
$$\exp[-\mathrm{i}s\,\alpha_\sigma'' x_\sigma] \exp[-s\,\gamma^0(x_3 - \Delta x_3, \alpha_\nu'')\,\Delta x_3]\,\mathcal{N}_{\alpha_\nu'', \Delta x_3}$$
$$\Big\{ \int \mathrm{d}x_1'\mathrm{d}x_2' \exp[\mathrm{i}s\,\alpha_\sigma'' x_\sigma'] \exp[-s\varepsilon\,\xi_{[1]}^{[1]}(x_\nu', x_3 - \tfrac{1}{2}\Delta x_3) a_{[1]}^{[1]}(x_3 - \tfrac{1}{2}\Delta x_3, 0)\,\Delta x_3]\,(\cdot)$$
$$-s\,\Delta x_3\,[a_{[1]}^{[1]}(x_3 - \tfrac{1}{2}\Delta x_3, \alpha_\nu'') - a_{[1]}^{[1]}(x_3 - \tfrac{1}{2}\Delta x_3, 0)] \int \mathrm{d}x_1'\mathrm{d}x_2' \exp[\mathrm{i}s\,\alpha_\sigma'' x_\sigma']$$
$$\varepsilon\,\xi_{[1]}^{[1]}(x_\nu', x_3 - \tfrac{1}{2}\Delta x_3) \exp[-s\varepsilon\,\xi_{[1]}^{[1]}(x_\nu', x_3 - \tfrac{1}{2}\Delta x_3) a_{[1]}^{[1]}(x_3 - \tfrac{1}{2}\Delta x_3, 0)\,\Delta x_3](\cdot) \Big\}$$

In this expression we have introduced a (windowed) normalizing operator $\mathcal{N}$ to restore the appropriate amplitude behavior which was destroyed by the Taylor expansion of the exponential in equation (3.112),

$$\mathcal{N}\{y(1 + p + \mathrm{i}q)\} = y \exp(\mathrm{i}q) \left|1 + \frac{p}{1 + \mathrm{i}q}\right|^{-1} \left[1 + \frac{p}{1 + \mathrm{i}q}\right], \quad |y| = 1\,.$$

Every additional order in the generalized-screen expansion (3.99), in equation (3.113) requires an additional inverse Fourier transform. The phase-screen approximation is obtained by omitting the second terms – proportional to Δx_3 – in expressions (3.113), (3.114). The numerical procedure is discussed in Le Rousseau and De Hoop (2001b) (Chapter 4) and is illustrated in Figure 3.5. This figure is the counterpart of Figure 3.4.

The key simplification of the 'exact' thin-slab propagator accomplished by the (generalized) screen approximation is, that the inverse (scaled) Fourier transforms with respect to α_ν'' *no longer* have to be evaluated for each x_μ *separately*; compare equation (3.113) with equation (3.32). This feature was inherited from the split-step Fourier or phase-screen approach, and also appears in the action of the pseudo-differential operators involved in the Bremmer series computation. The functions $\overset{\lambda}{\xi}{}_{[1-m]}^{[n]}(x_\mu)$ in equation (3.101) constitute the generalized screen, while the functions $\overset{\lambda}{a}{}_{[1-m]}^{[n]}(\alpha_\nu)$ extend the 'phase shift', see Figure 3.1. Further, we note that the concept of generalized screen has been inspired by the Rytov approximation.

In equation (3.113) we recognize the Laplace-domain Green's functions in the background medium,

$$\int (s/2\pi)^2 \mathrm{d}\alpha_1''\mathrm{d}\alpha_2'' \exp[-s\,\{\mathrm{i}\alpha_\sigma''(x_\sigma - x_\sigma') + \gamma^0(x_3 - \Delta x_3, \alpha_\nu'')\,\Delta x_3\}]$$

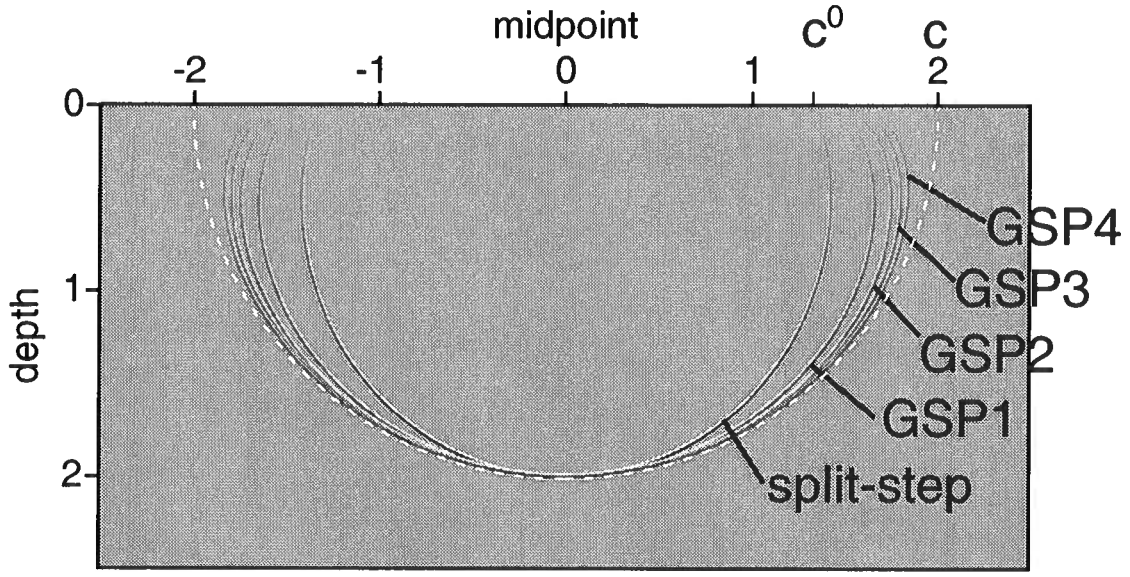

Figure 3.5. Wavefield snapshots associated with the various generalized-screen approximations.

[the pressure response due to a vertical point force] and

$$\int (s/2\pi)^2 \mathrm{d}\alpha_1'' \mathrm{d}\alpha_2'' \, a_{[1]}^{[1]}(x_3 - \tfrac{1}{2}\Delta x_3, \alpha_\nu'') \, \exp[-s\,\{\mathrm{i}\alpha_\sigma''(x_\sigma - x_\sigma') + \gamma^0(x_3 - \Delta x_3, \alpha_\nu'')\,\Delta x_3\}]$$

[the pressure response due to a point injection source]. This is no surprise, as is illucidated in Appendix E. With the aid of the Cagniard-De Hoop method [see, for example, Achenbach (1973)], the transformation of those functions back to the time domain can be carried out analytically. (Such a procedure was carried out for the paraxial approximations by De Hoop and De Hoop (1992).) The (space-)time domain expression for $\hat{g}^{(+)}$ can then be obtained also, using the facts that multiplication by the exponential in the first line of equation (3.113) transforms into a time shift, whereas multiplication by s in the third line becomes a time differentiation.

3.6.7 The windowed screen propagator

To improve the accuracy of our propagator for a given order, we briefly consider the extension of the generalized-screen approach based on a single reference or background medium to one with multiple reference media. Thus, per window, the medium contrast is reduced. To this end, we will have to localize our analysis in the horizontal directions. For this we will employ the windowed Fourier transform:

$$\int \mathrm{d}x_1' \mathrm{d}x_2' \, \exp[\mathrm{i}s\,\alpha_\sigma'' x_\sigma'] \, \chi(x_\nu' - \overline{x_\nu})$$

with the associated inverse transform

$$\int \mathrm{d}\overline{x_1}\mathrm{d}\overline{x_2}\,\chi^*(x_\nu - \overline{x_\nu}) \int (s/2\pi)^2 \mathrm{d}\alpha_1'' \mathrm{d}\alpha_2'' \exp[-\mathrm{i}s\,\alpha_\sigma'' x_\sigma]$$

such that

$$\int \mathrm{d}\overline{x_1}\mathrm{d}\overline{x_2}\,|\chi(x_\nu - \overline{x_\nu})|^2 = 1\,.$$

Equation (3.114) in windowed form, for example, becomes

$$\begin{aligned}
&\int \mathrm{d}x_1'\mathrm{d}x_2'\hat{g}^{(+)}(x_\mu, x_3; x_\nu', x_3 - \Delta x_3)(\cdot) \simeq \\
&\qquad \int \mathrm{d}\overline{x_1}\mathrm{d}\overline{x_2}\,\chi^*(x_\nu - \overline{x_\nu}) \int (s/2\pi)^2 \mathrm{d}\alpha_1'' \mathrm{d}\alpha_2'' \exp[-\mathrm{i}s\,\alpha_\sigma'' x_\sigma] \\
&\qquad \exp[-s\,\gamma^0(x_3 - \Delta x_3, \alpha_\nu'')\,\Delta x_3]\mathcal{N}_{\alpha_\nu'', \Delta x_3}\Big\{ \int \mathrm{d}x_1'\mathrm{d}x_2' \exp[\mathrm{i}s\,\alpha_\sigma'' x_\sigma'] \\
&\qquad \chi(x_\nu' - \overline{x_\nu}) \exp[-s\varepsilon\,\xi_{[1]}^{[1]}(x_\nu', x_3 - \tfrac{1}{2}\Delta x_3) a_{[1]}^{[1]}(x_3 - \tfrac{1}{2}\Delta x_3, 0)\,\Delta x_3]\,(\cdot) \\
&\qquad -s\,\Delta x_3\,[a_{[1]}^{[1]}(x_3 - \tfrac{1}{2}\Delta x_3, \alpha_\nu'') - a_{[1]}^{[1]}(x_3 - \tfrac{1}{2}\Delta x_3, 0)] \\
&\qquad\quad \int \mathrm{d}x_1'\mathrm{d}x_2'\chi(x_\nu' - \overline{x_\nu}) \exp[\mathrm{i}s\,\alpha_\sigma'' x_\sigma']\,\varepsilon\,\xi_{[1]}^{[1]}(x_\nu', x_3 - \tfrac{1}{2}\Delta x_3) \\
&\qquad\qquad \exp[-s\varepsilon\,\xi_{[1]}^{[1]}(x_\nu', x_3 - \tfrac{1}{2}\Delta x_3) a_{[1]}^{[1]}(x_3 - \tfrac{1}{2}\Delta x_3, 0)\ \Delta x_3](\cdot)\Big\}
\end{aligned}$$

Each window is associated with a particular reference medium.

3.6.8 The P(hase) S(hift) P(lus) I(nterpolation) propagator

If, in each window, the medium is supposed to be *constant*, and if the windowing is replaced by interpolation, we recover the P(hase) S(hift) P(lus) I(nterpolation) procedure (Gazdag & Sguazzero, 1984). Let us return to the thin-slab propagator in equation (3.32). In PSPI we restrict our vertical slowness left symbol to its principal part [cf., equation (3.99)],

$$\begin{aligned}
&\hat{\gamma}^{(+)}(x_\mu, x_3 - \tfrac{1}{2}\Delta x_3, \alpha_\nu'') \\
&\qquad \sim \hat{\gamma}_1(x_\mu, x_3 - \tfrac{1}{2}\Delta x_3, \alpha_\nu'') = \sqrt{\hat{\mathrm{a}}_2^0(x_3 - \Delta x_3, \alpha_\nu'') + \hat{\mathrm{a}}_2^1(x_\mu, x_3 - \tfrac{1}{2}\Delta x_3)}
\end{aligned}$$

whereas we sample the thin-slab propagator at the coordinate values $\{x_\mu^{(i)}\}_{i=1}^I$ such that the set $\{\hat{\gamma}_1(x_\mu^{(i)}, x_3 - \frac{1}{2}\Delta x_3, 0)\}_{i=1}^I$ regularly samples the range of medium velocities encountered across the current slab. Let

$$\begin{aligned}
\hat{g}^{(i)}(x_3; x_\nu', x_3 - \Delta x_3) = &\int (s/2\pi)^2 \mathrm{d}\alpha_1'' \mathrm{d}\alpha_2'' \\
&\exp[-\mathrm{i}s\,\alpha_\sigma''(x_\sigma^{(i)} - x_\sigma')] \exp[-s\,\hat{\gamma}_1(x_\mu^{(i)}, x_3 - \tfrac{1}{2}\Delta x_3, \alpha_\nu'')\Delta x_3]\,, \qquad (3.115)
\end{aligned}$$

which are simply homogeneous medium propagators. The thin-slab propagator $\hat{g}^{(+)}(.,x_3;x'_\nu,x'_3)$ at any x_μ is then obtained by carrying out an interpolation based on $\{\hat{g}^{(i)}\}_{i=1}^{I}$.

3.7 Screen representations of the (de)composition operators

3.7.1 The composition operator

For the generalized-screen expansion of the composition operator [cf., equation (3.19)] we have to expand (the symbol of) the vertical slowness operator itself. The action of the vertical slowness operator $\hat{\Gamma}^{(+)}$ can be cast in a form compatible with the thin-slab propagator (equation (3.111)) and represented by its Schwartz kernel (Schwartz, 1966b; Hörmander, 1990) $\hat{\mathcal{C}}^{(+)}$, obtained from the left symbol $\hat{\gamma}^{(+)}$ through the inverse Fourier transforms,

$$\hat{\mathcal{C}}^{(+)}(x_\mu,x'_\nu;x_3)=\int(s/2\pi)^2\mathrm{d}\alpha''_1\mathrm{d}\alpha''_2\,\exp[-\mathrm{i}s\,\alpha''_\sigma(x_\sigma-x'_\sigma)]\;\hat{\gamma}^{(+)}(x_\mu,x_3,\alpha''_\nu)\;. \tag{3.116}$$

In accordance with equation (3.114) the Schwartz kernel for the vertical slowness is thus approximated by

$$\begin{aligned}\hat{\mathcal{C}}^{(+)}(x_\mu,x'_\nu;x_3)\simeq&\int(s/2\pi)^2\mathrm{d}\alpha''_1\mathrm{d}\alpha''_2\exp[-\mathrm{i}s\,\alpha''_\sigma x_\sigma]\,\gamma^0(x_3,\alpha''_\nu)\;\exp[\mathrm{i}s\,\alpha''_\sigma x'_\sigma]\\&+\varepsilon\,\xi^{[1]}_{[1]}(x_\mu,x_3)\,a^{[1]}_{[1]}(x_3,0)\;\delta(x_\mu-x'_\mu)\\&+\varepsilon\,\xi^{[1]}_{[1]}(x_\mu,x_3)\int(s/2\pi)^2\mathrm{d}\alpha''_1\mathrm{d}\alpha''_2\exp[-\mathrm{i}s\,\alpha''_\sigma x_\sigma]\\&\qquad[a^{[1]}_{[1]}(x_3,\alpha''_\nu)-a^{[1]}_{[1]}(x_3,0)]\;\exp[\mathrm{i}s\,\alpha''_\sigma x'_\sigma]\;.\end{aligned} \tag{3.117}$$

Switching from left to right symbols yields

$$\begin{aligned}\hat{\mathcal{C}}^{(+)}(x_\mu,x'_\nu;x_3)\simeq&\int(s/2\pi)^2\mathrm{d}\alpha''_1\mathrm{d}\alpha''_2\exp[-\mathrm{i}s\,\alpha''_\sigma x_\sigma]\,\gamma^0(x_3,\alpha''_\nu)\;\exp[\mathrm{i}s\,\alpha''_\sigma x'_\sigma]\\&+\varepsilon\,\xi^{[1]}_{[1]}(x_\mu,x_3)\,a^{[1]}_{[1]}(x_3,0)\;\delta(x_\mu-x'_\mu)\\&+\int(s/2\pi)^2\mathrm{d}\alpha''_1\mathrm{d}\alpha''_2\exp[-\mathrm{i}s\,\alpha''_\sigma x_\sigma][a^{[1]}_{[1]}(x_3,\alpha''_\nu)-a^{[1]}_{[1]}(x_3,0)]\\&\qquad\varepsilon\,\xi^{[1]}_{[1]}(x'_\nu,x_3)\;\exp[\mathrm{i}s\,\alpha''_\sigma x'_\sigma]\;.\end{aligned} \tag{3.118}$$

In the wide-angle approximation, we substitute equation (3.103) in the equations above. With optimization it would be equation (3.107) or equation (3.108). Every additional order requires an additional inverse Fourier transform.

The phase-screen approximation is obtained by omitting the third terms on the right-hand sides of equations (3.117)-(3.118).

3.7.2 The decomposition operator

The screen representation of the decomposition operator [cf., equation (3.20)] requires a screen approximation of the inverse vertical slowness operator. To this end, the reciprocal vertical slowness symbol must be expanded as in equations (3.88)-(3.90). The reciprocal vertical slowness operator is of order -1 and hence we denote its constituent symbols as $\eta^{-1[n]}_{[-1-m]}$.

As a consequence of the expansion in ε, the constituent symbols are all separable in the phase space coordinates, x_μ and α_ν,

$$\eta^{-1[n]}_{[-1-m]}(x_\mu,\alpha_\nu)=\sum_{\lambda}\overset{\lambda}{\xi}{}^{-1[n]}_{[-1-m]}(x_\mu)\;\overset{\lambda}{a}{}^{-1[n]}_{[-1-m]}(\alpha_\nu)\,,\qquad m=0,1,\cdots \tag{3.119}$$

(If $n=1$ and $m=0$ we have one term only in which case we omit the λ.) The expansion for the reciprocal vertical slowness left symbol up to $\mathcal{O}(\Omega^0)$ (the principal parts) follows the series

$$\frac{1}{\hat\gamma_1}=\frac{1}{\sqrt{\hat a_2^0+\hat a_2^1}}=\frac{1}{\gamma^0\sqrt{1+(\hat a_2^1/\hat a_2^0)}}\sim\frac{1}{\gamma^0}+\sum_{n=1}^{\infty}\varepsilon^n\,\eta^{-1[n]}_{[-1]}\,. \tag{3.120}$$

Up to $\mathcal{O}(\varepsilon)$ we arrive at the wide-angle approximation,

$$\eta^{-1[1]}_{[-1]}(x_\mu,\alpha_\nu)=\xi^{-1[1]}_{[-1]}(x_\mu)\,a^{-1[1]}_{[-1]}(\alpha_\nu)\,,\qquad \xi^{-1[1]}_{[-1]}=-\tfrac12\hat a_2^1\,,\quad a^{-1[1]}_{[-1]}=\frac{1}{(\gamma^0)^3}\,. \tag{3.121}$$

Carrying out a Taylor series expansion about $\alpha_\nu=0$ to zero order yields

$$a^{-1[1]}_{[-1]}(\alpha_\nu)\simeq a^{-1[1]}_{[-1]}(0)=(c^0)^3\,, \tag{3.122}$$

which leads to the phase-screen or split-step approximation.

In analogy with equation (3.120), the $\mathcal{O}(\Omega)$ correction term is found to be (De Hoop, 1996, Section VIII)

$$\begin{aligned}&-\frac{1}{2\,[\hat a_2^0+\hat a_2^1]^{5/2}}\left[\hat a_1^1\,[\hat a_2^0+\hat a_2^1]+\tfrac32\mathrm{i}\alpha_\sigma(D_{x_\sigma}\hat a_2^1)\right] \\ &=-\frac{1}{2(\gamma^0)^5\,[1+(\hat a_2^1/\hat a_2^0)]^{5/2}}\left[(\gamma^0)^2\hat a_1^1\,[1+(\hat a_2^1/\hat a_2^0)]+\tfrac32\mathrm{i}\alpha_\sigma(D_{x_\sigma}\hat a_2^1)\right]\sim\sum_{n=1}^{\infty}\varepsilon^n\eta^{-1[n]}_{[-2]}\,.\end{aligned} \tag{3.123}$$

Up to $\mathcal{O}(\varepsilon)$ we get

$$\eta^{-1[1]}_{[-2]}=-\tfrac12\hat a_1^1\,\frac{1}{(\gamma^0)^3}-\tfrac34(D_{x_\sigma}\hat a_2^1)\,\frac{\mathrm{i}\alpha_\sigma}{(\gamma^0)^5}\,, \tag{3.124}$$

which extends the wide-angle approximation equation (3.121).

The Schwartz kernel of the inverse vertical slowness operator has a representation as

in equation (3.117) or (3.118).

3.8 Screen representations of the reflection/transmission operators

The interaction operator in equations (3.22)-(3.23) allows a screen representation as well. The interaction operator consists of a superposition of contributions from the density variations and the vertical wave slowness variations.

The symbol of the multiplication operator $\frac{1}{2}\hat{A}_{1,2}^{-1}(\partial_3\hat{A}_{1,2})$ (density variation) on the right-hand side of equation (3.23) follows as

$$\frac{1}{2\rho}\,(\partial_3\rho) = \varepsilon\,\frac{1}{2\,(1+\varepsilon\,\mathsf{e}_\rho)}\,(\partial_3\mathsf{e}_\rho) \sim \tfrac{1}{2}\varepsilon\,(\partial_3\mathsf{e}_\rho) + \cdots \tag{3.125}$$

which reveals an inherent separation of phase space coordinates.

The symbol of the operator $\frac{1}{2}\hat{\Gamma}^{-1}(\partial_3\hat{\Gamma})$ (vertical wave slowness variation) on the right-hand side of equation (3.23) requires the composition of symbols

$$\tfrac{1}{2}\exp\left[-\mathrm{i}\,\partial_{\alpha'_\sigma}D_{x'_\sigma}\right]\,\hat{\gamma}^{-1}(x_\mu,x_3,\alpha'_\sigma)\;(\partial_3\hat{\gamma})(x'_\sigma,x_3,\alpha_\nu)\Big|_{(x'_\mu,\alpha'_\nu)=(x_\mu,\alpha_\nu)}\,,$$

in which we employ the expansions in accordance with equations (3.101) and (3.119). The principal part is thus found to be [cf., equations (3.99), (3.120)]

$$\frac{1}{2\hat{\gamma}_1}\,(\partial_3\hat{\gamma}_1) = \frac{\partial_3[\hat{\mathsf{a}}_2^0+\hat{\mathsf{a}}_2^1]}{4\hat{\mathsf{a}}_2^0\,[1+(\hat{\mathsf{a}}_2^1/\hat{\mathsf{a}}_2^0)]} \sim \frac{\partial_3[\hat{\mathsf{a}}_2^0+\hat{\mathsf{a}}_2^1]}{4(\gamma^0)^2}\left[1-(\hat{\mathsf{a}}_2^1/\hat{\mathsf{a}}_2^0)+\cdots\right]. \tag{3.126}$$

In Figure 3.6, upon applying a centered difference to the vertical derivative ∂_3, the (exact) principal part of the reflection left symbol (the left-hand side) is compared with the plane-wave reflection coefficient. In equation (3.126), the expansion in ε, again, reveals a separation of phase space coordinates in the constituent terms.

Carrying out a Taylor series expansion about $\alpha_\nu = 0$ to zero order yields

$$\frac{1}{4(\gamma^0)^2} \simeq \frac{(c^0)^2}{4}\,, \tag{3.127}$$

which leads to the phase-screen or split-step approximation to equation (3.126).

In analogy with equation (3.120), the $\mathcal{O}(\Omega)$ correction term is found to be

$$\frac{1}{2\,[\hat{\mathsf{a}}_2^0+\hat{\mathsf{a}}_2^1]^3}\,\Big[-\tfrac{1}{2}[\hat{\mathsf{a}}_2^0+\hat{\mathsf{a}}_2^1]\,(\partial_3[\hat{\mathsf{a}}_2^0+\hat{\mathsf{a}}_2^1])\,\hat{\mathsf{a}}_1^1 + \tfrac{1}{2}[\hat{\mathsf{a}}_2^0+\hat{\mathsf{a}}_2^1]^2(\partial_3\hat{\mathsf{a}}_1^1)$$
$$-\mathrm{i}\alpha_\sigma(\partial_3[\hat{\mathsf{a}}_2^0+\hat{\mathsf{a}}_2^1])\,(D_{x_\sigma}\hat{\mathsf{a}}_2^1) + \tfrac{3}{4}\mathrm{i}\alpha_\sigma[\hat{\mathsf{a}}_2^0+\hat{\mathsf{a}}_2^1]\,(D_{x_\sigma}\partial_3\hat{\mathsf{a}}_2^1)\Big]\,. \tag{3.128}$$

Hence, to $\mathcal{O}(\varepsilon)$ we get

$$\frac{1}{2\,(\gamma^0)^6}\left[-\tfrac{1}{2}(\gamma^0)^2\,(\partial_3\hat{\mathrm{a}}_2^0)\,\hat{\mathrm{a}}_1^1+\tfrac{1}{2}(\gamma^0)^4\,(\partial_3\hat{\mathrm{a}}_1^1)\right.$$
$$\left.-\mathrm{i}\alpha_\sigma(\partial_3\hat{\mathrm{a}}_2^0)\,(D_{x_\sigma}\hat{\mathrm{a}}_2^1)+\tfrac{3}{4}\mathrm{i}\alpha_\sigma(\gamma^0)^2\,(D_{x_\sigma}\partial_3\hat{\mathrm{a}}_2^1)\right] \tag{3.129}$$

which extends the wide-angle approximation (leading order in equation (3.126)). In Appendix F the relation between the transmission symbol and the wide-angle screen correction to the vertical slowness symbol is discussed.

3.8.1 The screen reflection kernel

The Schwartz kernel of the interaction operator has a representation as in equation (3.117) or (3.118). As in the subsection on the screen propagator, we will show the representation of the screen reflection kernel explicitly for the principal symbol, up to the second order in ε.

As in equation (3.112), we separate the contribution to the kernel from the symbol at 'vertical incidence', i.e. $\alpha_\nu''=0$. Thus, with [cf., equations (3.73) and (3.76)-(3.78)]

$$[\hat{\mathrm{a}}_2^0+\hat{\mathrm{a}}_2^1](x_\mu,x_3,0)=[c(x_\mu,x_3)]^{-2}\,,$$

we rewrite equation (3.126) in the form

$$\frac{1}{2\hat{\gamma}_1}(\partial_3\hat{\gamma}_1)(x_\mu,x_3,\alpha_\nu)\sim\frac{(\partial_3c^{-2})(x_\mu,x_3)}{4c^{-2}(x_\mu,x_3)}+\tfrac{1}{4}(\partial_3c^{-2})(x_\mu,x_3)$$
$$\left[\left(\frac{1}{\hat{\mathrm{a}}_2^0(x_3,\alpha_\nu)}-\frac{1}{\hat{\mathrm{a}}_2^0(x_3,0)}\right)-\hat{\mathrm{a}}_2^1(x_\mu,x_3)\left(\frac{1}{[\hat{\mathrm{a}}_2^0(x_3,\alpha_\nu)]^2}-\frac{1}{[\hat{\mathrm{a}}_2^0(x_3,0)]^2}\right)+\cdots\right] \tag{3.130}$$

In Figure 3.7, upon applying a centered difference to the vertical derivative ∂_3, the exact principal part of the reflection left symbol is compared with its first and second order generalized screen approximations, in accordance with the equation above.

The Schwartz kernel then follows as [cf., equation (3.117)]

$$\hat{\mathcal{R}}(x_\mu, x'_\nu; x_3) \simeq \frac{(\partial_3 c^{-2})(x_\mu, x_3)}{4c^{-2}(x_\mu, x_3)}\, \delta(x_\mu - x'_\mu) \tag{3.131}$$

$$+\tfrac{1}{4}(\partial_3 c^{-2})(x_\mu, x_3) \int (s/2\pi)^2 \mathrm{d}\alpha''_1 \mathrm{d}\alpha''_2 \exp[-\mathrm{i}s\, \alpha''_\sigma x_\sigma]$$

$$\left(\frac{1}{\hat{\mathrm{a}}_2^0(x_3, \alpha''_\nu)} - \frac{1}{\hat{\mathrm{a}}_2^0(x_3, 0)}\right) \exp[\mathrm{i}s\, \alpha''_\sigma x'_\sigma]$$

$$-\tfrac{1}{4}(\partial_3 c^{-2})(x_\mu, x_3)\, \hat{\mathrm{a}}_2^1(x_\mu, x_3) \int (s/2\pi)^2 \mathrm{d}\alpha''_1 \mathrm{d}\alpha''_2 \exp[-\mathrm{i}s\, \alpha''_\sigma x_\sigma]$$

$$\left(\frac{1}{[\hat{\mathrm{a}}_2^0(x_3, \alpha''_\nu)]^2} - \frac{1}{[\hat{\mathrm{a}}_2^0(x_3, 0)]^2}\right) \exp[\mathrm{i}s\, \alpha''_\sigma x'_\sigma]\,.$$

3.8.2 Comparison with the De Wolf approximation

According to equation (3.46) the leading order backscattered field is given by

$$\hat{W}_2^{(1)} = \hat{\mathrm{K}}_{2,1} \hat{W}_1^{(0)}\,, \tag{3.132}$$

which can be cast into a recursion for $\hat{I}_{2,1}^{(1)}$ using equation (3.61). This equation bears resemblance with the De Wolf approximation (Wu & Huang, 1995) though the interaction operator follows from scattering across level surfaces rather than from thin volumes. The algorithm is described by equation (3.63) ($J = 2$) for the slab $[k\Delta x_3, (k+1)\Delta x_3]$.

3.9 Concluding remarks

We have developed a class of screen-like algorithms for the multi-dimensional (generalized) Bremmer coupling series. The key ingredient was a separation of variables of the vertical slowness in horizontal phase space. This separation originated from an embedding procedure and an expansion of all relevant quantities in magnitude and smoothness of the medium contrast with respect to the embedding. Our scheme has added to the standard phase-screen method in the following ways: we considered larger medium variations in the lateral directions; we enhanced the accuracy for larger scattering angles; we introduced (de)composition operators to incorporate any desired source- or receiver-type with the appropriate radiation characteristics; we have taken care of the backscattered field with the aid of the Bremmer coupling series. The backscattered field includes phenomena like turning ray waves; the screen propagator accounts for focussing and defocussing effects also. The screen approximation, however, does not model critical-angle phenomena such as head waves, though it captures some of the evanescent wave contributions.

The methodology followed in this chapter provides a platform from which one can evaluate the generalized-screen expansion for wave propagation and scattering up to any desired level of accuracy. However, the validity of the methodology is restricted to the

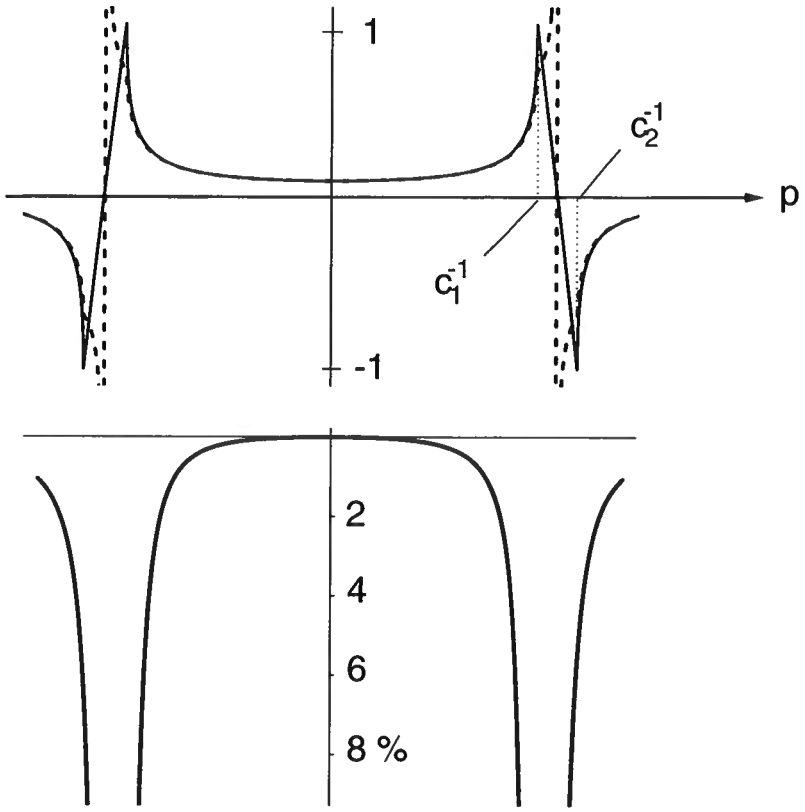

Figure 3.6. The centered difference (in x_3) representation of the principal part of the reflection symbol (dashed) and the corresponding plane-wave reflection coefficient (solid): real parts. The relative difference between the two is shown at the bottom.

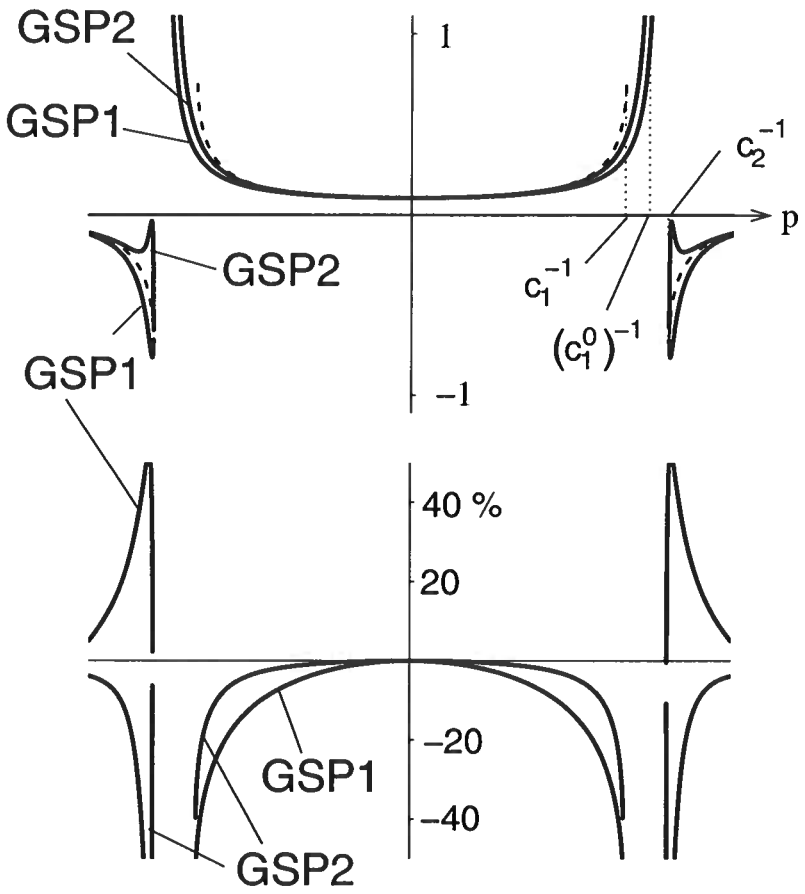

Figure 3.7. Principal parts of the generalized screen reflection left symbols: first order (GSP1) and second order (GSP2). The exact reflection symbol is dashed. The relative differences between the generalized screen and the exact reflection symbols are shown in the bottom part.

time-Laplace domain. Termwise, with the aid of complex analysis, the generalized-screen expansion can be reformulated and given appropriate meaning in the time-Fourier domain – taking special care of the branch cuts associated with the vertical wave slowness in the embedding.

Not only have we investigated the accuracy of the generalized-screen approximations on the wavefront using the locally frozen values for medium properties; we have analyzed the influence of the rate of change of the medium properties also. Our formulae can be used to quantify the leading-order contribution to the scattering process due to those rates.

The computational complexity of our algorithm is given by $(2+m)\,(N \log N + N)$ where m is the order of the generalized-screen approximation, and N is the number of nodes at which the wavefield is sampled in the horizontal directions, multiplied by the number of vertical steps and by the number of terms in the Bremmer series. In principle, this complexity is comparable to the one associated with the P(arabolic) E(quation) algorithms. However, *implicit*, stable PE algorithms require the solution of a (sparse) system of equations at each vertical propagation step. Whatever method used, in three dimensions, the computational complexity of the solution procedure will be greater than the one of the generalized-screen approach.

There are various fields of application of the method presented in this chapter. One concerns the numerical implementation of wave equation solvers in acoustics and electromagnetics. Some, benchmark numerical results have been published by Le Rousseau and De Hoop (Le Rousseau & De Hoop, 1998). Otherwise, in the study of propagation of waves in smoothly varying random media, the method has been proven to be useful. Finally, the lowest order approximations discussed in this chapter have already found application in seismic imaging (Huang & Wu, 1996; Wu & Jin, 1997; Huang *et al.*, 1999). A first step towards extending the procedure to elasticity can be found in (Wu & Xie, 1994).

Chapter 4

Modeling and imaging with the scalar generalized-screen algorithms in isotropic media[1]

4.1 Summary

The phase-screen and the split-step Fourier methods, which allow modeling and migration in laterally heterogeneous media, are generalized here so as to increase their accuracies for media with large and rapid lateral variations. The medium is defined in terms of a background medium and a perturbation. Such a contrast formulation induces a series expansion of the vertical slowness in which we recognize the first term as the split-step Fourier approximation and the addition of higher-order terms of the expansion increases the accuracy. Employing this expansion in the one-way scalar propagator yields the scalar one-way generalized-screen propagator. We also introduce a generalized-screen representation of the reflection operator. The interaction between the up- and downgoing fields is taken into account by a Bremmer series. These results are then cast into numerical algorithms. We analyze the accuracy of the generalized-screen method in complex structures using synthetic models that exhibit significant multi-pathing: the IFP 2D Marmousi model and the SEG-EAGE 3D salt model. As compared with the split-step Fourier method, in the presence of lateral medium variations, the generalized-screen methods exhibit an increased accuracy at wider angles of propagation and scattering. As a result, in the process of migration, we can choose a member of the family of our generalized-screen algorithms in accordance with the complexity of the medium (velocity model).

4.2 Introduction

The concept of screen approximations to the propagation of waves has been around for many years. The phase-screen approximation has been applied to light transmission through the atmosphere (Ratcliffe, 1956; Mercier, 1962; Filice, 1984; Martin & Flatté, 1988), propagation of light in optical fibers (Feit & Fleck, 1978), propagation of radio signals through the ionosphere (Buckley, 1975; Bramley, 1977; Knepp, 1983), propagation of acoustic waves in the ocean (Flatté *et al.*, 1979; Thomson & Chapman, 1983), and propagation of seismic waves in the earth (Stoffa *et al.*, 1990), renamed as the split-step Fourier method. More recently, the phase-screen method has been extended to elastic

[1]This chapter was published in *Geophysics*, **66**, (2001) pp.1551-1568, with M.V. de Hoop.

waves (Fisk & McCartor, 1991; Fisk *et al.*, 1992; Wu, 1994).

The original phase-screen method was designed for multiple downward scattering of waves, the downward direction being the preferred direction of propagation. It included phenomena such as focusing and defocusing associated with multi-pathing. The applicability of the phase-screen method generally requires that the screen interval satisfies the following criteria: small medium variations (weak scattering), transversely smooth medium variations (narrow-angle scattering), and even smoother variations in the preferred direction (negligible backscattering). With the generalized-screen (GS) approach, we access the accuracy of the phase-screen method, and generalize it to larger-contrast, wider-angle, and back-scattering.

In realistic geological models, heterogeneity in medium properties is such that the phenomenon of multiple scattering is significant. We distinguish two classes of multiple scattering: one in which the multiples are identified with respect to the projection of their propagation paths onto the *vertical* direction (depth), and one where the multiples are identified with respect to the projection of their propagation paths onto the *horizontal* plane. (The analysis underlying this distinction is shown in Chapter 3.) In the asymptotic framework of wavefront analysis, paths are rays. The *first* class of multiple scattering is associated with 'turning rays' and 'internal multiples' as well as 'surface multiples', the *second*, possibly combined with the first class of multiple scattering, is associated with 'multi-pathing'.

Seismic imaging and inversion are now commonly applied to regions where geologic complexities are present. An important part of the seismic energy is not contained in the 'first' arrival. An accurate prediction of multi-pathing and 'second' arrivals is the key to a better processing. A ray-theoretic treatment of the multi-pathing is not straightforward and is algorithmically rather involved (De Hoop & Brandsberg-Dahl, 2000). Wave extrapolation methods are able to predict multi-pathing (second class of multiple scattering), with no need to follow the formation of caustics explicitly. Also, with 3D surveys becoming standard practice, fast 3D algorithms are in demand. On the one hand, the full 3D extension of finite-difference methods is costly and restrict their application. One the other hand, methods such as the phase-screen (Ratcliffe, 1956) and the closely related split-step Fourier (Stoffa *et al.*, 1990) methods yield a faster 3D algorithm. They are, however, limited in their capacity to predict large-angle propagation where significant lateral heterogeneities are present. Because of their attractive properties (3D, multi-pathing), we propose, here, to generalize this latter family of algorithms, enhancing their accuracy. Since this algorithmic structure coincides with the one of the classical phase-screen propagator, we denote our approximations as generalized screens. Also, we propose to predict the first class of multiple scattering by the introduction of the Bremmer series (De Hoop, 1996).

Our approach accounts for the *first* class of multiple scattering through use of the generalized Bremmer series (De Hoop, 1996), and for the *second* class of multi-pathing by means of the GS propagator (De Hoop *et al.*, 2000).

A scattering theory that follows the ray picture but accounts for full-wave behavior has been developed by De Hoop (1996). It is based on an extension of the Bremmer coupling series to multi-dimensionally varying media. Bremmer's method decomposes the wavefield

into a recursion of one-way propagation operators each using the previous wavefield as a source. Thus, the method first generates a wavefield dominated by downward propagation, then generates a 'first' upward propagating wavefield, then a 'second' downward propagating field, etc. In this manner, multiple reflections (class one multiples) are accounted for in a controlled manner. The Bremmer series in acoustic media have already found application in Van Stralen *et al.*(1998) where the one-way wave operator is approximated with an accurate optimal finite-difference algorithm based on a rational expansion as opposed to a GS expansion.

The propagator that generates the Bremmer series can be represented by a Hamiltonian path integral (De Witte-Morette *et al.*, 1979; Fishman & McCoy, 1984a; Fishman & McCoy, 1984b; De Hoop, 1996) that accounts for not only the energy traveling along the ray but also for the transport along non-stationary paths. These path integrals contain all possible multi-pathing. In the path integral, 'time' is identified with depth, and 'momenta' are identified with the horizontal wave slownesses which, in the ray-theoretic limit, coincide with the horizontal components of the gradient of travel time. The (square-root) Hamiltonian, appearing in the phase of the path integral, is identified with vertical wave slowness, which, in the ray-theoretic limit, coincides with the vertical component of the gradient of travel time (De Hoop, 1996).

The problem with the path integrals is the computational complexity of their numerical evaluation. De Hoop *et al.* (2000) have developed a method that dramatically reduces the computational complexity of such evaluation, at the cost of approximating the acoustics (the shape of wavefronts). The result is an algorithm that, for each propagation step, is built from the sequence: forward Fourier transform, multiplication, inverse Fourier transform, multiplication -where the transform is in the horizontal directions and may be windowed. We have designed a hierarchy of increasingly accurate approximations. Underlying these approximations is an expansion of the medium wave-speed model simultaneously into magnitude and smoothness of variation.

We analyze the accuracy of the GS method in complex structures using synthetic models that exhibit significant multi-pathing: the IFP 2D Marmousi model and the SEG-EAGE 3D salt model. These two models represent two fundamentally different geological situations. In the Marmousi model, complexity arises from faulting and tectonic deformation in a sedimentary region. In the SEG-EAGE 3D salt model, it arises from the intrusion of a salt body the wave speed of which is significantly higher than in the surrounding formations. These models commonly yield poor imaging below these complex structures. With the help of the GS propagator, which we prove to be accurate in these situations, we shall illustrate that the origin of this problem is possibly associated with multi-pathing.

We first present the GS representation of the thin-slab propagator as well as the reflection operator. These results are then cast into numerical algorithms, and our accuracy analysis is carried out by modeling primarily. We analyze the migration operator before stacking that is conventionally performed in the process of imaging. We focus on multi-pathing and 'second'-arrival energy. We illustrate the modeling capacity of the GS method in 2D and 3D. For completeness, we show some prestack depth migration results in 2D.

Throughout this chapter, we assume that the medium is isotropic. In Le Rousseau

and De Hoop (2001c) (Chapter 5), we extend the method to media that are transversely isotropic with vertical symmetry axis.

4.3 The scalar generalized-screen propagator

4.3.1 The scalar one-way Green's function

Selecting the direction of preference along the x_3-axis (or 'vertical' axis) and denoting the remaining ('transverse' or 'horizontal') coordinates by x_μ, $\mu = 1, 2$, the one-way acoustic Green's function $\mathcal{G}^{(\pm)}$ is defined by the equation

$$[\partial_3 \mp \mathrm{i}\omega\Gamma(x_\mu, x_3; D_\nu)]\, \mathcal{G}^{(\pm)}(x_\mu, x_3; x'_\nu, x'_3) = \delta(x_\mu - x'_\mu)\, \delta(x_3 - x'_3) \tag{4.1}$$

in the frequency-space domain. The one-way Green's functions propagate waves in an arbitrary inhomogeneous medium, ignoring class one multiples, taking class two multiples into account. The left-hand side of equation (4.1), $\partial_3 \mp \mathrm{i}\omega\Gamma$, is the one-way wave operator. The choice of sign discriminates upgoing ($\mathcal{G}^{(-)}$) from downgoing ($\mathcal{G}^{(+)}$) Green's functions. For uniform density ρ, the operator Γ satisfies the characteristic equation,

$$\Gamma^2 = \mathrm{A}\ , \quad \mathrm{A} = c^{-2} - D_\nu D_\nu\ , \tag{4.2}$$

where c is the medium wave speed and

$$D_\nu \equiv \frac{1}{\mathrm{i}\omega}\, \partial_\nu\ , \tag{4.3}$$

has the interpretation of *horizontal slowness* operator; $\Gamma = \Gamma(x_\mu, x_3; D_\nu)$ is the *vertical slowness* operator. In equation (4.2) and throughout the chapter we use the summation convention for repeated indices.

For variable density media, De Hoop (1996) derived that

$$\Gamma^2 = -D_\nu D_\nu + \kappa\rho - \rho^{-1}(D_\nu\rho)\, D_\nu - \rho^{-1}(D_\nu D_\nu\rho) + \rho^{-2}(D_\nu\rho)(D_\nu\rho)\ , \tag{4.4}$$

equal to the transverse Helmholtz operator in the acoustic pressure-normalization analog (De Hoop, 1996; De Hoop *et al.*, 2000); ρ is the volume density of mass [kg/m^3], and κ is the compressibility [Pa^{-1}], with the wave speed defined as $c^{-2} = \kappa\rho$.

The thin-slab propagator In the present development, it is advantageous to use the Laplace transform with respect to time, t, and the Fourier transform with respect to the horizontal spatial coordinates, x_μ. We introduce the notation

$$s = -\mathrm{i}\omega\ , \tag{4.5}$$

$$\alpha_\nu = \frac{1}{\mathrm{i}\omega}\, k_\nu = -\frac{1}{s}\, k_\nu\ , \tag{4.6}$$

where ω and k_ν are the frequency and the horizontal wavenumber components (the inverse Laplace transform is anticipated to be evaluated along the Bromwich contour). In the Laplace (s) domain with $\mathrm{Re}(s) > 0$, the operator A becomes strictly elliptic, which enables us to consider any of its fractional powers with the aid of pseudodifferential calculus (Treves, 1980a). Here, we are interested in its square root, Γ. Using the Fourier transform with respect to the horizontal spatial coordinates we can associate with Γ and A their 'left symbols' (Treves, 1980a; Hörmander, 1985a), γ and a respectively, i.e., let ϕ be a test function, then

$$\begin{aligned}(\Gamma\phi)(x_\mu, x_3) &= \int (s/2\pi)^2 \mathrm{d}\alpha_1 \mathrm{d}\alpha_2 \int \mathrm{d}x_1' \mathrm{d}x_2' \ \exp[-\mathrm{i}s(x_\sigma - x_\sigma')\alpha_\sigma] \\ &\qquad \gamma(x_\mu, x_3; \alpha_\nu)\ \phi(x_\upsilon', x_3)\ , \\ (\mathrm{A}\phi)(x_\mu, x_3) &= \int (s/2\pi)^2 \mathrm{d}\alpha_1 \mathrm{d}\alpha_2 \int \mathrm{d}x_1' \mathrm{d}x_2' \ \exp[-\mathrm{i}s(x_\sigma - x_\sigma')\alpha_\sigma] \\ &\qquad \mathrm{a}(x_\mu, x_3; \alpha_\nu)\ \phi(x_\upsilon', x_3)\ ,\end{aligned}$$

where the symbol a is obtained, after equation (4.4), as

$$\mathrm{a} = \alpha_\nu\alpha_\nu + \kappa\rho - \rho^{-1}(D_\nu\rho)\,\mathrm{i}\alpha_\nu - \rho^{-1}(D_\nu D_\nu\rho) + \rho^{-2}(D_\nu\rho)(D_\nu\rho)\ ,$$

since $\mathrm{i}\alpha_\nu$ is the left symbol[2] of D_ν. For uniform density, a reduces to $\alpha_\nu\alpha_\nu + \kappa\rho$, consistent with equation (4.2). Equation (4.2) transforms into a characteristic equation for left symbols:

$$\exp\left[-\mathrm{i}\,\partial_{\alpha_\sigma'} D_{x_\sigma'}\right]\ \gamma(x_\mu; \alpha_\sigma')\gamma(x_\sigma'; \alpha_\nu)\Big|_{(x_\mu', \alpha_\nu') = (x_\mu, \alpha_\nu)} = \mathrm{a}(x_\mu; \alpha_\nu)\ , \tag{4.7}$$

as given by symbol calculus of pseudodifferential operators (Treves, 1980a; Hörmander, 1985a; De Hoop, 1996, equation (A12)).

With the vertical slowness left symbol, the one-way Green's function, $\mathcal{G}^{(\pm)}$, from equation (4.1) can be represented by a Hamiltonian path-integral representation (Cohen-Tannoudji *et al.*, 1977; Schulman, 1981; Fishman & McCoy, 1984b; De Hoop *et al.*, 2000). We define the scalar one-way propagator, $g^{(\pm)}$, through

$$\mathcal{G}^{(\pm)} = \pm H(\pm[x_3 - x_3'])\ g^{(\pm)}\ ,$$

where the Heaviside function H generates the Dirac distribution in equation (4.1) (cf., Appendix G). For a sufficiently small vertical step $\Delta x_3 = x_3 - x_3'$ (thin slab), and a medium sufficiently smooth, the Hamiltonian path-integral representation for the one-way

[2] $(D_\nu\phi)(x_\mu, x_3) = \int (s/2\pi)^2 \mathrm{d}\alpha_1 \mathrm{d}\alpha_2 \int \mathrm{d}x_1' \mathrm{d}x_2'\ \mathrm{i}\alpha_\nu \exp[-\mathrm{i}s(x_\sigma - x_\sigma')\alpha_\sigma]\ \phi(x_\upsilon', x_3)$.

thin-slab propagator reduces to (see Chapter 2) (De Hoop *et al.*, 2000):

$$g^{(\pm)}(x_\mu, x_3; x'_\upsilon, x'_3) \simeq$$
$$\int (1/2\pi)^2 \mathrm{d}k_1 \mathrm{d}k_2 \exp[\mathrm{i}\, k_\sigma (x_\sigma - x'_\sigma)] \exp[\pm \mathrm{i}\omega\, \gamma(x_\mu, \bar{x}_3; \mathrm{i}k_\nu/\omega) \Delta x_3]$$
$$= \int (s/2\pi)^2 \mathrm{d}\alpha_1 \mathrm{d}\alpha_2 \exp[-\mathrm{i}s\, \alpha_\sigma (x_\sigma - x'_\sigma)] \exp[\mp s\, \gamma(x_\mu, \bar{x}_3; \alpha_\nu) \Delta x_3] \,, \qquad (4.8)$$

with

$$\bar{x}_3 = x_3 - \tfrac{1}{2}\Delta x_3 = x'_3 + \tfrac{1}{2}\Delta x_3 \,.$$

In the limit of a laterally homogeneous thin slab, γ will not depend on x_μ, and the thin-slab propagator reduces to Gazdag's phase-shift operator (Gazdag, 1978). The operator is composed of a forward Fourier transform, a multiplication by a phase factor (the phase is proportional to the vertical slowness) and an inverse Fourier transform. In the general case of equation (4.8), the thin-slab propagator has a similar structure except that the phase factor is dependent upon the output point, x_μ. Every output point requires its own evaluation of equation (4.8), which represents a considerable computational effort. The GS approximation of the thin-slab propagator enforces a simplification of this computational complexity, while allowing laterally varying media.

High-frequency approximation Throughout this chapter, we will use a 'high-frequency' approximation. Then the pseudodifferential operator Γ reduces to its principal part Γ_1, and the associated left symbol, γ, reduces to its principal symbol, γ_1. The principal symbol, γ_1, follows from taking the high-frequency limit of equation (4.7) (cf., Appendix H):

$$\gamma_1(x_\mu, x_3; \alpha_\nu) = \sqrt{[c(x_\mu, x_3)]^{-2} + \alpha_\nu \alpha_\nu} \,. \qquad (4.9)$$

The triplet $(\mathrm{i}\alpha_1, \mathrm{i}\alpha_2, \gamma_1)$ represents the components of the gradient of the travel time. Then, the scalar one-way thin-slab propagator becomes

$$g^{(\pm)}(x_\mu, x_3; x'_\upsilon, x'_3) \simeq \qquad (4.10)$$
$$\int (s/2\pi)^2 \mathrm{d}\alpha_1 \mathrm{d}\alpha_2 \exp[-\mathrm{i}s\, \alpha_\sigma (x_\sigma - x'_\sigma)] \exp[\mp s\, \gamma_1(x_\mu, \bar{x}_3; \alpha_\nu) \Delta x_3] \,.$$

Note that the wavefront set (Hörmander, 1990) of propagator (4.10) is equal to the one of propagator (4.8). Singularities of the wavefield propagate along the characteristics which are solely determined by the principal parts of the pseudodifferential equation (4.1) (Hörmander, 1985a, Theorem 18.1.28). Using the principal part only, we do not alter the geometrical aspects of the wave propagation, i.e., the wavefront set. Any departure from the principal parts results in smoother contributions (e.g. on a Soboloev scale) to the wavefield.

4.3.2 Generalized-screen principal-slowness surface

The contrast formulation For the subsequent analysis, we employ a 'contrast formulation' that allows us to take lateral heterogeneity into account in the thin-slab propagation. In the slab $[x_3', x_3]$ we introduce a background medium with wave speed c^0. The background medium is constant in the slab, but may vary from one slab to another. We express this by letting $c^0 = c^0(x_3)$. A medium perturbation term u is then introduced as

$$u(x_\mu, x_3) = [c(x_\mu, x_3)]^{-2} - [c^0(x_3)]^{-2} . \tag{4.11}$$

To avoid having an artificial branch point enter the propagating-wave domain (see below), we impose the condition

$$c^0(x_3) \leq c(x_\mu, \zeta) \quad \text{for} \quad \zeta \in [x_3', x_3] . \tag{4.12}$$

We will expand the principal symbol of the vertical slowness left symbol, γ_1, into the perturbation u about the background medium.

Generalized-screen expansion Assuming small vertical medium variation across the thin slab, i.e., if the thin slab is sufficiently small, we set

$$\begin{aligned} \gamma^0(\zeta; \alpha_\nu) &= \sqrt{[c^0(x_3)]^{-2} + \alpha_\nu \alpha_\nu} \\ &= \gamma^0(x_3; \alpha_\nu) \quad \text{for} \quad \zeta \in [x_3', x_3] , \end{aligned} \tag{4.13}$$

the vertical slowness associated with the background medium. The principal symbol of the vertical slowness, γ_1, can then be decomposed into a background component, γ^0, and a perturbation , γ_1^1, i.e.,

$$\gamma_1(x_\mu, x_3; \alpha_\nu) = \gamma^0(x_3; \alpha_\nu) + \gamma_1^1(x_\mu, x_3; \alpha_\nu). \tag{4.14}$$

To find an explicit form for γ_1^1 we use relationship (4.9), which can be rewritten as

$$\begin{aligned} \gamma_1(x_\mu, x_3; \alpha_\nu) &= \sqrt{[c^0(x_3)]^{-2} + u(x_\mu, x_3) + \alpha_\nu \alpha_\nu} \\ &= \gamma^0(x_3; \alpha_\nu) \sqrt{1 + \frac{u(x_\mu, x_3)}{[\gamma^0(x_3; \alpha_\nu)]^2}} , \end{aligned} \tag{4.15}$$

and expand the result in a Taylor series according to

$$\begin{aligned} \gamma_1(x_\mu, x_3; \alpha_\nu) &= \gamma^0(x_3; \alpha_\nu) + \gamma_1^1(x_\mu, x_3; \alpha_\nu) \\ &= \gamma^0(x_3; \alpha_\nu) + \sum_{j=1}^{n} a_j \frac{[u(x_\mu, x_3)]^j}{[\gamma^0(x_3; \alpha_\nu)]^{2j-1}} + \mathrm{o}(u(x_\mu, x_3))^n , \end{aligned} \tag{4.16}$$

where

$$a_j = (-1)^{j+1}\,\frac{1\cdot 3\cdots(2j-3)}{j!\;2^j}\,. \tag{4.17}$$

In practice, we shall limit ourselves to the fourth-order expansion,

$$\gamma_1(x_\mu,x_3;\alpha_\nu)=\gamma^0(x_3;\alpha_\nu)+\frac{1}{2}\frac{u(x_\mu,x_3)}{\gamma^0(x_3;\alpha_\nu)}-\frac{1}{8}\frac{[u(x_\mu,x_3)]^2}{[\gamma^0(x_3;\alpha_\nu)]^3}+\frac{1}{16}\frac{[u(x_\mu,x_3)]^3}{[\gamma^0(x_3;\alpha_\nu)]^5}$$
$$-\frac{5}{128}\frac{[u(x_\mu,x_3)]^4}{[\gamma^0(x_3;\alpha_\nu)]^7}+\mathrm{o}(u(x_\mu,x_3))^4. \tag{4.18}$$

It is important to note that in each term of the expansion, the dependencies on x_μ and on α_ν are factorized. This property will induce the structure of the GS propagator. Justification of expansion (4.16) is given in De Hoop *et al.* (2000), where the full symbol γ is analyzed; here we have restricted ourselves to its principal symbol, γ_1. Where normal mode expansions of the one-way propagator apply, the factorization, in fact, occurs naturally (Fishman *et al.*, 2000).

Phase-screen and split-step Fourier approximations The phase-screen approximation follows from expansion (4.16) by setting $n = 1$ and approximating $1/\gamma^0$ by its zero-order Taylor expansion in α_ν about 0 (vertical propagation),

$$\gamma_1(x_\mu,x_3;\alpha_\nu)\simeq\gamma^0(x_3;\alpha_\nu)+\tfrac{1}{2}\,c^0\,u(x_\mu,x_3)\,. \tag{4.19}$$

This leads to the approximation of the vertical slowness symbol employed by Stoffa *et al.* (1990), since

$$u=c^{-2}-(c^0)^{-2}\simeq 2(c^0)^{-1}(c^{-1}-(c^0)^{-1})\,,$$

which yields with equation (4.19),

$$\gamma_1(x_\mu,x_3;\alpha_\nu)\simeq\gamma^0(x_3;\alpha_\nu)+[c(x_\mu,x_3)]^{-1}-[c^0(x_3)]^{-1}\,, \tag{4.20}$$

as found in the split-step Fourier method.

Figure 4.1 illustrates the principal slowness surfaces (γ_1 as a function of the horizontal slowness $p=\sqrt{-\alpha_\nu\alpha_\nu}$) of the GS expansions for $n = 1, 2$ and 3 as given in equation (4.16), and the split-step Fourier one. The split-step approximation approaches the actual slowness surface by simply vertically *shifting* the background slowness surface. Adding higher-order terms in the GS expansion, the *shape* of the slowness surface is improved and, hence, the accuracy for wider-angle propagation is increased. This observation indicates that for the extension to anisotropic media, the split-step approximation does not have the degree of freedom to shape the slowness surface appropriately (Le Rousseau & De Hoop, 2001c; Thomsen, 1998); the influence of the anisotropic parameters occurs only at non vertical propagation.

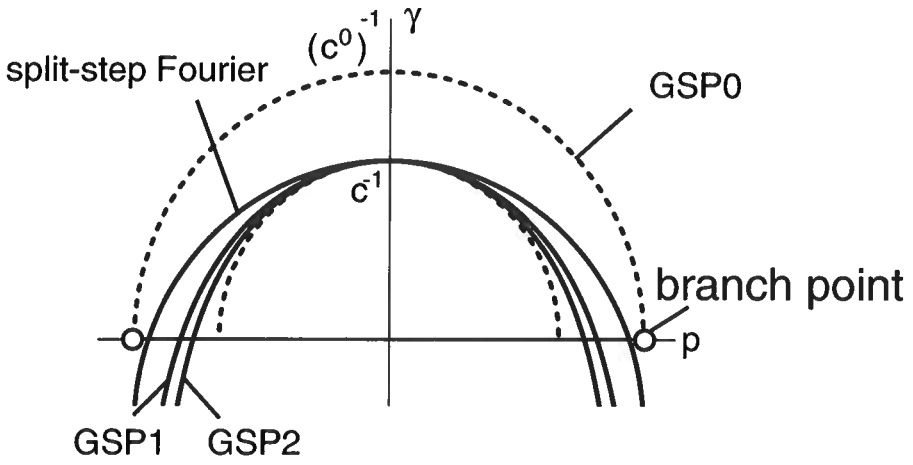

Figure 4.1. Principal parts of the generalized-screen vertical slowness; zero-order (GSP0), first-order (GSP1) and second-order (GSP2) as a function of the horizontal slowness p. Also shown is the principal part of the vertical slowness for the split-step Fourier method. The principal part of the exact vertical slowness is shown with the inner dashed curve.

The GS expansion as shown in equation (4.16) reveals the introduction of reciprocal powers of γ^0 and hence contains branch points at $\alpha_\nu\alpha_\nu = -[c^0]^{-2}$, as illustrated in Figure 4.1. The vicinity of the branch point should be treated carefully. To ensure that the branch point is out of the propagation regime within the thin-slab, we have chosen c^0 smaller than the minimum medium wave speed within the slab, as illustrated in Figure 4.1. Unlike the GS expansion, the split-step Fourier method does not suffer from the presence of a branch point. The choice of a background wave speed c^0 greater than the minimum wave speed in each thin-slab is therefore possible for this approximation. One may then choose, for example, the mean or the median of the medium velocities in the slab as a reference. Different choices yield different operators; It is not obvious how to find the 'optimum' background medium.

In the phase-screen approximation [cf., equation (4.19)], the Taylor expansion of $1/\gamma^0$ in $\alpha_\nu\alpha_\nu$ was truncated after the first term. The accuracy of this approximation is increased by simply adding more terms, e.g.,

$$\gamma_1(x_\mu, x_3; \alpha_\nu) \simeq \gamma^0(x_3; \alpha_\nu) + \tfrac{1}{2}\, u(x_\mu, x_3)\, [c^0(x_3) - \tfrac{1}{2}\alpha_\nu\alpha_\nu (c^0(x_3))^3]\,, \qquad (4.21)$$

yielding an angular correction in the vertical slowness. The accuracy, however, is bounded by the accuracy of the first-order GS expansion (Chapter 4, Figure 3.3) (De Hoop *et al.*, 2000, Figure 3).

4.3.3 The scalar generalized-screen propagator

With the analysis given in equation (4.16), we write equation (4.10) in the form

$$g^{(\pm)}(x_\mu, x_3; x'_\upsilon, x'_3) \simeq \int (s/2\pi)^2 \mathrm{d}\alpha_1 \mathrm{d}\alpha_2 \exp[-\mathrm{i}s\,\alpha_\sigma(x_\sigma - x'_\sigma)] \cdot \exp[\mp s\,\{\gamma^0(\bar{x}_3; \alpha_\nu) + \gamma_1^1(x_\mu, \bar{x}_3; \alpha_\nu)\}\,\Delta x_3]\,, \tag{4.22}$$

where

$$\bar{x}_3 = x_3 - \tfrac{1}{2}\Delta x_3 = x'_3 + \tfrac{1}{2}\Delta x_3\,. \tag{4.23}$$

Expanding the exponential, we seek an approximation of the propagator that matches the structure of the GS expansion. We therefore expand the perturbation term about vertical propagation and write

$$\gamma_1^1(x_\mu, \bar{x}_3; \alpha_\nu) = \gamma_1^1(x_\mu, \bar{x}_3; 0) + [\gamma_1^1(x_\mu, \bar{x}_3; \alpha_\nu) - \gamma_1^1(x_\mu, \bar{x}_3; 0)]\,,$$

and

$$\exp[\mp s(\gamma_1^1(x_\mu, \bar{x}_3; \alpha_\nu) - \gamma_1^1(x_\mu, \bar{x}_3; 0))\,\Delta x_3] \simeq 1 \mp s\,[\gamma_1^1(x_\mu, \bar{x}_3; \alpha_\nu) - \gamma_1^1(x_\mu, \bar{x}_3; 0)]\;\Delta x_3\,. \tag{4.24}$$

Expanding the exponential separates dependencies of the propagator on x_μ and on α_ν, which allows spatial dependencies to be taken out of the Fourier integral (4.22). We have accomplished that the inverse Fourier transforms with respect to α_ν *no longer* have to be evaluated for each x_μ *separately*, which is the key simplification of the GS propagator compared with the 'exact' thin-slab propagator. We obtain

$$g^{(\pm)}(x_\mu, x_3; x'_\upsilon, x'_3) \simeq g^{0(\pm)}(x_\mu, x_3; x'_\upsilon, x'_3) + g^{1(\pm)}(x_\mu, x_3; x'_\upsilon, x'_3)\,, \tag{4.25}$$

with

$$g^{0(\pm)}(x_\mu, x_3; x'_\upsilon, x'_3) = \exp[\mp s\,\gamma_1^1(x_\mu, \bar{x}_3; 0)\,\Delta x_3] \cdot \int (s/2\pi)^2 \mathrm{d}\alpha_1 \mathrm{d}\alpha_2 \exp[-\mathrm{i}s\,\alpha_\sigma(x_\sigma - x'_\sigma)]\;\exp[\mp s\,\gamma^0(\bar{x}_3; \alpha_\nu)\,\Delta x_3]\,, \tag{4.26}$$

and

$$g^{1(\pm)}(x_\mu, x_3; x'_\upsilon, x'_3) = \exp[\mp s\,\gamma_1^1(x_\mu, \bar{x}_3; 0)\,\Delta x_3] \cdot \int (s/2\pi)^2 \mathrm{d}\alpha_1 \mathrm{d}\alpha_2\;\exp[-\mathrm{i}s\,\alpha_\sigma(x_\sigma - x'_\sigma)]\;\exp[\mp s\,\gamma^0(\bar{x}_3; \alpha_\nu)\,\Delta x_3] \cdot \Delta x_3\;\left[\mp s(\gamma_1^1(x_\mu, \bar{x}_3; \alpha_\nu) - \gamma_1^1(x_\mu, \bar{x}_3; 0))\right]\,. \tag{4.27}$$

Since

$$\gamma_1^1(x_\mu, \bar{x}_3; 0) \sim \sum_{j=1}^{\infty} a_j \frac{[u(x_\mu, \bar{x}_3)]^j}{[\gamma^0(\bar{x}_3; 0)]^{2j-1}} = [c(x_\mu, \bar{x}_3)]^{-1} - [c^0(x_\mu, \bar{x}_3)]^{-1} ,$$

which is a spatial phase correction term that may be found in the split-step Fourier method (Stoffa *et al.*, 1990), we obtain

$$g^{0(\pm)}(x_\mu, x_3; x'_\upsilon, x'_3) = \exp\left[\mp s \left([c(x_\mu, \bar{x}_3)]^{-1} - [c^0(\bar{x}_3)]^{-1}\right) \Delta x_3\right] \tag{4.28}$$
$$\cdot \int (s/2\pi)^2 \mathrm{d}\alpha_1 \mathrm{d}\alpha_2 \exp[-\mathrm{i}s\,\alpha_\sigma(x_\sigma - x'_\sigma)] \exp[\mp s\,\gamma^0(\bar{x}_3; \alpha_\nu)\,\Delta x_3] .$$

The leading-order constituent term of the GS propagator, $g^{0(\pm)}$, is the propagator of the split-step Fourier method, i.e., a propagator associated with the background medium for the thin-slab and a phase correction term in space that is accurate for the vertical propagation only. The higher-order term in the GS propagator then follows as

$$g^{1(\pm)}(x_\mu, x_3; x'_\upsilon, x'_3) = \exp\left[\mp s \left([c(x_\mu, \bar{x}_3)]^{-1} - [c^0(\bar{x}_3)]^{-1}\right) \Delta x_3\right] \tag{4.29}$$
$$\cdot \int (s/2\pi)^2 \mathrm{d}\alpha_1 \mathrm{d}\alpha_2 \exp[-\mathrm{i}s\,\alpha_\sigma(x_\sigma - x'_\sigma)] \exp[\mp s\,\gamma^0(\bar{x}_3; \alpha_\nu)\,\Delta x_3]$$
$$\cdot \Delta x_3 \left[\mp s(\gamma_1^1(x_\mu, \bar{x}_3; \alpha_\nu) - \gamma_1^1(x_\mu, \bar{x}_3; 0))\right] ,$$

which, upon replacing γ_1^1 by its truncated expression as in equation (4.16), gives

$$g^{1(\pm)}(x_\mu, x_3; x'_\upsilon, x'_3) = \exp\left[\mp s \left([c(x_\mu, \bar{x}_3)]^{-1} - [c^0(\bar{x}_3)]^{-1}\right) \Delta x_3\right] \tag{4.30}$$
$$\cdot \mp s\Delta x_3 \sum_{j=1}^{n} \left\{ a_j \left[u(x_\mu, \bar{x}_3)\right]^j \int (s/2\pi)^2 \mathrm{d}\alpha_1 \mathrm{d}\alpha_2 \exp[-\mathrm{i}s\,\alpha_\sigma(x_\sigma - x'_\sigma)] \right.$$
$$\left. \cdot \exp[\mp s\,\gamma^0(\bar{x}_3; \alpha_\nu)\,\Delta x_3] \left[\frac{1}{[\gamma^0(\bar{x}_3; \alpha_\nu)]^{2j-1}} - \frac{1}{[\gamma^0(\bar{x}_3; 0)]^{2j-1}}\right] \right\} .$$

The second constituent term of the GS propagator, $g^{1(\pm)}$, arises from the higher-order terms of the GS expansion. We call n the order of the GS approximation. As mentioned, the higher the order, the higher the accuracy for wide-angle propagation.

The split-step Fourier propagator simply yields a shuttling between the frequency-horizontal space and frequency-horizontal slowness domains and a multiplication in each domain. Each additional term of the GS expansion (4.16) requires an additional inverse Fourier transform in space as expressed in equation (4.30). As the *computational complexity* of the downward continuation in the split-step Fourier method is proportional to $2N_1N_2 \log_2 N_1N_2$ (N_μ denoting the numbers of samples in the x_μ-direction), the complexity of our n^{th}-order GS approach is proportional to $(2+n)N_1N_2 \log_2 N_1N_2$.

4.3.4 Normalization of the scalar generalized-screen propagator

The Taylor expansion of the exponential in equation (4.24) destroys the unitarity of propagator (4.8) and hence the amplitude characteristics of the propagator; depending on the wavenumber, or the local angle of propagation, part of the energy may be amplified or attenuated incorrectly. It can also lead to a numerical algorithm that is unstable over a large range of downward continuation. To restore, approximately, the amplitude behavior, we apply a normalizing operator and obtain the GS propagator g_{GSP}

$$g^{(\pm)}_{GSP}(x_\mu, x_3; x'_\upsilon, x'_3) = g^{0(\pm)}(x_\mu, x_3; x'_\upsilon, x'_3)\, \mathcal{N}\left[1 + \frac{g^{1(\pm)}(x_\mu, x_3; x'_\upsilon, x'_3)}{g^{0(\pm)}(x_\mu, x_3; x'_\upsilon, x'_3)}\right] ,$$

the division being carried out in some stable sense, and the normalizing operator $\mathcal{N}$ being given by (De Hoop *et al.*, 2000)

$$\mathcal{N}[1 + p + \mathrm{i}q] = \exp(\mathrm{i}q)\, \left|1 + \frac{p}{1 + \mathrm{i}q}\right|^{-1} \left[1 + \frac{p}{1 + \mathrm{i}q}\right] .$$

In effect, this normalization corrects for the error introduced by the expansion of the exponential in equation (4.24), and restores the amplitude behavior exactly in the case of a constant perturbation u, i.e., a medium with wave speed higher than the reference wave speed.

4.4 The scalar generalized-screen algorithm

Here, we discuss the GS algorithm based upon equations (4.22) through (4.30). We denote the (one-way) wavefield by W, and carry out the wave propagation in the frequency domain, with each frequency component computed independently. The downward continuation for modeling and imaging with the one-way propagator is performed according to the decomposition of the vertical slowness symbol into one background term and a series of perturbation terms as in equation (4.16).

Let the current depth be set to $x'_3 = z$, and set $\bar{x}_3 = x'_3 + \frac{1}{2}\Delta x_3$ as before. Following equation (4.30), we introduce the intermediate field quantities $w_0, \cdots, w_n$ according to (*step 1*)

$$\begin{aligned}
w_0(x_\mu, s) &= \exp\left[-s\,\Delta x_3\,\left([c(x_\mu, \bar{x}_3)]^{-1} - [c^0(\bar{x}_3)]^{-1}\right)\right]\, W(x_\mu, x'_3, s) ,\\
w_1(x_\mu, s) &= -s\,\Delta x_3\, a_1\, u(x_\mu, \bar{x}_3)\, w_0(x_\mu, s) ,\\
w_2(x_\mu, s) &= -s\,\Delta x_3\, a_2\, u^2(x_\mu, \bar{x}_3)\, w_0(x_\mu, s) ,\\
&\vdots\\
w_n(x_\mu, s) &= -s\,\Delta x_3\, a_n\, u^n(x_\mu, \bar{x}_3)\, w_0(x_\mu, s) .
\end{aligned}$$

The quantity w_0 represents the split-step Fourier term; the higher-order terms increase the

accuracy for wider-angle propagation. The intermediate field quantities are then Fourier transformed to the horizontal-wavenumber domain (*step 2*),

$$\begin{aligned}\tilde{w}_j(\alpha_\nu, s) &= \int w_j(x_\mu, s)\ \exp\left[-\mathrm{i}x_\sigma k_\sigma\right] dx_\mu \\ &= \int w_j(x_\mu, s)\ \exp\left[\mathrm{i}s x_\sigma \alpha_\sigma\right] dx_\mu\ , \qquad j = 0, \cdots, n\ .\end{aligned} \tag{4.31}$$

The wavefield at depth $x_3 = z + \Delta x_3$ then follows as

$$\begin{aligned}\tilde{W}(x_3; \alpha_\nu, s) = \tilde{w}_0(\alpha_\nu, s)\ &\exp[-s\Delta x_3 \gamma^0(\bar{x}_3; \alpha_\nu)] \\ \cdot\mathcal{N}\Bigg[1 + \frac{\tilde{w}_1(\alpha_\nu, s)}{\tilde{w}_0(\alpha_\nu, s)}\ &\left(\frac{1}{\gamma^0(\bar{x}_3; \alpha_\nu)} - c^0(\bar{x}_3)\right) \\ + \cdots + \frac{\tilde{w}_n(\alpha_\nu, s)}{\tilde{w}_0(\alpha_\nu, s)}\ &\left(\frac{1}{[\gamma^0(\bar{x}_3; \alpha_\nu]^{2n-1}} - [c^0(\bar{x}_3)]^{2n-1}\right)\Bigg]\ .\end{aligned}$$

(*step 3*). Finally, we carry out the inverse Fourier transform $\tilde{W}(x_3; \alpha_\nu, s) \rightarrow W(x_\mu, x_3; s)$, (*step 4*).

The sequence of steps illustrates the shuttling between the frequency-horizontal space domain and frequency-horizontal wavenumber domain that is performed with the GS approach. The method departs from the exact solution through the (approximate) expansion of the vertical slowness operator. The case of a constant medium perturbation provides insight in how wavefronts evolve based on Huygens' principle (Huygens, 1690; Hörmander, 1990). Let the background medium be characterized by a wave speed c^0 that is 2/3 of the true wave speed. The top of Figure 4.2 shows (instantaneous) wavefronts constructed as the polar reciprocal of the local slowness surface shown in Figure 4.1. In the bottom part of Figure 4.2 we show numerical impulse responses of the one-way propagator for different orders of generalized screens, as well as for the split-step Fourier method. For a constant perturbation, the predicted wavefronts and the actual computed wavefronts can be overlain exactly. The exact response is plotted dashed in the top part of the figure. Note that the accuracy varies with propagation angle (or migration dip upon imaging), and that this accuracy varies with (local) medium perturbation. In all the approximations, independent of order n, the propagation speed in the horizontal directions approaches c^0, which causes any approximate wavefront to fold inwards away from the true wavefront. Indeed, the normal to any slowness surface in Figure 4.1 is horizontal or converges to horizontal when the horizontal slowness is $1/c^0$. As such, the GS approximation differs, for example, from the paraxial approximation where the accuracy with dip is independent of the medium (De Hoop & De Hoop, 1992). The GS inaccuracy at horizontal propagation is inherited from the GS expansion of the vertical slowness symbol. Note, however, that for non-horizontal propagation, including very large angle propagation, any accuracy can be obtained depending on the order of the GS approximation chosen. We should also note that the large error seen here for horizontal propagation is due to the choice of c^0: c^0 is only 2/3 of the actual wave speed c.

Figure 4.3 compares 3D computations for the first four orders of the GS propagators

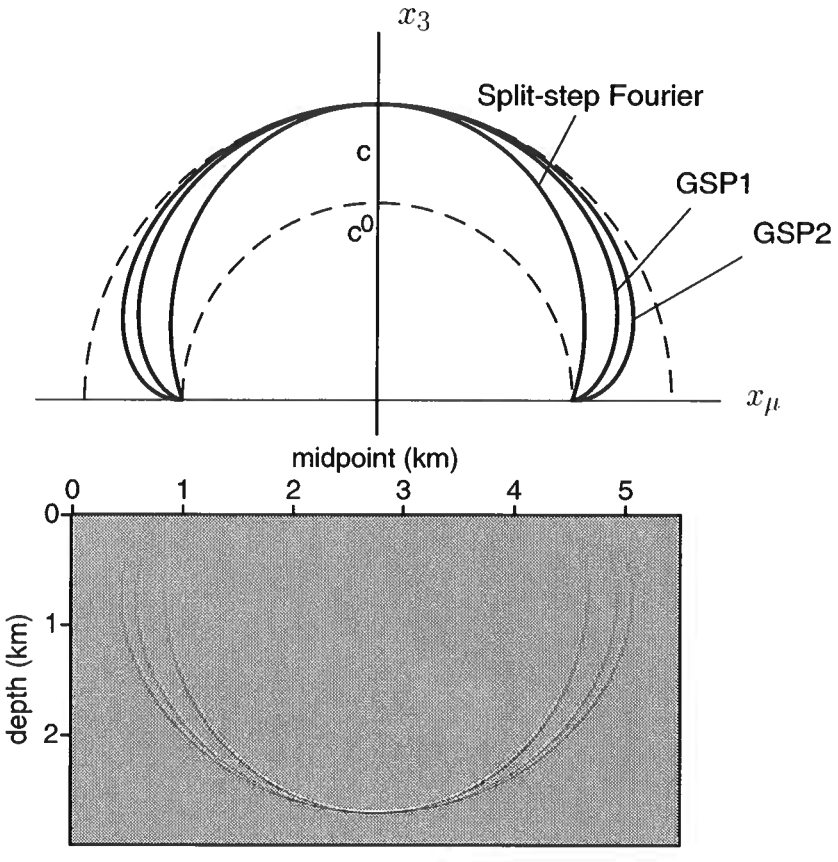

Figure 4.2. Wavefronts in a constant-perturbation medium associated with the various generalized-screen approximations: second-order (GSP2), first-order (GSP1) and split-step Fourier; top: as calculated as polar reciprocal of the slowness surface; the exact and background wavefronts are shown dashed; bottom: numerical wavefront.

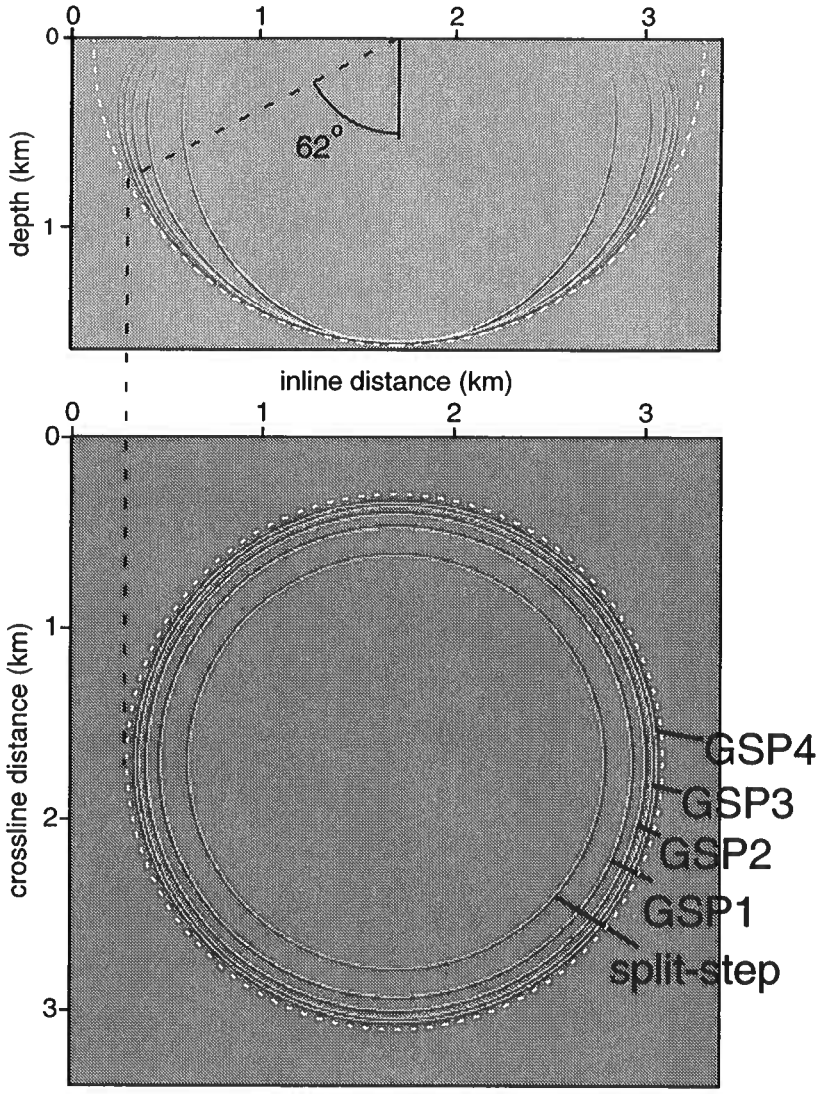

Figure 4.3. 3D wavefield snapshots in a constant-perturbation medium associated with the various generalized screen approximations: fourth-order (GSP4), third-order (GSP3), second-order (GSP2), first-order (GSP1), and split-step Fourier. The exact wavefield is shown dashed.

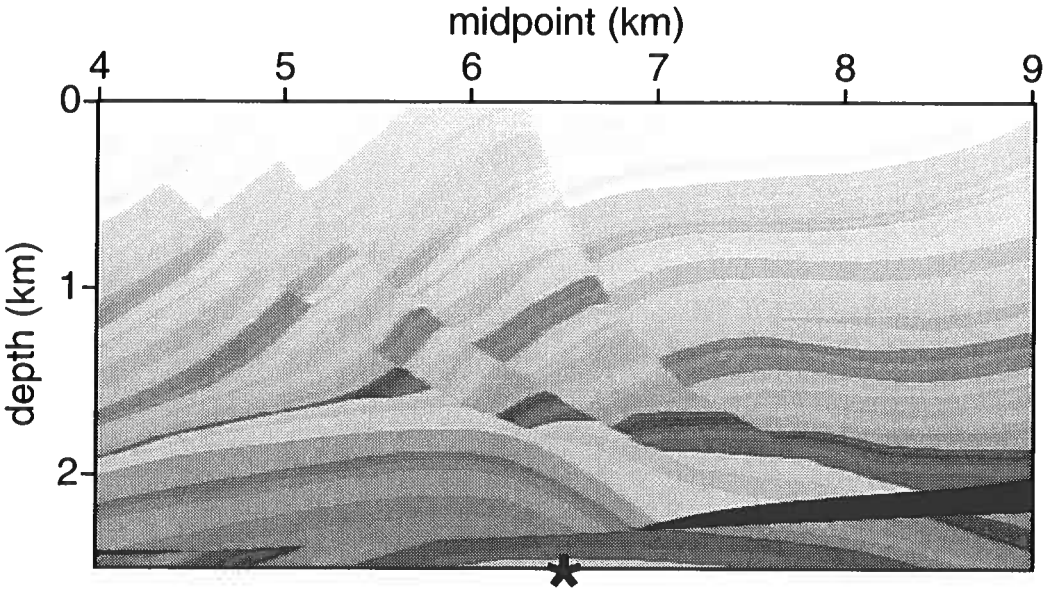

Figure 4.4. Part of the Marmousi wave speed model used to generate the snapshots of Figure 4.5(a), Figure 4.5(b) and Figure 4.7 to Figure 4.12. The star locates the position of the source. The maximum wave speed is 5500 m/s (black). The minimum wave speed is 1500 m/s (white).

and for the split-step Fourier method. Again, the dashed curves show the true wavefront location. From Figure 4.3 we conjecture that, as a rule of thumb, the split-step Fourier method is accurate up to 17°, the first-order GS is accurate up to 34°, the second-order GS up to 48°, the third-order GS up to 55°, and the fourth-order GS up to 62°, when such a perturbation occurs (the background wave speed being only 2/3 of the actual wave speed). The rate of convergence with order is also suggestive in Figure 4.3. As in any Taylor expansion, the first terms in the GS expansion bring the main contribution to the operator, and the higher-order terms have lesser contributions, slowly increasing the accuracy.

4.5 Branch points

The terms in GS expansion contain powers of $1/\gamma^0$ increasing with order [cf., equation (4.16)]. These powers induce branch points at $\alpha_\nu \alpha_\nu = -[c^0]^{-2}$, corresponding to grazing propagation in the background medium (cf., Figure 4.1). The branch points also appear in expansion (4.30) for the GS propagator.

For a constant-perturbation medium, the normalization operator exactly compensates the errors arising from the expansion of the exponential in equation (4.24). Yet, in laterally heterogeneous media such as the Marmousi model (cf., Figure 4.4), these approximations

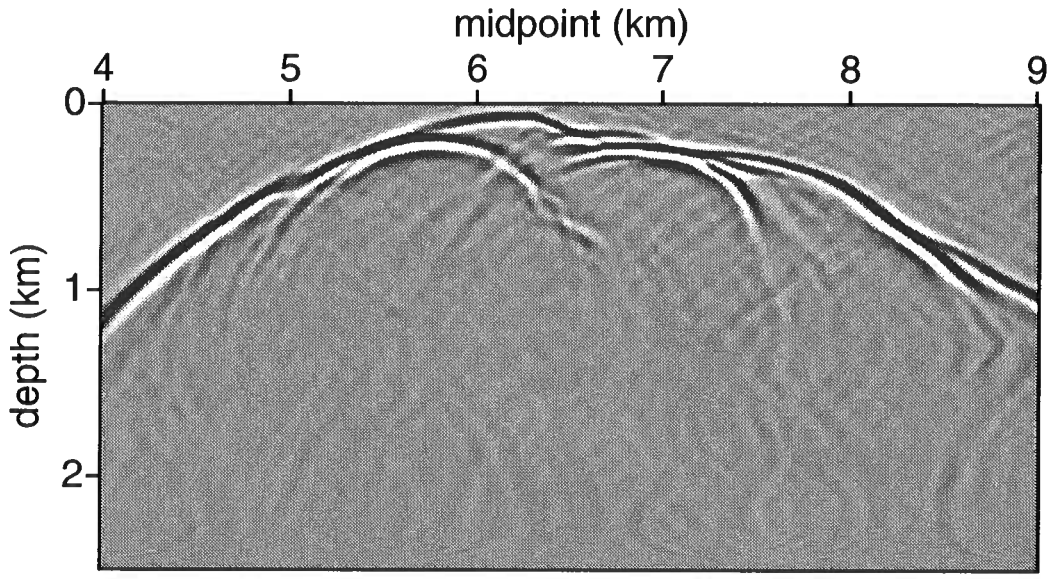

(a)

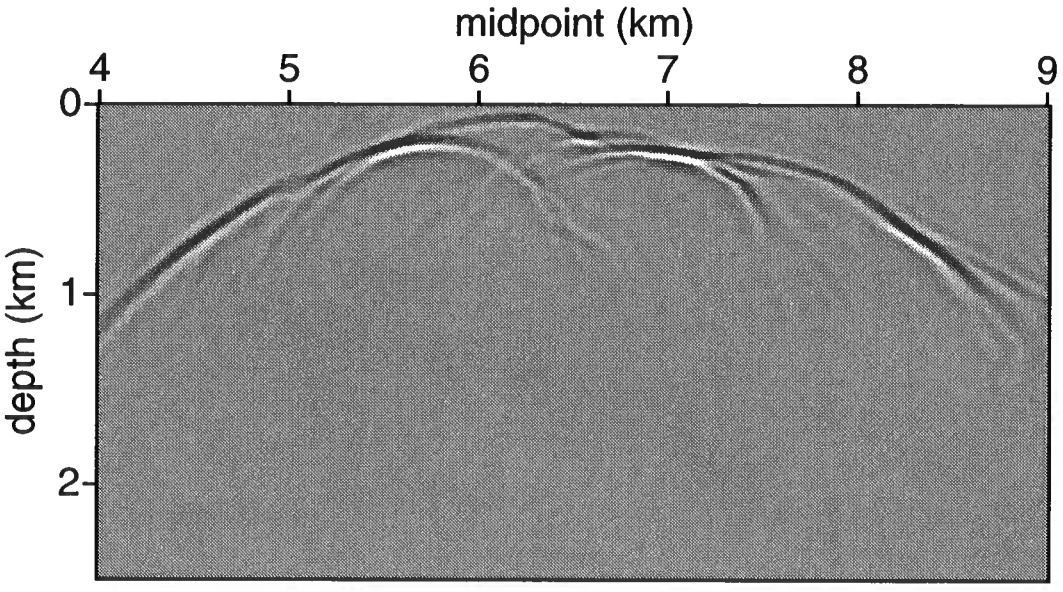

(b)

Figure 4.5. Snapshot of the wavefield at time $t = 0.95$ s computed with the second order of the generalized-screen method, (a) no contour deformation applied, (b) contour deformation applied as in Figure 4.6. Figure 4.4 shows the wave speed model used and the source location.

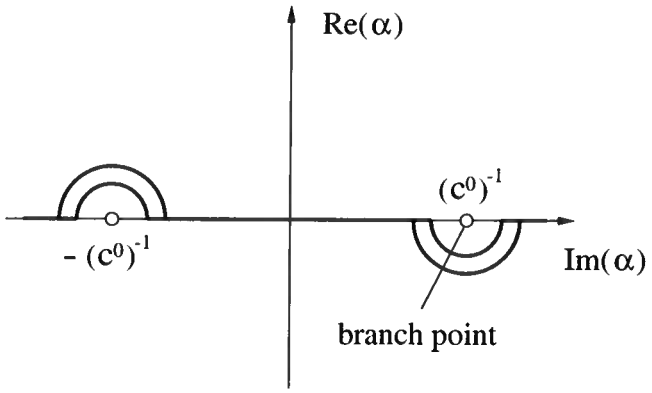

Figure 4.6. Applied contour deformation.

can create errors that can be boosted by large values of $1/\gamma^0$ close to the branch point. Figure 4.5(a) shows a snapshot of the wave field, computed with the second-order GS algorithm, in the region of the Marmousi model shown in Figure 4.4 when the wavenumber is allowed to get close to the branch point. The source is located at a star in Figure 4.4. The result is noisy; the noise is associated with high-angle propagation, i.e., when wavenumbers reach the vicinity of the branch point.

In equation (4.30), the path of integration in the α_1-plane should be chosen appropriately around the branch cuts. To avoid getting too close to the artificial branch points, we use contour deformation in the complex plane, as illustrated in Figure 4.6. Comparing the result in Figure 4.5(a) with that in Figure 4.5(b), where the contour deformation has been applied, note the removal of the noise associated with high-angle propagating energy.

In practice, all factors appearing in the GS algorithm are computed on the actual deformed contour except for the intermediate field quantities in the wavenumber domain that are evaluated on the real axis. The latter quantities are assumed to vary smoothly in the vicinity of the real axis and hence are approximated by their values on the real axis as evaluated with the (fast) Fourier transforms. We therefore make a zero-order Taylor approximation for the regions where the contour departs from the real axis. On the one hand, the higher the power of $[\gamma^0]^{-1}$, the further the path should depart from the real axis in the vicinity of the branch points; thus we use different deformations for the different terms in the GS expansions. On the other hand, such incomplete contour deformation does affect the source signature. This enforces us to keep the contours as close as possible to the real axis. Hence, the precise choice of contours is a compromise.

4.6 Accuracy analysis

We illustrate the accuracy of the GS algorithm for two scenarios: the 2D Marmousi model, and the SEG-EAGE 3D salt model. Our analysis emphasizes numerical modeling. We generate Green's functions and focus our observations on second-arrival energy and

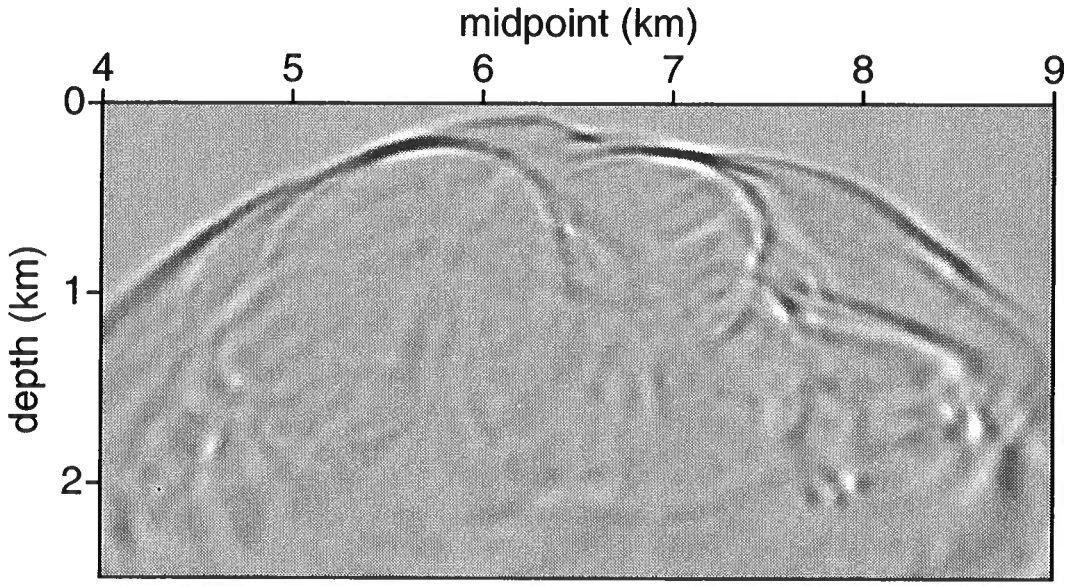

Figure 4.7. Snapshot of the wavefield at time $t = 0.95$ s with the full two-way acoustic wave equation.

multi-pathing. Imaging invokes an averaging (stacking) process; to learn about the prestack migration operator, we hence favor to analyze modeling instead. We shall, however, show depth-migration results in the Marmousi model.

4.6.1 Modeling

Marmousi model The medium complexity and the maximum propagation angle determine the sophistication of the approximation required. To illustrate this, we consider a region of the Institut Français du Pétrole (IFP)'s Marmousi model that includes the target reservoir (Figure 4.4). A point source (star) is located at the reservoir horizon, below a complex part of the model (anticline, unconformity, faults) that exhibits significant horizontal wave speed variations. Being based on actual geology (Bourgeois *et al.*, 1991), the Marmousi model introduces complexities that can be encountered in practice. The source is excited at time t = 0, and the pressure field is imaged at time t = 0.95 s, creating the snapshots in Figure 4.7 through Figure 4.10. For comparison, we modeled the two-way wavefield with the full acoustic wave equation (finite-difference time-domain, second order in space, second order in time), and shall use that wavefield (Figure 4.7) as a reference (the computational complexity of the full acoustic wave equation method in 2D, and even more so in 3D, compares unfavorably with the fast algorithms developed here). In modeling the upgoing wavefield, we compare the GS method with the split-step Fourier and the phase-shift-plus-interpolation (PSPI) methods. In the PSPI method (Gazdag & Sguazzero, 1984), wave components are upward or downward continued as if the medium were laterally

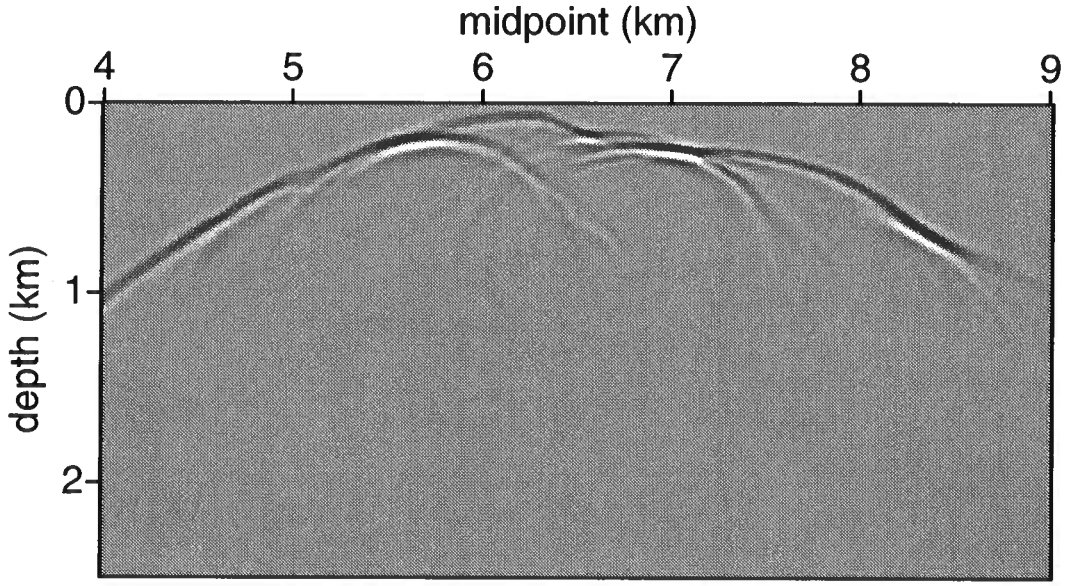

Figure 4.8. Snapshot of the wavefield at time $t = 0.95$ s with the split-step Fourier method.

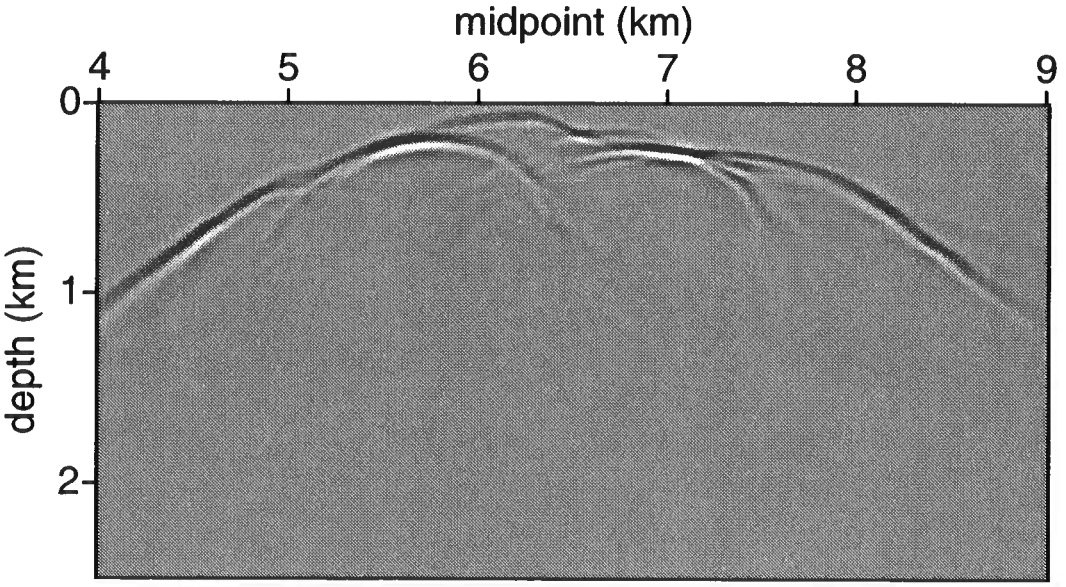

Figure 4.9. Snapshot of the wavefield at time $t = 0.95$ s with the phase-shift-plus-interpolation method (PSPI).

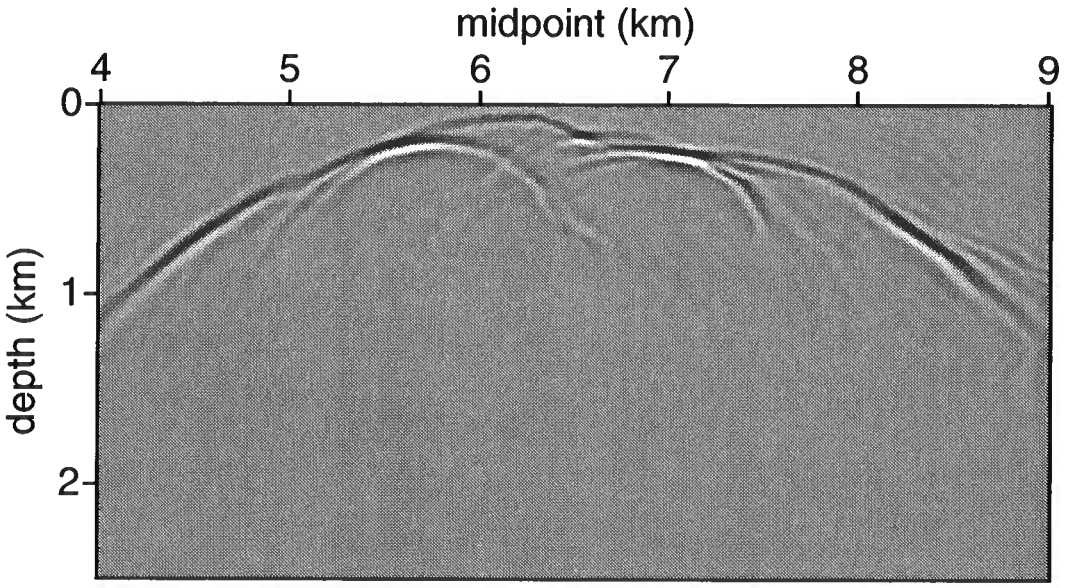

Figure 4.10. Snapshot of the wavefield at time $t = 0.95$ s with the fourth order of the generalized-screen method.

homogeneous but using several reference velocities to accommodate lateral wave speed variations: in the frequency-space domain, at any point in depth, an interpolation is performed using two fields associated with the two adjacent reference velocities.

Unlike the GS methods, the split-step Fourier method does not suffer from the presence of a branch point. We can therefore use a background wave speed c^0 that is greater than the minimum wave speed in each thin-slab. In Figure 4.8, we use the arithmetic mean of the wave speed across the thin-slab as a reference wave speed. Use of the median $[\frac{1}{2}(c_{max} - c_{min})]$ for the reference wave speed would give a poor result (not shown here). Use of the same reference wave speed as for the GS method (i.e., the minimum wave speed in the thin slab) yields even poorer result, for it increases the contrast between the true medium and the background medium.

With the number of reference velocities chosen for the PSPI method, we guaranteed a better accuracy, but at higher cost, than that of the split-step Fourier method. To compare algorithm accuracies, we look at the degree at which the wavefront is curved downward or upward with respect to the full-acoustic wave-equation generated wavefront. The split-step Fourier (Figure 4.8) result gives an impulse response with a wider shape (upward curved) for the first arrival than the full-wave result, whereas the PSPI method (Figure 4.9) gives a correct general shape for the first arrival. Neither of these methods gives, however, accurate images of the second-arrival energy (although the PSPI method still yields a better result). This second-arrival energy results from multi-pathing associated with the complexity and the heterogeneity of the Marmousi model. The multi-pathing here occurs with scattering at

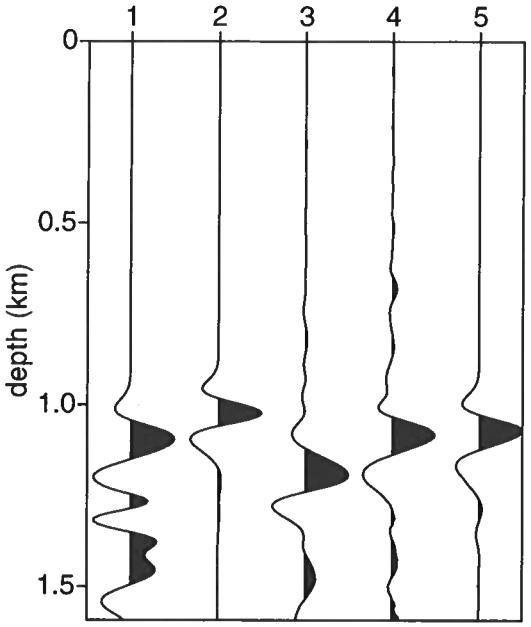

Figure 4.11. First trace on the left of the snapshots shown in Figures 4.7, 4.8, 4.5(b), 4.10, and 4.9: (1) finite difference, (2) split-step Fourier, (3) second-order generalized-screen, (4) fourth-order generalized-screen, (5) phase-shift-plus-interpolation (PSPI).

reasonably wide angles. For the split-step Fourier method, the limited accuracy for wide-angle propagation explains the poor modeling for the second-arrival energy. For the PSPI method, inaccuracies are attributable to the *linear* interpolation scheme.

To begin with the results of the various orders of the GS method, the second-order algorithm (Figure 4.5(b)) creates a wave front whose shape, as expected, is slightly curved downward with respect to the full-acoustic wave-equation wavefront. As the order of the GS expansion increases, the GS wavefront matches the true one more closely. The wavefront of the fourth-order solution (Figure 4.10) closely approaches the true wavefront. With the second-order GS method (Figure 4.5(b)) one can already see good definition of the second-arrival energy, due to a higher accuracy for wide-angle propagation than that in the split-step Fourier method. The better positioning and modeling of the later-arrival energy constitutes a key contribution to the imaging of complex structures such as those in the Marmousi model where these arrivals carry a significant part of the energy. Observe that subtle differences in Figures 4.8 through 4.10 represent differences in positioning of the order of a hundred meter according to the scale used. To highlight the conservation of source signature for the different orders of the GS expansion – under the incomplete

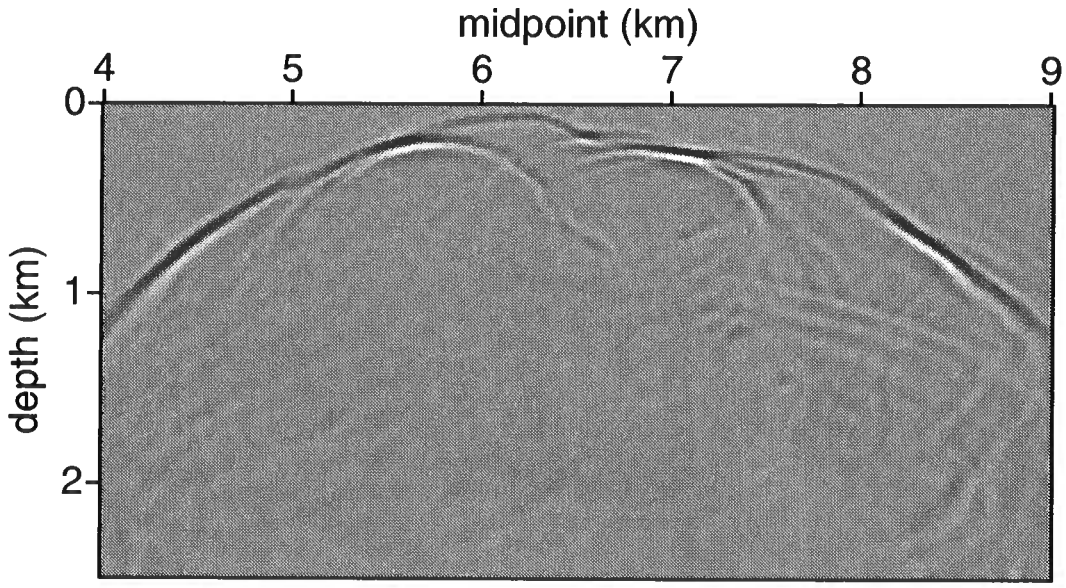

Figure 4.12. Snapshot of the wavefield at time $t = 0.95$ s with the fourth order of the generalized-screen modeling the three first terms of the Bremmer series. Some amplitude differences can be observed with Figure 4.7. These are mainly due to a low order (GS) representation of the reflection operator (see Appendix I) while some reflections are associated with wide-angle propagation especially close to the source (see Figure 4.4).

contour deformation – and the finite-difference, PSPI, and split-step Fourier approaches, we extract a single trace on the far left out of the snapshots shown in Figures 4.7, 4.8, 4.5(b), 4.10, and 4.9. These traces are combined in Figure 4.11. Observe that the 'arrival' of the fourth-order GS and PSPI methods align with the one obtained with the finite-difference computation, unlike the ones obtained with the split-step Fourier and the second-order GS methods. At these propagation angles, the fourth-order GS approximation suffices whereas the lower orders would not. The source signature, in particular in the fourth-order GS approximation, is clearly preserved at the expense of creating a weak precursor associated with the compromise in contour deformation. Such precursor is also visible in Figures 4.5(b) and 4.10.

Furthermore, when taking multiples into account, wide-angle propagation can be particularly significant, as mentioned before. Incorporating multiples is achieved with the use of the Bremmer series (De Hoop, 1996; Van Stralen *et al.*, 1998; De Hoop *et al.*, 2000), which necessitates the introduction of a GS representation of the reflection kernel (Appendix I). It is illustrated in Figure 4.12, where the fourth-order GS algorithm is used to calculate the first three terms of the Bremmer series. The first term corresponds to the upcoming energy as given by the one-way operator. The second term corresponds to energy that first travels upward then downward. The third term corresponds to energy that travels upward,

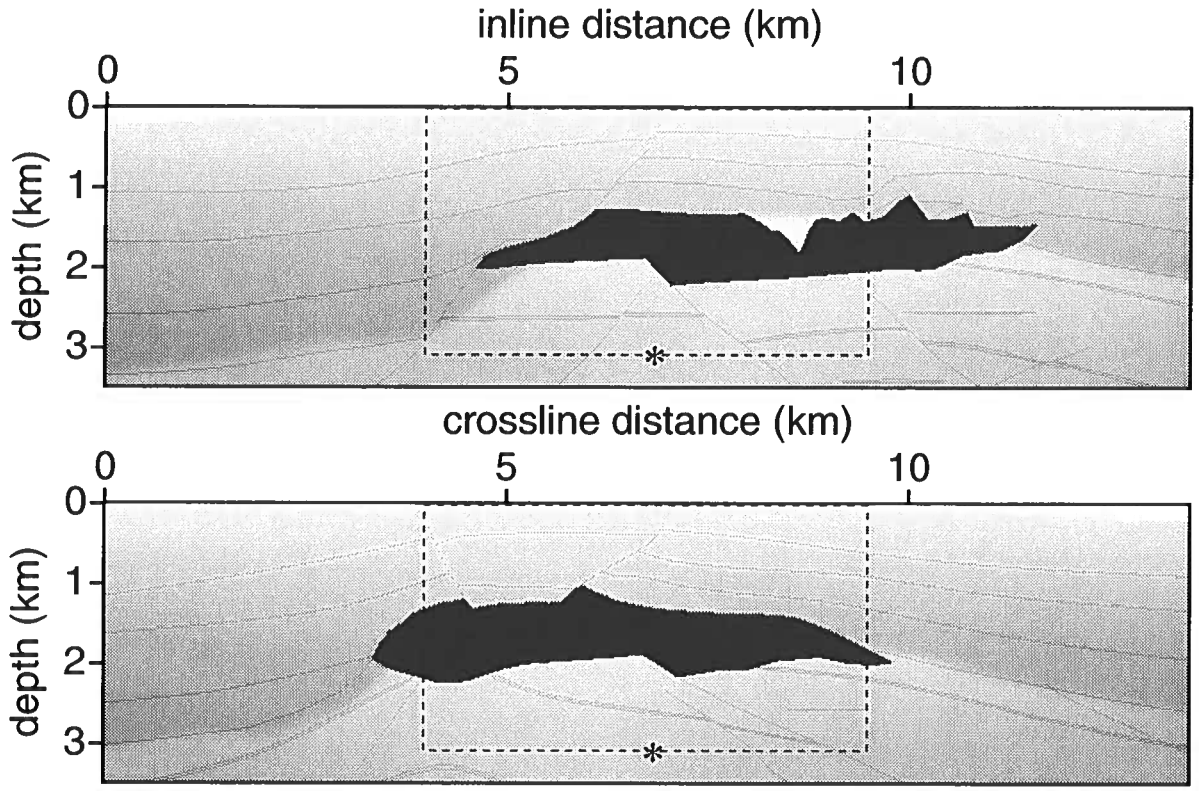

Figure 4.13. Vertical profiles across the center of the SEG-EAGE salt model. The asterisk locates the position of the source; the dashed line indicates the region detailed in Figure 4.14 through 4.18. The maximum wave speed is 4500 m/s (black). The minimum wave speed is 1500 m/s (white).

downward and upward again. Here, we also make use of the first-order GS representation of the reflection operator as described in Appendix I. Note that some of the multiple events found in Figure 4.7 are missing because they would belong to yet higher-order terms in the Bremmer series. Note in Figure 4.12 that some branches of the wavefronts do propagate almost horizontally and accurate results require higher order GS.

SEG-EAGE 3D salt model For a 3D modeling demonstration, we use the SEG-EAGE 3D salt model. Significant multi-pathing occurs in this model, and we shall illustrate how well the GS propagator accounts for this. Figure 4.13 shows two vertical profiles of wave speed across the SEG-EAGE 3D salt model, one parallel to the so-called in-line direction, and the second one parallel to the orthogonal cross-line direction. The profiles intersect at the center of the model. As in the Marmousi model, we place a point source in the zone of interest, i.e., beneath the salt body. The source location is represented by an asterisk in

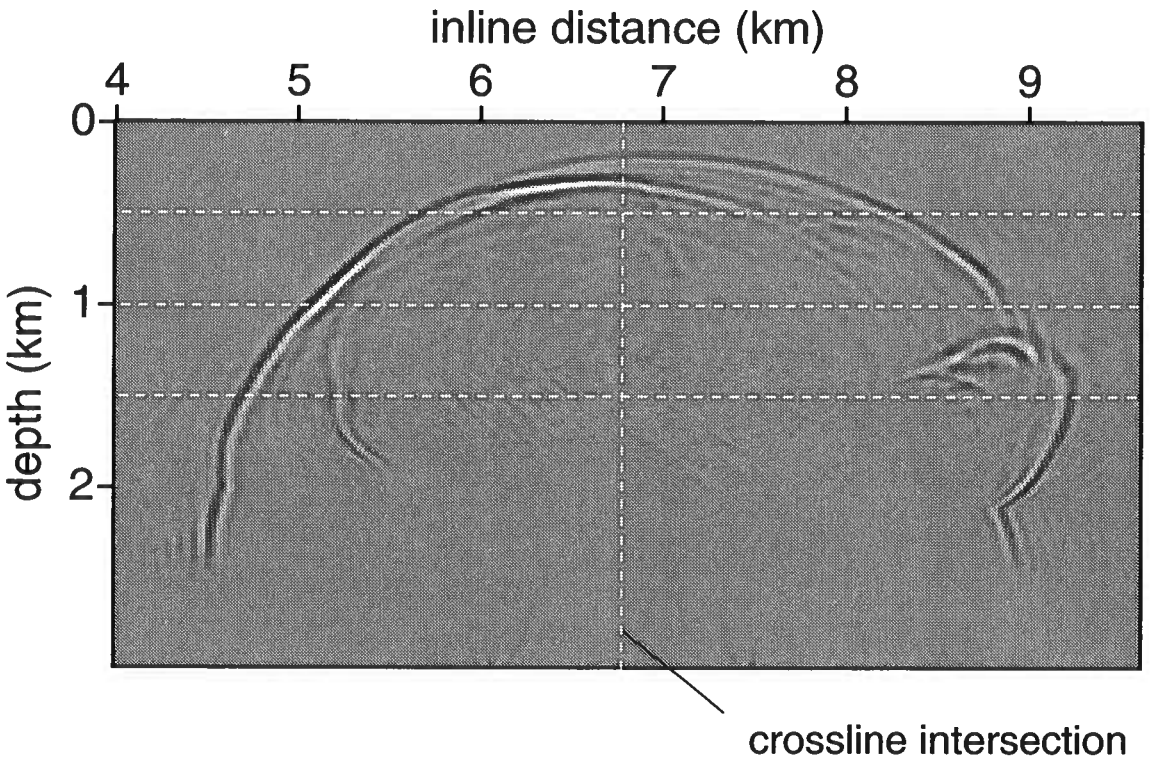

Figure 4.14. Snapshot of the wavefield at time $t = 1.2$ s with the second order of the generalized-screen method; in-line section. The three horizontal dashed lines represent the depth location of the horizontal sections of figures 4.16 through 4.18.

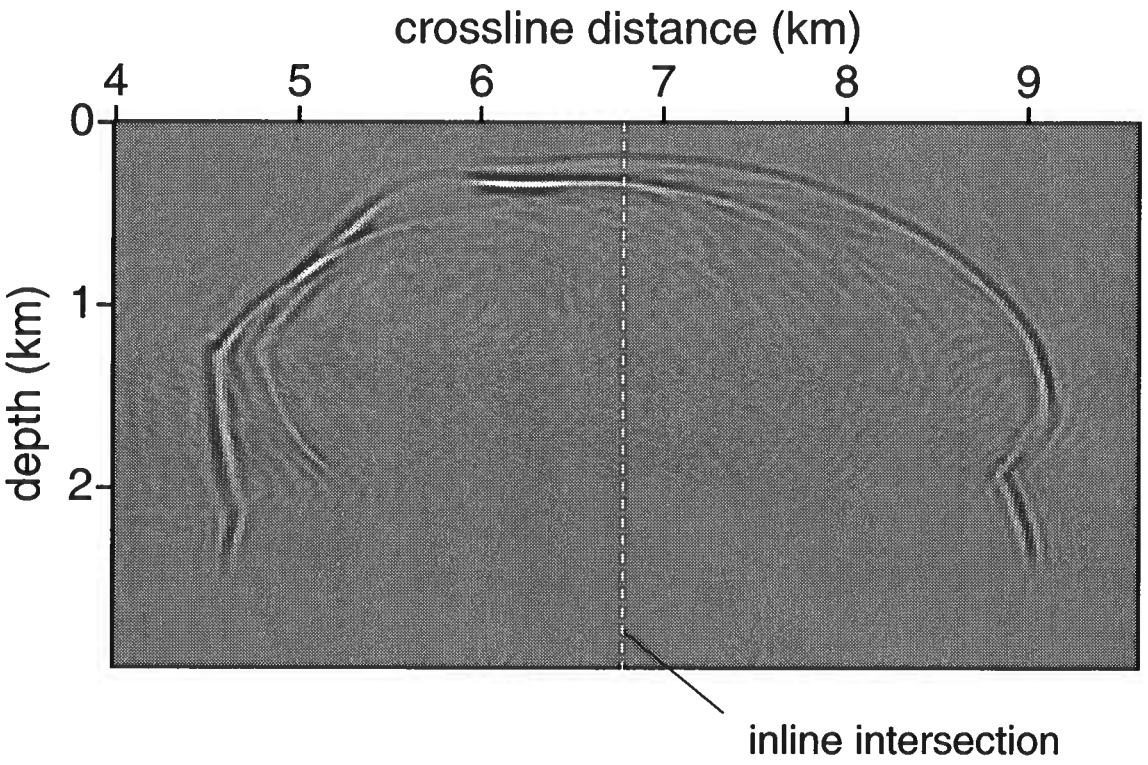

Figure 4.15. Snapshot of the wavefield at time $t = 1.2$ s with the second order of the generalized-screen method; cross-line section.

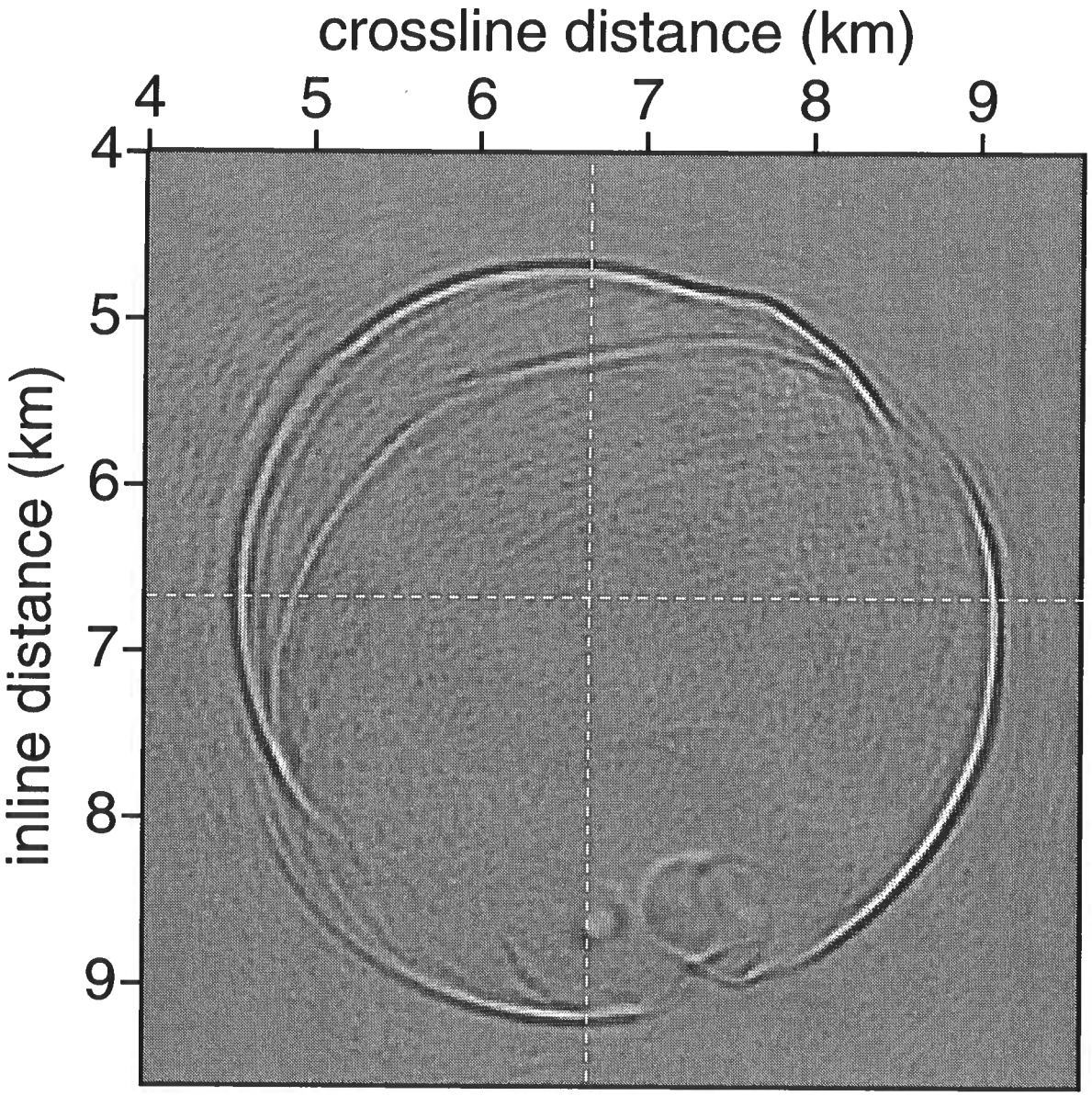

Figure 4.16. Snapshot of the wavefield at time $t = 1.2$ s with the second order of the generalized-screen method; horizontal section at depth 1500 m. The dashed lines represent the vertical sections as shown in figures 4.14 and 4.15. A weak precursor associated with the compromise in contour deformation is visible.

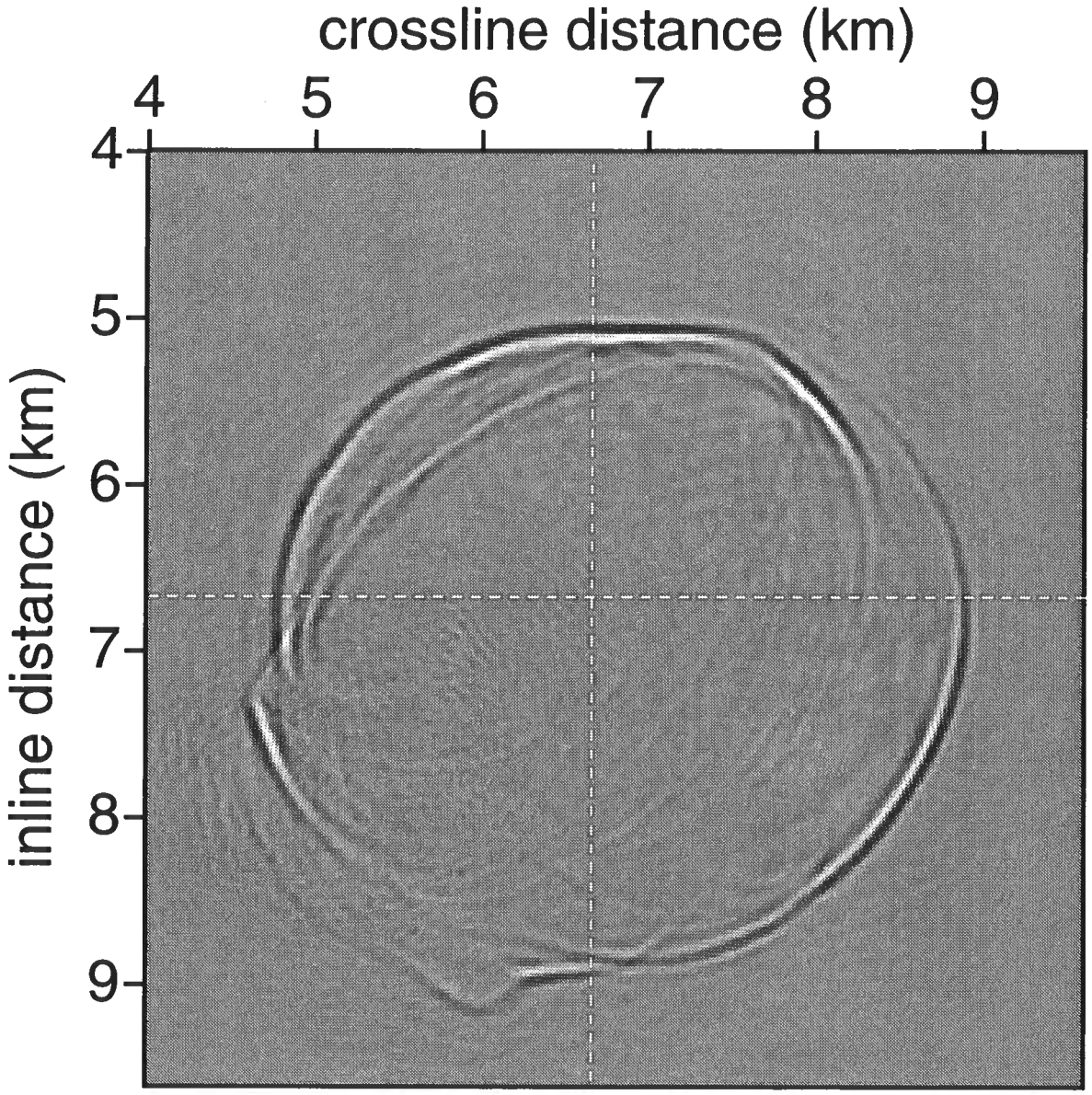

Figure 4.17. Snapshot of the wavefield at time $t = 1.2$ s with the second order of the generalized-screen method; horizontal section at depth 1000 m. The dashed lines represent the vertical sections as shown in figures 4.14 and 4.15.

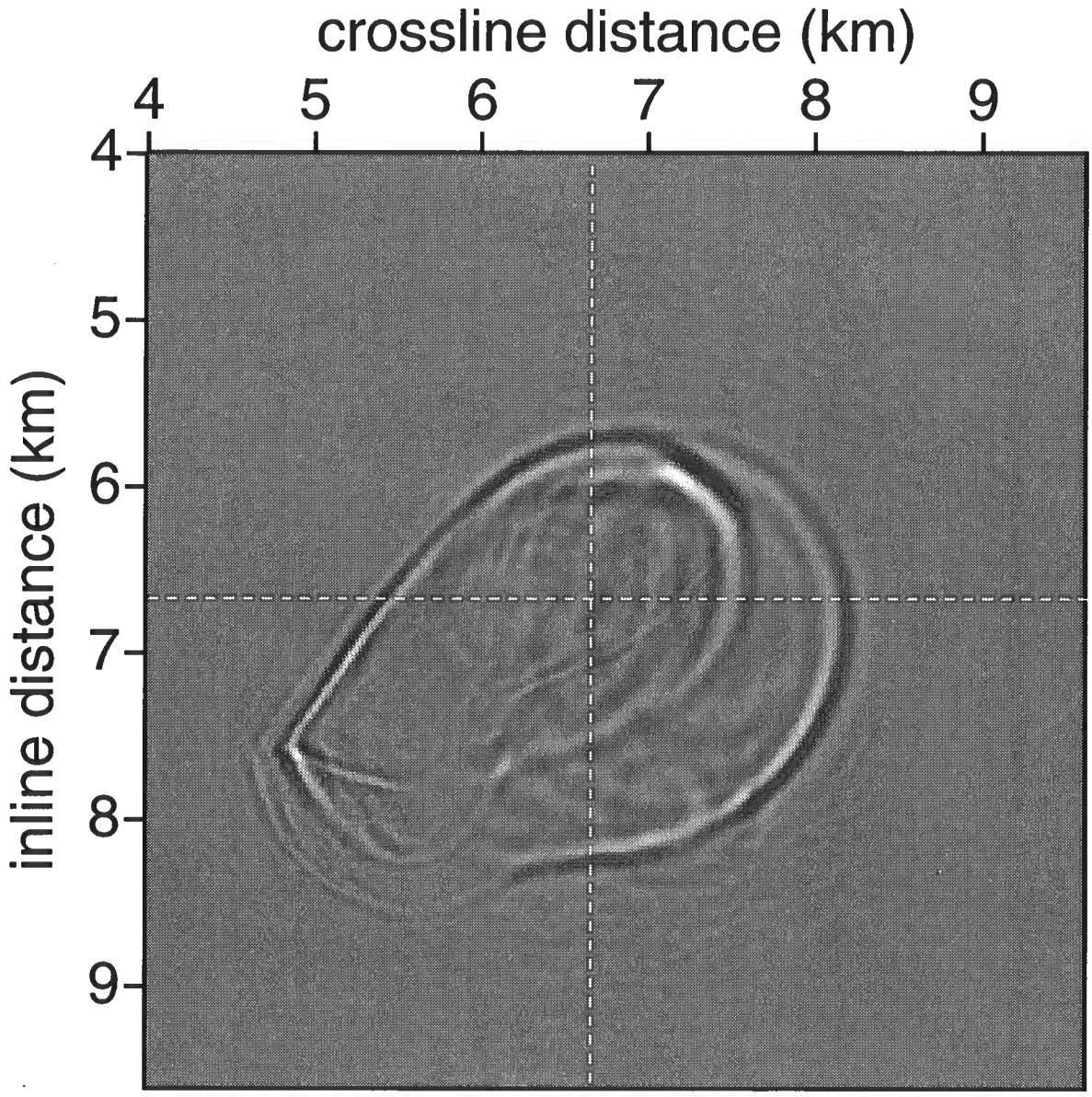

Figure 4.18. Snapshot of the wavefield at time $t = 1.2$ s with the second order of the generalized-screen method; horizontal section at depth 500 m. The dashed lines represent the vertical sections as shown in figures 4.14 and 4.15.

Figure 4.13. Note the stairstep shape of the base of the salt body. We expect this artificial roughness, which is due to the coarse sampling of the model in depth, to create diffractions that will appear as 'noise' in the wavefield.

In our example, the source is excited at time t = 0 and we use the second-order GS algorithm to image the field at time t = 1.2 s (snapshots in Figure 4.14 through Figure 4.18). Both the in-line section in Figure 4.14 and the cross-line section in Figure 4.15 show that second arrivals carry a significant part of the upgoing energy. They both show that, with the geometry of the salt body, partial waveguiding can occur, which could imply that a significant part of information is contained at large offsets in the scattered field recorded at the surface. Note the occurrence of a triplication in the cross-line section in Figure 4.15. The various horizontal sections of the 3D image (Figure 4.16 through Figure 4.18) illustrate the strong imprint that the salt structure imposes on the wavefront. The deepest slices (Figure 4.16) intersect the salt body, which explains the higher 'noise' level also visible in the vertical sections; this noise, again, corresponds to diffracted energy from the rough salt bottom.

4.6.2 Imaging

Laterally varying medium The difference in accuracy between the split-step Fourier method and the GS approach is illustrated with a 2D imaging experiment (Figure 4.19). The 2D section is composed of various reflectors with dips ranging from 0° to 75°. The wave speed profile is characterized by a gradient with a horizontal component of 0.1 s^{-1} and a vertical component of 0.4 s^{-1}. Figure 4.19 shows results after migrations of a zero-offset section (not shown) with the split-step Fourier algorithm and the fourth-order GS method. In the split-step Fourier result, reflectors steeper than about 45° are mispositioned with an error that grows with dip. Again, the accuracy with dip is a function of the lateral medium variation for both the split-step Fourier method and the GS approach. In the GS generated section, reflectors are accurately positioned because the wide-angle propagation, associated with the steepest events, is better handled. Note that the steepest event appears weaker on the GS generated section than on the split-step Fourier section. This is due to the proximity of the branch point to the propagation angles associated with the steepest reflector dip. The cascade of the expansion of the thin-slab propagator and the normalization are progressively less accurate for the phase as one departs from vertical propagation and constant medium perturbation. This introduces some amplitude inaccuracy.

Application to prestack depth migration To illustrate the accuracy of the different GS expansions for imaging, we incorporated the GS algorithm in prestack depth migration of shot gathers using the entire Marmousi data set (Figure 4.20). In the migration procedure, the fields associated with the source and receivers are downward continued. For each point in the subsurface the two fields are correlated at zero time lag (Claerbout, 1986).

Figures 4.21(a) and 4.21(b) compare the images obtained with the split-step Fourier version of the phase-screen method and the second-order GS approach. The latter gives a

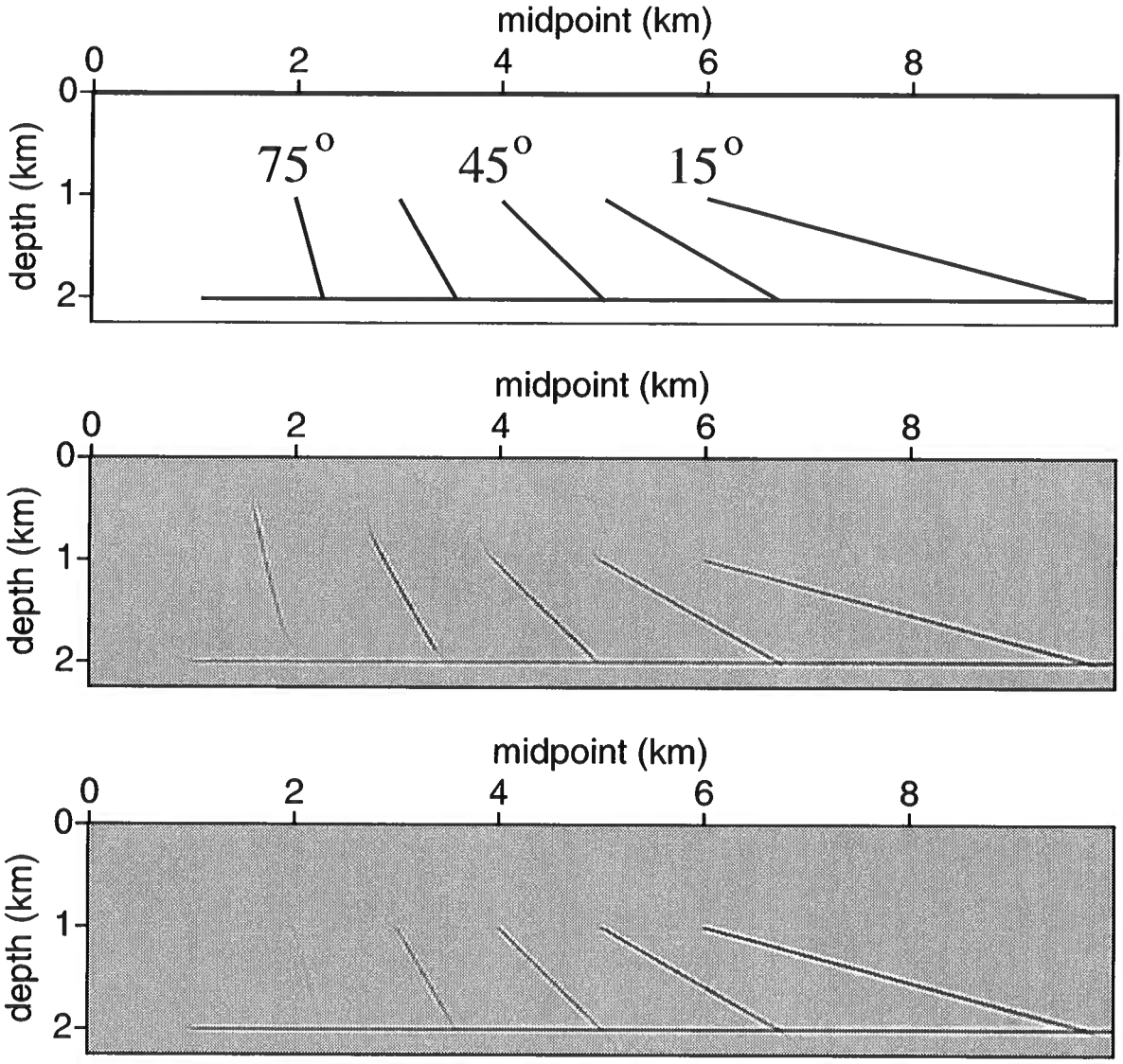

Figure 4.19. Top: model having reflectors with dips of 0°, 15°, 30°, 45°, 60° and 75°. Middle: migration of the modeled data with split-step Fourier method. Bottom: migration of the fourth-order generalized-screen method (GSP 4).

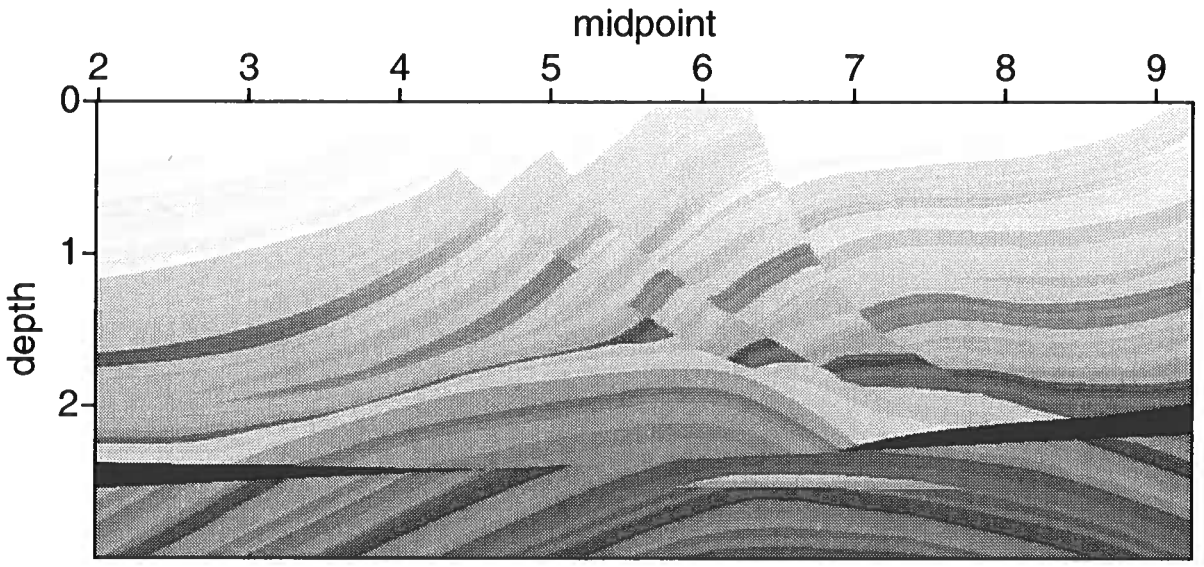

Figure 4.20. Marmousi wave speed model.The maximum wave speed is 5500 m/s (black). The minimum wave speed is 1500 m/s (white).

better result; because of the two additional correction terms appearing in the expansion, dipping events are more accurately positioned and better focused by the GS approach. Regions where significant differences occur are highlighted in Figures 4.21(a) and 4.21(b). The anticline (above the reservoir) of the Marmousi model poses a challenge to imaging for any migration algorithm because of multi-pathing and wide-angle scattering. The GS method accommodates these phenomena better than does the split-step method and yields more continuity in, and less deformation of, the reflectors.

4.7 Discussion

The generalized-screen (GS) wave extrapolation method is based on the decomposition of the medium into a background component and a perturbation. In lowest order, the GS approximation may be simplified to yield the phase-screen and split-step Fourier methods. The GS method extends these two methods and can accommodate more significant and rapid horizontal wave speed variations. In the process of migration, the GS method provides a choice of algorithm suitable for the complexity of a particular medium.

With the GS representation of the propagator is associated a vertical slowness symbol that generalizes the phase-screen and split-step Fourier symbol and has the dependencies on the spatial coordinates and the dependencies on the wavenumber factorized, inducing the structure of the GS propagator. The GS expansion of the vertical slowness symbol is justified in De Hoop *et al.* (2000). The GS expansion provides a fundamental simplification of the one-way operator; the propagator does not have to be evaluated at every output point.

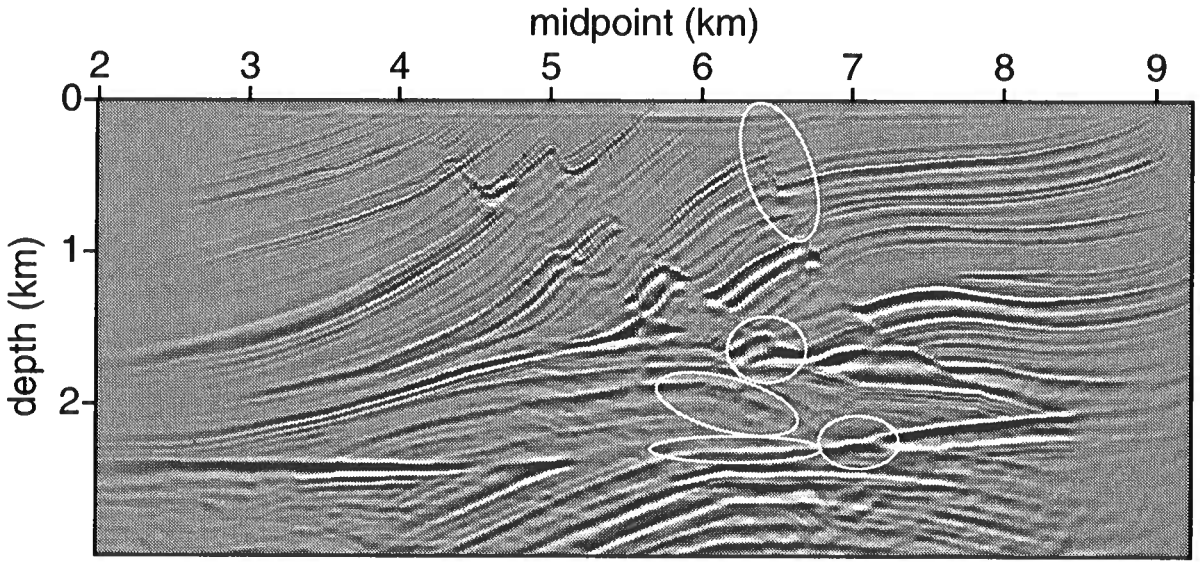

(a)

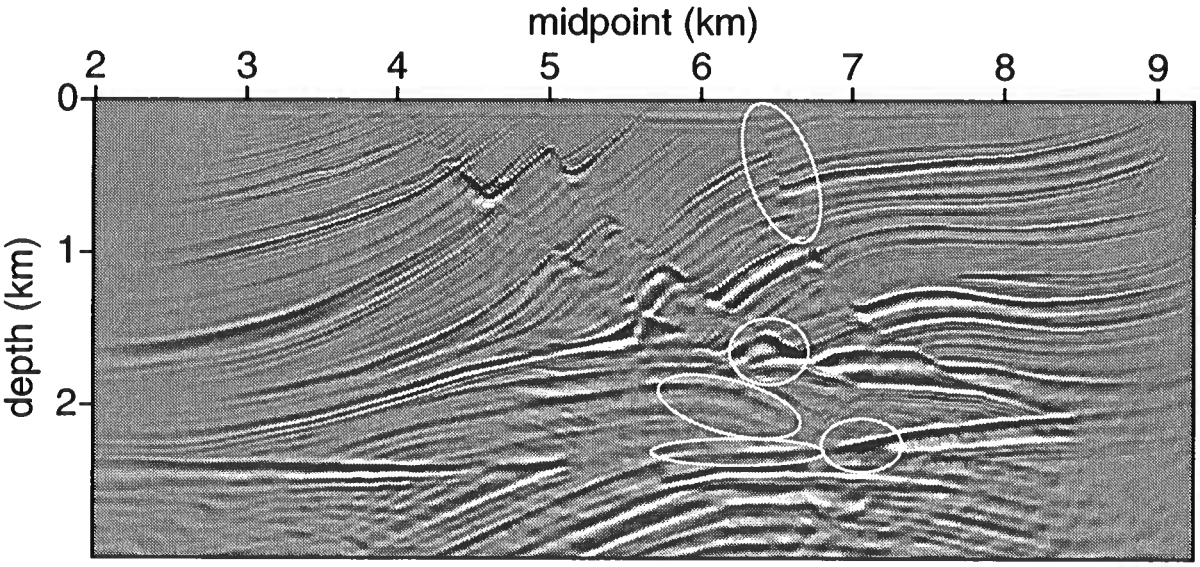

(b)

Figure 4.21. Prestack depth migration of the Marmousi data (a) with the split-step Fourier method, and (b) with the second-order generalized-screen method. Highlighted are features where clear differences can be observed between the two sections.

We obtained an algorithm that works as a shuttling between the frequency-horizontal space domain and the frequency-horizontal wavenumber domain. Each additional term in the GS expansion increases the accuracy. This amounts to an additional Fourier transform for each additional order in the expansion. In anisotropic media such as transversely isotropic media with a vertical symmetry axis, the influence of the anisotropic parameters in the vertical slowness symbol occurs only at non-vertical propagation. The split-step-Fourier type approximation (Stoffa *et al.*, 1990) does not have the degree of freedom to account for anisotropy or to shape the slowness surface appropriately, because of its accuracy restricted to near-vertical propagation. The GS methods can be extended to these media as shown in the companion chapter (Le Rousseau & De Hoop, 2001c) (Chapter5).

We illustrated the GS propagator's accuracy primarily through modeling. The mathematical accuracy analysis of the GS approximation was carried out by De Hoop *et al.* (2000). Here we focused on its numerical counterpart. We chose two synthetic models, both representative of the real world: the Marmousi model (off-shore Africa) and the SEG/EAGE 3D salt model (Gulf of Mexico). Each of these models provided insight into the capacity of the GS method to perform wave extrapolation, and showed how it compares with the split-step Fourier method, as well as PSPI and full-wave time-domain finite-difference methods. The GS modeling capacity is illustrated in both 2D and 3D. In this chapter we focused on the computation of Green's functions rather than on imaging. Imaging invokes an averaging procedure that hides propagation inaccuracies of the various methods. For completeness, however, we showed some prestack imaging results in 2D.

We have compared the GS method with some of its competitive algorithms. All these algorithms account up to a certain degree for multi-pathing: one-way (split-step Fourier, PSPI), two-way (finite differences). Another approach to approximate the one-way propagator (4.10) is the filter approach. Like our approach, the filter approach aims at approximating the propagation of singularities. Unlike our approach, it does not yield a comprehensive recursion that generates increasingly accurate one-way propagators on and away from the wavefront set. The filter approach was introduced by Holberg (1988) and Blacquière *et al.* (1989), and extended to 3D by Hale (1991b; 1991a). Those methods are described and compared to the GS method in Appendix J. Concerning the filter-McClellan approach the following can be said: (i) the filter will not be exact even in an (almost) homogeneous medium, (ii) the accuracy of the filter will depend on the sampling rate which for fixed frequency will depend on the local medium properties, i.e., the accuracy will vary with location, (iii) the same remarks apply to the McClellan transformation, (iv) intrinsic instability enforces dense sampling to 'open up' the wavefront set. These features are avoided in the GS method. As far as the computational complexity is concerned, the filter-McClellan and GS methods compare as follows, $52N_h - 46$ (Hale, 1991a) versus $(2+n)\log_2 N_1 N_2$. Typically, $N_h = 20$, $n = 2$, $N_1 = N_2 = 10^3$, whence the filter-McClellan approach is more than 10 times less efficient than the GS method.

The GS method, with its $(2+n)N_1 N_2 \log_2 N_1 N_2$ computational complexity (n is the order of the GS approximation and N_μ are the numbers of samples in the x_μ-direction), makes feasible 'wave equation' modeling and imaging in 3D. Finite-difference methods extend to 3D, but yield algorithms with greater computational complexity. In comparison, the com-

putational complexity of the split-step Fourier method follows as $2N_1N_2 \log_2 N_1N_2$, whereas the computational complexity of the PSPI approach is $(1 + n_{\text{ref}})N_1N_2 \log_2 N_1N_2 + 2N_1N_2$, where n_{ref} is the number of reference velocities dependent on the degree of lateral heterogeneities. Nowadays, 3D surveys are common, and some areas present geologic complexities where multi-pathing cannot be ignored. Unlike traditional efficient asymptotic methods (such as Kirchhoff) that use a single arrival (first or maximal energy), the GS method can predict the effect of multi-pathing. The introduction of the Bremmer coupling series yields a computation of the two-way Green's functions. The GS-Bremmer approach yields a tool box that can be used for processing multiples, velocity analysis, and inversion (De Hoop & De Hoop, 2000). The lowest order GS approximations has already found application in seismic imaging (Huang & Wu, 1996; Wu & Jin, 1997; Huang *et al.*, 1999).

Chapter 5

Scalar generalized-screen algorithms in transversely isotropic media with a vertical symmetry axis[1]

5.1 Summary

The scalar generalized-screen method in isotropic media is extended here to transversely isotropic media with a vertical symmetry axis (VTI). Although wave propagation in a transversely isotropic medium is essentially elastic, we use an equivalent 'acoustic' system of equations for the qP-waves which we prove to be accurate for both the dispersion relation and the polarization angle, in the case of 'mild' anisotropy. The enhanced accuracy of the generalized-screen method as compared to the split-step Fourier methods allows the extension to VTI media. The generalized-screen expansion of the one-way propagator follows closely the method used in the isotropic case. The medium is defined in terms of a background and a perturbation. The generalized-screen expansion of the vertical slowness is based upon an expansion of the medium parameters simultaneously into magnitude and smoothness of variation. We cast the theory into numerical algorithms, and assess the accuracy of the generalized-screen method in a particular VTI medium with complex structure, viz. the BP Amoco Valhall model, in which multi-pathing is significant.

5.2 Introduction

In realistic geological models, heterogeneity in medium properties is such that the phenomenon of multiple scattering is significant. Wave extrapolation methods are able to account for multi-pathing, with no need to follow the formation of caustics explicitly. However, their computational complexity is significant and hence fast, approximate, algorithms are of interest, in particular for 3D configurations. Methods such as the phase-screen (Ratcliffe, 1956) and the closely related split-step Fourier (Stoffa *et al.*, 1990) methods yield fast 3D algorithms. They are, however, limited in their capacity to predict large-angle propagation where significant lateral heterogeneities are present. Because of their attractive properties (3D, multi-pathing), De Hoop *et al.* (2000) and Le Rousseau and De Hoop (2001b) generalized the latter family of algorithms, enhancing their accuracy. With the generalized-screen (GS) approach, the accuracy of the phase-screen method is extended to larger-contrast,

[1]This chapter was published in *Geophysics*, **66**, (2001) pp.1538-1550, with M.V. de Hoop.

wider-angle, and back-scattering. We propose here to extend the GS method further to anisotropic media, in particular to transversely isotropic media with a vertical symmetry axis (VTI media). The enhanced accuracy resulting from the GS approach becomes a necessity in the application to VTI media.

The one-way propagator can be represented by a Hamiltonian path integral (De Witte-Morette *et al.*, 1979; Fishman & McCoy, 1984a; Fishman & McCoy, 1984b; De Hoop, 1996) that accounts for not only the energy traveling along the ray but also for the transport along non-stationary paths. These path integrals contain all possible multi-pathing. In the path integral, 'time' is identified with depth, and 'momenta' are identified with the horizontal wave slownesses which, in the ray-theoretic limit, coincide with the horizontal components of the gradient of travel time. The (square-root) Hamiltonian, appearing in the phase of the path integral, is identified with vertical wave slowness. The GS approach yields a fast algorithm for the path integrals.

Wave propagation in VTI media is essentially elastic. Yet, in various applications the propagation of qP waves only is considered as if the medium were acoustic (Alkhalifah, 1998a; Alkhalifah, 1998b). Following the concept introduced by Alkhalifah (1998a) and the methodology of Schoenberg and De Hoop (2000), we introduce an equivalent 'acoustic' system of equations for VTI qP-wave propagation. This first-order system, rather than the induced second-order wave equation, is required to arrive at the appropriate directional wavefield decomposition procedure that leads to the one-way wave equation and its associated propagator. In Appendix K, we show the accuracy of the equivalent 'acoustic' system for the qP-wave propagation not only for the dispersion relation (Alkhalifah, 1998a, (A-9)), i.e., the wavefront set, but also for the polarization vectors. In Appendix L, we follow the procedure introduced by De Hoop (1996) to decompose the wavefield into up- and down-going components. Doing so, we introduce the vertical slowness operator for the equivalent 'acoustic' medium and give the general form for the one-way wave propagator in such a medium.

We analyze the accuracy of the GS method in complex VTI structures using the BP Amoco VTI Valhall model (Brandsberg-Dahl *et al.*, 1999). This model induces significant multi-pathing and is representative of a North Sea geology. In the Valhall model, a so-called 'gas cloud' in the overburden creates a low velocity zone for qP waves. This geologic situation yields poor imaging below the 'gas cloud' with standard single-path methods using the qP-qP events only. With the help of the GS propagator, which we prove to be accurate in these situations, we shall illustrate that the origin of this problem is possibly associated with multi-pathing.

We first present the dispersion relation for qP waves in VTI media and the approximate, yet accurate, simplification discussed by Schoenberg and De Hoop (2000). Starting from that simplified dispersion relation, we derive the GS representation of the thin-slab propagator in VTI media. The results are then cast into a numerical algorithm. We carry out our accuracy analysis through modeling and therefore indirectly analyze the prestack migration operator. We focus on studying multi-pathing and second-arrival energy.

5.3 The scalar generalized-screen propagator in transversely isotropic media with a vertical symmetry axis

For transversely isotropic (TI) media, the dispersion relation associated with qP-wave propagation is not quite as simple as in the isotropic case [e.g., see (Le Rousseau & De Hoop, 2001b, (9))]. Because the phase velocity is a function of phase angle, the slowness surface is not a sphere. Nevertheless, to apply a GS-type expansion (De Hoop *et al.*, 2000; Le Rousseau & De Hoop, 2001b) as in the isotropic case, one would like to have a dispersion relation as close as possible to the one for the isotropic case. This is accomplished here by using a rational expansion of the dispersion relation in TI media developed by Schoenberg and De Hoop (2000), the first order of which can be made accurate by means of an appropriate limiting procedure (Alkhalifah, 1998a; Alkhalifah, 1998b).

5.3.1 Transversely isotropic media with a vertical symmetry axis

Throughout the chapter, we shall treat the qP wave as a scalar wave. In the scalar approximation, we neglect any type of mode conversion. We consider the case of TI media with a vertical symmetry axis (VTI), so without loss of generality one can confine attention to a single vertical plane.

An elastic medium is defined by its stiffness tensor (C_{ijkl}). With the so-called Voigt notation (Thomsen, 1986), one can represent the medium by a 6×6 matrix in accordance with

$$\begin{array}{lcccccc} ij \text{ or } kl: & 11 & 22 & 33 & 32=23 & 31=13 & 12=21\,. \\ & \downarrow & \downarrow & \downarrow & \downarrow & \downarrow & \downarrow \\ & 1 & 2 & 3 & 4 & 5 & 6 \end{array}$$

In the case of a TI medium, the non-zero entries are given by

$$\begin{pmatrix} c_{11} & c_{11}-2c_{66} & c_{13} & & & \\ c_{11}-2c_{66} & c_{11} & c_{13} & & & \\ c_{13} & c_{13} & c_{33} & & & \\ & & & c_{55} & & \\ & & & & c_{55} & \\ & & & & & c_{66} \end{pmatrix}. \tag{5.1}$$

5.3.2 Simplified dispersion relation for qP-wave propagation

We select the direction of preference along the x_3-axis (or 'vertical' axis) and denoting the remaining ('transverse' or 'horizontal') coordinates by x_μ, $\mu = 1, 2$. Terms $\tilde{c}_{ij}$ represent the elastic moduli c_{ij} divided by the density ρ, and thus have dimension of velocity squared.

In the present development, it is advantageous to use the Laplace transform with respect to time, t, and the Fourier transform with respect to the horizontal spatial coordinates,

x_μ. We introduce the notation

$$s = -\mathrm{i}\omega\,, \tag{5.2}$$

$$\alpha_\nu = \frac{1}{\mathrm{i}\omega}\,k_\nu = -\frac{1}{s}\,k_\nu\,, \tag{5.3}$$

where ω and k_ν are the frequency and the horizontal wavenumber components. Let γ_1 be the vertical slowness[2],

$$\gamma_1 = \frac{k_3}{\omega}\,, \tag{5.4}$$

where k_3 is the vertical wavenumber. We denote $\boldsymbol{u}$ the particle displacement. We work in a vertical plane without loss of generality and use α instead of α_1 and α_2 ($\alpha^2 = \alpha_\nu\alpha_\nu$). We write u_h and u_3 as the horizontal and vertical components of the particle displacement respectively. Throughout the chapter we use the summation convention for repeated indices. From the Christoffel equation [associated with equation (5.1)], describing the wave propagation in the time-Laplace space-Fourier domain,

$$\begin{pmatrix} -\tilde{c}_{11}\alpha^2 + \tilde{c}_{55}\gamma_1^2 - 1 & (\tilde{c}_{55} + \tilde{c}_{13})\mathrm{i}\alpha\gamma_1 \\ (\tilde{c}_{55} + \tilde{c}_{13})\mathrm{i}\alpha\gamma_1 & -\tilde{c}_{55}\alpha^2 + \tilde{c}_{33}\gamma_1^2 - 1 \end{pmatrix} \begin{pmatrix} u_h \\ u_3 \end{pmatrix} = \begin{pmatrix} 0 \\ 0 \end{pmatrix}\,, \tag{5.5}$$

we obtain the dispersion relation

$$\begin{aligned} &\tilde{c}_{11}\tilde{c}_{55}(\alpha^2)^2 - \left[(\tilde{c}_{11} + \tilde{c}_{33})\tilde{c}_{55} + E^2\right]\alpha^2\gamma_1^2 + \tilde{c}_{33}\tilde{c}_{55}(\gamma_1^2)^2 \\ &\quad +(\tilde{c}_{11} + \tilde{c}_{55})\alpha^2 - (\tilde{c}_{33} + \tilde{c}_{55})\gamma_1^2 + 1 = 0\,, \end{aligned} \tag{5.6}$$

expressing the vanishing determinant of the system of linear equations (5.5), where

$$E^2 = (\tilde{c}_{11} - \tilde{c}_{55})(\tilde{c}_{33} - \tilde{c}_{55}) - (\tilde{c}_{13} + \tilde{c}_{55})^2\,. \tag{5.7}$$

To analyze the qP-wave behavior, we carry out the change of variables

$$X = -\tilde{c}_{11}\alpha^2\,;\quad Z = \tilde{c}_{33}\gamma_1^2\,. \tag{5.8}$$

The dispersion relation becomes

$$\begin{aligned} \frac{\tilde{c}_{55}}{\tilde{c}_{11}}X^2 + \left[\left(\frac{\tilde{c}_{55}}{\tilde{c}_{11}} + \frac{\tilde{c}_{55}}{\tilde{c}_{33}}\right) + \frac{E^2}{\tilde{c}_{11}\tilde{c}_{33}}\right]XZ + \frac{\tilde{c}_{55}}{\tilde{c}_{33}}Z^2 \\ - \left(1 + \frac{\tilde{c}_{11}}{\tilde{c}_{55}}\right)X - \left(1 + \frac{\tilde{c}_{33}}{\tilde{c}_{55}}\right)Z + 1 = 0\,, \end{aligned} \tag{5.9}$$

and can be rewritten as $Z = 1 - X + f(X, E^2)$, in which f can be expanded in terms $X(1 - X)$. This ensures accuracy at both normal ($X = 0$) and grazing ($X = 1$) incidence.

[2]We explain the subscript 1 in γ_1 in Appendix L.

The exact solution for the qP slowness depends weakly on $\tilde{c}_{13}$ and $\tilde{c}_{55}$ individually but strongly on $\tilde{a} = \tilde{c}_{13} + 2\tilde{c}_{55}$ in the case of 'mild' anisotropy [for detailed discussion on 'mild' anisotropy, see Schoenberg and De Hoop (2000)]. Alkhalifah (1998a) and Schoenberg and De Hoop (2000) propose then the following transformation

$$\tilde{c}_{13} \to \tilde{a} \ , \ \tilde{c}_{55} \to 0 \ . \tag{5.10}$$

In this limit, equation (5.9) simplifies to

$$\left[1 - \left(1 - \frac{\tilde{a}^2}{\tilde{c}_{11}\tilde{c}_{33}}\right) X\right] Z = 1 - X \ , \tag{5.11}$$

which is an exact rational representation of Z [Alkhalifah, 1998-a, (A-9); Schoenberg & De Hoop, 2000, (37),(38)].

More generally, this limit (5.10) can be applied to the vector wave equation as is done in Appendix K. There we show that not only is approximation (5.10) accurate for the dispersion relation, i.e., for the wavefront set [note that we recover equation (5.11) in equation (K.32)], but also for the polarization vectors of the qP waves.

If we introduce Thomsen's parameters ε and δ (Thomsen, 1986)

$$\varepsilon = \frac{c_{11} - c_{33}}{2c_{33}} \ ,$$
$$\delta = \frac{(c_{13} + c_{55})^2 - (c_{33} - c_{55})^2}{2c_{33}(c_{33} - c_{55})} \ ,$$

with δ becoming

$$\delta = \frac{a^2 - c_{33}^2}{2c_{33}^2} \ ,$$

in the framework of the limit (5.10), and use c_V as the vertical qP-wave wave speed, i.e.,

$$c_V = \sqrt{\tilde{c}_{33}} \ ,$$

relation (5.11) becomes

$$\gamma_1^2 = c_V^{-2} \frac{1 + c_V^2 \alpha^2 (1 + 2\varepsilon)}{1 - 2c_V^2 \alpha^2 (\delta - \varepsilon)} \ , \tag{5.12}$$

which, away from a vertical plane, can be written as

$$\gamma_1(\boldsymbol{x}; \alpha_\nu) = \sqrt{[c_V(\boldsymbol{x})]^{-2} \ \frac{1 + [c_V(\boldsymbol{x})]^2 \ \alpha_\nu \alpha_\nu \ [1 + 2\varepsilon(\boldsymbol{x})]}{1 - 2[c_V(\boldsymbol{x})]^2 \ \alpha_\nu \alpha_\nu \ [\delta(\boldsymbol{x}) - \varepsilon(\boldsymbol{x})]}} \ . \tag{5.13}$$

Note that letting ε and δ go to zero leads to the dispersion equation in the isotropic case, as

it should. The vector $(\mathrm{i}\alpha_1, \mathrm{i}\alpha_2, \gamma_1)$ is the gradient of travel time consistent with the eikonal equation. We use the dispersion relation (5.13) to derive the anisotropic scalar one-way propagator.

5.3.3 The scalar one-way propagator

For a sufficiently small vertical step Δx_3, and a sufficiently smooth medium, the Hamiltonian path-integral representation for the one-way thin-slab propagator reduces to the Fourier representation (De Hoop *et al.*, 2000):

$$g^{(\pm)}(x_\mu, x_3; x'_\upsilon, x'_3) \simeq \int (s/2\pi)^2 \mathrm{d}\alpha_1 \mathrm{d}\alpha_2 \exp[-\mathrm{i}s\,\alpha_\sigma(x_\sigma - x'_\sigma)] \exp[\mp s\,\gamma_1(x_\mu, \bar{x}_3; \alpha_\nu)\Delta x_3] \,, \quad (5.14)$$

with

$$\Delta x_3 = x_3 - x'_3 \,,$$

$$\bar{x}_3 = x_3 - \tfrac{1}{2}\Delta x_3 = x'_3 + \tfrac{1}{2}\Delta x_3 \,,$$

and where γ_1 is given by the dispersion relation (5.13). In Appendix K, we introduce an equivalent 'acoustic' system for the elastic propagation of qP waves in VTI media. In Appendix L we work out the wavefield decomposition from this equivalent 'acoustic' system similar to the decomposition in the isotropic case (De Hoop, 1996). Also, we show that γ_1 has the interpretation of the symbol of the principal part of the vertical slowness operator, i.e., the value of the vertical slowness symbol if we freeze the medium locally ['high-frequency' approximation; see also Appendix H]. Then the expression of the one-way wave propagator follows the same as in the isotropic case, hence the form of equation (5.14).

In the limit of a laterally homogeneous thin slab, γ_1 will not depend on x_μ, and the thin-slab propagator reduces to Gazdag's phase-shift operator, introduced in the isotropic case (Gazdag, 1978). The operator is composed of a forward Fourier transform, a multiplication by a phase factor (the phase is proportional to the vertical slowness) and an inverse Fourier transform. In the general case of equation (5.14), the thin-slab propagator has a similar structure except that the phase factor is dependent upon the output point, x_μ. Every output point requires its own evaluation of equation (5.14), which represents a considerable computational effort. The GS approximation of the thin-slab propagator enforces a simplification of this computational complexity, while allowing laterally varying media.

5.3.4 Generalized-screen principal-slowness surface

Medium parameterization and contrast formulation For the subsequent analysis, we employ a 'contrast formulation' that allows us to take lateral heterogeneity into account in the thin-slab propagation. In the slab $[x'_3, x_3]$ we introduce a background medium

with vertical medium wave speed, c_V^0, and the two Thomsen's parameters ε^0 and δ^0. The background medium is constant in the slab, but may vary from one slab to another. We then introduce a triplet of medium perturbations:

$$u_V(x_\mu, x_3) = [c_V(x_\mu, x_3)]^{-2} - [c_V^0(x_3)]^{-2} , \tag{5.15}$$

$$u_\varepsilon(x_\mu, x_3) = \varepsilon(x_\mu, x_3) - \varepsilon^0(x_3) , \tag{5.16}$$

$$u_\delta(x_\mu, x_3) = \delta(x_\mu, x_3) - \delta^0(x_3) . \tag{5.17}$$

We will expand the vertical slowness left principal symbol, γ_1, into the perturbations u_V, u_ε, and u_δ about the background medium.

Generalized-screen expansion Assuming small vertical medium variation across the thin slab (the slab is sufficiently thin), we set

$$\gamma^0(\zeta; \alpha_\nu) = \sqrt{[c_V^0]^{-2} \frac{1 + [c_V^0]^2 \alpha_\nu \alpha_\nu (1 + 2\varepsilon^0)}{1 - 2[c_V^0]^2 \alpha_\nu \alpha_\nu (\delta^0 - \varepsilon^0)}}$$
$$= \gamma^0(x_3; \alpha_\nu) \quad \text{if} \quad \zeta \in [x_3', x_3] , \tag{5.18}$$

consistent with equation (5.13) evaluated in the background medium. The principal symbol of the vertical slowness, γ_1, will be expanded in u_V, u_ε, and u_δ. This can be done, for instance, by first expanding γ_1 in u_V, then in u_ε, and finally in u_δ. The principal symbol of the vertical slowness, γ_1, can be decomposed into a background term, γ^0, and a perturbation, γ_1^1,

$$\gamma_1(x_\mu, x_3; \alpha_\nu) = \gamma^0(x_3; \alpha_\nu) + \gamma_1^1(x_\mu, x_3; \alpha_\nu) . \tag{5.19}$$

When expanding in the three variables u_V, u_ε, and u_δ simultaneously, we discard terms that contain products of perturbation terms. We justify this approximation by recognizing that the primary deformation of the slowness surface is caused by the perturbation in the medium-vertical slowness squared; variations in the anisotropy parameter influence the higher order terms. This yields the form,

$$\gamma_1^1 \simeq \gamma_{u_V}^1 + \gamma_{u_\varepsilon}^1 + \gamma_{u_\delta}^1 , \tag{5.20}$$

where $\gamma_{u_V}^1$, $\gamma_{u_\varepsilon}^1$, and $\gamma_{u_\delta}^1$ follow the general structures

$$\gamma_{u_V}^1(x_\mu, x_3; \alpha_\nu) = \sum_{j=1}^{n_{u_V}} \psi_{V,j}(x_3; \alpha_\nu) \, [u_V(x_\mu, x_3)]^j , \tag{5.21}$$

$$\gamma_{u_\varepsilon}^1(x_\mu, x_3; \alpha_\nu) = \sum_{j=1}^{n_{u_\varepsilon}} \psi_{\varepsilon,j}(x_3; \alpha_\nu) \, [u_\varepsilon(x_\mu, x_3)]^j , \tag{5.22}$$

$$\gamma^1_{u_\delta}(x_\mu, x_3; \alpha_\nu) = \sum_{j=1}^{n_{u_\delta}} \psi_{\delta,j}(x_3; \alpha_\nu) \, [u_\delta(x_\mu, x_3)]^j \, . \tag{5.23}$$

In practice, we limit ourselves to an expansion up to the first order in the anisotropy-parameter perturbations ($n_{u_\varepsilon} = n_{u_\delta} = 1$) , and to fourth order in the medium-vertical-slowness-squared perturbation ($n_{u_V} \leq 4$), compatible with the isotropic case (Le Rousseau & De Hoop, 2001b, (18)). Here, the use of equation (5.13) is particularly fruitful for it allows us to avoid using intricate formulas for the different terms of the GS expansion. The first-order expansions in each perturbation are given by

$$\gamma^1_{u_V}(x_\mu, x_3; \alpha_\nu) = u_V(x_\mu, x_3) \left[\frac{1 - 4[c_V^0(x_3)]^2 \alpha_\nu \alpha_\nu (\delta^0(x_3) - \varepsilon^0(x_3))}{\sigma(x_3; \alpha_\nu)} \right. \tag{5.24}$$
$$\left. - \frac{2[c_V^0(x_3)]^4 (\alpha_\nu \alpha_\nu)^2 (\delta^0(x_3) - \varepsilon^0(x_3))(1 + 2\varepsilon^0(x_3))}{\sigma(x_3; \alpha_\nu)} \right] ,$$

$$\gamma^1_{u_\varepsilon}(x_\mu, x_3; \alpha_\nu) = u_\varepsilon(x_\mu, x_3) \, \frac{[c_V^0(x_3)]^2 (\alpha_\nu \alpha_\nu)^2 (1 + 2\delta^0(x_3))}{\sigma(x_3; \alpha_\nu)} \, , \tag{5.25}$$

$$\gamma^1_{u_\delta}(x_\mu, x_3; \alpha_\nu) = u_\delta(x_\mu, x_3) \, \frac{[c_V^0(x_3)]^2 \alpha_\nu \alpha_\nu \gamma^0(x_3; \alpha_\nu)}{1 - 2[c_V^0(x_3)]^2 \alpha_\nu \alpha_\nu (\delta^0(x_3) - \varepsilon^0(x_3))} \, , \tag{5.26}$$

where

$$\sigma(x_3; \alpha_\nu) = 2 \left(1 - 2[c_V^0(x_3)]^2 \alpha_\nu \alpha_\nu (\delta^0(x_3) - \varepsilon^0(x_3))\right)^2 \gamma^0(x_3; \alpha_\nu) \, . \tag{5.27}$$

Note that, in each term in equations (5.21) through (5.23), dependencies on x_μ and α_ν are separated. As in the isotropic case (Le Rousseau & De Hoop, 2001b), this property induces the simplified structure of the GS propagator.

The accuracy of each term, $\gamma^1_{u_V}$, $\gamma^1_{u_\varepsilon}$, and $\gamma^1_{u_\delta}$, can be considered independently. The expansion term $\gamma^1_{u_V}$ provides the same accuracy as its counterpart γ^1_1 in the isotropic case (Le Rousseau & De Hoop, 2001b, (16)). Figures 5.1 and 5.2 illustrate the increasing accuracy of the GS expansion of the vertical-slowness principal symbol (γ_1 as a function of the horizontal slowness $p = \sqrt{-\alpha_\nu \alpha_\nu}$) in the contrast in medium-vertical slowness squared, u_V. In Figure 5.1 the medium is characterized by elliptic anisotropy, i.e., $\varepsilon = \delta$. In Figure 5.2 the medium is anelliptic (here $\varepsilon = 0.2$ and $\delta = 0.0$). Adding higher-order terms in the GS expansion (in the medium-vertical-slowness-squared perturbation, u_V), the shape of the slowness surface improves, as it is in the isotropic case (Le Rousseau & De Hoop, 2001b).

A first-order expansion in the perturbation u_ε in ε proves to be sufficiently accurate up to 50° as illustrated in Figure 5.3, where the contrast between the actual ε and the background ε^0 is 0.2. This accuracy is comparable to the one of $\gamma^1_{u_V}$ with the second-order expansion in the contrast in medium-vertical slowness squared, u_V, and is sufficient for most practical purposes. The behavior of the GS expansion for the perturbation in δ is illustrated in Figure 5.4. Although the contrast between the actual (local) and the background values is 0.2, the GS expansion shows a close to perfect result. For all practical purposes, the leading term is sufficiently accurate. This is due to the fact that equation (5.13) is exact

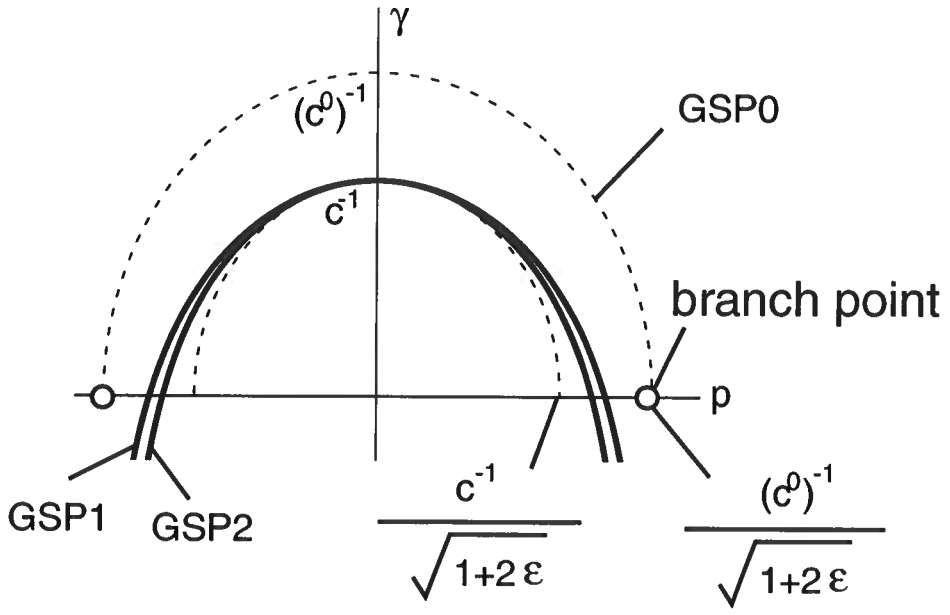

Figure 5.1. Principal parts of the generalized-screen vertical slowness, as a function of the horizontal slowness p, in the elliptical VTI case ($\varepsilon = 0.3$, $\delta = 0.3$) in a constant-wave speed perturbation medium: zero-order (GSP0), first-order (GSP1) and second-order (GSP2). The principal part of the exact vertical slowness is shown with the inner dashed curve.

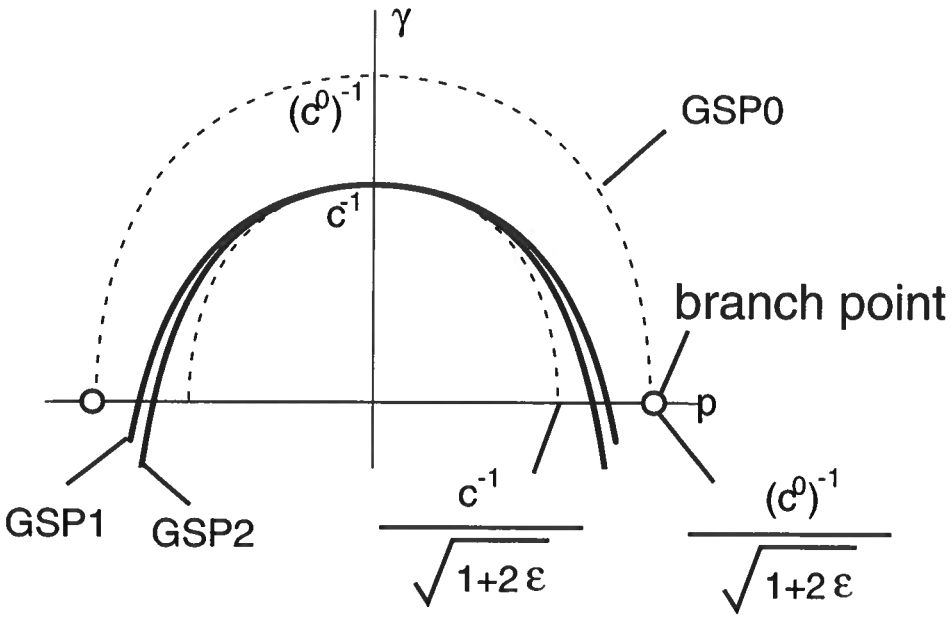

Figure 5.2. Principal parts of the generalized-screen vertical slowness, as a function of the horizontal slowness p, in the VTI case ($\varepsilon = 0.2$, $\delta = 0.0$) in a constant-wave speed perturbation medium: zero-order (GSP0), first-order (GSP1) and second-order (GSP2). The principal part of the exact vertical slowness is shown with the inner dashed curve.

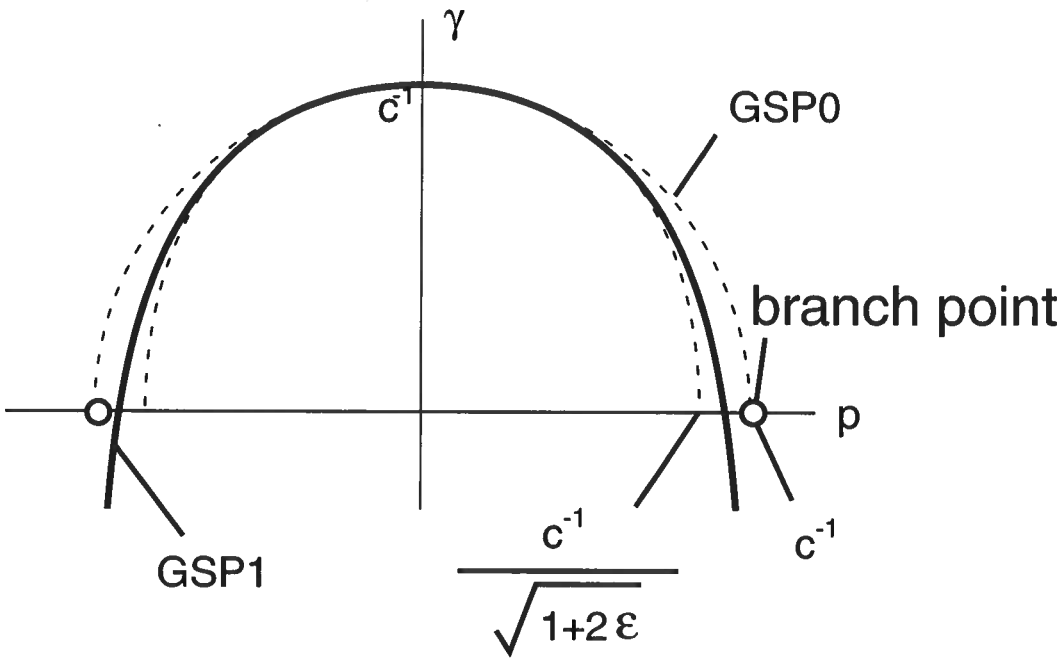

Figure 5.3. Principal parts of the generalized-screen vertical slowness, as a function of the horizontal slowness p, in the VTI case in a constant-ε perturbation medium: zero-order (GSP0) and first-order (GSP1).The principal part of the exact vertical slowness is shown with the inner dashed curve.

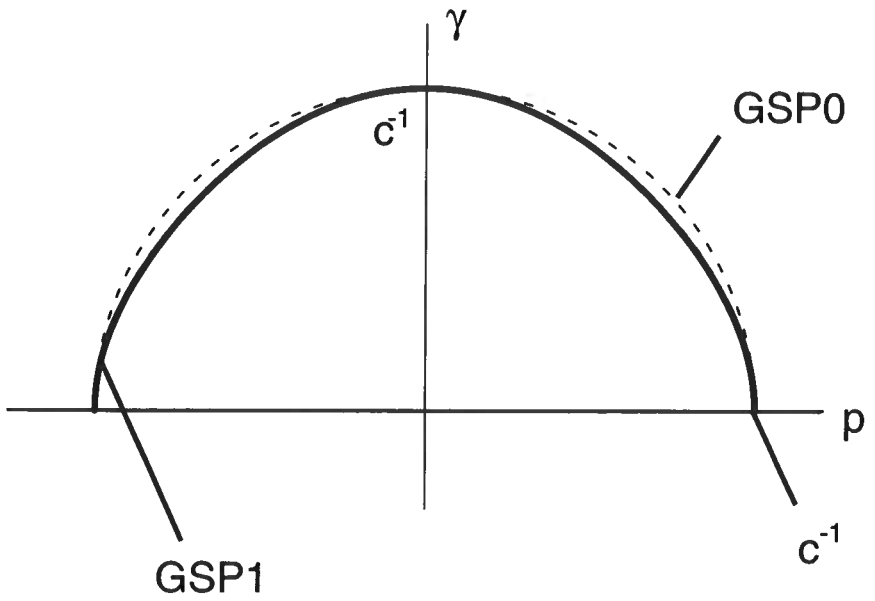

Figure 5.4. Principal parts of the generalized-screen vertical slowness, as a function of the horizontal slowness p, in the VTI case in a constant-δ perturbation medium: zero-order (GSP0) and first-order (GSP1).The principal part of the exact vertical slowness is shown with the inner dashed curve.

at vertical and grazing angles while δ influences the slowness at intermediate angles only. Also, in equation (5.13) δ appears in the denominator. This avoids the creation of a branch point when expanding in u_δ.

Unlike the generalized screens, the split-step-Fourier type approximation (Stoffa *et al.*, 1990) does not have the degrees of freedom to account for anisotropy, i.e., to shape the slowness surface appropriately where lateral heterogeneities are present. Le Rousseau and De Hoop (2001b) show that the split-step Fourier method is accurate for near-vertical propagation only. The influence of the anisotropic parameters (e.g., ε and δ) in the vertical slowness symbol occurs only at non-vertical wave propagation. As mentioned before, variations in the anisotropy parameters are of higher order than variations in the medium-vertical slowness squared, c_V^{-2}. The influence of the anisotropy parameters is comparable to the higher-order terms of the GS expansion that are absent in the split-step Fourier formulation (Le Rousseau & De Hoop, 2001b; Thomsen, 1998). In laterally varying medium, taking anisotropy into account in the framework of the split-step Fourier approximation does not enhance the accuracy of the vertical slowness principal symbol, γ_1, and, hence, of the associated propagator [cf., next section and Le Rousseau and De Hoop (2001b)].

The explicit GS expansion as shown in equations (5.25) and (5.26) reveals the introduction of reciprocal powers of γ^0 and hence contains branch points at $\alpha_\nu\alpha_\nu = -[c_V^0]^{-2}/(1+2\varepsilon^0)$. The vicinity of the branch point should be treated carefully. We refer the reader to Le Rousseau and De Hoop (2001b) for the treatment of branch points. To ensure that the

branch point is out of the propagating regime within the thin-slab, one has to choose c_V^0 smaller than the minimum medium vertical wave speed, and to choose ε^0 smaller than the minimum ε, within the slab as illustrated in Figures 5.1 through 5.3.

5.3.5 The scalar generalized-screen propagator VTI media

We have seen that the GS expansion of the slowness surface in the VTI case is quite similar to the one in the isotropic case. The GS expansion of the propagator is hence similar as well,

$$g^{(\pm)}(x_\mu, x_3; x'_\nu, x'_3) \simeq \int (s/2\pi)^2 \mathrm{d}\alpha_1 \mathrm{d}\alpha_2 \exp[-\mathrm{i}s\,\alpha_\sigma(x_\sigma - x'_\sigma)] \tag{5.28}$$
$$\cdot \exp[\mp s\,\{\gamma^0(\bar{x}_3;\alpha_\nu) + \gamma^1_{u_V}(x_\mu,\bar{x}_3;\alpha_\nu) + \gamma^1_{u_\varepsilon}(x_\mu,\bar{x}_3;\alpha_\nu) + \gamma^1_{u_\delta}(x_\mu,\bar{x}_3;\alpha_\nu)\}\,\Delta x_3]\,.$$

As in the isotropic case, we perform the expansion of the exponential in $\gamma^1_{u_V}$ about vertical propagation (Le Rousseau & De Hoop, 2001b, (24)). For the two additional terms, $\gamma^1_{u_\varepsilon}$ and $\gamma^1_{u_\delta}$, the expansion of the exponential simplifies because these terms vanish at vertical propagation. One can thus decompose the propagator as

$$g^{(\pm)} \simeq g^{0(\pm)} + g^{u_V(\pm)} + g^{u_\varepsilon(\pm)} + g^{u_\delta(\pm)}\,, \tag{5.29}$$

where cross terms have been discarded when expanding the exponential in $\gamma^1_{u_V}$. The leading term in equation (5.29) is

$$g^{0(\pm)}(x_\mu, x_3; x'_\nu, x'_3) = \exp\left[\mp s\,\left([c_V(x_\mu,\bar{x}_3)]^{-1} - [c_V^0(\bar{x}_3)]^{-1}\right)\,\Delta x_3\right] \tag{5.30}$$
$$\cdot \int (s/2\pi)^2 \mathrm{d}\alpha_1 \mathrm{d}\alpha_2 \exp[-\mathrm{i}s\,\alpha_\sigma(x_\sigma - x'_\sigma)]\,\exp[\mp s\,\gamma^0(\bar{x}_3;\alpha_\nu)\,\Delta x_3]\,,$$

with γ^0 given by equation (5.18). This term corresponds to the propagator of the split-step Fourier approach when extended to VTI media. The phase factor applied in the space domain corrects for vertical propagation only. Next order contributions, $g^{u_V(\pm)}$, $g^{u_\varepsilon(\pm)}$, and $g^{u_\delta(\pm)}$, have the same form: for $g^{u_V(\pm)}$ we have

$$g^{u_V(\pm)}(x_\mu, x_3; x'_\nu, x'_3) = \exp\left[\mp s\,\left([c_V(x_\mu,\bar{x}_3)]^{-1} - [c_V^0(\bar{x}_3)]^{-1}\right)\,\Delta x_3\right] \tag{5.31}$$
$$\cdot \int (s/2\pi)^2 \mathrm{d}\alpha_1 \mathrm{d}\alpha_2 \Delta x_3 \exp[\mathrm{i}s\,\alpha_\sigma(x_\sigma - x'_\sigma)]\,\exp[\mp s\,\gamma^0(\bar{x}_3;\alpha_\nu)\,\Delta x_3]$$
$$\cdot \mp s\Delta x_3\,\left[\gamma^1_{u_V}(x_\mu,\bar{x}_3;\alpha_\nu) - \gamma^1_{u_V}(x_\mu,\bar{x}_3;0)\right]\,,$$

which gives, upon substituting equation (5.21),

$$g^{u_V(\pm)}(x_\mu, x_3; x'_\upsilon, x'_3) = \mp s\Delta x_3 \exp\left[\mp s\ \left([c_V(x_\mu, \bar{x}_3)]^{-1} - [c_V^0(\bar{x}_3)]^{-1}\right)\ \Delta x_3\right] \quad (5.32)$$
$$\cdot \sum_{j=1}^{n_{u_V}} \Bigg\{ [u(x_\mu, \bar{x}_3)]^j \int (s/2\pi)^2 \mathrm{d}\alpha_1 \mathrm{d}\alpha_2 \Delta x_3 \exp[-\mathrm{i}s\,\alpha_\sigma(x_\sigma - x'_\sigma)]$$
$$\cdot \exp[\mp s\,\gamma^0(\bar{x}_3; \alpha_\nu)\,\Delta x_3]\ [\psi_{V,j}(\bar{x}_3; \alpha_\nu) - \psi_{V,j}(\bar{x}_3; 0)] \Bigg\} .$$

For the term $g^{u_\varepsilon(\pm)}$, the expression $[\gamma^1_{u_V}(x_\mu, \bar{x}_3; \alpha_\nu) - \gamma^1_{u_V}(x_\mu, \bar{x}_3; 0)]$ inside the Fourier integral should be replaced by $\gamma^1_{u_\varepsilon}(x_\mu, \bar{x}_3; \alpha_\nu)$; we find

$$g^{u_\varepsilon(\pm)}(x_\mu, x_3; x'_\upsilon, x'_3) = \exp\left[\mp s\ \left([c_V(x_\mu, \bar{x}_3)]^{-1} - [c_V^0(\bar{x}_3)]^{-1}\right)\ \Delta x_3\right] \quad (5.33)$$
$$\cdot \int (s/2\pi)^2 \mathrm{d}\alpha_1 \mathrm{d}\alpha_2 \Delta x_3 \exp[\mathrm{i}s\,\alpha_\sigma(x_\sigma - x'_\sigma)]\ \exp[- \mp s\,\gamma^0(\bar{x}_3; \alpha_\nu)\,\Delta x_3]$$
$$\cdot \mp s\Delta x_3\ \gamma^1_{u_\varepsilon}(x_\mu, \bar{x}_3; \alpha_\nu) ,$$

which gives, upon substituting equation (5.22),

$$g^{u_\varepsilon(\pm)}(x_\mu, x_3; x'_\upsilon, x'_3) = \mp s\Delta x_3 \exp\left[\mp s\ \left([c_V(x_\mu, \bar{x}_3)]^{-1} - [c_V^0(\bar{x}_3)]^{-1}\right)\ \Delta x_3\right] \quad (5.34)$$
$$\cdot \sum_{j=1}^{n_{u_\varepsilon}} \Bigg\{ [u_\varepsilon(x_\mu, \bar{x}_3)]^j \int (s/2\pi)^2 \mathrm{d}\alpha_1 \mathrm{d}\alpha_2 \Delta x_3 \exp[-\mathrm{i}s\,\alpha_\sigma(x_\sigma - x'_\sigma)]$$
$$\cdot \exp[\mp s\,\gamma^0(\bar{x}_3; \alpha_\nu)\,\Delta x_3]\ \psi_{\varepsilon,j}(\bar{x}_3; \alpha_\nu) \Bigg\} .$$

For the term $g^{u_\delta(\pm)}$, the expression $[\gamma^1_{u_V}(x_\mu, \bar{x}_3; \alpha_\nu) - \gamma^1_{u_V}(x_\mu, \bar{x}_3; 0)]$ inside the Fourier integral should be replaced by $\gamma^1_{u_\delta}(x_\mu, \bar{x}_3; \alpha_\nu)$. In each constituent propagator, $g^{u_V(\pm)}$, $g^{u_\varepsilon(\pm)}$, and $g^{u_\delta(\pm)}$, the spatial dependency of the propagator can be taken out of the integral, since it has been separated from the wavenumber dependency via the GS expansion. The GS algorithm in the VTI case therefore has the same structure as in the isotropic case (Le Rousseau & De Hoop, 2001b). The additional computational complexity as compared with the isotropic GS algorithm is of the order of two additional inverse Fourier transforms for the first-order terms in u_ε and u_δ.

Figures 5.5 and 5.6 show the (instantaneous) wavefronts associated to the slowness surfaces shown in Figures 5.1 and 5.2 respectively. Figures 5.7 and 5.8 are associated with Figures 5.3 and 5.4. Figures 5.5 through 5.8 also show the numerical response of the GS propagator in VTI media subject to the same constant perturbation as in Figures 5.1 through 5.4.

As the *computational complexity* of a Fourier transform is $N_1 N_2 \log_2(N_1 N_2)$ (N_μ denoting the numbers of samples in the x_μ-direction), the complexity of our n^{th}-order GS algorithm is proportional to $(2+n)N_1 N_2 \log_2(N_1 N_2)$, where n is the cumulative order of

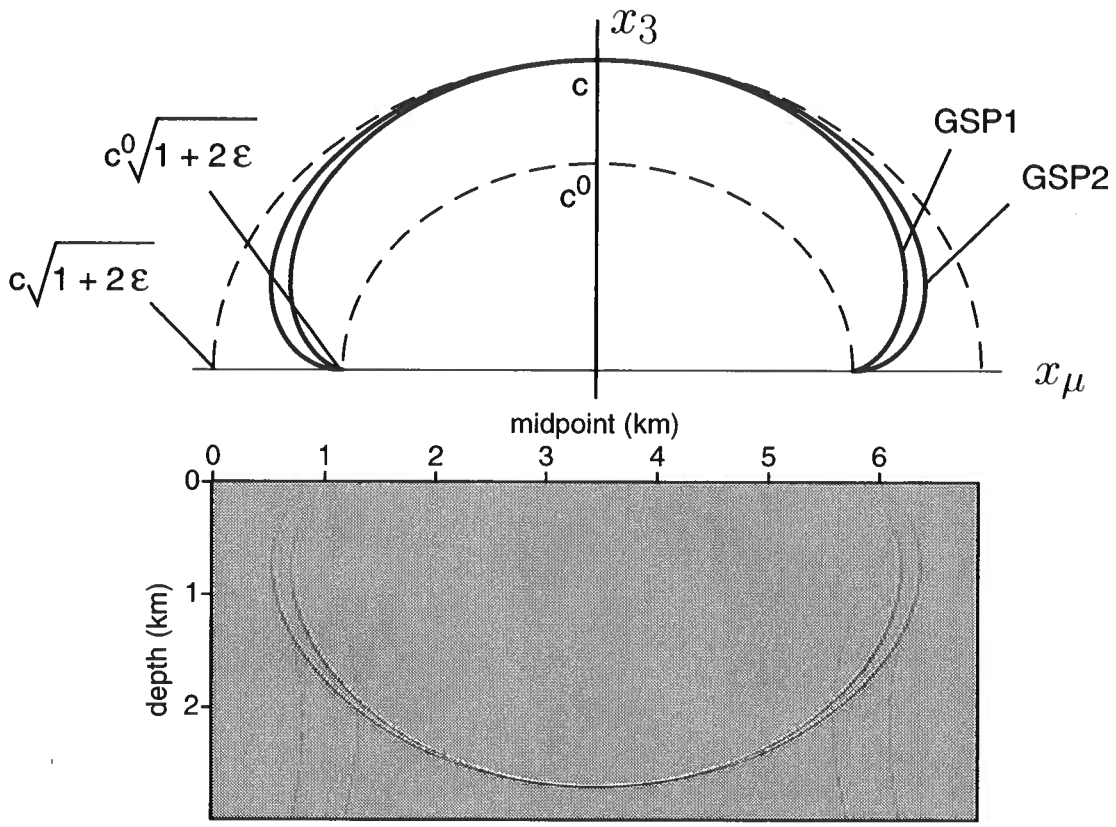

Figure 5.5. Wavefronts in a constant-wave speed perturbation VTI medium ($\varepsilon = 0.3$, $\delta = 0.3$) associated with the various generalized-screen approximations: second-order (GSP2), first-order (GSP1); top: as calculated as polar reciprocal of the slowness surface; bottom: numerical wavefront. The artifacts at the bottom correspond to wrap-around in time and boundary conditions on the sides of the model.

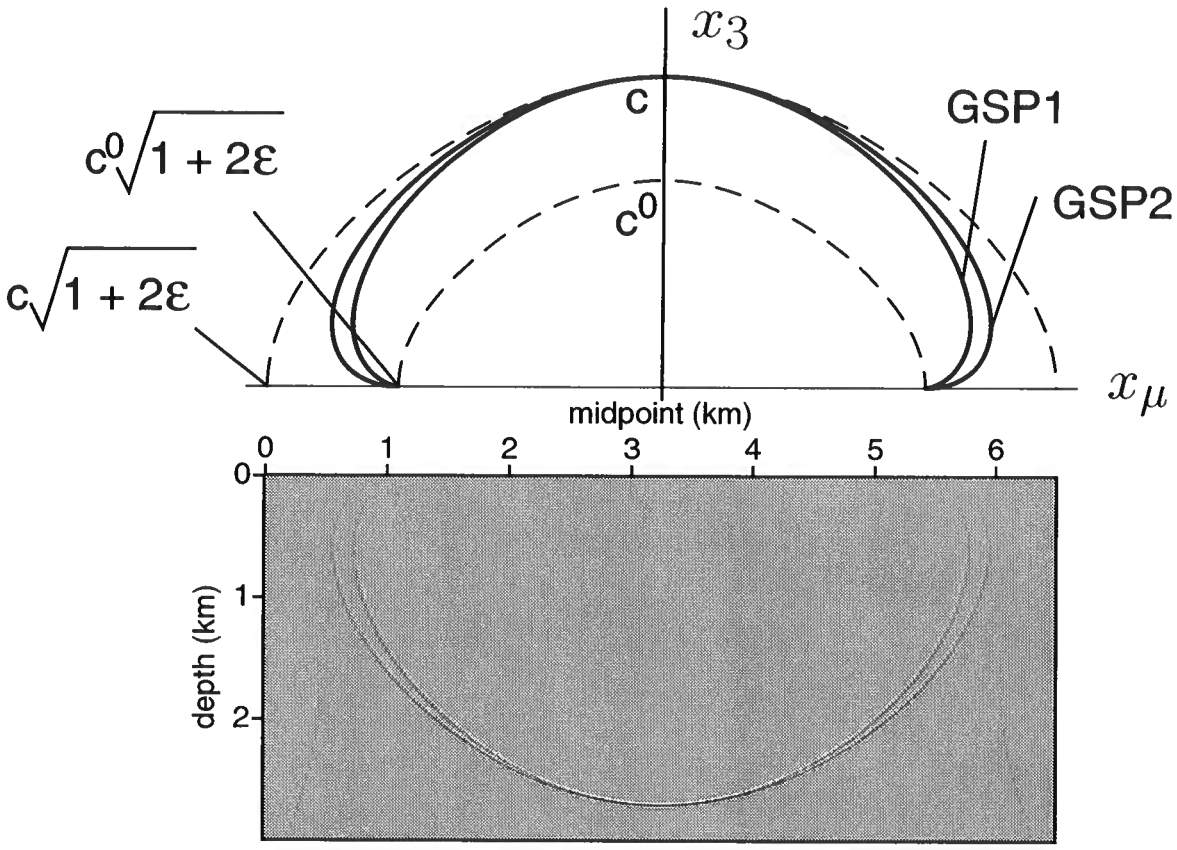

Figure 5.6. Wavefronts in a constant-wave speed perturbation VTI medium ($\varepsilon = 0.2\,, \delta = 0.0$) associated with the various generalized-screen approximations: second-order (GSP2), first-order (GSP1); top: as calculated as polar reciprocal of the slowness surface; bottom: numerical wavefront. The artifacts at the bottom correspond to wrap-around in time and boundary conditions on the sides of the model.

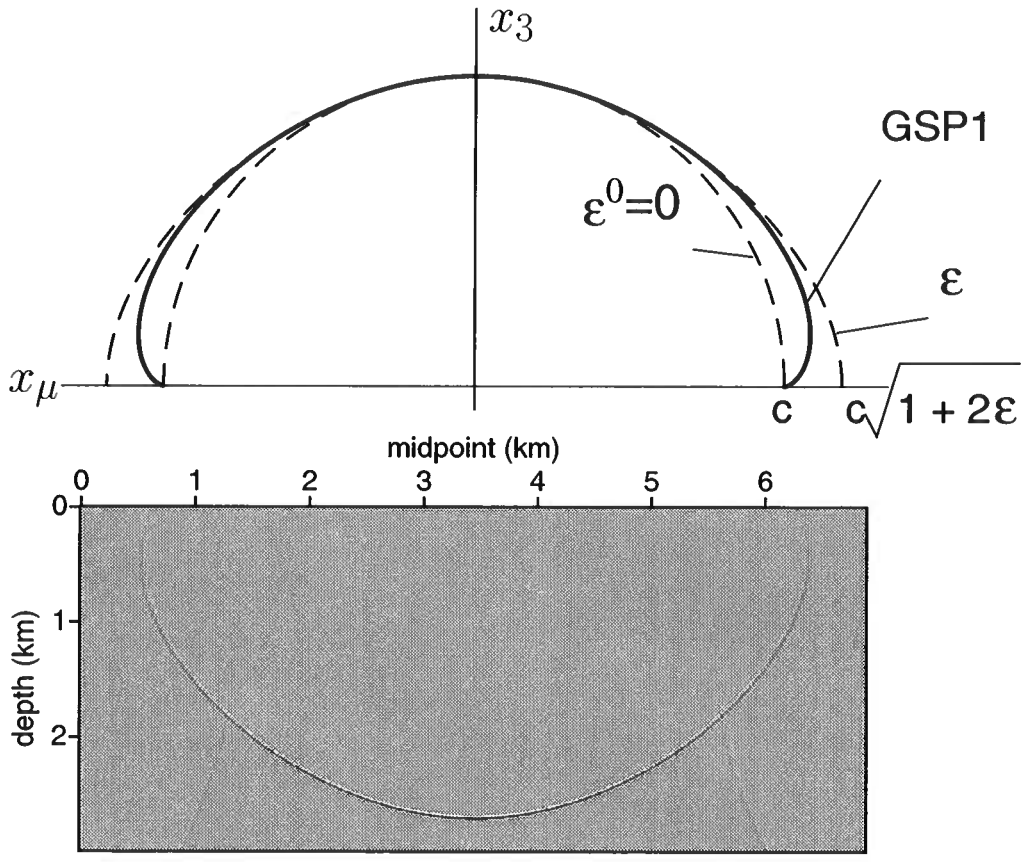

Figure 5.7. Wavefronts in a constant-ε perturbation VTI medium associated with the first-order(GSP1) approximation; top: as calculated as polar reciprocal of the slowness surface; bottom: numerical wavefront. The artifacts at the bottom correspond to wrap-around in time and boundary conditions on the sides of the model.

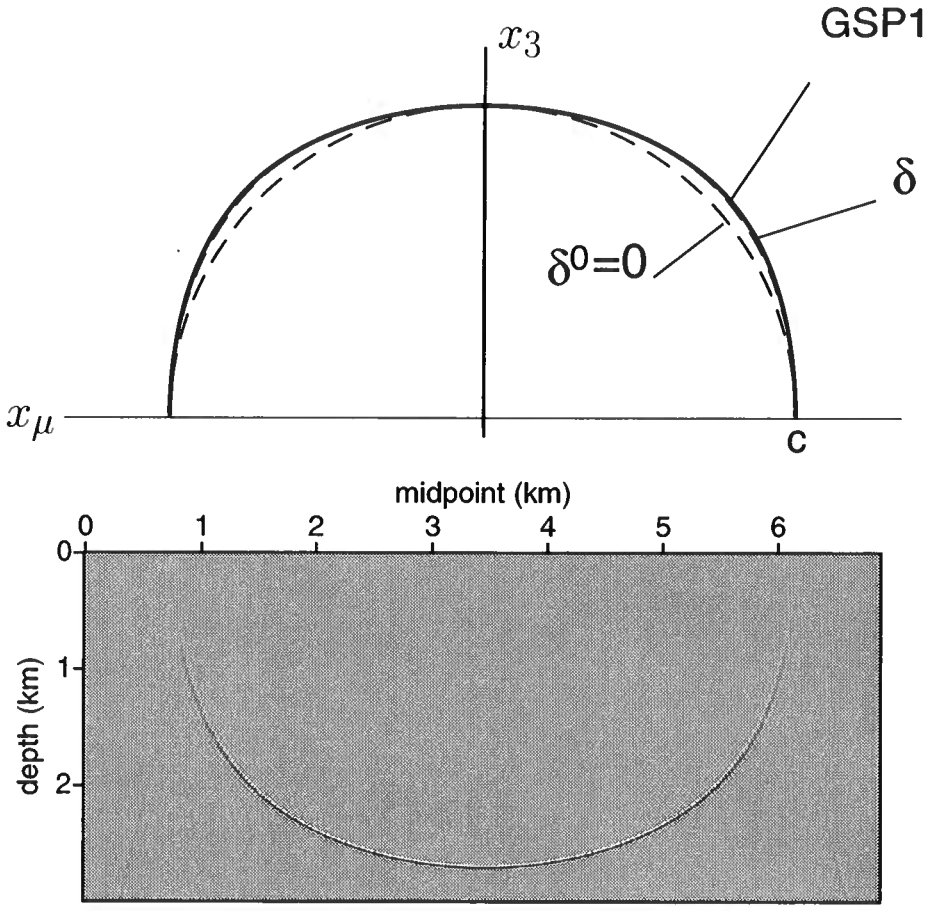

Figure 5.8. Wavefronts in a constant-δ perturbation VTI medium associated with the first-order(GSP1) approximation; top: as calculated as polar reciprocal of the slowness surface; bottom: numerical wavefront. The artifacts at the bottom correspond to wrap-around in time and boundary conditions on the sides of the model.

the GS expansion in the three perturbation terms (u_V, u_ε, and u_δ), i.e., $n = n_{u_V} + n_{u_\varepsilon} + n_{u_\delta}$. Again, in most practical cases, taking $n_{u_\varepsilon} = n_{u_\delta} = 1$ provides sufficient accuracy; then the computational complexity of the GS method is $(4 + n_{u_V}) N_1 N_2 \log_2(N_1 N_2)$.

5.4 The scalar generalized-screen algorithm

Here, we discuss the GS algorithm based upon equations (5.30) through (5.34). We denote the (one-way) wavefield by W, and carry out the wave propagation in the frequency domain, with each frequency component computed independently. The downward continuation for modeling and imaging with the one-way propagator is performed according to the decomposition of the vertical slowness symbol into one background term and a series of perturbation terms as in equations (5.21) through (5.23).

Let the current depth be set to $x_3' = z$, and set $\bar{x}_3 = x_3' + \frac{1}{2}\Delta x_3$ as before. Following equations (5.32) and (5.34), we introduce the intermediate field quantities $w_0, w_1, \cdots, w_n$ (to simplify the notation n_{u_V} is replaced by n in this section only), w_ε, and w_δ according to (*step 1*)

$$w_0(x_\mu, s) = \exp\left[-s\,\Delta x_3\,\left([c_V(x_\mu, \bar{x}_3)]^{-1} - [c_V^0(\bar{x}_3)]^{-1}\right)\right]\, W(x_\mu, x_3', s)\,, \tag{5.35}$$

$$w_1(x_\mu, s) = -s\,\Delta x_3\, u_V(x_\mu, \bar{x}_3)\, w_0(x_\mu, s)\,, \tag{5.36}$$

$$w_2(x_\mu, s) = -s\,\Delta x_3\, u_V^2(x_\mu, \bar{x}_3)\, w_0(x_\mu, s)\,, \tag{5.37}$$

$$\vdots$$

$$w_n(x_\mu, s) = -s\,\Delta x_3\, u_V^n(x_\mu, \bar{x}_3)\, w_0(x_\mu, s)\,, \tag{5.38}$$

$$w_\varepsilon(x_\mu, s) = -s\,\Delta x_3\, u_\varepsilon(x_\mu, \bar{x}_3)\, w_0(x_\mu, s)\,, \tag{5.39}$$

$$w_\delta(x_\mu, s) = -s\,\Delta x_3\, u_\delta(x_\mu, \bar{x}_3)\, w_0(x_\mu, s)\,, \tag{5.40}$$

motivated by the expansions in u_V, u_ε, and u_δ.

The higher-order terms in u_V, u_ε, and u_δ increase the accuracy for wider propagation angles. Again, for practical purposes, we limit ourselves to the first-order expansion of the principal slowness symbols in Thomsen parameter perturbations , u_ε and u_δ. The intermediate field quantities are then Fourier transformed to the horizontal-wavenumber domain (*step 2*),

$$\tilde{w}_j(\alpha_\nu, s) = \tilde{w}_j(k_\nu/s, s) = \int w_j(x_\mu, s)\, \exp\left[-\mathrm{i} x_\sigma k_\sigma\right] dx_\mu \tag{5.41}$$

$$= \int w_j(x_\mu, s)\, \exp\left[\mathrm{i} s x_\sigma \alpha_\sigma\right] dx_\mu\,, \qquad j = 0, 1, \cdots, n, \varepsilon, \delta\,.$$

The wavefield at depth $x_3 = z + \Delta x_3$ then follows as [cf., equations (5.32) and (5.34)]

$$\begin{aligned}\tilde{W}(x_3;\alpha_\nu,s) &= \tilde{w}_0(\alpha_\nu,s)\ \exp[-s\Delta x_3\gamma^0(\bar{x}_3;\alpha_\nu)]\\ &\cdot\mathcal{N}\left[1+\frac{\tilde{w}_1(\alpha_\nu,s)}{\tilde{w}_0(\alpha_\nu,s)}\ [\psi_{V,1}(\alpha_\nu,s)-\psi_{V,1}(0,s)]\right.\\ &\quad+\cdots+\frac{\tilde{w}_n(\alpha_\nu,s)}{\tilde{w}_0(\alpha_\nu,s)}\ [\psi_{V,n}(\alpha_\nu,s)-\psi_{V,n}(0,s)]\\ &\quad\left.+\frac{\tilde{w}_\varepsilon(\alpha_\nu,s)}{\tilde{w}_0(\alpha_\nu,s)}\ \psi_{\varepsilon,1}(\alpha_\nu,s)+\frac{\tilde{w}_\delta(\alpha_\nu,s)}{\tilde{w}_0(\alpha_\nu,s)}\ \psi_{\delta,1}(\alpha_\nu,s)\right]\ ,\end{aligned}$$

(*step 3*), the divisions being carried out in some stable sense, and the normalization operator, $\mathcal{N}$, being given by

$$\mathcal{N}[1+p+\mathrm{i}q]=\exp(\mathrm{i}q)\ \left|1+\frac{p}{1+\mathrm{i}q}\right|^{-1}\left[1+\frac{p}{1+\mathrm{i}q}\right]\ .$$

The Taylor expansion of the exponential in equation (5.28) destroys the unitarity of the thin-slab propagator, hence the introduction of the normalization operator (De Hoop *et al.*, 2000). Finally, we carry out the inverse Fourier transform $\tilde{W}(x_3;\alpha_\nu,s)\rightarrow W(x_\mu,x_3;s)$ (*step 4*).

5.5 Accuracy analysis

We illustrate the accuracy of the GS algorithm with the BP Amoco VTI Valhall model. We base our analysis on numerical modeling. We generate Green's functions and focus our observations on second-arrival energy and multi-pathing. Imaging invokes an averaging (stacking) process; to learn about the prestack migration operator, we hence prefer to analyze modeling instead. Depth-migration results for the isotropic case are, however, presented in Le Rousseau and De Hoop (2001b) (Chapter 4).

The wave speed model (vertical wave speed for *qP* waves) of the VTI Valhall model is illustrated in Figure 5.9. This model, created by BP Amoco (Brandsberg-Dahl *et al.*, 1999), is based on real data studies of the Valhall field in the North Sea. Profiles for Thomsen's parameters ε and δ are shown in Figures 5.10(a) and 5.10(b), respectively. Note that the model contains fine detail of the vertical wave speed. Because of the presence of gas in the overburden of the reservoir, attenuation and multi-pathing occur which yields poor imaging of the *qP* waves for conventional asymptotic methods (first arrivals or maximum energy arrivals). 'Gas clouds' act as a dissipative and low wave-speed zone for the *qP* waves. Alternative methods, such as imaging using converted waves, have been applied to obtain better imaging (Thomsen *et al.*, 1997). The *qS* waves are indeed not affected by the presence of gas.

We place a point source beneath the reservoir (at depth 3900 m). The source location is represented by an asterisk in Figure 5.9. The source is excited at time t = 0. The propagating 'pressure' field is imaged at time t = 1.6 s. We compare results generated with

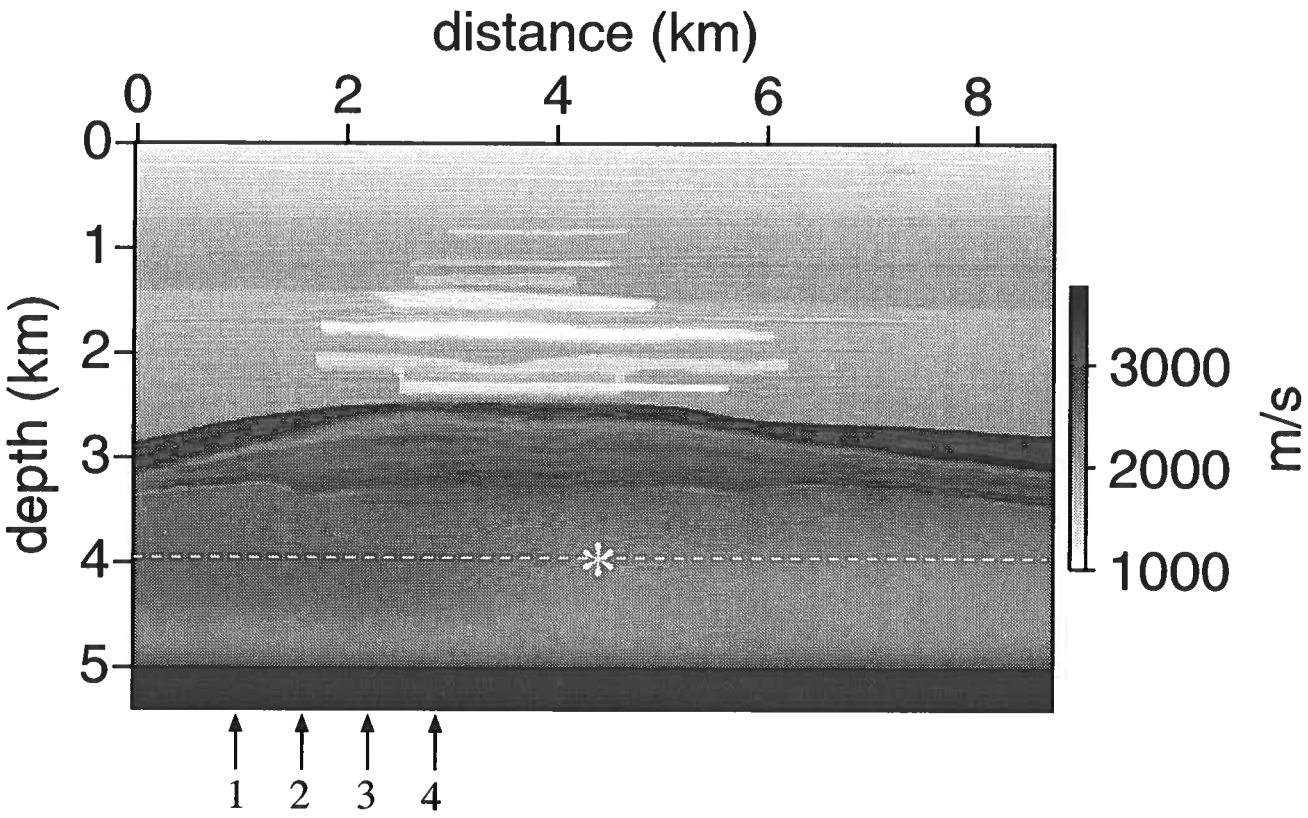

Figure 5.9. Vertical wavespeed of the VTI model of the Valhall field. The asterisk locates the position of the source (at depth 3900 m); the dashed line indicates the region detailed in Figure 5.11(a) and Figure 5.11(b). The vertical arrows labeled 1 to 4 show the location of the traces shown in Figure 5.12.

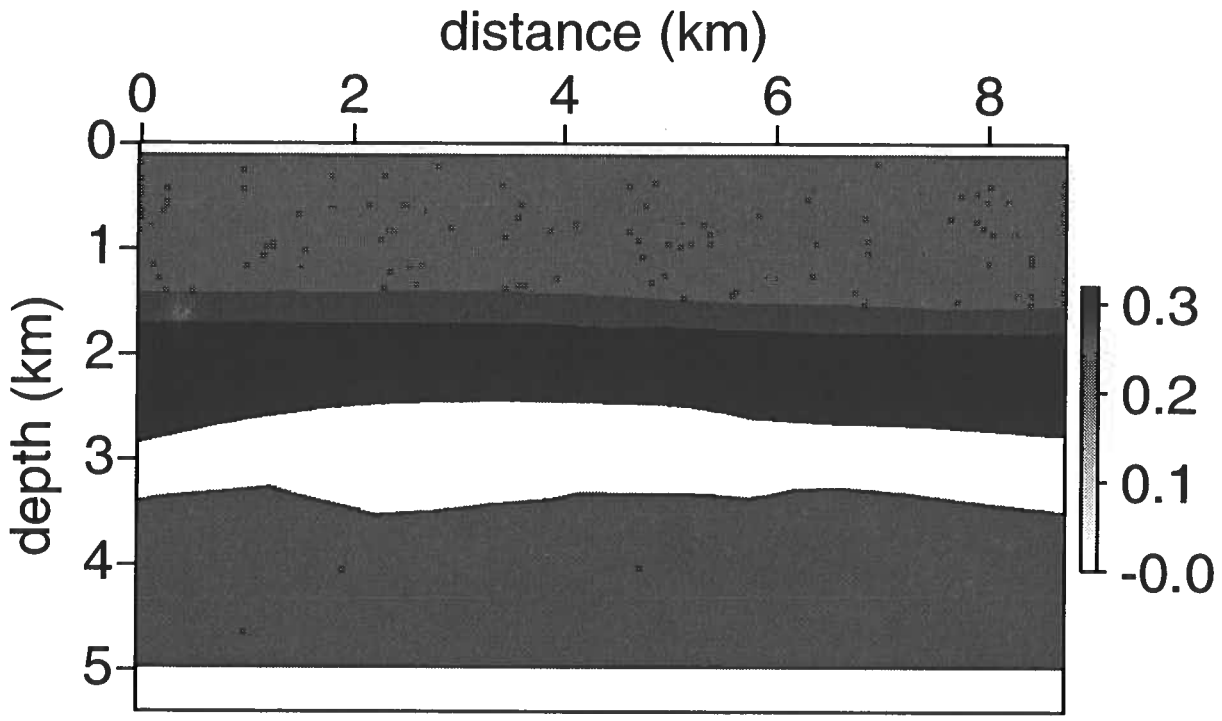

(a)

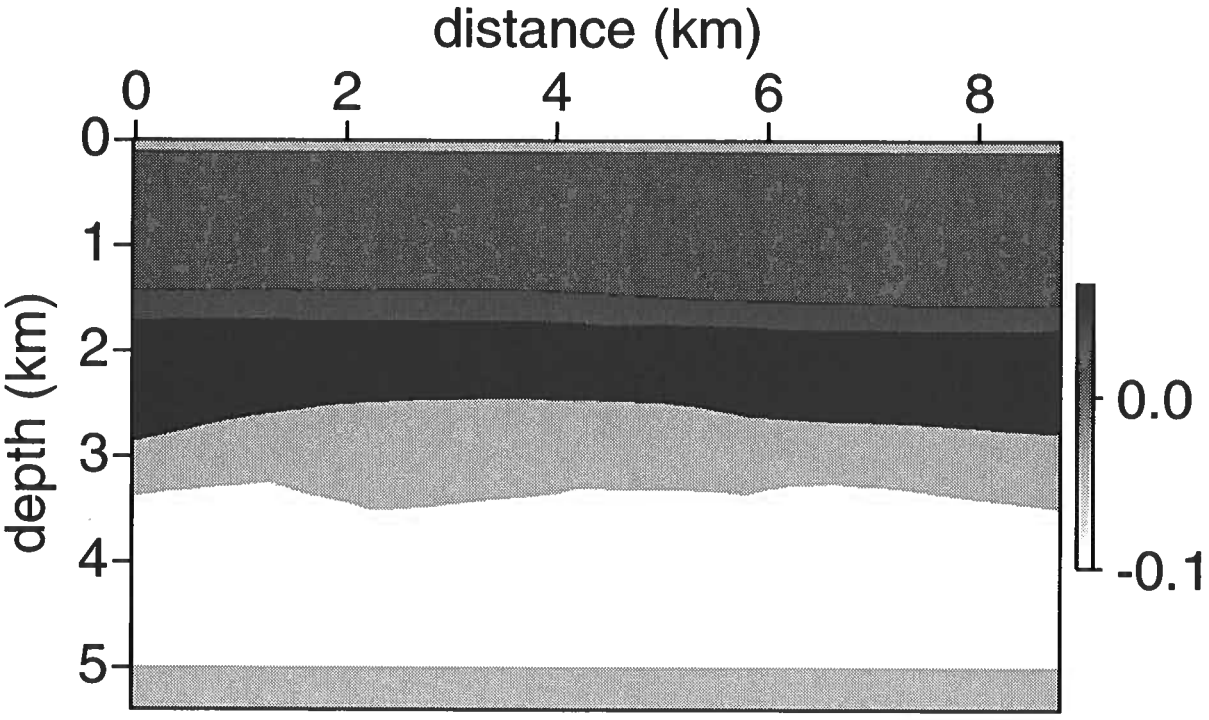

(b)

Figure 5.10. VTI model of the Valhall field for (a) ε and (b) δ.

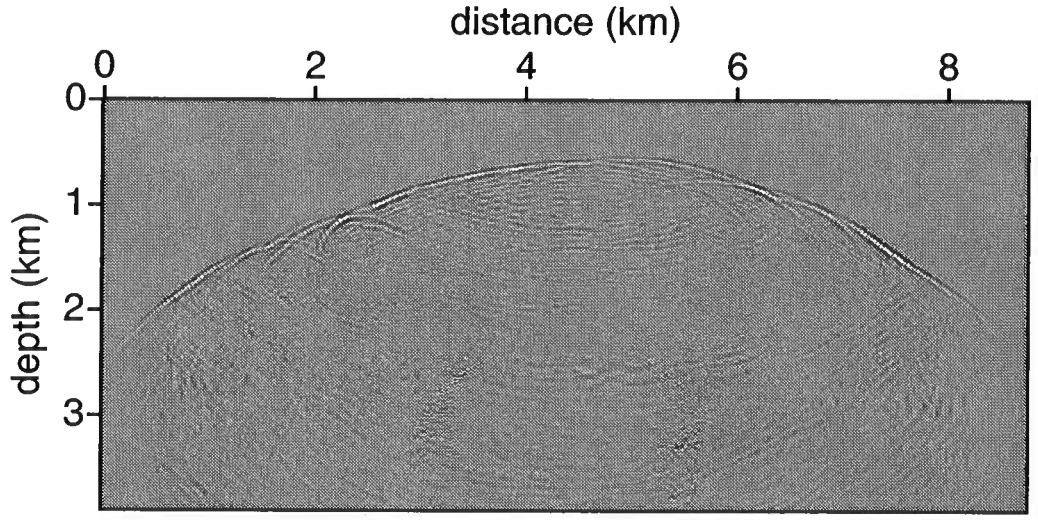

(a)

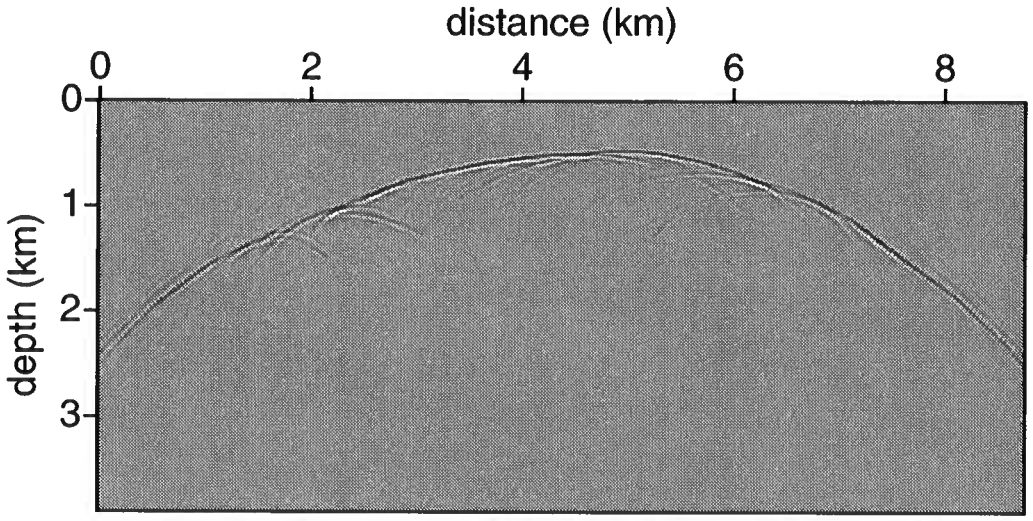

(b)

Figure 5.11. Snapshots in the Valhall model at time $t = 1.6$ s of the pressure field (a) with the full elastic wave equation and (b) with the second order of the generalized-screen method. A weak precursor associated with the compromise in contour deformation is visible (see Chapter 4).

the full elastic wave equation (finite-difference time-domain, fourth order in space, second order in time) modeling (Figure 5.11(a)) with the GS (second order in the perturbation in the medium-vertical slowness squared and first order in the perturbation in ε and δ) method (Figure 5.11(b)). We use the wavefield modeled by the full elastic wave equation as a reference. The ε section exhibits not so 'weak' anisotropy in parts of the model: ε reaches values as high as 0.3. Yet, the dispersion relation (5.11) used in VTI media for the GS method is accurate, since it requires 'mild' (Schoenberg & De Hoop, 2000) and not 'weak' anisotropy (Thomsen, 1986).

The wavefront in the finite-difference section shows significant multi-pathing at various locations, due to lateral variations in the medium properties, especially due to the 'gas cloud', i.e., 'gas lenses'. Also, one can notice significant multiple scattering due to the fine layering of the model. Comparison with Figure 5.11(b) shows the capability of the GS method to accurately model wave propagation in a complex medium. The wavefront of the GS method closely resembles the reference one. In Figure 5.12, we show comparisons of traces extracted from the snapshots shown in Figures 5.11(a) and 5.11(b) at the four locations indicated in Figure 5.9. Note that the accuracy of the GS propagator follows according to the behavior observed in Figures 5.1 to 5.8: the wavefront bends inwards for large angles of propagation associated with significant medium variations in the overburden. Introducing additional terms in the GS expansion in the perturbation in the medium-vertical slowness squared, u_V, yields increased accuracy as illustrated in Le Rousseau and De Hoop (2001b) with the Marmousi model. The traces in Figure 5.12 reveal the occurrence of internal multiple scattering that is accounted for in the finite-difference method but not in the GS approach. The computation of the multiple scattering can be addressed by the introduction of higher order terms in the Bremmer series, the one-way propagator representing the leading order term (De Hoop, 1996; De Hoop *et al.*, 2000; Le Rousseau & De Hoop, 2001b).

In Figures 5.11(a) and 5.11(b), and also in Figure 5.12, note that second-arrival energy is accurately positioned. The better positioning and modeling of the later-arrival energy constitutes a key contribution to the imaging of complex structures, where these arrivals carry a significant part of the energy. The poor imaging obtained with single-path methods using *PP* events [as illustrated in Thomsen *et al.* (1997)] originates from the multi-pathing induced by the 'gas cloud' which we show here. Approaches taking such multi-pathing into account lead to an accurate imaging of the reservoir with *PP* events only (Brandsberg-Dahl *et al.*, 2000). We do not address the question of attenuation due to the gas cloud here, though attenuation can be accounted for in the GS approach (Le Rousseau *et al.*, 2000).

The efficiencies of the finite-difference and the GS algorithms for the computation of the previous snapshots compare as follow. The computational complexity of the time domain finite-difference approach is given by $MN_1N_2N_3N_t$ where M is the size of the finite-difference stencil (M is about 25 in our case) and N_μ ($\mu = 1, 2$), N_3, and N_t are the number of samples in the horizontal, vertical, and time directions. The associated computational complexity of the GS is given by $N_\omega N_3(4 + n_{u_V})N_1N_2 \log_2(N_1N_2)$ where N_ω is the number of frequencies used in the computation. The major difference in computational complexities can be attributed to the difference between N_t and N_ω. Typically, N_t is 10 to 100 times

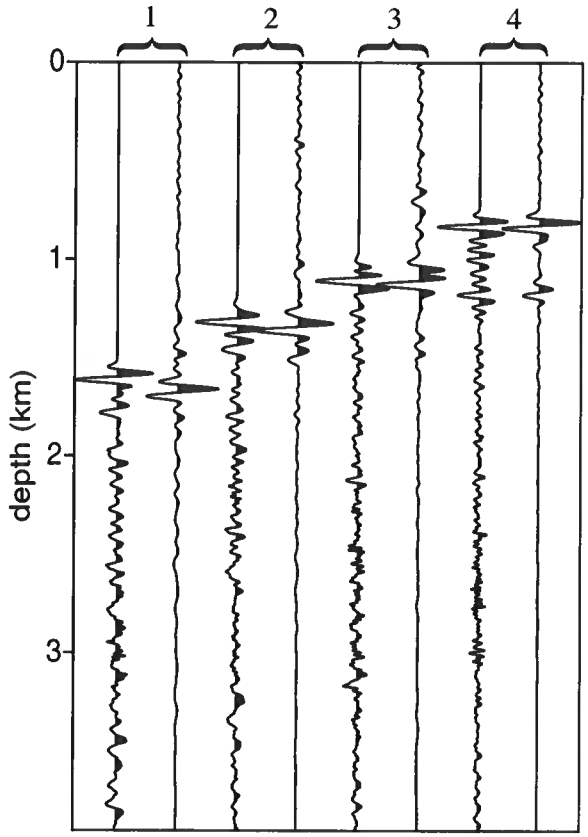

Figure 5.12. Traces extracted from the two snapshots in Figure 5.11, which spatial locations are shown in Figure 5.9. For each pair of traces, the trace on the left corresponds to the full elastic wave equation computation, the trace on the right to the the second order of the generalized-screen method computation. Weak precursors associated with the compromise in contour deformation are visible (see Chapter 4).

larger than N_ω.

5.6 Discussion

The generalized-screen (GS) method is based on the decomposition of the medium into a background component and a perturbation. The GS method can accommodate more significant and rapid horizontal wave speed variations. Its enhanced accuracy (as compared to the phase-screen and split-step method) allows accurate modeling of the wavefields in complex structures where multi-pathing is significant. Unlike the phase-screen and split-step methods, the GS method extends to laterally heterogeneous media with low symmetry, such as transversely isotropic media with a vertical axis of symmetry (VTI). The medium is then characterized by additional parameters (e.g., Thomsen's parameters ε and δ (Thomsen, 1986)), for which background and perturbation terms are defined. Expansion with respect to the anisotropy parameter perturbation terms are truncated to their lowest order term for this accuracy is sufficient in most practical applications.

With the GS representation of the propagator, $g^{(\pm)}$, is associated a 'generalized' vertical slowness, $\gamma^0 + \gamma^1_{u_V} + \gamma^1_{u_\varepsilon} + \gamma^1_{u_\delta}$, in which the dependencies on the horizontal spatial coordinates and the dependencies on the horizontal wavenumber coordinates are factorized. This induces the structure of the GS propagator. The GS expansion provides a fundamental simplification of the one-way propagator. We obtain an algorithm that is based on a shuttling between the frequency-horizontal space domain and the frequency-horizontal wavenumber domain. Each additional term in the GS expansion increases its accuracy – an additional Fourier transform is required for each additional order in the expansion (in the perturbation in the medium-vertical slowness squared and the anisotropic parameters). The extension of the GS algorithm to orthorhombic media can be accomplished in a similar fashion.

We have illustrated the GS propagator's accuracy primarily through modeling. The mathematical accuracy analysis of the GS approximation was carried out by De Hoop *et al.* (2000). Here we focus on its numerical counterpart. We chose the BP Amoco VTI Valhall model as a synthetic model representative of a geologic situation. We focused on the computation of Green's functions rather than on imaging because, doing so, we do not hide any details in a prestack migration operator; imaging involves an averaging of these details. The extension of the GS method from isotropic to VTI yields an accuracy comparable with its isotropic counterpart. The wavefront modeled with the GS method approaches closely the true one even for second-arrival energy due to multi-pathing in complex structures.

The GS method, with its $(4 + n_{u_V})N_1N_2\log_2(N_1N_2)$ (n_{u_V} is the order of the GS approximation in the medium-vertical-slowness-squared perturbation, u_V, and N_μ are the numbers of samples in the horizontal directions) computational complexity, makes feasible 'wave equation' modeling and imaging in 3D VTI media.

Chapter 6

3D depth imaging: A case study

6.1 Summary

We illustrate the performance of the generalized-screen propagator on real data for 3D zero-offset and pre-stack depth imaging. We use TotalFinaElf's L7D data set from the North Sea. The data acquired is that of a 3D marine survey thus containing limited azimuthal coverage. The subsurface shows significant tectonic deformation including the intrusion of a salt body in sedimentary sequences. A common-azimuth transformation is applied prior to the 3D pre-stack depth imaging procedure. We compare the performance of the generalized screen propagator with that of a hybrid PSPI/split-step Fourier method. 3D pre-stack results confirm the more accurate handling of multipathing by the generalized-screen method. Comparison are also given with Kirchhoff migration results. The results differ mainly in the texture of the image and not in the wave front set of the image. Using synthetic models of similar structure (the SEG/EAGE salt model) we further illustrate the importance of multipathing as well as that of multiple scattering.

6.2 Introduction

The generalized-screen (GS) method (De Hoop *et al.*, 2000; Le Rousseau & De Hoop, 2001b) (Chapter 3, 4, and 5) has been developed for the reduction of the computational complexity of the Trotter product representation of the depth imaging operator (De Hoop *et al.*, 2001a) (Chapter 2). This imaging operator solves the so-called double-square-root equation (Claerbout, 1986; Popovici, 1996). Such a reduction is accomplished with a finite number of terms in the GS expansion at the cost of approximating the wave front set of the propagator as part of the imaging operator. In Le Rousseau and De Hoop (2001b) (Chapter 4), an extensive accuracy analysis of the propagator was conducted concluding that with the hierarchy of approximations at hand multipathing and wide-angle propagation could be accurately predicted by the GS propagators. Here we apply the GS approach to a real data example.

We use TotalFinaElf's L7D data set and velocity model. The main feature of this 3D marine data set from the North Sea is the presence of an intrusive salt body in a surrounding sedimentary sequence. Subsequent tectonic deformation created faults at various depths that we hope to identify in the imaging process. The salt body yields large lateral wave-speed variations, which makes the imaging procedure challenging for Fourier-transform based wave-extrapolation methods (Stolt, 1978; Gazdag & Sguazzero, 1984; Stoffa *et al.*,

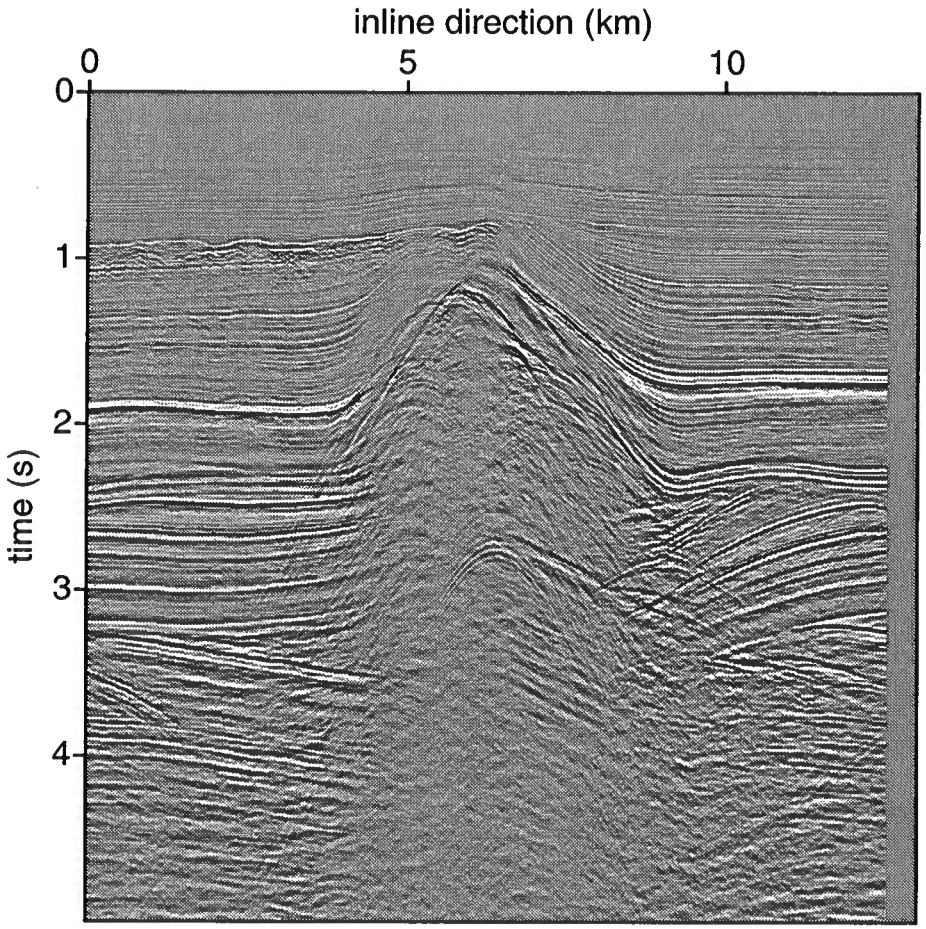

Figure 6.1. 2D section in the inline direction extracted from a 3D stack of TotalFinaElf's L7D data set.

1990). Such a data set then seems adequate for the testing of the GS propagator for depth imaging.

We first illustrate the zero-offset migration performance upon applying a transformation to zero offset to the data (reducing the acquisition variables by 2). Zero-offset migration, based upon the exploding reflector model, however, fails to show whether multipathing is properly accounted for. The isochrones (and canonical relation) of the pre-stack (multiple offset) imaging operator can be much more complex than the ones of the zero-offset imaging operator because the pre-stack migration allows for paths to differ in the up and down propagations between the source, the scattering point and the receiver. We illustrate this aspect further by showing isochrones in a 2D section of the the SEG/EAGE salt model. Not taking multipathing into account in such complex regions leads to partial imaging only, and the generation of artifacts.

For 3D pre-stack depth imaging, in view of the marine acquisition, we transform the data to common azimuth (reducing the acquisition variables by 1). To reduce the computational complexity we then apply a global common-azimuth approximation [see Biondi and Palacharla (1996) and Appendix D]. Such an approximation assumes a single azimuth for downward continued data at all depths. We compare the accuracy of the GS propagator and a hybrid PSPI/split-step Fourier propagator [for details on the PSPI propagator see Gazdag and Sguazzero (1984); for details on the split-step Fourier propagator see Stoffa *et al.* (1990) and Chapter 4] with the same common-azimuth approximation. While the two methods yield similar performance for the zero-offset migration of the L7D data set, the pre-stack results are in favor of the GS method. A precise comparison of computational complexities of the different methods can be found in Le Rousseau and De Hoop (Le Rousseau & De Hoop, 2001b) (Chapter 4): The GS method compares favorably. The results confirm that pre-stack imaging in complex regions relies on multipathing and that the GS approximations predict such multipathing accurately. To illustrate that wave-equation imaging is microlocally equivalent to Kirchhoff/GRT imaging-inversion (De Hoop *et al.*, 2001a) (Chapter 2) we compare our GS results with those with a Kirchhoff approach.

Though multipathing is the common theme in this chapter we illustrate the effect of internal multiple scattering on the imaging also. To control the generation of internal multiples in a synthetic example (2D section of the SEG/EAGE salt model) we use the GS method combined with the generalized Bremmer series approach (Le Rousseau & De Hoop, 2001b) to model the data and the hybrid PSPI/split-step Fourier approach to image the data. The artifacts are interpreted.

6.3 The L7D data set

TotalFinaElf's L7D 3D marine data set was acquired in the North Sea. The subsurface contains a salt dome structure which implies strong lateral wave-speed variations. Such a geology and the subsequent complexities are typical for data sets from the North Sea. Strong lateral variations result in transverse left-right scattering of waves and is at the origin of significant multipathing and illuminations problems. This makes this model and data a challenge for imaging methods.

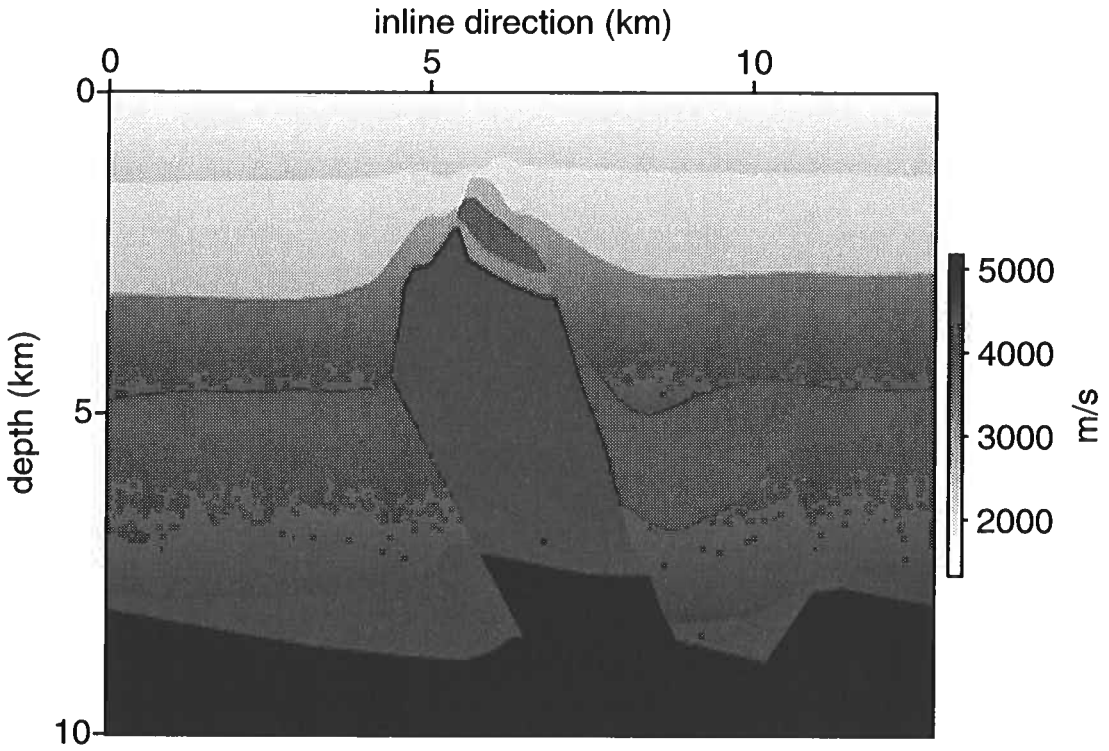

Figure 6.2. Synthetic 2D wave-speed model for the L7D field.

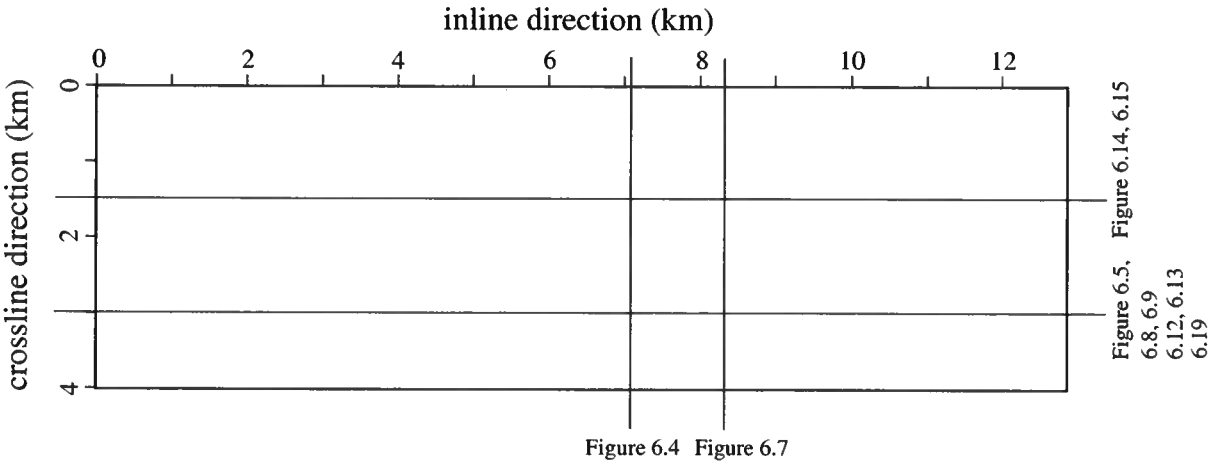

Figure 6.3. Locations of the (vertical) sections of the L7D images.

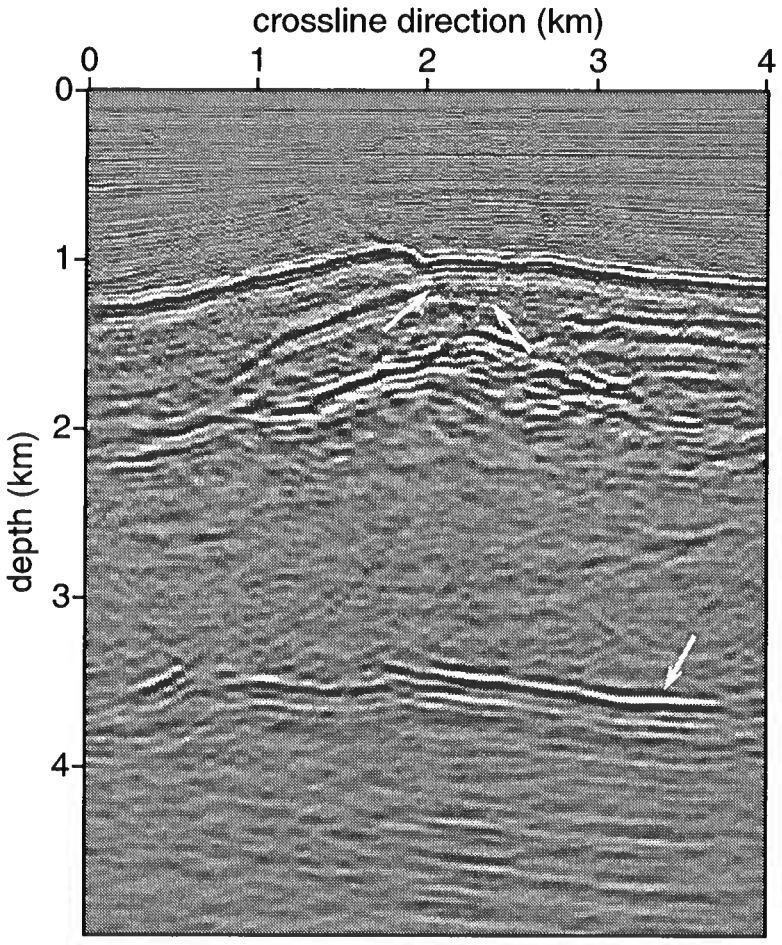

Figure 6.4. Vertical section in the crossline direction of the 3D pre-stack common-azimuth image of the L7D data set with the second-order GS propagator. The inline distance is 7150 m. The white arrows point to the graben structure and the base of the salt.

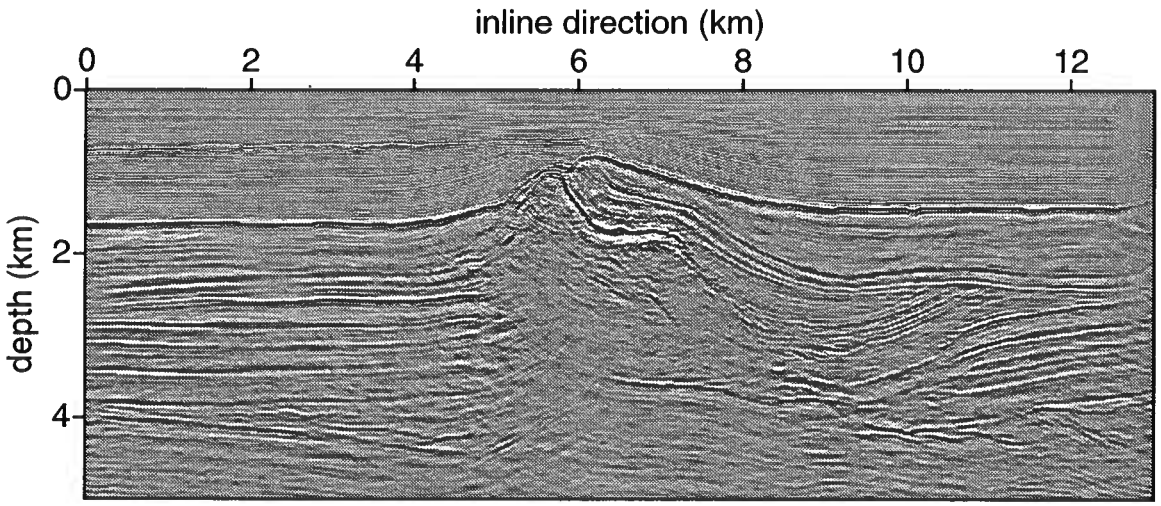

Figure 6.5. Vertical section in the inline direction of the 3D pre-stack common-azimuth image of the L7D data set with the second-order GS propagator. The crossline distance is 3000 m.

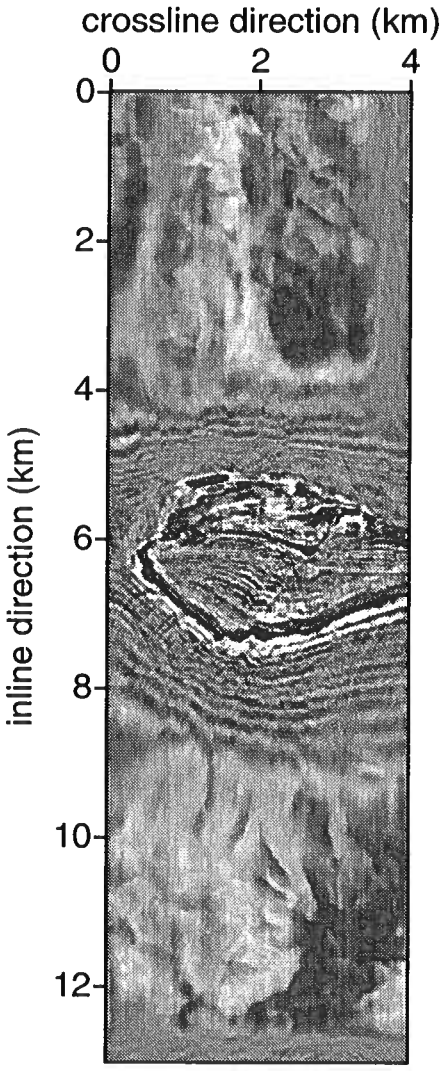

Figure 6.6. Horizontal section the 3D pre-stack common-azimuth image of the L7D data set with the second-order GS propagator. The depth is 1050 m.

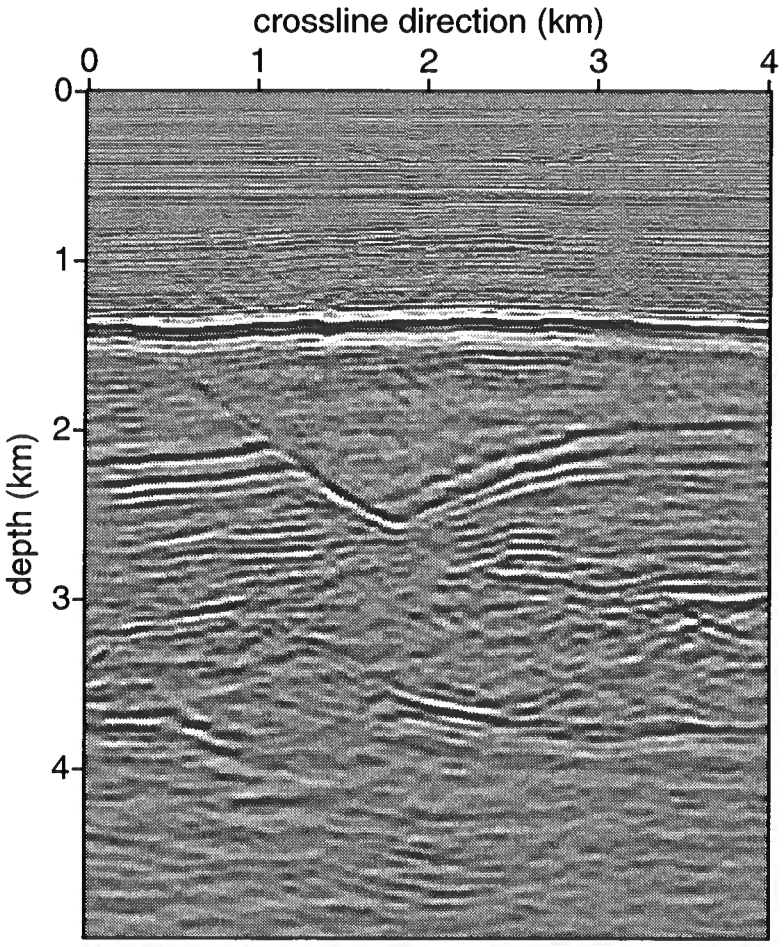

Figure 6.7. Vertical section in the crossline direction of the 3D pre-stack common-azimuth image of the L7D data set with the second-order GS propagator. The inline distance is 8300 m.

In Figure 6.1 we show a 2D section of the 3D zero-offset data where the salt structure can be identified. In Figure 6.2 we show a wave-speed model synthesized from the model used for imaging the L7D data as well the final image itself. Even though this wave-speed model was not used in the processing of the data it gives a rough idea of what the model looks like.

Further geologic information is obtained from the image sections. For orientation, the locations of the vertical sections of L7D images used in this chapters are shown in Figure 6.3. Figure 6.4 shows a vertical section in the crossline direction of the 3D pre-stack common-azimuth image of the L7D data set evaluated with the second-order GS propagator. In Figure 6.4 one can see the effect of the intrusion of the salt body in the sedimentary layers. A graben structure along with faults can be identified in the upper part of the section. Note that the base of the salt body is clearly visible in this section. We observe noise associated with the (pre-stack) imaging operator especially in the upper part of the model. Also, boundaries were not perfectly absorbing. Those are due to not enough tapering and padding on the side of the model. Figure 6.5 shows a vertical section in the inline direction of the same 3D image. Again the base of the salt body can be identified while its flank can be located with the help of the surrounding sedimentary layers. In this image no turning rays were used yielding no image of the flanks themselves. (The Bremmer series (De Hoop, 1996; De Hoop *et al.*, 2000) could be used to include those.) Figure 6.6 shows a horizontal section of the same 3D image. It illustrates how a large scale body such as a salt dome can penetrate sedimentary sequences. Such local tectonics induces erosion off the dome's flanks, and the depositional patterns, such as channels, associated with this erosion are well resolved. The quality of the focussing of the fault in the salt gives confidence in its positioning. The L7D data set also exhibits a normal fault with an offset of several hundred meters as can be seen in the crossline section in Figure 6.7.

The data underwent standard pre-processing such as deconvolution, geometrical spreading correction and multiple attenuation. Before wave-equation imaging, the data were regularized in source-receiver geometry; thus they could be subjected to regular fast Fourier transforms as needed in the algorithms used here (GS and hybrid PSPI/split-step Fourier propagators). A transformation to common-azimuth (AMO) was applied prior to the 3D pre-stack depth imaging procedure. Zero-offset data were obtained with the application of a transformation to zero offset (DMO).

6.4 3D zero-offset depth migration

In this section we test the GS propagator on zero-offset data from L7D. A vertical section of the migrated image obtained with the second-order GS propagator can be found in Figure 6.8. The section shows that 3D wave propagation is properly handled yielding an acceptable result. Note that the base of the salt is imaged. Some of the reflectors lack continuity including one associated with deep sedimentary formations. Note also the noise associated with the imaging operator in the upper part of the model. A comparison between Figures 6.5 and 6.8 shows that the pre-stack method improves the quality of the image in particular for the base of the salt body and the continuity of the deeper reflectors. It also

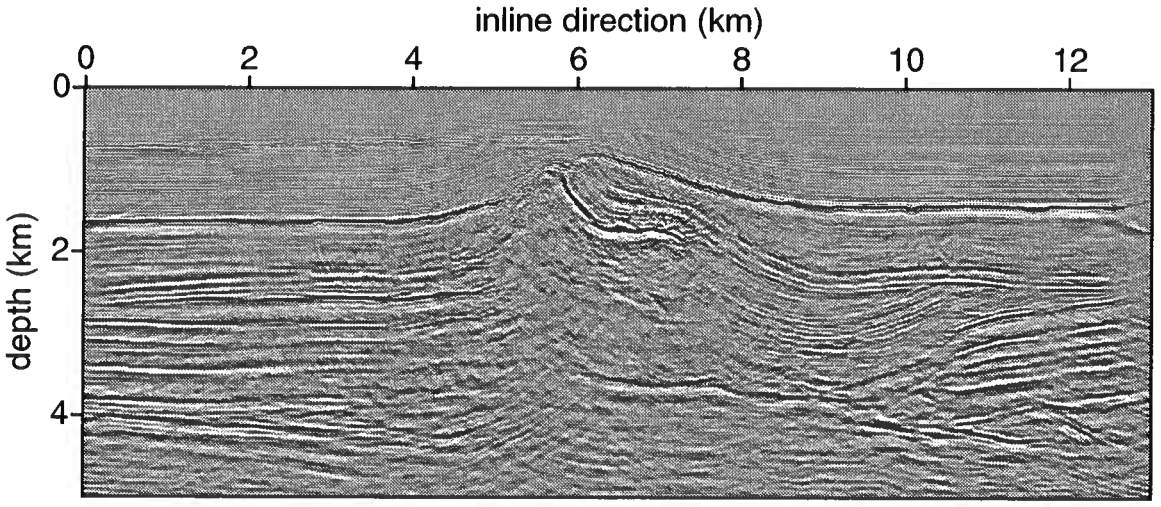

Figure 6.8. Vertical section in the inline direction of the 3D zero-offset image of the L7D data set with the second-order GS propagator. The crossline distance is 3000 m.

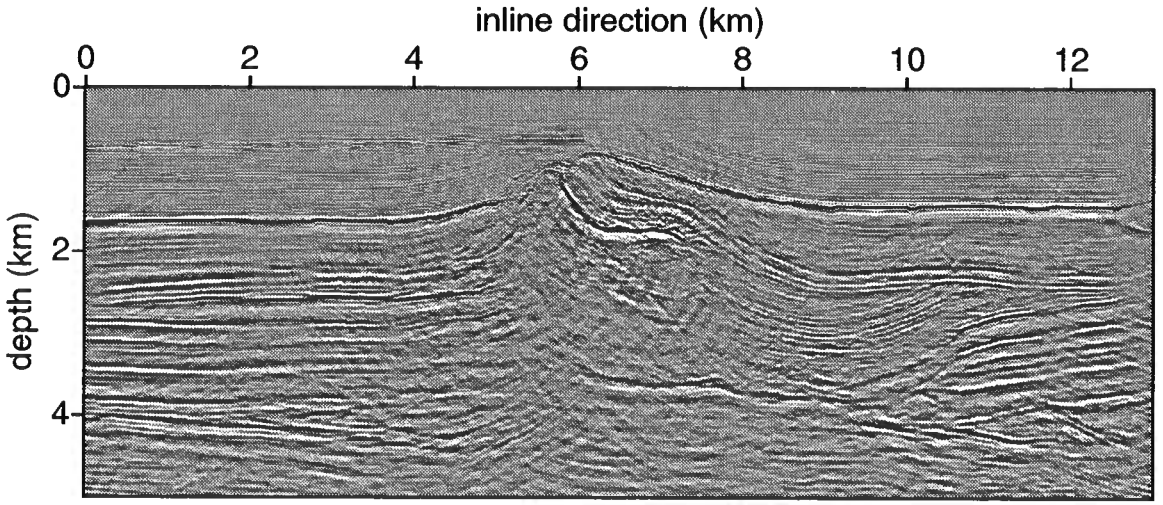

Figure 6.9. Vertical section in the inline direction of the 3D zero-offset image of the L7D data set with a hybrid PSPI/split-step Fourier method. The crossline distance is 3000 m. Note the difference with Figure 6.8 in the artifacts in the strongly heterogeneous part of the medium, e.g., the salt body.

yields a better definition of the flanks of the salt body. A proper handling of multipathing is the main cause for such an improvement.

Figure 6.9 is the result of the same zero-offset migration with a hybrid PSPI/split-step Fourier propagator. The wave extrapolation over a vertical step Δx_3 is performed with a split-step Fourier approximation with various background wave speeds, $v_1 < v_2 < \cdots < v_{n-1} < v_n$. If we use the spatial coordinates $\boldsymbol{x} = (x_{1,2}, x_3)$, then at each node $(x_{1,2})$, in the next depth section, $x_3 + \Delta x_3$, there is a j such that $v_j \leq v(x_{1,2}, x_3 + \Delta x_3) \leq v_{j+1}$ where $v(x_{1,2}, x_3 + \Delta x_3)$ is the actual wave speed at $(x_{1,2}, x_3 + \Delta x_3)$. The wave field at $(x_{1,2}, x_3 + \Delta x_3)$ is then computed as an interpolation of the two wave fields associated with v_j and v_{j+1}. (An oscillatory integral interpretation of this procedure is given in De Hoop *et al.* (2000).) The additional interpolation feature yields a more accurate propagator than a simple split-step Fourier propagator. A comparison of the sections in Figures 6.8 and 6.9 shows differences in the artifacts in the strongly heterogeneous part of the medium. With the (quantitative) analysis of Chapter 4 one would expect a degradation of the image when using a split-step Fourier approximation despite the interpolation procedure. However in Chapter 4 we have shown that differences in accuracy between the two approximations were mainly associated with multipathing and wide-angle propagation. In zero-offset processing multipathing is not accounted for properly since one assumes that the stationary path is the same for waves going up and going down, invoking normal reflections. Hence a zero-offset testing showed that 3D wave propagation is honored by the two wave extrapolation (Trotter) methods but could not reveal the accuracies of the two methods.

6.5 Illustration of multipathing in the imaging kernel

In Chapter 4 we illustrated the importance of multipathing looking at one-way wave propagation. We show how this naturally extends to the imaging kernel. For that purpose we use a 2D section of the SEG/EAGE salt model as shown in Figure 6.10. We apply the imaging operator to one single trace. This allows one to observe various impulse responses associated with different times, since the trace contains several seismic events in time. The singular supports of these responses, i.e., the isochrones, correspond to the source and the receiver positions associated with the given trace.

We first compute such a migration impulse response with a single-arrival Kirchhoff migration scheme (Figure 6.11-a). It naturally yields isochrones with no triplications. If we now make use of the first five arrivals in the Kirchhoff migration scheme, we obtain isochrones that show triplications (Figure 6.11-b). The differences between the two wave fronts are quite significant and advocate once again a proper handling of multipathing in imaging procedures in complex regions such as salt bodies. Note that the isochrones in Figure 6.11 in fact correspond to a low-dimensional projection of the canonical relation of the imaging operator (Stolk & De Hoop, 2000; De Hoop *et al.*, 2001a).

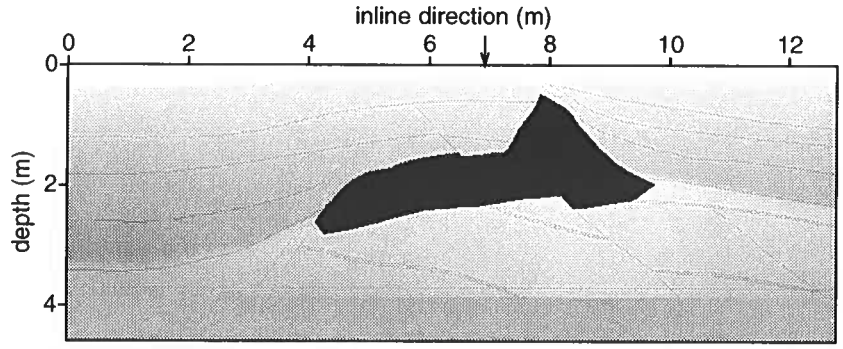

Figure 6.10. A 2D section in the inline direction of the 3D SEG/EAGE salt model. The arrow shows the source and receiver position (zero-offset) for the single trace migration of Figure 6.11

6.6 Common-azimuth 3D pre-stack depth migration

We turn now our attention to the 3D pre-stack depth imaging of TotalFinaElf's L7D data set. Exploiting the narrow range of azimuths in the acquisition (marine acquisition) we employ a common-azimuth approximation [see Biondi and Palacharla (1996) and Appendix D]. Via a stationary-phase analysis in one variable, this approximation suppresses an integral in the Trotter product representation of the imaging operator (see Chapter 2). This yields a lower computational complexity at the cost of approximating some of the 3D scattering effects (see Appendix D). In Section 6.3 we already introduced the migration results obtained with the second-order GS propagator. In the GS results many geological features of the model are recovered. Note that subsalt features are identifiable. An improvement of the wave-speed model could yield better results in the deeper part of the model. This could be achieved according to the method exposed in De Hoop *et al.* (De Hoop *et al.*, 2001a) (Chapter 2) and the velocity analysis scheme of Brandsberg-Dahl *et al.* (Brandsberg-Dahl *et al.*, 2001).

6.6.1 Comparison with a hybrid PSPI/split-step Fourier scheme

Having noticed the importance of multipathing for pre-stack imaging we now compare the performance of the second-order GS propagator with the one of the hybrid PSPI/split-step Fourier propagator. In Figures 6.13 and 6.15 we show inline sections at two different crossline distances (1500 m and 3000 m) for the two methods. In both figures we point out with white arrows the features that show significant differences between the two methods applied. Those differences are mainly located in the middle-upper part of the model. In the deep section of the model, such as the base of the salt body, the two methods yield

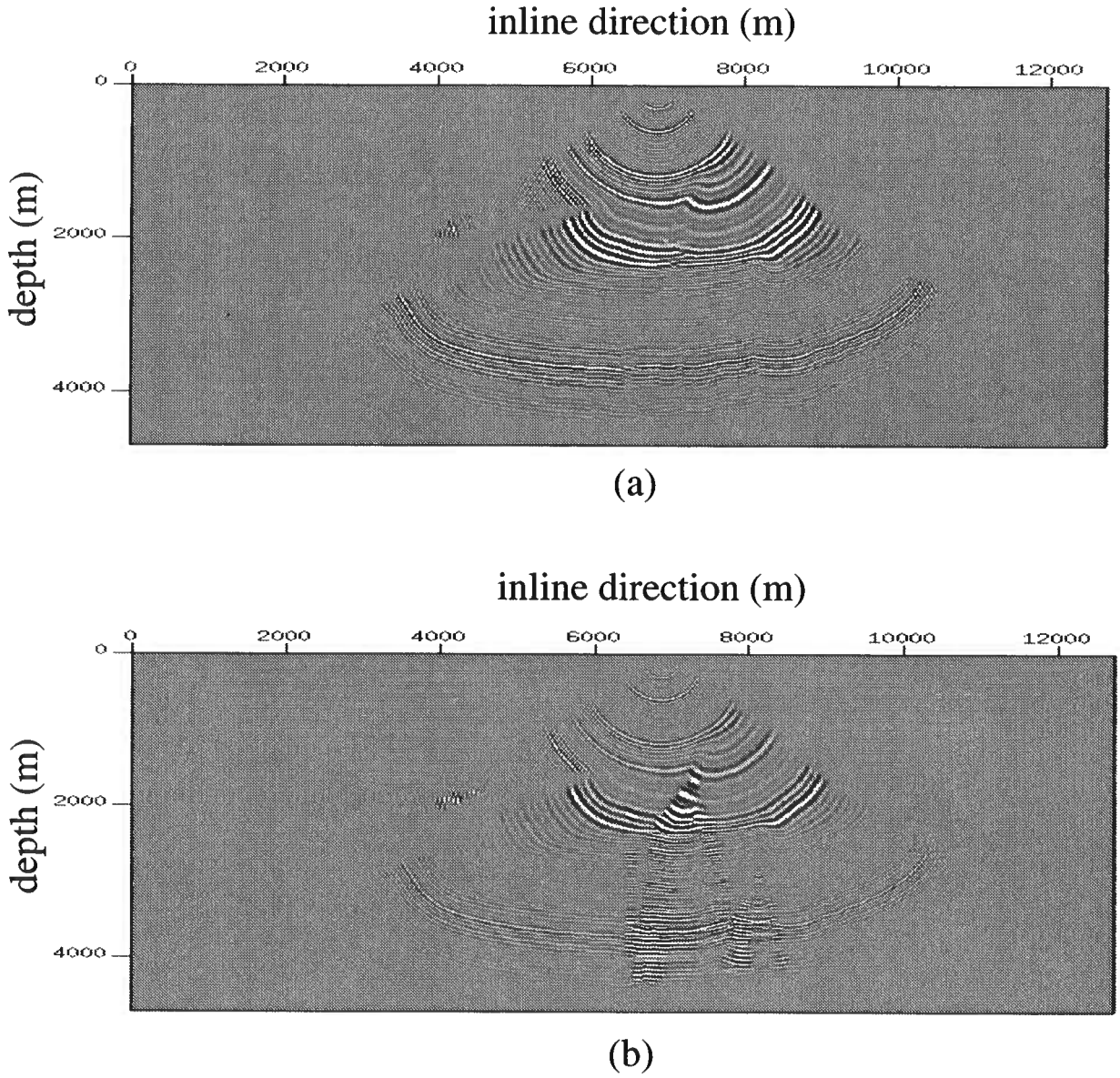

Figure 6.11. Migration of a single trace using Kirchhoff method accounting for (a) one arrival only and (b) five arrivals. See Figure 6.10 for the trace position.

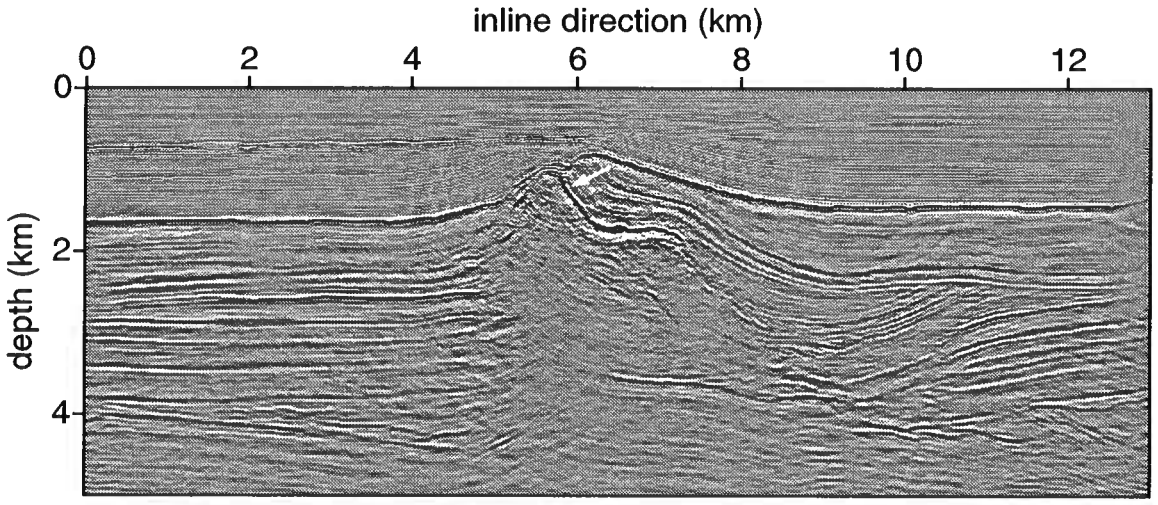

Figure 6.12. Vertical section in the inline direction of the 3D pre-stack common-azimuth image of the L7D data set with the second-order GS propagator. The crossline distance is 3000 m.

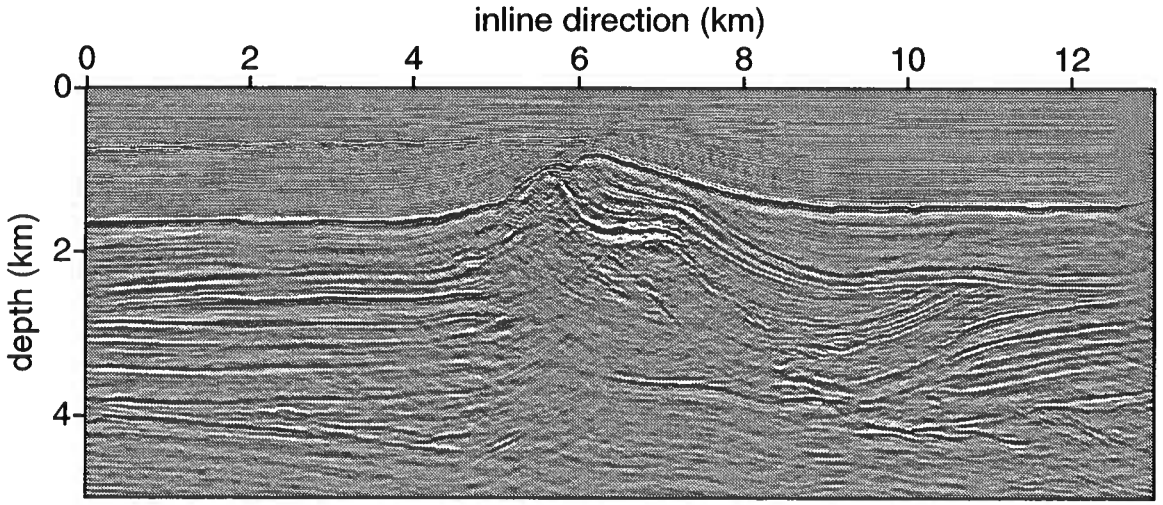

Figure 6.13. Vertical section in the inline direction of the 3D zero-offset image of the L7D data set with a hybrid PSPI/split-step Fourier method. The crossline distance is 3000 m.

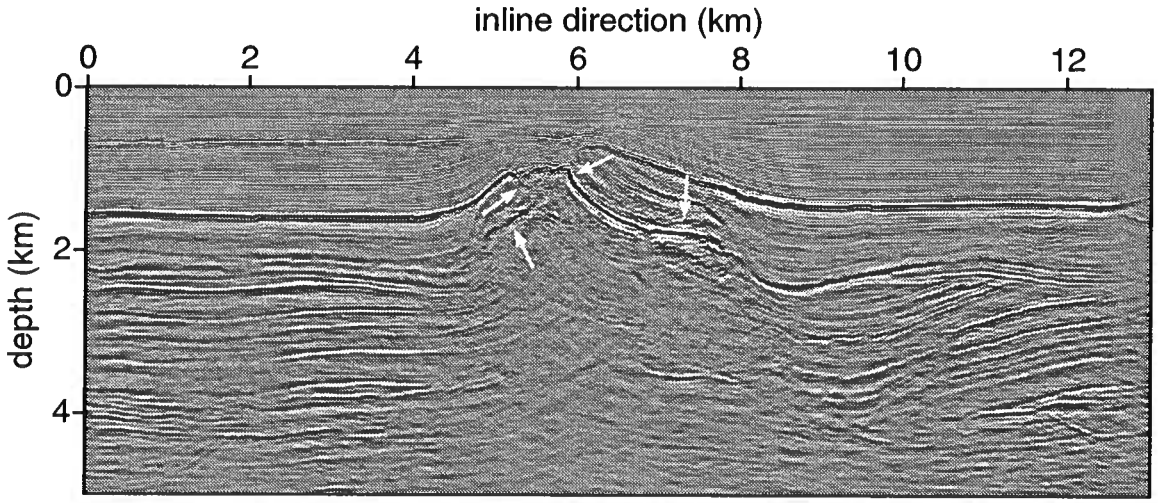

Figure 6.14. Vertical section in the inline direction of the 3D zero-offset image of the L7D data set with the second-order GS propagator. The crossline distance is 1500 m.

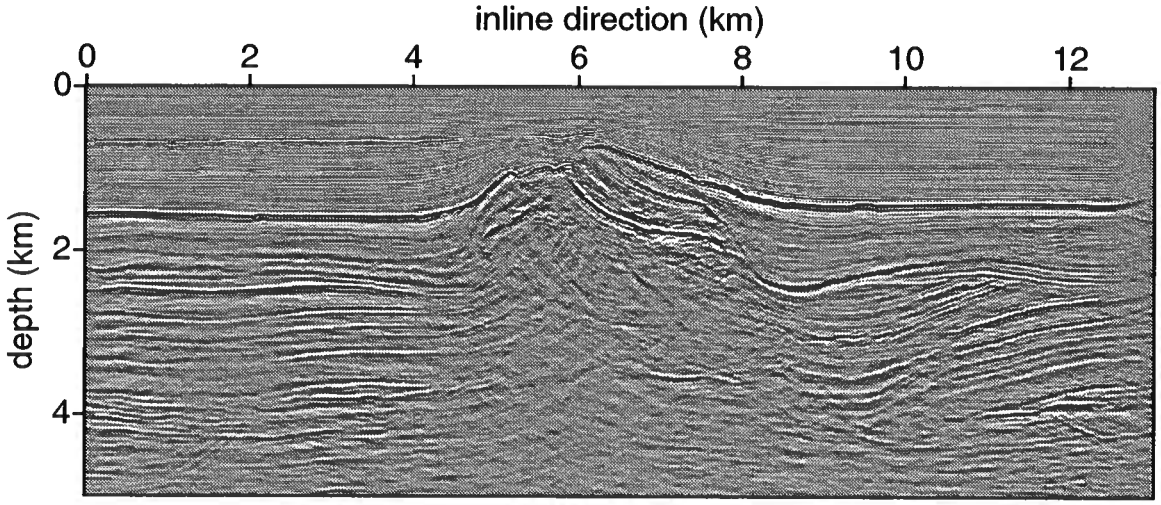

Figure 6.15. Vertical section in the inline direction of the 3D zero-offset image of the L7D data set with a hybrid PSPI/split-step Fourier method. The crossline distance is 1500 m.

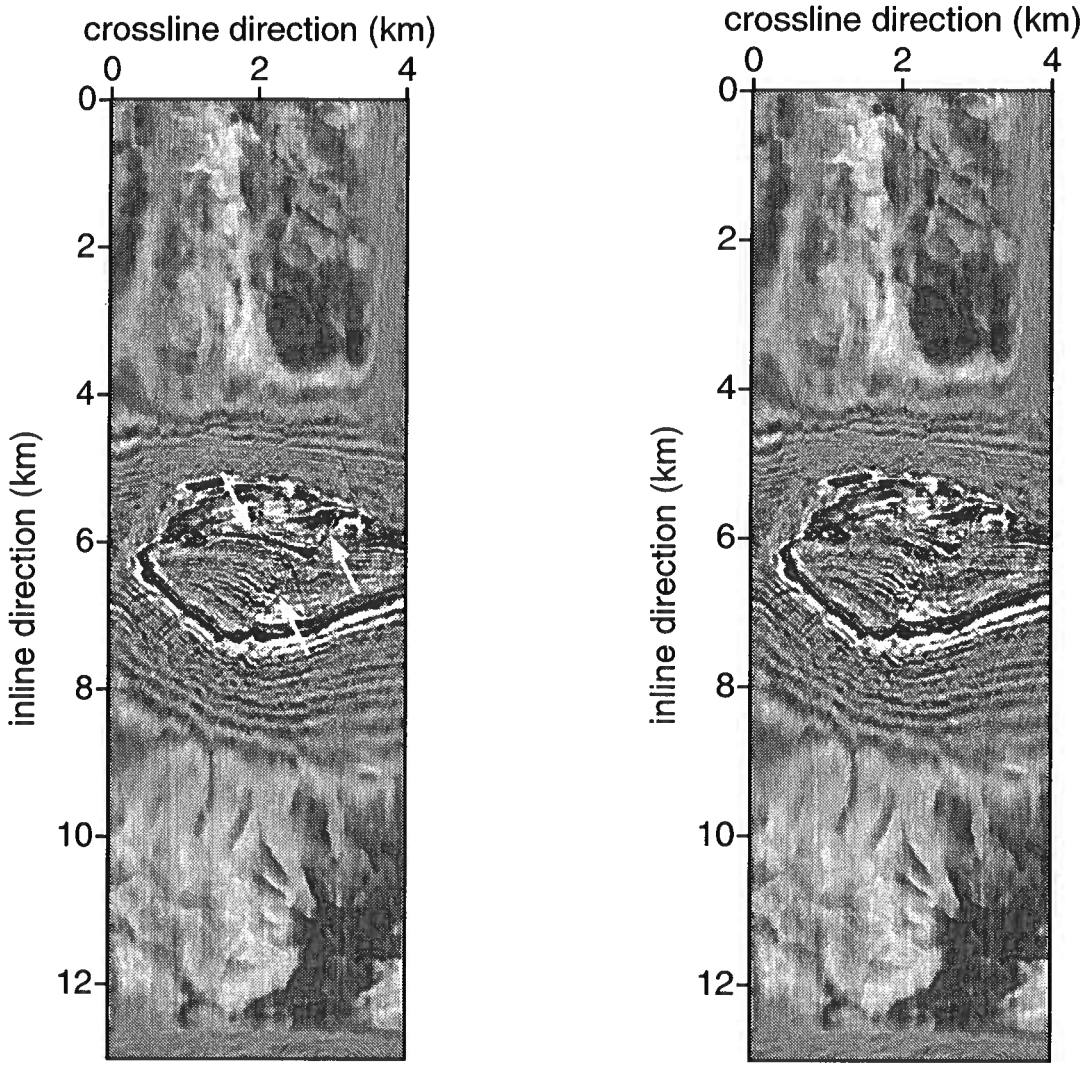

(a) (b)

Figure 6.16. Horizontal sections the 3D pre-stack common-azimuth image of the L7D data set with a) the second-order GS propagator and b) a hybrid PSPI/split-step Fourier propagator. The depth is 1050 m.

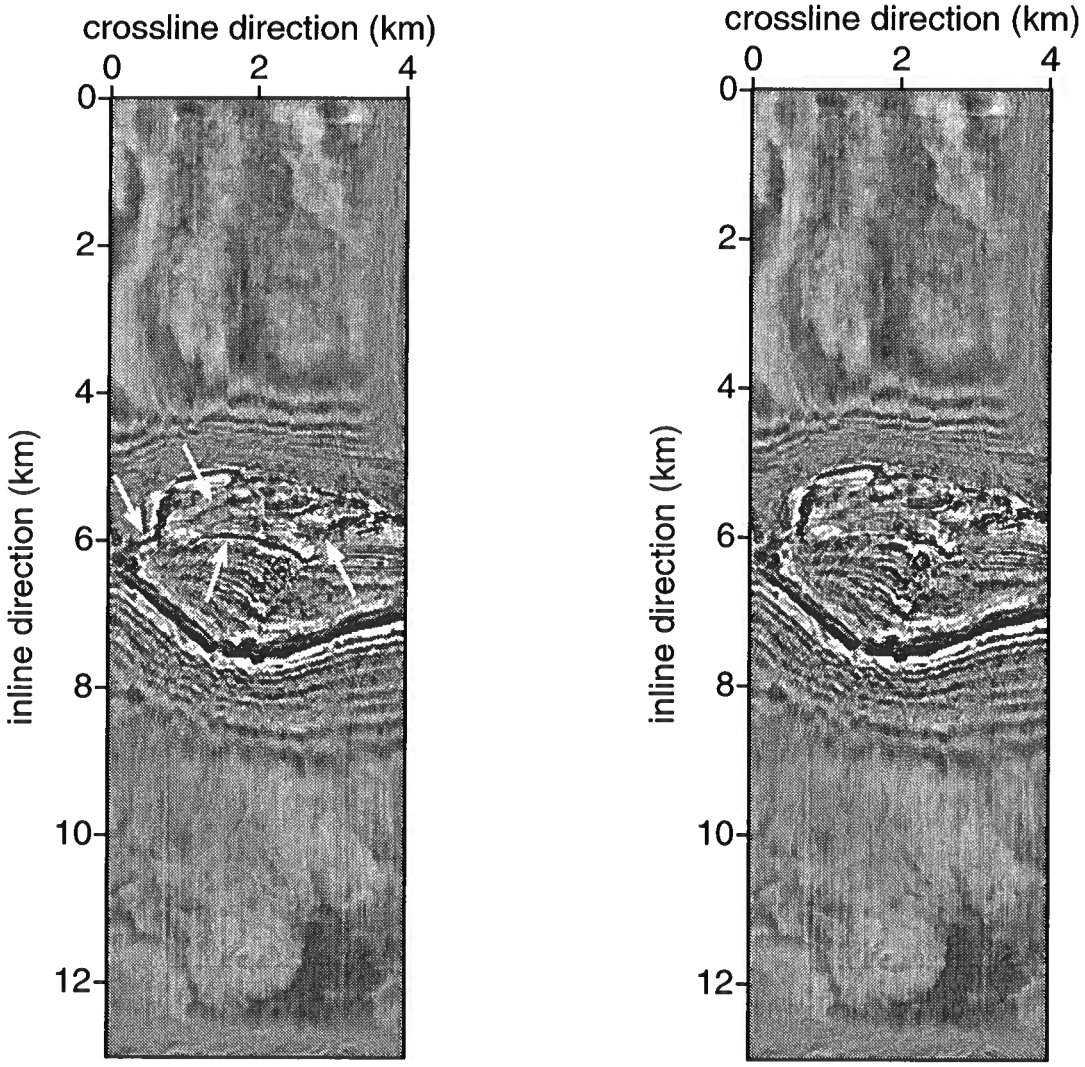

(a) (b)

Figure 6.17. Horizontal sections the 3D pre-stack common-azimuth image of the L7D data set with a) the second-order GS propagator and b) a hybrid PSPI/split-step Fourier propagator. The depth is 1125 m.

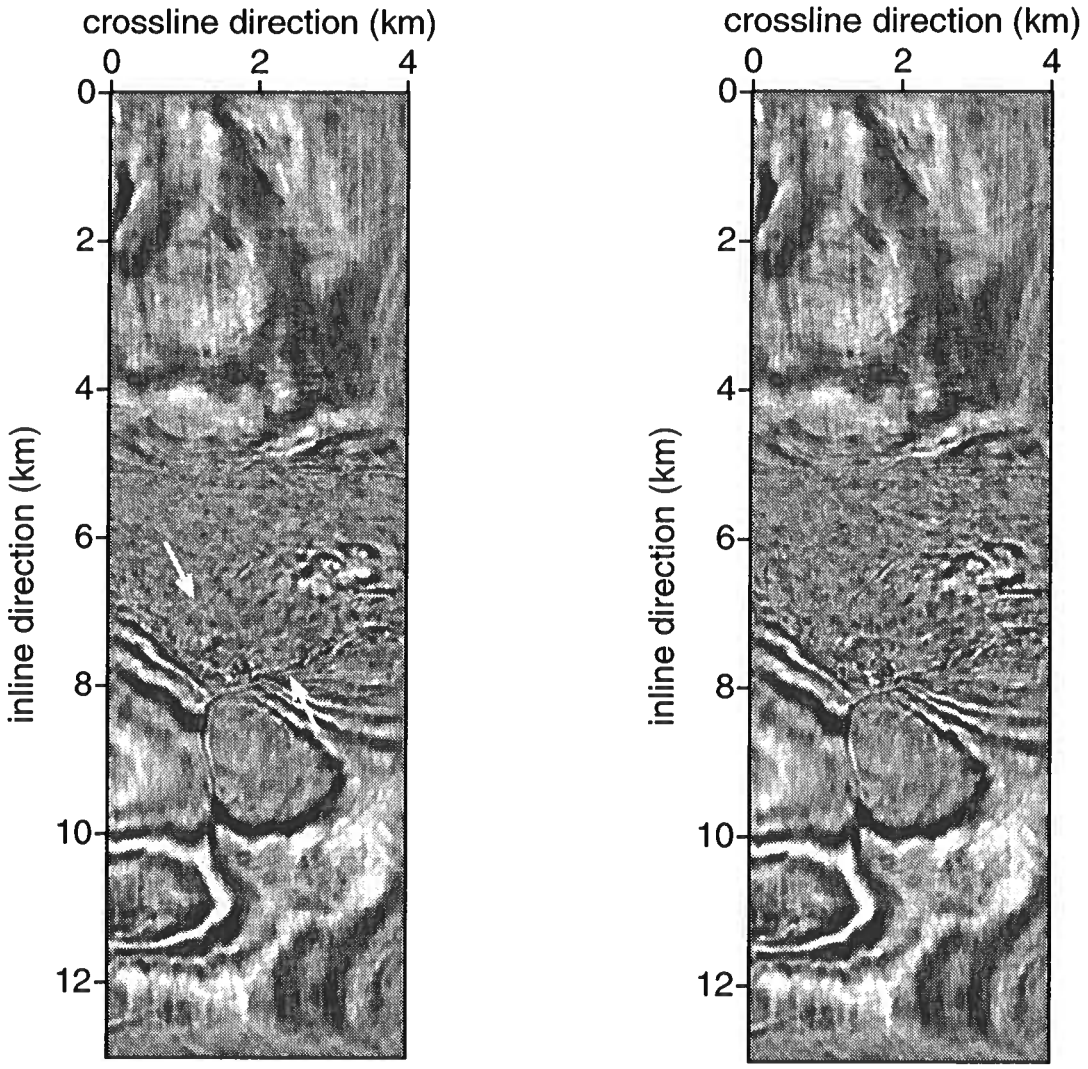

(a) (b)

Figure 6.18. Horizontal sections the 3D pre-stack common-azimuth image of the L7D data set with a) the second-order GS propagator and b) a hybrid PSPI/split-step Fourier propagator. The depth is 2250 m.

comparable results. In the features highlighted in Figures 6.13 and 6.15 some faults and reflectors are better imaged and focussed with the second-order GS propagator. To further highlight those differences we show horizontal sections that correspond to the middle-upper part of the model in Figures 6.16 and 6.17(b). These horizontal sections further confirm a better imaging of features such as faults with the GS method. We also highlight some reflectors the continuity of which is enhanced by the GS method. In the deeper part of the model, horizontal sections show some differences between the two migration results. In Figure 6.18 the depth is set at 2250 m. As in shallower parts the faults are better resolved by the GS propagator. One of those faults correspond to the major fault visible in Figure 6.7. Overall the real data case shows better results for the GS propagator as far as reflector continuity and definition of the faults for the L7D data set.

6.6.2 Comparison with a Kirchhoff scheme

GSPCAM-120-small.ps.gz To further assess the imaging performances of the GS approach we now compare it to a Kirchhoff scheme. Figure 6.19 shows the corresponding result. This Kirchhoff scheme only uses the most energetic arrival, i.e., does not honor multipathing. It should be noted also that the same regularized data was used for the Kirchhoff imaging. One sees that the bottom of the salt and the general geologic structures are imaged. This confirms that apart from differences in texture wave-equation-based methods and asymptotic methods yield similar images on the wave front set (De Hoop *et al.*, 2001a) (Chapter 2). As in the previous comparisons between the two wave-equation schemes (GS and hybrid PSPI/split-step Fourier), differences are noticeable in the upper part of the salt body (as marked with white arrows in Figure 6.19). There, a better imaging is obtained with the wave-equation based methods with more focussed reflectors. The upper part of the model actually shows complexity and lens-like wave-speed perturbations as shown in Figure 6.2. One can therefore suspect the occurrence of multipathing in the upper part of the model, which is properly accounted for by the wave-equation methods and not by the single-arrival Kirchhoff scheme. To further exhibit the differences in focusing in that shallow region we show a comparison of horizontal sections in Figure 6.20. It should be noted that those differences correspond also to dipping reflectors. Hence, a limited aperture in the Kirchhoff scheme can also yield a poor imaging. The bottom part of the model, e.g., the salt bottom, does not exhibit such differences. Multipathing must not be so significant in that part of the model, possibly because of illumination from the right hand side of the model instead of directly through the salt body. This further explains the little differences found between for the two wave-equation scheme (GS and hybrid PSPI/split-step Fourier) in the lower part of the model (see Figures 6.12 and 6.13).

6.7 The influence of multiple scattering on depth imaging

The generalized Bremmer coupling series (Chapter 3) (De Hoop, 1996; De Hoop *et al.*, 2000) give the capability to control the up-down multiple scattering when modeling seismic data. This opens the door to the investigations of the importance of multiples in imaging and

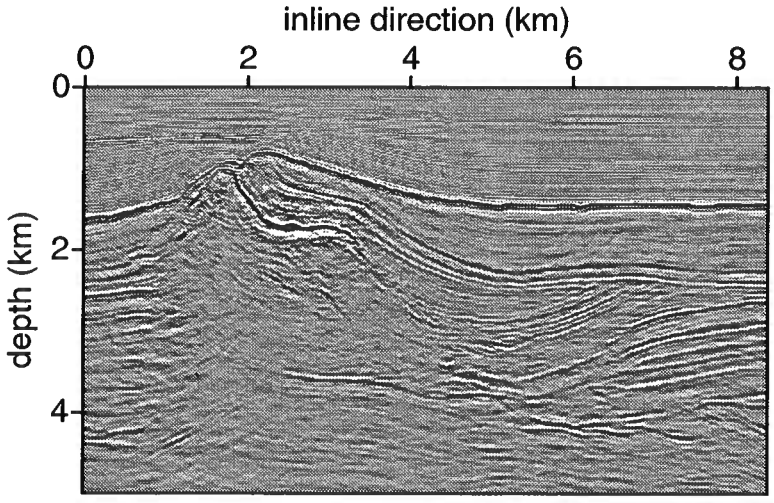

(a)

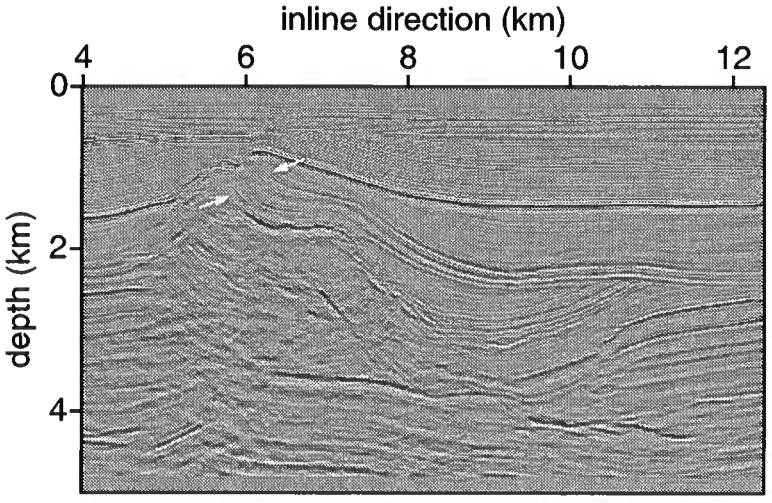

(b)

Figure 6.19. Vertical section in the inline direction of the 3D pre-stack image of the L7D data set with a) the second-order GS propagator (common azimuth scheme) and b) a single-arrival Kirchhoff scheme. The crossline distance is 3000 m.

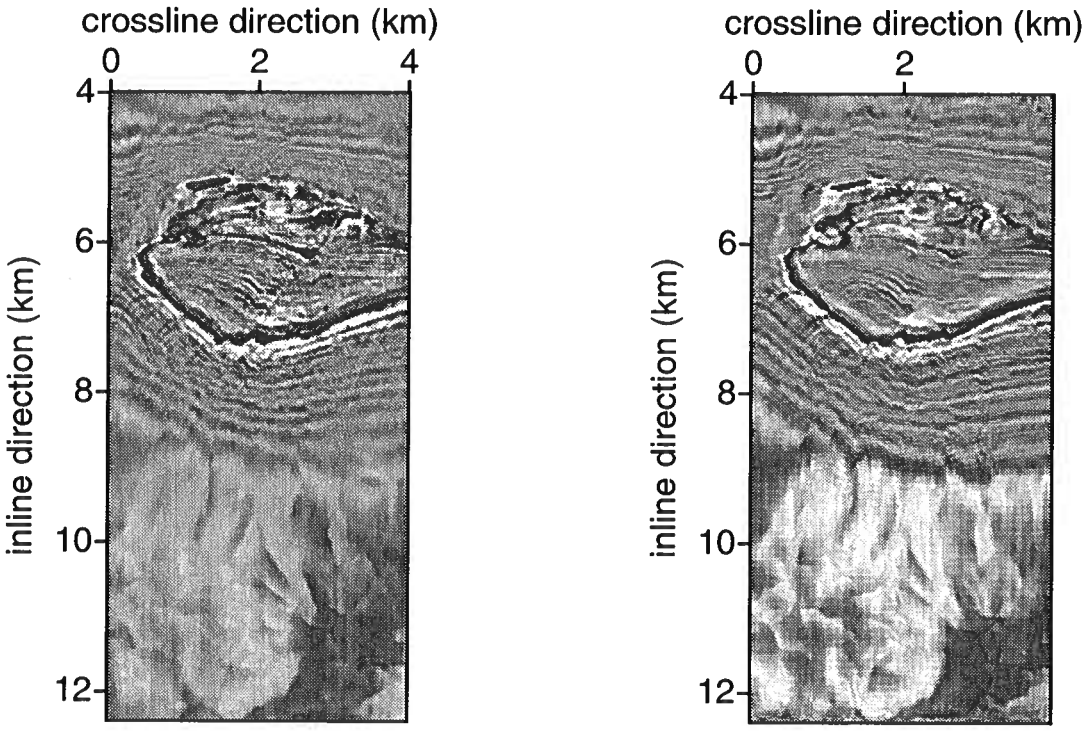

(a) (b)

Figure 6.20. a) Horizontal sections the 3D pre-stack common-azimuth image of the L7D data set with the second-order GS propagator; b) Horizontal sections the 3D pre-stack image of the L7D data set with a single-arrival Kirchhoff scheme. The square pattern in b) is due to travel time grid interpolation. The depth is 1050 m.

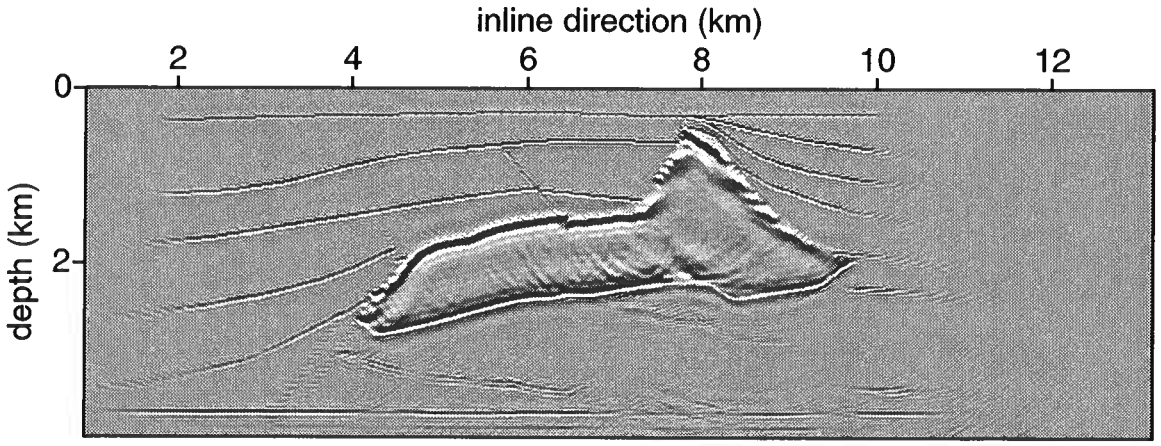

Figure 6.21. 2D image of the synthetic data generated by the second-order GS propagator. Only the primary arrival was generated. A hybrid PSPI/split-step Fourier propagator was used in the imaging procedure.

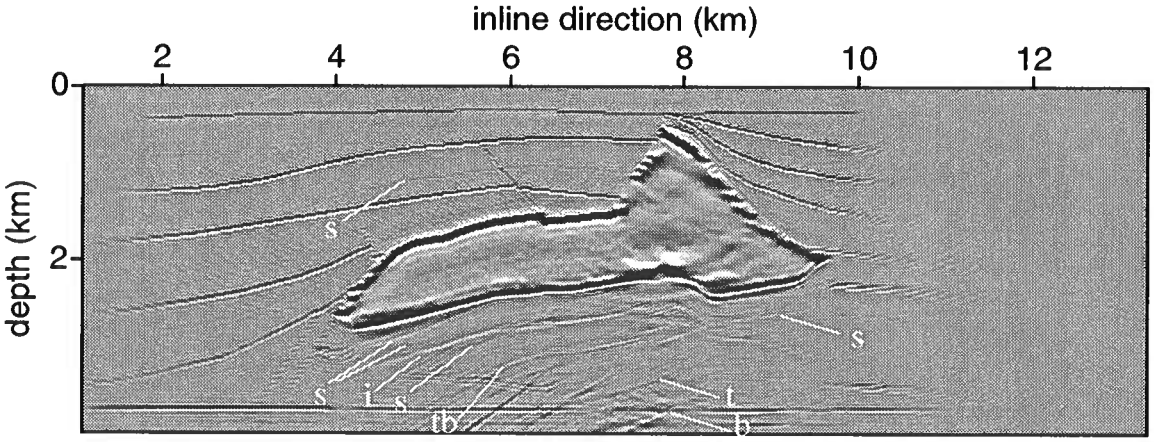

Figure 6.22. 2D image of the synthetic data generated by the second-order GS propagator. The primary arrival and the first multiple were generated with the Bremmer series. A hybrid PSPI/split-step Fourier propagator was used in the imaging procedure. The model of Figure 6.10 shows only strong contrasts in wave speed at the the transition between the water and the subsurface and at the salt boundaries. This allows to identify multiples. The label 's' denotes water-layer multiples; 'i' denotes internal multiples, i.e. internal to the salt body; 't' denotes multiples associated with the top of the salt body and the water surface;'b' denotes multiples associated with the bottom of the salt body and the water surface; 'tb' denotes multiples with the path surface-top salt-surface-bottom salt-surface.

a proper treatment of those. To illustrate this point we show imaging results on synthetic data that were generated with the aid of the Bremmer series. The imaging was performed with a hybrid PSPI/split-step Fourier propagator as described above. The modeling was done with the second-order generalized-screen propagator as the generator of the Bremmer coupling series. The model used is the same as in Figure 6.10. We simulated a marine-type seismic data acquisition. In Figure 6.21 the data used contained the primary arrival only, i.e., the first two terms in the Bremmer series. One can see that the model is properly imaged. Some subsalt features are not properly in place due to a poor handling of wide-angle propagation by the hybrid PSPI/split-step Fourier method. In Figure 6.22 the data used contained the primary reflected data as well as the first multiple, i.e., the first four terms in the Bremmer series. The imaging then exhibits 'phantom' reflectors due the non-proper handling of the multiples. (For instance the deeper part of the section in Figure 6.22 shows strong multiple events; the deepest one are associated with the salt body boundaries.) For the treatment of field data, prior to an imaging-inversion, multiples are usually attenuated. However a proper treatment of those will yield an improvement in image quality, including signal to noise ratio.

6.8 Conclusion

The case study of TotalFinaElf's 3D North-Sea L7D marine data set is conclusive. We not only illustrate the capability of the GS method for 3D depth imaging, both zero-offset and pre-stack, but we also confirm that the accurate prediction of and the accounting for multipathing is key to an optimal image in complex regions. The GS approach falls into the category of wave-equation imaging. The GS propagator with its higher accuracy at wide-angle propagation and scattering performs superior to a hybrid PSPI/split-step Fourier propagator on the L7D data set. For this data set we have shown enhanced resolution and improved positioning of faults and texture of some reflectors. While a proper treatment of multipathing is a key step towards improved imaging, the question remains whether the inclusion of internal multiples could improve the imaging further. To improve the computational efficiency of the GS method further, we can employ (i) a multi-grid approach adapted to the constituent frequency bands, (ii) adapt the variable step size (in depth) in terms of the lateral rate of change in wave speed (De Hoop *et al.*, 2001a), and (iii) adapt the GS order of expansion with the maximum lateral wave-speed variation. To improve upon our subsalt imaging, the use of mode converted (S) waves seems to be natural. A vector GS theory has been developed for elastic wave propagation accounting for phenomena such as the continuous mode coupling between P and S (Le Rousseau & De Hoop, 2001a) (Chapter 7).

Chapter 7

Generalized-screen approximation and algorithm for the scattering of elastic waves[1]

7.1 Summary

We describe the propagation and scattering of elastic waves in heterogeneous media. Decomposing the elastic wavefield into up- and downgoing constituents allows the introduction of the 'one-way' wave equations and propagators. Such propagators account for transverse scattering and mode coupling. The generalized-screen expansion of the symbol of the one-way wave equation in medium contrast and medium smoothness induces an approximation of the propagator with an associated computational complexity of the one of the phase screen approximation. The generalized-screen expansion extends the phase-screen approach. It allows for larger medium fluctuations and wider-angle propagation. We illustrate the accuracy of the generalized-screen with numerical examples.

7.2 Introduction

The multi-mode elastic phase-screen approximation to one-way wave propagation was introduced by Fisk and McCartor (1991; 1992), fundamentally refined by Wu (1994) and simplified by Wild and Hudson (1998). Wu (1994) extended the scalar phase-screen approach for modeling acoustic waves to elastic waves and, in that process, developed the vector complex-screen approximation. In the acoustic case De Hoop *et al.* (2000)(Chapter 3) and Le Rousseau and De Hoop (2001b) provided a systematic treatment and generalization of the phase-screen approach, maintaining its algorithmic structure while developing a hierarchy of increasingly accurate approximations of the one-way wave propagator. The generalized-screen (GS) method allows for larger medium fluctuations, wider-angle propagation, and back-scattering. In this chapter, we carry out the likewise extension of Wu's complex screen approximation, which results in the elastic GS expansion.

A scattering theory that follows the ray picture but accounts for full-wave behavior has been developed by De Hoop (1996). The method consists of three main steps: (i) *decomposing* the field into two constituents, *propagating* upward or downward along a preferred direction (here vertical) , (ii) computing the interaction (*coupling*) of the counter-propagating constituents, and (iii) *re-composing* the constituents into observables at the

[1]This chapter, co-authored by M.V. de Hoop, has been accepted for publication in the *Quaterly Journal of Mechanics and Applied Mathematics*

positions of interest. Such a method is based on an extension of the Bremmer coupling series to multi-dimensionally varying media. Bremmer's method decomposes the wavefield into a recursion of one-way propagations and up-down reflections-transmissions. The one-way operators propagate waves in the preferred vertical direction and account for scattering in the transverse direction while reflection-transmission operators account for scattering in the vertical direction. Thus, the method first generates a wavefield dominated by downward propagation, then generates a 'first' upward propagating wavefield, then a 'second' downward propagating field, etc. In this manner, multiple reflections are accounted for in a controlled manner. The Bremmer series in acoustic media have already found application in Van Stralen *et al.* (1998) where the one-way wave operator is approximated with an accurate optimal finite-difference algorithm based on a rational expansion as opposed to the GS expansion by Le Rousseau and De Hoop (2001b).

The propagator that generates the Bremmer series can be represented by a Hamiltonian path integral (De Witte-Morette *et al.*, 1979; Fishman & McCoy, 1984a; Fishman & McCoy, 1984b; De Hoop, 1996) that accounts for not only the energy traveling along the ray but also for the transport along non-stationary paths. These path integrals contain all possible multi-pathing. In the path integral, 'time' is identified with depth, and 'momenta' are identified with the horizontal wave slownesses which, in the ray-theoretic limit, coincide with the horizontal components of the gradient of travel time. The (square-root) Hamiltonian, appearing in the phase of the path integral, is identified with vertical wave slowness, which, in the ray-theoretic limit, coincides with the vertical component of the gradient of travel time (De Hoop, 1996).

The problem with the path integrals is the computational complexity of their numerical evaluation. To propagate waves across a thin slab one has to perform a Fourier transform of the wave field in the horizontal directions, a phase shift and an inverse Fourier transform. The phase shift is a function of both the space variables (input and/or output points) and phase variables (wavenumber). The sequence of operations has therefore to be performed for every output point at the next depth level (and every wavenumber if there is dependency on the input point) which yields a high computational complexity. De Hoop *et al.* (2000) have developed a method that dramatically reduces the computational complexity of such evaluation, at the cost of departing from the exact shape of wavefronts. The result is an algorithm that, for each propagation step, is built from the sequence: (several) forward Fourier transform(s), multiplication, inverse Fourier transform, multiplication –where the transform is in the horizontal directions and may be windowed. To achieve such a structure the phase shift is expanded in a series which separates space and phase dependencies. The series expansion constitute the GS expansion. Truncating the GS expansion at increasing orders yields a hierarchy of increasingly accurate approximations. The number of forward (fast) Fourier transforms in the algorithm depends on the number of terms used in the GS expansion but is *not* proportional to the number of nodes in the horizontal direction for which the wavefield is computed. Underlying these approximations of the exact phase-shift is an expansion of the medium wave speed model simultaneously into smoothness and magnitude of variation with respect to a background medium.

The concept of screen approximations to the propagation of scalar waves has been

around for many years. The phase-screen approximation has been applied to light transmission through the atmosphere (Ratcliffe, 1956; Mercier, 1962; Filice, 1984; Martin & Flatté, 1988), propagation of light in optical fibers (Feit & Fleck, 1978), propagation of radio signals through the ionosphere (Buckley, 1975; Bramley, 1977; Knepp, 1983), propagation of acoustic waves in the ocean (Flatté *et al.*, 1979; Thomson & Chapman, 1983); in the seismic literature the phase-screen approximation is known as the split-step Fourier method (Stoffa *et al.*, 1990). The isotropic phase-screen method has been extended to P waves in anisotropic hexagonal media (Le Rousseau & De Hoop, 2001c).

The first extension in 2D of a phase-screen approach to elastic waves was that of Landers and Claerbout (1972). Hudson (1980) followed a similar procedure in 3D. Their papers assumed a single principle wavenumber. Fisk and McCartor (1991) treated the P and S constituents as two separate fields. They simulated the scattering effects by passing the P and S waves through two separate screens. The PS conversion was obtained by projecting the distorted P-wave component to the corresponding S-wave component. Such projections do not truly account for conversions and certainly not for continuous mode coupling. Such inconsistencies are naturally removed in our GS approach. Wu (1994) generalized the split-step Fourier algorithm to elastic wave propagation and applied a small angle (parabolic) approximation to obtain his elastic complex screen. Wu maintained consistency with Thomson and Chapman's 'wide-angle' scalar phase screen (Thomson & Chapman, 1983) when applying a small angle approximation for the interaction term only keeping the propagation part unchanged. Out of our GS approach follows also an alternative split-step Fourier method. A 'vector' GS expansion has already been introduced for electromagnetic wave propagation by Le Rousseau *et al.* (2000), where they show that losses can be accounted for in the GS approach.

For large scale geophysical configurations, efficient 3D propagation algorithms are in demand. On the one hand, full-wave 3D finite-difference and finite-element methods are costly. One the other hand, the phase-screen approach, though approximate, yields a much more efficient algorithm in 3D. The phase-screen method was designed for multiple downward scattering of scalar waves, the downward direction being the principle direction of propagation. The screen method is a marching algorithm in which computation of the next wavefront requires only knowledge of the current wavefront. It includes phenomena such as focusing and defocusing associated with multi-pathing.

In strongly heterogeneous media we have to be concerned with the continuous coupling between P and S waves. In particular a primary P wave gets converted into S wave energy almost everywhere. To illustrate this, we consider a region of the Institut Français du Pétrole (IFP)'s *acoustic* Marmousi model (Bourgeois *et al.*, 1991)(Figure 7.1) that is representative for the upper crust of an off-shore region in west Africa. A point source (star) is located at a medium interface below a truly heterogeneous part of the model (anticline, unconformity, faults) that exhibits significant horizontal wave speed variations. The source is excited at time $t = 0$, and the pressure wavefield is imaged at time $t = 0.95$ s, creating the snapshot in Figure 7.2 computed with the scalar GS method (Le Rousseau & De Hoop, 2001b) for an explosion source. Note the occurrence of significant multi-pathing due to the complexity of the medium. Le Rousseau and De Hoop (2001b) showed that such multi-pathing is

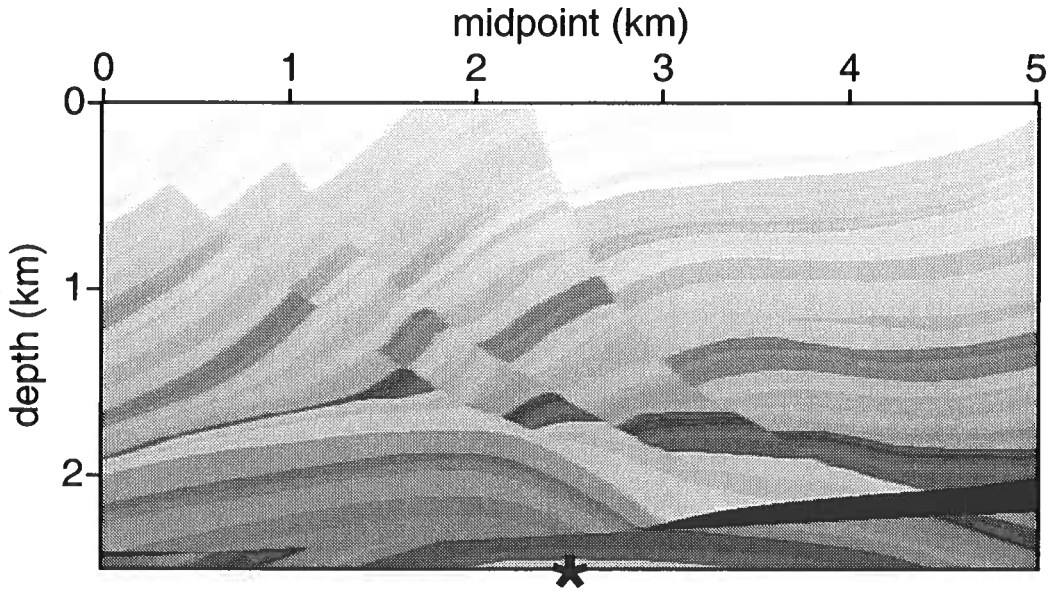

Figure 7.1. Part of the Marmousi wave speed model used to generate the snapshots of Figures 7.2 to 7.4(b). The star locates the position of the source. The maximum wave speed is 5500 m/s (black). The minimum wave speed is 1500 m/s (white).

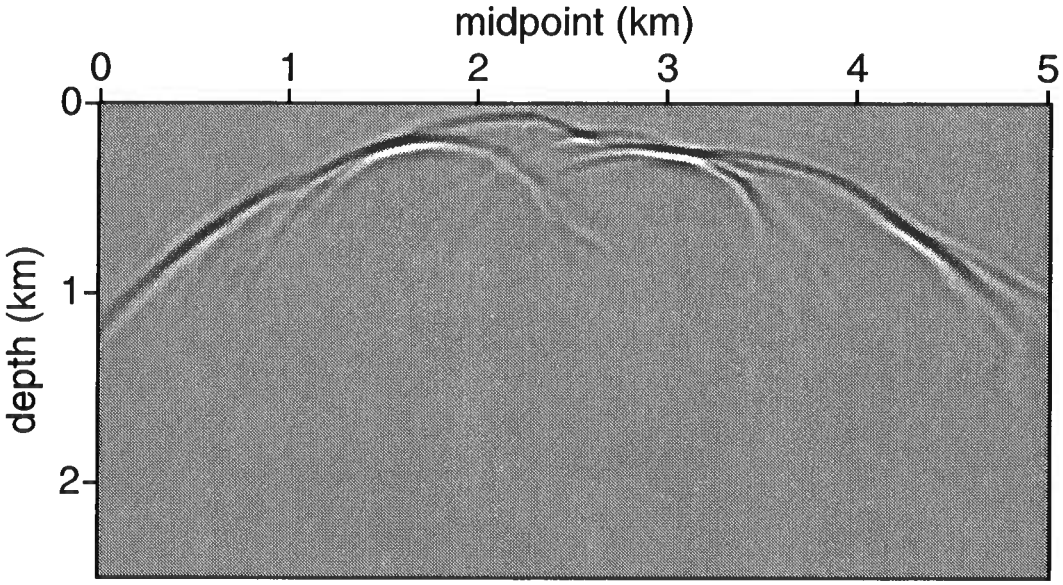

Figure 7.2. Snapshot of the pressure wavefield at time $t = 0.95$ s computed with the second order of the generalized-screen method for an explosion source. Figure 7.1 shows the wave speed model used and the source location. The gray scales represents amplitudes. A weak precursor associated with the compromise in contour deformation is visible (see Chapter 3).

accurately predicted by the GS method, because the GS method stays close to the path-integral representation for wave propagation. We now consider an elastic model where the P wave speed is given by Figure 7.1 and the S wave speed is simply given as half the P wave speed. All the following snapshots were computed by the *elastic* GS method which is the subject of this chapter. Again since the GS method stays close to the path-integral representation for wave propagation, it has no difficulty to account for continuous mode coupling between P and S. In the case of a horizontal point force, the horizontal particle velocity at time $t = 0.95$ s is shown in Figure 7.3(a); the vertical particle velocity at time $t = 0.95$ s is shown in Figure 7.3(b). The position of the P wavefront is identical to the one in Figure 7.2. Note the occurrence of mode coupling between the P and S wavefronts. Note also that S-wave energy is generated at the source. To observe the occurrence of S waves from converted P waves only we now invoke an explosion source. The horizontal particle velocity at time t = 0.95 s is shown in Figure 7.4(a); the vertical particle velocity at time $t = 0.95$ s is shown in Figure 7.4(b). In particular, comparing Figure 7.4(a) with Figure 7.2 illustrates the significant mode coupling occurring in such a medium.

We first introduce the wavefield directional decomposition procedure (Section 7.3). Directional decomposition maps the 'two-way' elastic wavefield into constituents that satisfy a coupled system of 'one-way' equations (Section 7.3.2). We then introduce the subsequent path-integral representations of the associated one-way wave propagators which

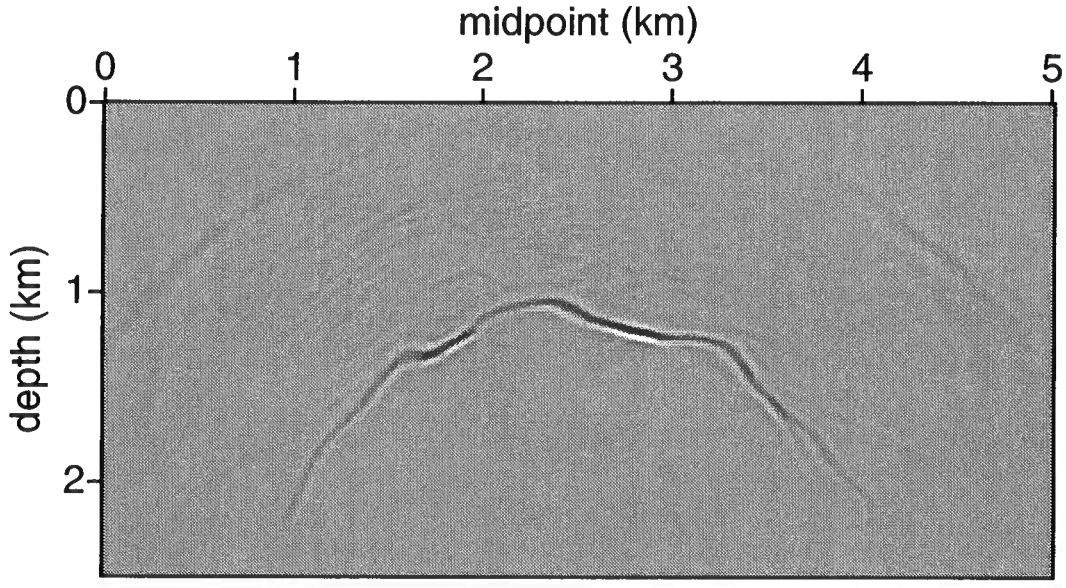

(a)

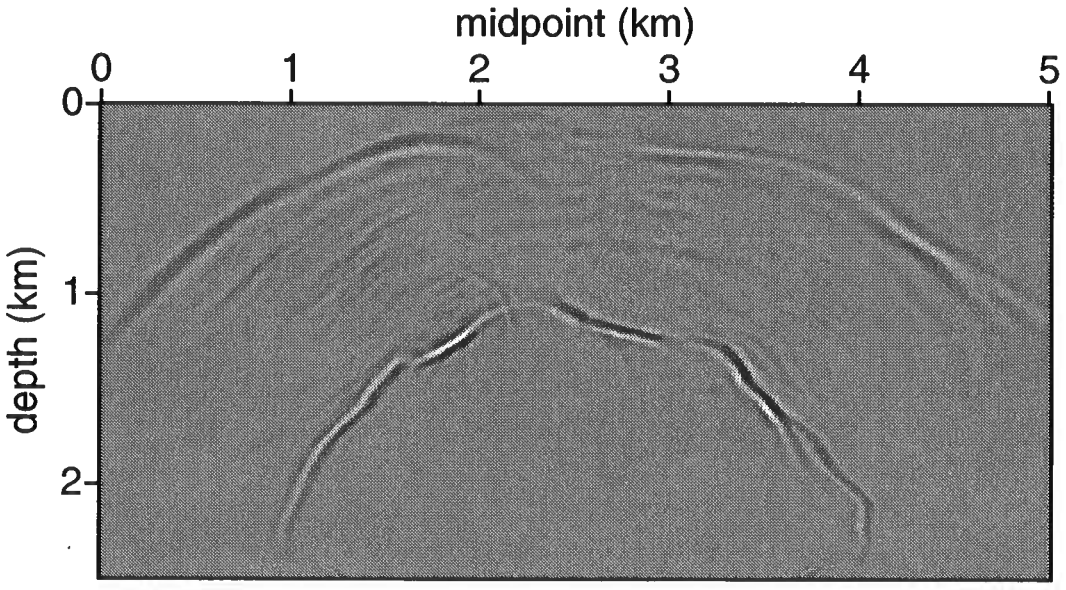

(b)

Figure 7.3. Snapshot of (a) the horizontal particle velocity and (b) vertical particle velocity at time $t = 0.95$ s computed with the first order of the generalized-screen method for a horizontal point force. Figure 7.1 shows the P wave speed model used and the source location.

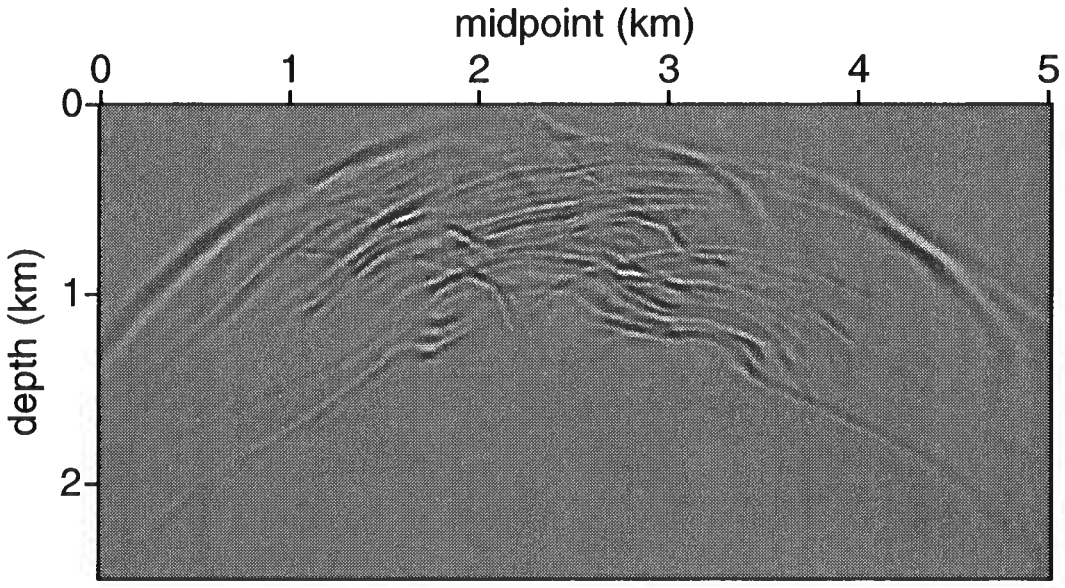

(a)

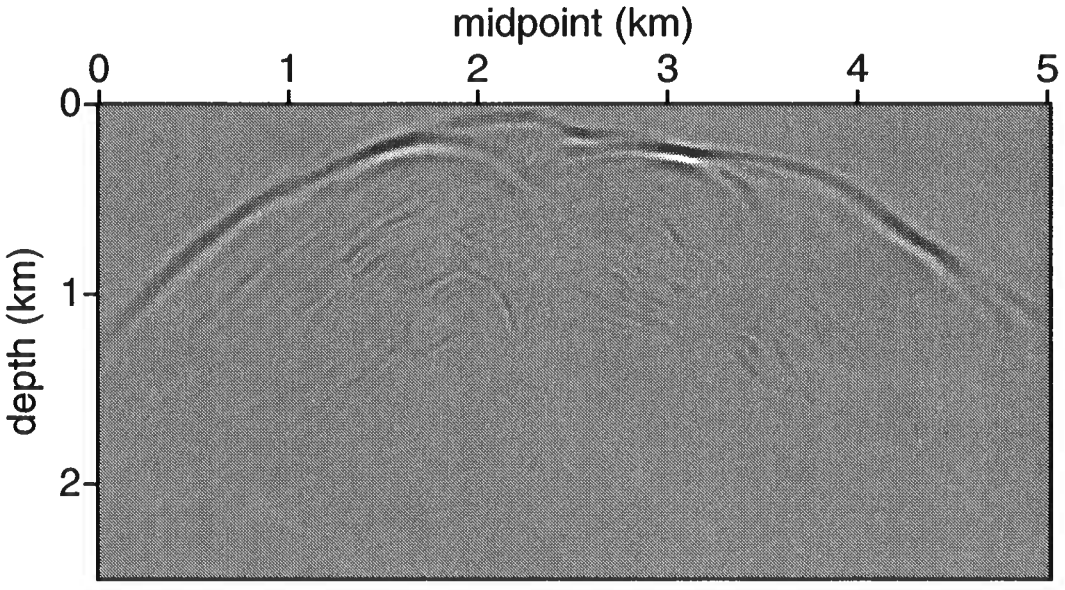

(b)

Figure 7.4. Snapshot of (a) the horizontal particle velocity and (b) vertical particle velocity at time $t = 0.95$ s computed with the first order of the generalized-screen method for an explosion source. Figure 7.1 shows the P wave speed model used and the source location.

are composed of a (cascade of) (i) forward Fourier transform, (ii) a multiplication by a phase factor, (iii) and an inverse Fourier transform (Section 7.4.1). Through the Fourier transforms, the space and wavenumber domains are 'dual' to one another. The applied phase-shift is proportional to the square-root Hamiltonian, an amplitude (Treves, 1980a) of the pseudodifferential operator that accounts for the scattering due to heterogeneities in the horizontal directions. We identify this operator as vertical slowness operator since the square-root Hamiltonian associates with vertical wave slowness. We discuss the choice of such an amplitude and make the choice to use the right (or dual) symbol (Treves, 1980a; Hörmander, 1985a; Shubin, 1987) of the vertical slowness operator.

The outline of the further analysis is as follows. We distinguish two parts. Part one focuses on the construction of the square-root Hamiltonian. Part two discusses the implementation of the associated one-way propagator. [Part one] Concerning the square-root Hamiltonian we have to solve an operator characteristic equation (Section 7.3.2) which induces the characteristic equation for the respective symbols (Section 7.5.3). As far as the right-hand side of the equation is concerned we distinguish the following steps: (i) Introduce a scaling to ensure ellipticity of the characteristic partial differential operator and (ii) decompose the operator symbol into terms of decreasing operator order (Section 7.3.3); (iii) switch from standard (left) to dual (right) symbol representation to simplify the necessary renormalization of the one-way wave propagator in the GS approximation (Sections 7.3.3 and 7.4.1); (iv) introduce an appropriate embedding and invoke a medium contrast formulation (Section 7.5.1); (v) re-expand decomposition (ii) with respect to smoothness and magnitude of medium contrast (Section 7.5.2) and (vi) introduce associated scaling parameters (Section 7.5.4). As far as the equality is concerned we employ the composition calculus of pseudodifferential operators (Section 7.5.3). As far as the left-hand side of the equation is concerned we distinguish steps: (i) introduce an expansion for the root (solution) of the type invoked for the right-hand side (v) which we anticipate from the framework of microlocal analysis (Section 7.5.5); (ii) substitute the expansion into the characteristic equation and identify terms of equal orders which leads to (iii) a recursion of symbol-matrix equations (Section 7.5.6); (iv) solve these equations with the aid of a diagonalization procedure to be taken in the embedding only (Section 7.5.7). The outlined procedure leads to a symbol expansion in which the space and phase dependencies are term-wise separated (the GS expansion).

[Part two] Concerning the one-way wave propagator we distinguish the following steps: (i) Introduce its Trotter-product representation (Section 7.4.1) out of which (ii) we extract the thin-slab propagator (Section 7.4.2); (iii) substitute the background and contrast terms for the square-root Hamiltonian appearing in the phase of the thin-slab propagator (Section 7.6.1); (iv) separate (approximately) the P and S constituents in the embedding (Section 7.6.1); (v) the embedding term is left in the exponential. The exponential containing the contrast terms is expanded about vertical propagation (first-order Taylor) and (vi) obtain an explicit split-step and contrast contribution (Section 7.6.2); (vii) substitute the GS expansion for the vertical slowness right symbol in the contrast contributions of the propagator (Section 7.6.3); (viii) renormalize to restore unitarity after the expansion of the exponential in (v) (Section 7.6.4).

7.3 Directional wavefield decomposition for elastic waves

The point at which the wave motion is observed is specified by the coordinates $\{x_1, x_2, x_3\}$ in a right-handed, orthogonal, Cartesian frame of reference. The direction of preference or principal direction is taken along the x_3-axis (or 'vertical' axis) and the remaining ('lateral', 'horizontal', or 'transverse') coordinates are denoted by x_μ, $\mu = 1, 2$.

In the case of an instantaneously reacting medium, the elastic wavefield satisfies the linear hyperbolic system of first-order partial differential equations,

$$\rho \partial_t \hat{v}_i - \partial_j \hat{\tau}_{ij} = \hat{f}_i \ , \quad i = 1, 2, 3 \ , \tag{7.1}$$

$$-\partial_t \hat{\tau}_{ij} + c_{ijkl} \, \tfrac{1}{2} (\partial_l \hat{v}_k + \partial_k \hat{v}_l) = c_{ijkl} \, \hat{h}_{kl} \ , \quad i, j = 1, 2, 3 \ , \tag{7.2}$$

where $\hat{\tau}_{ij}$ = stress, $\hat{v}_i$ = particle velocity, ρ = volume density of mass, c_{ijkl} = stiffness tensor, $\hat{f}_i$ = volume source density of force, $\hat{h}_{ij} = \hat{h}_{ji}$ = volume source density of deformation rate. The volume source density of force term, $\hat{f}$ is of importance for explosion sources, e.g., air-gun, while the volume source density of deformation rate term, $\hat{h}$, describes rupture mechanisms, e.g., earthquake sources (Dahlen & Tromp, 1998). The hats ($\hat{}$) are here used to denote the time domain. They will be removed once in the Laplace domain. For the analysis that we follow here we assume ρ and c_{ijkl} to be smooth whereas $\hat{f}$ and $\hat{h}_{ij}$ are allowed to be distributional.

The causality of the wave motion can be taken into account by carrying out a one-sided Laplace transform with respect to time, t, taking the Laplace-transform parameter, s, which in general is complex-valued, to be in the right half ($\mathrm{Re}(s) > 0$) of the complex s-plane. To show the notation, we give the expression for the particle velocity, at $\boldsymbol{x} = (x_1, x_2, x_3)$,

$$v_i(\boldsymbol{x}, s) = \int_0^\infty \hat{v}_i(\boldsymbol{x}, t) \exp[-st] \mathrm{d}t \ . \tag{7.3}$$

Under this transformation, we have $\partial_t \to s$. For an isotropic medium, we have

$$c_{ijkl} = (\kappa_P^{-1} - 2\kappa_S^{-1}) \delta_{ij} \delta_{kl} + \kappa_S^{-1} (\delta_{ik} \delta_{jl} + \delta_{il} \delta_{jk}) \ , \tag{7.4}$$

with $\kappa_P = (\lambda + 2\mu)^{-1}$ and $\kappa_S = \mu^{-1}$, where λ and μ are the Lamé parameters depending on the spatial coordinate only.

7.3.1 The reduced system of equations

In preparation of the directional decomposition, we extract the horizontal stresses, τ_{11}, τ_{12}, τ_{22} through

$$\partial_3 v_3 = \kappa_P \left(\kappa_P^{-1} h_{33} + \lambda (h_{11} + h_{22}) + s\tau_{33} - \lambda (\partial_1 v_1 + \partial_2 v_2) \right) \ , \tag{7.5}$$

which yields

$$-\tau_{11} = s^{-1}\Big[\kappa_P^{-1}h_{11} + \lambda(h_{22}+h_{33}) - \kappa_P^{-1}\partial_1 v_1 - \lambda\partial_2 v_2 \\ -\lambda\kappa_P\Big(\kappa_P^{-1}h_{33} + \lambda(h_{11}+h_{22}) + s\tau_{33} - \lambda(\partial_1 v_1 + \partial_2 v_2)\Big)\Big] , \tag{7.6}$$

$$-\tau_{22} = s^{-1}\Big[\kappa_P^{-1}h_{22} + \lambda(h_{11}+h_{33}) - \lambda\partial_1 v_1 - \kappa_P^{-1}\partial_2 v_2 \\ -\lambda\kappa_P\Big(\kappa_P^{-1}h_{33} + \lambda(h_{11}+h_{22}) + s\tau_{33} - \lambda(\partial_1 v_1 + \partial_2 v_2)\Big)\Big] , \tag{7.7}$$

$$-\tau_{12} = s^{-1}\left[2\kappa_S^{-1}h_{12} - \kappa_S^{-1}\left(\partial_1 v_2 + \partial_2 v_1\right)\right] . \tag{7.8}$$

Let

$$D_\nu = -s^{-1}\partial_\nu , \quad \nu = 1,2 , \tag{7.9}$$

represent the *horizontal slowness* operators. We introduce the composite field vectors F_I, $I = 1,2$ as

$$F_1 = \left(v_1, v_2, -\tau'_{33}\right)^T \quad \text{with } \tau'_{33} = \kappa_P^{1/2}\rho^{-1/2}\tau_{33} , \tag{7.10}$$

$$F_2 = \left(-\tau'_{13}, -\tau'_{23}, v_3\right)^T \quad \text{with } \tau'_{13} = \kappa_S^{1/2}\rho^{-1/2}\,\tau_{13} \text{ and } \tau'_{23} = \kappa_S^{1/2}\rho^{-1/2}\,\tau_{23} . \tag{7.11}$$

Here, we have normalized the traction entries to the dimensions of particle velocity following De Hoop and De Hoop (1994). In the Laplace domain, the system of equations (7.1)-(7.2) can then be cast in the form

$$(\partial_3\delta_{IJ} + sO_{IJ}(x_\mu, D_\nu, x_3))F_J = N_I - \Xi_{IJ}F_J , \tag{7.12}$$

where the differential operators O is a 2×2 matrix. The form of system (7.12) prepares for the diagonalization performed in the next section. Each block O_{IJ}, $I,J = 1,2$, is a 3×3 matrix given by $O_{11} = 0$, $O_{22} = 0$ and

$$O_{12} = \begin{pmatrix} (\kappa_S\rho)^{1/2} & 0 & -D_1 \\ 0 & (\kappa_S\rho)^{1/2} & -D_2 \\ -\kappa_P^{1/2}\rho^{-1/2}D_1(\kappa_S^{-1/2}\rho^{1/2}\,\cdot) & -\kappa_P^{1/2}\rho^{-1/2}D_2(\kappa_S^{-1/2}\rho^{1/2}\,\cdot) & (\kappa_P\rho)^{1/2} \end{pmatrix} .$$

O_{21} has entries $(O_{21})_{ij}$, $i,j = 1,2$, given by

$$(O_{21})_{11} = \kappa_S^{1/2}\rho^{-1/2}\left[\rho - D_1\left(d_{11}D_1\,\cdot\right) - D_2\left(\kappa_S^{-1}D_2\,\cdot\right)\right] ,$$

$$(O_{21})_{12} = -\kappa_S^{1/2}\rho^{-1/2}\left[D_1\left(d_{12}D_2\,\cdot\right) + D_2\left(\kappa_S^{-1}D_1\,\cdot\right)\right] ,$$

$$(O_{21})_{13} = -\kappa_S^{1/2}\rho^{-1/2}\left[D_1\left(\lambda\kappa_P^{1/2}\rho^{1/2}\,\cdot\right)\right] ,$$

$$(O_{21})_{31} = -\lambda\kappa_P(D_1\,\cdot) , (O_{21})_{33} = \kappa_P^{1/2}\rho^{1/2} .$$

Upon interchanging D_1 and D_2, the terms $(O_{21})_{21}$, $(O_{21})_{22}$, $(O_{21})_{23}$, and $(O_{21})_{32}$ are obtained from $(O_{21})_{22}$, $(O_{21})_{11}$, $(O_{21})_{13}$, and $(O_{21})_{31}$, respectively. When such 'symmetry' is present, we can restrict our analysis to the entries '11', '12', '13', '31' and '33' and infer results for the remaining entries. The parameters d_{11} and d_{12} were introduced by De Hoop and De Hoop (1994), and in an isotropic medium reduce to

$$d_{11} = 4\mu(\lambda+\mu)(\lambda+2\mu)^{-1} = 4\kappa_S^{-2}(\kappa_S-\kappa_P)\,, \tag{7.13}$$

$$d_{12} = 2\lambda\mu(\lambda+2\mu)^{-1} = 2\kappa_S^{-2}(\kappa_S-2\kappa_P)\,. \tag{7.14}$$

The 6×6 matrix Ξ, originating from the normalization of the traction entries (7.10) and (7.11), has three non-zero entries: $\Xi_{33} = \kappa_P^{1/2}\rho^{-1/2}\partial_3(\kappa_P^{-1/2}\rho^{1/2})$ and $\Xi_{44} = \Xi_{55} = \kappa_S^{1/2}\rho^{-1/2}\partial_3(\kappa_S^{-1/2}\rho^{1/2})$.

In the left hand side of system (7.12) we collect the terms in which medium parameters are subjected to differentiations in the horizontal directions. After diagonalization the left-hand side will account for the left-right scattering in the horizontal directions while the right-hand side will generate the up-down scattering in the vertical direction. The terms $\Xi_{IJ}F_J$ should occur on the right-hand side of system (7.12) because they involve differentiations of the medium parameter with respect to the vertical direction.

The (notional) source vectors, N_I, $I=1,2$ are given by
$N_1 = \left(2h_{13}, 2h_{23}, \kappa_P^{1/2}\rho^{-1/2}f_3\right)^T$ and

$$N_2 = \begin{pmatrix} \kappa_S^{1/2}\rho^{-1/2}\left[f_1 + D_1(d_{11}h_{11}+d_{12}h_{22}) + D_2(2\kappa_S^{-1}h_{12})\right] \\ \kappa_S^{1/2}\rho^{-1/2}\left[f_2 + D_2(d_{12}h_{11}+d_{11}h_{22}) + D_1(2\kappa_S^{-1}h_{12})\right] \\ \kappa_S^{-1}(\kappa_S-2\kappa_P)(h_{11}+h_{22}) + h_{33} \end{pmatrix}\,. \tag{7.15}$$

7.3.2 Directional decomposition

To achieve a directional decomposition of the elastic wavefield, we diagonalize system (7.12) – note that the vertical derivative contribution is already diagonal in the left-hand side of system (7.12). We write

$$F_I = L_{IJ}W_J\,, \tag{7.16}$$

where W_I is the composite wave vector, and W_1 and W_2 will be shown to relate to the down- and up-going wave constituents. The matrix L_{IJ} represents the change of basis in the diagonalization of system (7.12), i.e., is composed of the generalized eigenvectors of O. We call L_{IJ} the composition operator; L is a pseudodifferential operator (Shubin, 1987; Treves, 1980a; Hörmander, 1985a) acting on the horizontal coordinates, x_1 and x_2. Note that the elements of the wave matrix, W_I, may be physically 'non-observable'. We now show the construction of such an operator L.

Substituting the composition equation (7.16) into system (7.12) we obtain the following

system

$$\partial_3 L_{1J} W_J + s\, O_{12} L_{2J} W_J = -\Xi_{1I} L_{IJ} W_J + N_1 \,, \tag{7.17}$$
$$s\, O_{21} L_{1J} W_J + \partial_3 L_{2J} W_J = -\Xi_{2I} L_{IJ} W_J + N_2 \,. \tag{7.18}$$

Using the commutation relation

$$[\partial_3, L_{IJ}](\cdot) = \partial_3(L_{IJ}(\cdot)) - L_{IJ}\partial_3(\cdot) = (\partial_3 L_{IJ})(\cdot) \,, \tag{7.19}$$

(since the operator L_{IJ} depends on the x_3 variable, whereas it only acts on x_1 and x_2) we obtain

$$L_{1J}\partial_3 W_J + s\, O_{12} L_{2J} W_J = -((\partial_3 L_{1J}) + \Xi_{1I} L_{IJ}) W_J + N_1 \,, \tag{7.20}$$
$$s\, O_{21} L_{1J} W_J + L_{2J}\partial_3 W_J = -((\partial_3 L_{2J}) + \Xi_{1I} L_{IJ}) W_J + N_2 \,. \tag{7.21}$$

We shall construct the appropriate linear operator, L_{IJ}, such that the left-hand side of this system attains the form

$$L_{IJ}(\partial_3 \delta_{JM} + s\Lambda_{JM}) W_M = -((\partial_3 L_{IJ}) + \Xi_{IK} L_{KJ}) W_J + N_I \,, \tag{7.22}$$

such that the linear operator Λ_{IJ} is diagonal. The two diagonal entries of Λ_{IJ} will have opposite signs and be pseudodifferential with respect the horizontal directions, i.e., for $I = 1, 2$ $\Lambda_{II} = \Lambda_{II}(x_\mu, x_3, D_1, D_2)$. The diagonal entries of $\partial_3 \delta_{JM} + s\Lambda_{JM}$ therefore have the form of up- and down-going one-way wave operators, which have the appearance of a first-order hyperbolic operator in x_3 and t. Here the vertical direction, x_3, represents the evolution (continuation) parameter.

The associated generalized operator eigenvalue-eigenvector problem is represented by

$$O_{12} L_{21} = L_{11}\Lambda_{11} \,, \quad O_{12} L_{22} = L_{12}\Lambda_{22} \,, \tag{7.23}$$
$$O_{21} L_{11} = L_{21}\Lambda_{11} \,, \quad O_{21} L_{12} = L_{22}\Lambda_{22} \,, \tag{7.24}$$

which is obtained by comparing systems (7.20) and (7.21) with system (7.22). Let the diagonal entries of Λ_{IJ} be denoted as

$$\Lambda_{11} = \Gamma^{(+)} \,, \quad \Lambda_{22} = \Gamma^{(-)} \,.$$

To solve the generalized eigenvalue-eigenvector problem, we introduce the Ansatz

$$[L_{2J}, O_{21} O_{12}] = 0 \,, \quad J = 1, 2 \,. \tag{7.25}$$

It follows that $\Gamma^{(\pm)}$ must then satisfy the characteristic equation

$$\Gamma^{(\pm)} \Gamma^{(\pm)} = A \,, \quad A = O_{21} O_{12} \,, \tag{7.26}$$

(we call A the characteristic operator) while the L_{11} and L_{12} must satisfy

$$\left[O_{12}^{-1}L_{1J}, O_{21}O_{12}\right] = 0\,, \quad J = 1,2\,. \tag{7.27}$$

Reflecting the up-down symmetry of the medium, the solutions of equation (7.26) are

$$\Gamma^{(+)} = -\Gamma^{(-)} = \Gamma = A^{\frac{1}{2}}\,. \tag{7.28}$$

The square-root of A is well defined (with the aid of pseudodifferential calculus for instance (Treves, 1980a)) because we require $\mathrm{Re}(s) > 0$. If we want to relax such a condition, i.e., $s \to \mathrm{i}\omega$ we need to apply a microlocal cut-off; this corresponds to 'filtering' out so-called turning rays (see Sections 7.3.3 and 7.4.1). Up to smoothing contributions $\Gamma^{(\pm)}$ are the unique square-roots of A.

Note that because of the normalizations (7.10) and (7.11) of the traction entries, τ_{i3}, $i = 1,2,3$, the entries of the matrix operator A have consistent dimensions, slowness squared. Its square root, Γ, has the interpretation of *vertical slowness* operator.

A possible solution of equation (7.27) constitutes the generalized eigenvectors, L, composing the *composition* operator

$$L = \begin{pmatrix} O_{12} & O_{12} \\ \Gamma & -\Gamma \end{pmatrix}\,. \tag{7.29}$$

In terms of the inverse vertical slowness operator, $\Gamma^{-1} = A^{-1/2}$, the *decomposition* operator then follows as

$$L^{-1} = \tfrac{1}{2}\begin{pmatrix} O_{12}^{-1} & \Gamma^{-1} \\ O_{12}^{-1} & -\Gamma^{-1} \end{pmatrix}\,. \tag{7.30}$$

The (de)composition operators account for the radiation patterns of the different source and receiver types.

Using the decomposition operator, system (7.22) is transformed into

$$(\partial_3\delta_{IJ} + s\Lambda_{IJ})W_J = -(L^{-1})_{IJ}((\partial_3 L_{JK}) + \Xi_{JL}L_{LK})W_K + (L^{-1})_{IJ}N_J\,, \tag{7.31}$$

which can be interpreted as a coupled system of one-way wave equations. The coupling between the counter-propagating components, W_1 and W_2, is apparent in the first source-like term on the right-hand side, which can be written in the form

$$-L^{-1}(\partial_3 L) = \begin{pmatrix} T & R \\ R & T \end{pmatrix}\,, \tag{7.32}$$

in which T and R represent the *transmission* and *reflection* operators, respectively. We find

$$-T = \tfrac{1}{2}O_{12}^{-1}(\partial_3 O_{12}) + \tfrac{1}{2}\Gamma^{-1}(\partial_3\Gamma)\,,\ R = -\tfrac{1}{2}O_{12}^{-1}(\partial_3 O_{12}) + \tfrac{1}{2}\Gamma^{-1}(\partial_3\Gamma)\,. \tag{7.33}$$

7.3.3 The characteristic operator

The differential operator $A = (A_{ij})$ [see equation (7.26)] can be identified with the transverse Helmholtz operator (De Hoop, 1996), and is given by

$$A_{11} = \rho\kappa_S - \kappa_S^{1/2}\rho^{-1/2}\Big\{D_1\left[d_{11}D_1((\kappa_S\rho)^{1/2}\,\cdot)\right] + D_2\left[\kappa_S^{-1}D_2((\kappa_S\rho)^{1/2}\,\cdot)\right] - D_1\left[\lambda\kappa_P(D_1\,\kappa_S^{-1/2}\rho^{1/2}\cdot)\right]\Big\}\,, \tag{7.34}$$

$$A_{12} = -\kappa_S^{1/2}\rho^{-1/2}\Big\{D_1\left[d_{12}D_2((\kappa_S\rho)^{1/2}\,\cdot)\right] + D_2\left[\kappa_S^{-1}D_1((\kappa_S\rho)^{1/2}\,\cdot)\right] - D_1\left[\lambda\kappa_P(D_2\,\cdot)\kappa_S^{-1/2}\rho^{1/2}\right]\Big\}\,, \tag{7.35}$$

$$A_{13} = \kappa_S^{1/2}\rho^{-1/2}\Big\{-\rho D_1 + D_1\left[d_{11}D_1^2\,\cdot\right] + 2D_2\left[\kappa_S^{-1}D_2D_1\,\cdot\right] + D_1\left[d_{12}D_2^2\,\cdot\right] - D_1\left[\lambda\kappa_P\rho\,\cdot\right]\Big\}\,, \tag{7.36}$$

$$A_{31} = -\lambda\kappa_P D_1(\kappa_S^{1/2}\rho^{1/2}\,\cdot) - \kappa_P D_1(\kappa_S^{-1/2}\rho^{1/2}\cdot)\,, \tag{7.37}$$

$$A_{33} = \lambda\kappa_P(D_1^2 + D_2^2) + \rho\kappa_P\,. \tag{7.38}$$

The (left) symbol[2] of D_ν is defined as $\mathrm{i}\alpha_\nu$, the horizontal slowness. We decompose the symbol a of the characteristic operator, A, according to the symbol order,

$$a = a_{[2]} + a_{[1]} + a_{[0]}\,. \tag{7.39}$$

This ordered polyhomogeneous expansion is defined according to

$$a_{[2-j]}(x_\mu, x_3; s\alpha_\nu, s\kappa_P, s\kappa_S, s\rho) = s^{2-j}\; a_{[2-j]}(x_\mu, x_3; \alpha_\nu, \kappa_P, \kappa_S, \rho)\,. \tag{7.40}$$

Note that the i^{th} term in decomposition (7.39) then contains i^{th}-order derivatives of the medium parameters. This will give us control over the smoothness of the terms in the GS expansion of the vertical slowness symbol with respect to the medium variations (see Section 7.5).

The principal part $a_{[2]} = (a_{ij\,[2]})$ corresponds to the higher-order term, i.e., the 'high-

[2]The (left) symbol h of a differential or pseudodifferential operator H in $\mathbb{R}^n$ is defined as

$$(H\varphi)(\boldsymbol{x}) = (s/2\pi)^n \iint \exp[-\mathrm{i}s(x_\sigma - y_\sigma)\alpha_\sigma]\, h(\boldsymbol{x}, \boldsymbol{\alpha})\, \varphi(y)\, \mathrm{d}\boldsymbol{y}\, \mathrm{d}\boldsymbol{\alpha}\,.$$

Note that because of the conventions used here we have changed variables, $\boldsymbol{\alpha} = \boldsymbol{\xi}/s$, in the original Fourier transform. The right symbol h_r of H is defined as

$$(H\varphi)(\boldsymbol{x}) = (s/2\pi)^n \iint \exp[-\mathrm{i}s(x_\sigma - y_\sigma)\alpha_\sigma]\, h_r(\boldsymbol{y}, \boldsymbol{\alpha})\, \varphi(y)\, \mathrm{d}\boldsymbol{y}\, \mathrm{d}\boldsymbol{\alpha}\,.$$

frequency' approximation of the symbol (Hörmander, 1985a, Chapter18), which is then given by

$$a_{11[2]} = \kappa_S\rho + 3\alpha_1^2 - 2\kappa_P\kappa_S^{-1}\alpha_1^2 + \alpha_2^2 , \tag{7.41}$$

$$a_{12[2]} = 2\alpha_1\alpha_2\kappa_S^{-1}(\kappa_S - \kappa_P) , \tag{7.42}$$

$$a_{13[2]} = 2\rho^{1/2}\kappa_S^{-1/2}(\kappa_P - \kappa_S)\mathrm{i}\alpha_1 + 4\rho^{-1/2}\kappa_S^{-1/2}(\kappa_S^{-1}\kappa_P - 1)\mathrm{i}(\alpha_1^3 + \alpha_1\alpha_2^2) , \tag{7.43}$$

$$a_{31[2]} = \rho^{1/2}\kappa_S^{-1/2}(\kappa_P - \kappa_S)\mathrm{i}\alpha_1 , \tag{7.44}$$

$$a_{33[2]} = \kappa_P\rho + (2\kappa_P - \kappa_S)\kappa_S^{-1}(\alpha_1^2 + \alpha_2^2) . \tag{7.45}$$

The principal symbol, $a_{[2]}$, is of interest since it governs the propagation of the singularities, i.e., the geometry of the wave propagation (Hörmander, 1985a, theorem 18.1.28). The eigenvalues of the symbol matrix $a_{[2]}$ are $\kappa_S\rho+\alpha_\nu\alpha_\nu = c_S^{-2}+\alpha_\nu\alpha_\nu$, with multiplicity 2, and $\kappa_P\rho+\alpha_\nu\alpha_\nu = c_P^{-2}+\alpha_\nu\alpha_\nu$, with multiplicity 1. Thus $\det(a_{[2]}) \neq 0$, which implies that A is an elliptic partial differential operator. This guarantees the existence of its (pseudodifferential) square-root, Γ (Treves, 1980a, proposition 4.2). This is however not valid anymore if the condition that $\mathrm{Re}(s) > 0$ is relaxed. The eigenvalues of the symbol matrix $a_{[2]}$ can then be zero for some values of α_1 and α_2 that correspond to (P and S) turning rays. With pseudodifferential cutoffs we can 'filter' out those turning rays and still use microlocal techniques to compute the square-root of A away from those turning rays. This is usually done in practice when one uses the Fourier transform in time rather than the Laplace transform in time. For an alternative method to compute the square-root of A that goes beyond the reach of microlocal analysis in the case of fluid-acoustics we refer to De Hoop and Gautesen (2001).

Note that in the present chapter, the analysis is carried out with the *right* (or *dual*) symbol calculus (see Section 7.4.1). The correspondence between left, a_l, and right, a_r, symbols of pseudodifferential operators is given by (Treves, 1980a; Hörmander, 1985a; Shubin, 1987)

$$a_r(x'_\mu, \alpha_\nu) = \exp\left[\,\mathrm{i}\partial_{\alpha_\sigma} D_{x_\sigma}\right] a_l(x_\mu, \alpha_\nu)\Big|_{x_\mu = x'_\mu} , \tag{7.46}$$

shown here for the characteristic operator, A. Note that the principal part, $a_{[2]}$, is shared by the left and right symbols.

Following equation (7.40) we decompose the right symbol a_r according to the symbol order: $a_r = a_{[2]} + a_{r[1]} + a_{r[0]} + a_{r[-1]}$. In Appendix M, we show the entries of the term $a_{r[1]}$.

7.4 The one-way wave propagator

In this section we introduce the Trotter-product representation of the one-way wave propagator (Section 7.4.1) out of which we extract the thin-slab propagator (Section 7.4.2).

To arrive at a coupled system of integral equations that is equivalent to equation (7.31) and that can be solved in terms of a Neumann expansion, we have to invert the operator

occurring on the left-hand side. Such Neumann expansion induces the Bremmer coupling series. We refer the reader to De Hoop (1996) and De Hoop *et al.* (2000) for details and discussions on the Bremmer series [practical implementation of the Bremmer coupling series can be found in Van Stralen *et al.* (1998) and Le Rousseau and De Hoop (2001b)].

We set $\mathrm{G}^{(\pm)} = (\partial_3 + s\Gamma^{(\pm)})^{-1}$. The one-sided elementary kernels $\mathcal{G}^{(\pm)}(x_\mu, x_3; x'_\nu, x'_3)$ associated with these operators are the so-called one-way Green's functions. They satisfy the equations

$$(\partial_3 + s\Gamma^{(\pm)})\mathcal{G}^{(\pm)} = \delta(x_\nu - x'_\nu)\,\delta(x_3 - x'_3)\;, \tag{7.47}$$

together with the condition of causality enforcing that $\mathcal{G}^{(\pm)}$ decays as $x_3 \to \pm\infty$.

7.4.1 The Trotter product representation

If the medium in the interval $[x'_3, x_3]$ were weakly varying in the vertical direction, the Green's function $\mathcal{G}^{(\pm)}$, can be represented by a Hamiltonian path integral (De Witte-Morette *et al.*, 1979), with measure $\mathcal{D}$ on configuration space, i.e., the space of all possible paths between the input point $\boldsymbol{x}'$ and the output point $\boldsymbol{x}$ (Robbin & Salamon, 1993),

$$\mathcal{G}^{(\pm)}(x_\mu, x_3; x'_\nu, x'_3) = \pm H(\mp[x'_3 - x_3]) \int_P \mathcal{D}(x''_\mu, \alpha''_\nu) \tag{7.48}$$
$$\exp\left[-s\int_{\zeta=x'_3}^{x_3} \mathrm{d}\zeta\{\mathrm{i}\alpha''_\sigma(d_\zeta x''_\sigma) + \gamma_a^{(\pm)}(x''_\mu, x''_\mu, \zeta, \alpha''_\nu)\}\right]\;,$$

P being a set of paths $(x''_\mu(\zeta),\ \alpha''_\nu(\zeta))$ in (horizontal) phase space satisfying $x''_\mu(\zeta = x'_3) = x'_\mu$, $x''_\mu(\zeta = x_3) = x_\mu$. Path integral representations for wave propagation were also considered by Fishman and McCoy (1984b). The path integral (7.48) is an integration over all the possible paths that connect the input point $\boldsymbol{x}'$ and the output point $\boldsymbol{x}$ with the proper phase evolution. It therefore not only accounts for energy traveling along the rays (stationary paths) but also for the transport along non-stationary paths. It then naturally contains all possible multi-pathing, and mode-coupling. The *phase* function in the propagator (7.48) is responsible for shape of the wave front set. The important term in the phase is $\gamma_a^{(\pm)}$[3]. It generates the pseudodifferential operator $\Gamma^{(\pm)}$ (vertical slowness operator): for ϕ a test function ($\phi \in \mathcal{C}_0^\infty$)

$$(\Gamma^{(\pm)}\phi)(x_\mu, \zeta) = (s/2\pi)^2 \int \mathrm{d}\alpha''_1 \mathrm{d}\alpha''_2$$
$$\int \mathrm{d}x'_1 \mathrm{d}x'_2\ \exp[-\mathrm{i}s(x_\sigma - x'_\sigma)\alpha''_\sigma]\ \gamma_a^{(\pm)}(x_\mu, x'_\sigma, \zeta, \alpha''_\nu)\ \phi(x'_\sigma, \zeta)\;.$$

[3]To be more precise only the principal part of $\gamma_a^{(\pm)}$ is responsible for the shape of the wave front set. The rest of the amplitude $\gamma_a^{(\pm)}$ is of order 0 and so is its exponential (Hörmander, 1971, proposition 1.1.8). That part therefore contributes to the amplitude of the fundamental solution.

In this sense the one-way wave propagator accounts for the transverse scattering. There is not a unique choice for $\gamma_a^{(\pm)}$ in this representation of the action of $\Gamma^{(\pm)}$ (Treves, 1980a, proof of Theorem 4.1). We refer to $\gamma_a^{(\pm)}$ as to *an* amplitude of $\Gamma^{(\pm)}$ (Treves, 1980a).

With the Trotter product formula (De Witte-Morette *et al.*, 1979; Schulman, 1981), the path integral in equation (7.48) is to be interpreted as

$$\mathcal{G}^{(\pm)}(x_\mu, x_3; x'_\nu, x'_3) = \pm H(\mp[x'_3 - x_3]) \lim_{K\to\infty} \int \prod_{i=1}^{K} (s/2\pi)^2 \mathrm{d}\alpha_1^{(i)} \mathrm{d}\alpha_2^{(i)} \prod_{j=1}^{K-1} \mathrm{d}x_1^{(j)} \mathrm{d}x_2^{(j)}$$
$$\exp\left[-s\sum_{k=1}^{K}\{\mathrm{i}\alpha_\sigma^{(k)}(x_\sigma^{(k)} - x_\sigma^{(k-1)}) + \gamma_a^{(\pm)}(x_\mu^{(k)}, x_\mu^{(k-1)}, \zeta_k - \tfrac{1}{2}K^{-1}\Delta x_3, \alpha_\nu^{(k)})K^{-1}\Delta x_3\}\right] \tag{7.49}$$

with $x_\mu^{(0)} = x'_\mu$, $x_\mu^{(K)} = x_\mu$, and $\Delta x_3 = x_3 - x'_3$. All the integrations are taken over the interval $(-\infty, \infty)$, $K^{-1}\Delta x_3$ is the step size in ζ, and $(x_\mu^{(j)}, \alpha_\nu^{(j)})$ are the coordinates of a path at the discrete values ζ_j of ζ as $j = 1, \cdots, K$. The Trotter product formula representation of the path integration shows how every path, now on a lattice, between the input point $\boldsymbol{x}'$ and the output point $\boldsymbol{x}$ is taken into account.

Note that for finite K, and Δx_3 small enough propagator (7.49) can be interpreted as a Lagrangian distribution (Hörmander, 1985b). De Hoop *et al.* (2001a) show that it can then be viewed as the kernel of the composition of K Fourier integral operators (Hörmander, 1985b; Treves, 1980b; Duistermaat, 1996). Observe that this is possible because one has inserted a (pseudodifferential) cut-off function in order to stay away from so-called 'turning' rays (De Hoop *et al.*, 2001a).

The issue of operator ordering in path integration (Mayes & Dowker, 1972; Dowker, 1976) is reflected by the particular choice of $\gamma_a^{(\pm)}$ in the phase function in propagator (7.49). A possible choice, commonly made in the context of quantum mechanics, is the Weyl symbol, $\gamma_w^{(\pm)}$ (Hörmander, 1979; Hörmander, 1985a); then

$$\gamma_a^{(\pm)}(x_\mu^{(k)}, x_\mu^{(k-1)}, \zeta_k - \tfrac{1}{2}K^{-1}\Delta x_3, \alpha_\nu^{(k)}) = \gamma_w^{(\pm)}((x_\mu^{(k)} + x_\mu^{(k-1)})/2, \zeta_k - \tfrac{1}{2}K^{-1}\Delta x_3, \alpha_\nu^{(k)}) \,.$$

The Weyl symbol calculus offers advantages such as the separation of heterogeneity from anisotropy (Fishman *et al.*, 2000) but implies more complex (implicit) numerical algorithms. Here, we make the choice of the right (or dual) symbol, $\gamma_r^{(\pm)}$:

$$\gamma_a^{(\pm)}(x_\mu^{(k)}, x_\mu^{(k-1)}, \zeta_k - \tfrac{1}{2}K^{-1}\Delta x_3, \alpha_\nu^{(k)}) = \gamma_r^{(\pm)}(x_\mu^{(k-1)}, \zeta_k - \tfrac{1}{2}K^{-1}\Delta x_3, \alpha_\nu^{(k)}) \,.$$

The GS expansion of the symbol (see below) breaks the unitarity of the exponential of the phase function in the oscillatory integral representation of the propagator which is (approximately) repaired by a normalization. This normalization procedure occurs in the Fourier $(\alpha_1 - \alpha_2)$ domain, which enforces the use of the right symbol. The asymptotic

relation between the right and Weyl symbols is given by

$$\gamma_r^{(\pm)}(x_\mu, \zeta_k - \tfrac{1}{2}K^{-1}\Delta x_3, \alpha_\nu) = \exp[\tfrac{1}{2}\mathrm{i}\partial_{\alpha_\sigma} D_{x_\sigma}]\, \gamma_w^{(\pm)}(x_\mu, \zeta_k - \tfrac{1}{2}K^{-1}\Delta x_3, \alpha_\nu)\ .$$

No matter what choice we make for $\gamma_a^{(\pm)}$ in propagator (7.49) it will have dependencies on both the spatial and Fourier variables. This induces high computational complexity for the direct (numerical) evaluation of propagator (7.49).

7.4.2 The thin-slab propagator

If Δx_3 is sufficiently small (thin slab), propagator (7.49) reduces to ($K = 1$)

$$\int \mathrm{d}x_1'\mathrm{d}x_2'\ g^{(\pm)}(x_\mu, x_3; x_\nu', x_3')(\cdot) \simeq \int (s/2\pi)^2 \mathrm{d}\alpha_1''\mathrm{d}\alpha_2'' \exp[-\mathrm{i}s\,\alpha_\sigma'' x_\sigma]$$
$$\int \mathrm{d}x_1'\mathrm{d}x_2' \exp[\mathrm{i}s\,\alpha_\sigma'' x_\sigma'] \exp[-s\,\gamma_r^{(\pm)}(x_\nu', x_3 - \tfrac{1}{2}\Delta x_3, \alpha_\nu'')\Delta x_3](\cdot)\ . \qquad (7.50)$$

Thus, thin-slab propagation is composed of a forward Fourier transform coupled to a multiplication by a phase factor (the phase is proportional to the vertical slowness right symbol) and an inverse Fourier transform. Wu's point of departure is the analysis of (plane) wave scattering from the thin slab in the Born approximation combined with a paraxial approximation (Wu, 1994). Thus Wu's approach accounts for small-angle scattering with *weak* medium contrasts and does not treat any back scattering. We employ no such approximations.

7.5 Generalized-screen recursion for the vertical slowness symbol

We show now that we can separate the space and phase dependencies of the vertical slowness right symbol. This will induce the reduction of the computational complexity of the (thin-slab) propagator. To obtain such a separation we first introduce an embedding and invoke a medium contrast formulation (Section 7.5.1); we then expand the symbol of the characteristic operator, A, with respect to smoothness (operator order) and magnitude of medium contrast (Section 7.5.2) and introduce the associated scaling parameters (Section 7.5.4); we introduce an expansion of the vertical slowness right symbol of the type invoked for the symbol of A, which we anticipate from the framework of microlocal analysis (Section 7.5.5); we substitute the expansion into the characteristic equation (Section 7.5.3) and identify terms of equal orders which leads to a recursion of symbol-matrix equations (Section 7.5.6); we solve these equations with the aid of a diagonalization procedure to be taken in the embedding only (Section 7.5.7). Such expansion of the vertical slowness right symbol is denoted as the generalized-screen expansion of the symbol. In this expansion the space and phase dependencies are term-wise separated. The analysis here involves matrix symbols rather than scalar symbol in the acoustic case. We analyze the form of the terms in the expansion in a basis that (approximately) separates P and S contributions (this basis is associated to the embedding only) and compare with the scalar case. On one hand, in the

first order terms in the GS expansion of the principal part of the vertical slowness symbol, we note that the diagonal entries of correspond with the first-order term of the mode-wise scalar screen expansion. On the other hand the off-diagonal entries contribute to the mode coupling.

Insertion of the expanded symbol in the thin-slab propagator (7.50) then yields the generalized screen thin-slab propagator (Section 7.6).

7.5.1 Contrast formulation

We introduce a background medium, with parameters ρ^0, κ_P^0, and κ_S^0 in the slab $[x_3', x_3]$ with thickness $\Delta x_3 = x_3 - x_3'$. The background medium is constant within the slab, but may vary from one slab to another: $\rho^0(\zeta) = \rho^0(x_3)$, $\kappa_P^0(\zeta) = \kappa_P^0(x_3)$ and $\kappa_S^0(\zeta) = \kappa_S^0(x_3)$ for $\zeta \in [x_3', x_3]$. We shall employ a *contrast* formulation. The medium perturbations, ϵ_ρ, ϵ_P, and ϵ_S, are given by

$$\kappa_P(x_\mu,\zeta) = \kappa_P^0(x_3)\,[1+\epsilon_P(x_\mu,\zeta)]\ , \quad \kappa_S(x_\mu,\zeta) = \kappa_S^0(x_3)\,[1+\epsilon_S(x_\mu,\zeta)]\ , \tag{7.51}$$

$$\rho(x_\mu,\zeta) = \rho^0(x_3)\,[1+\epsilon_\rho(x_\mu,\zeta)]\ , \tag{7.52}$$

for $\zeta \in [x_3', x_3]$. The wave speeds follow as

$$c_P = (\kappa_P\rho)^{-1/2}\ , \quad c_P^0 = (\kappa_P^0\rho^0)^{-1/2}\ , \quad c_S = (\kappa_S\rho)^{-1/2}\ , \quad c_S^0 = (\kappa_S^0\rho^0)^{-1/2}\ . \tag{7.53}$$

The background parameters should be chosen in such a way that the introduction of artificial branch points in the propagating-wave regime is avoided. This implies the conditions (De Hoop *et al.*, 2000; Le Rousseau & De Hoop, 2001b): $c_P(x_\mu,\zeta) \geq c_P^0(x_3)$, $c_S(x_\mu,\zeta) \geq c_S^0(x_3)$. However, because of the coupling between the P and S constituents in the wave matrix, W, this also implies the two additional conditions

$$c_P(x_\mu,\zeta) \geq c_S^0(x_3)\ , \quad c_S(x_\mu,\zeta) \geq c_P^0(x_3)\ . \tag{7.54}$$

On the one hand, the first condition in equation (7.54) is naturally satisfied. On the other hand, the second condition in equation (7.54) enforces the choice $c_P^0(x_3) = c_S^0(x_3)$, which would lead to inaccuracies in the further development. Instead, to circumvent those, we shall introduce two background media: one for each (P and S) constituent of the wave matrix (see Section 7.6 on the generalized-screen propagator).

7.5.2 Expansion of the characteristic operator symbol

We shall now expand the right symbol a_r of A, simultaneously in medium contrast (the order is indicated by a superscript) and in symbol (or operator) order (this order is indicated by a subscript). Expanding the right symbol a_r in symbol order yields the decomposition

$$a_r = a_{r[2]} + a_{r[1]} + a_{r[0]} + a_{r[-1]}\ , \tag{7.55}$$

whereas expanding each term in medium contrast yields

$$a_{r[2]} \sim a_{r\,[2]}^{[0]} + \sum_{i=1}^{\infty} a_{r\,[2]}^{[i]} \,,\; a_{r[1]} \sim \sum_{i=1}^{\infty} a_{r\,[1]}^{[i]} \,,\; a_{r[0]} \sim \sum_{i=2}^{\infty} a_{r\,[0]}^{[i]} \,,\; a_{r[-1]} \sim \sum_{i=2}^{\infty} a_{r\,[-1]}^{[i]} \,. \tag{7.56}$$

We show the first three terms of the expansion of the principal part $a_{r\,[2]}^{[0]} = a_{[2]}$. The background term, $a_{[2]}^{[0]} = (a_{r,ij\,[2]}^{[0]})$, zero order in medium contrast, zero order in operator order, is given by

$$a_{r,11\,[2]}^{[0]} = 3\alpha_1^2 + \alpha_2^2 - 2\alpha_1^2[c_S^0]^2[c_P^0]^{-2} + [c_S^0]^{-2} \,, \tag{7.57}$$

$$a_{r,12\,[2]}^{[0]} = 2\alpha_1\alpha_2[c_S^0]^2[c_{PS}^0]^{-2} \,, \tag{7.58}$$

$$a_{r,13\,[2]}^{[0]} = -2[c_{PS}^0]^{-2}c_S^0 \mathrm{i}\alpha_1 - 4\mathrm{i}[c_{PS}^0]^{-2}[c_S^0]^3\mathrm{i}(\alpha_1^3 + \alpha_1\alpha_2^2) \,, \tag{7.59}$$

$$a_{r,31\,[2]}^{[0]} = -[c_{PS}^0]^{-2}[c_S^0]\mathrm{i}\alpha_1 \,, \tag{7.60}$$

$$a_{r,33\,[2]}^{[0]} = [c_P^0]^{-2} + \alpha_\nu\alpha_\nu[c_S^0]^2(2[c_P^0]^{-2} - [c_S^0]^{-2}) \,. \tag{7.61}$$

with $[c_{PS}^0]^{-2} = [c_S^0]^{-2} - [c_P^0]^{-2}$. This background term is diagonalized according to

$$a_{r\,[2]}^{[0]} = M^0\,[\pi^0]^2\,[M^0]^{-1} \,, \tag{7.62}$$

where π^0 is the diagonal matrix

$$[\pi^0]^2 = \mathrm{diag}\,\left([c_S^0]^{-2} + \alpha_\nu\alpha_\nu,\; [c_S^0]^{-2} + \alpha_\nu\alpha_\nu,\; [c_P^0]^{-2} + \alpha_\nu\alpha_\nu\right) \,, \tag{7.63}$$

which reveals the three wave speeds of the P- and S-wave polarizations in the background medium. The diagonalizing matrix is given by

$$M^0 = \begin{pmatrix} -\frac{\mathrm{i}\alpha_1}{\sqrt{\alpha_\nu\alpha_\nu}}\left[1 + 2[c_S^0]^2(\alpha_\nu\alpha_\nu)\right] & -\frac{\mathrm{i}\alpha_2}{\sqrt{\alpha_\nu\alpha_\nu}} & 2\mathrm{i}c_S^0\alpha_1 \\ -\frac{\mathrm{i}\alpha_2}{\sqrt{\alpha_\nu\alpha_\nu}}\left[1 + 2[c_S^0]^2(\alpha_\nu\alpha_\nu)\right] & \frac{\mathrm{i}\alpha_1}{\sqrt{\alpha_\nu\alpha_\nu}} & 2\mathrm{i}c_S^0\alpha_2 \\ -c_S^0\sqrt{\alpha_\nu\alpha_\nu} & 0 & 1 \end{pmatrix} \,, \tag{7.64}$$

and its inverse by

$$[M^0]^{-1} = \begin{pmatrix} \frac{\mathrm{i}\alpha_1}{\sqrt{\alpha_\nu\alpha_\nu}} & \frac{\mathrm{i}\alpha_2}{\sqrt{\alpha_\nu\alpha_\nu}} & 2c_S^0\sqrt{\alpha_\nu\alpha_\nu} \\ \frac{\mathrm{i}\alpha_2}{\sqrt{\alpha_\nu\alpha_\nu}} & -\frac{\mathrm{i}\alpha_1}{\sqrt{\alpha_\nu\alpha_\nu}} & 0 \\ \mathrm{i}c_S^0\alpha_1 & \mathrm{i}c_S^0\alpha_2 & 1 + 2[c_S^0]^2(\alpha_\nu\alpha_\nu) \end{pmatrix} \,. \tag{7.65}$$

Observe that only the S wave speed appears in the separation of the P and S constituents of either wave matrix component.

Higher-order terms in both medium contrast and operator orders can be found in Ap-

pendix N. First-order terms in symbol order account for the gradient in medium properties.

7.5.3 The characteristic symbol equation

Given the symbol a_r, we now have to construct the vertical slowness right symbol, γ_r. This symbol satisfies a characteristic equation following the composition of operators in equation (7.28) (Treves, 1980a; Hörmander, 1985a; Shubin, 1987; De Hoop, 1996):

$$\exp\left[\mathrm{i}\,\partial_{\alpha'_\sigma} D_{x'_\sigma}\right]\,\gamma_r(x_\mu,\zeta,\alpha'_\sigma)\gamma_r(x'_\sigma,\zeta,\alpha_\nu)\Big|_{(x'_\mu,\alpha'_\nu)=(x_\mu,\alpha_\nu)} = a_r(x_\mu,\zeta,\alpha_\nu)\;. \tag{7.66}$$

This equation defines the generalized slowness surface. The two branches are $\gamma_r^{(\pm)}$ such that the real part of the eigenvalues of $\gamma_r^{(+)}$ are positive and the real part of the eigenvalues of $\gamma_r^{(-)}$ are negative. Due to the local up/down symmetry of the medium we have $\gamma_r^{(+)} = -\gamma_r^{(-)}$. Note that as $s \to \infty$ the composition of symbols tends to an ordinary multiplication, and the solution of equation (7.66) reduces to the principal parts of the symbols. The eigenvalues of the principal part of the vertical slowness symbol correspond to the vertical gradient of travel time for the three polarizations, in accordance with the eikonal equation [which can be obtained from the high-frequency approximation of the path integral, see De Hoop (1996)].

7.5.4 Scaling

The solution to equation (7.66), γ_r, will be constructed by means of a (polyhomogeneous) series expansion following the expansion of a_r introduced above. To ease the identification of medium-contrast and symbol orders in the construction, we introduce two dimensionless parameters, χ associated with the medium contrast and Ω associated with the symbol order. With these parameters, we control the *magnitude* of medium contrast (χ) and *smoothness* (Ω), i.e.,

$$\epsilon_P(x_\mu,\zeta) = \chi\,\mathsf{e}_P(\Omega x_\mu,\zeta)\;,\quad \epsilon_S(x_\mu,\zeta) = \chi\,\mathsf{e}_S(\Omega x_\mu,\zeta)\;,\quad \epsilon_\rho(x_\mu,\zeta) = \chi\,\mathsf{e}_\rho(\Omega x_\mu,\zeta). \tag{7.67}$$

We introduce the scaled horizontal slowness operators D_μ which differentiates with respect to Ωx_μ: $\mathsf{D}_\mu = \Omega^{-1} D_\mu$. Then, we have, for instance $D_\nu \mathsf{e}_P(\Omega x_\mu,\zeta) = \Omega \mathsf{D}_\nu \mathsf{e}_P(\Omega x_\mu,\zeta)$ which explicitly shows the operator order through the power of Ω. Thus, $a^{[j]}_{[2-i]}$ is homogeneous of degree i in Ω and homogeneous of degree j in χ. The introduction of scaling factors facilitates the identification of terms of the same order in medium contrast and medium smoothness in the following treatment.

7.5.5 The expansion of vertical slowness right symbol

In view of the contrast formulation, the vertical slowness in the laterally homogeneous embedding is introduced as

$$\gamma^0(\zeta,\alpha_\nu,s)\widehat{=}\left[a^{[0]}_{[2]}(x_3,\alpha_\nu)\right]^{1/2}=\gamma^0(x_3,\alpha_\nu)\ \text{ if }\ \zeta\in[x'_3,x_3]\,. \tag{7.68}$$

We assume that the vertical slowness symbol can be represented by a perturbation, γ^1_r say, superimposed on the vertical slowness in the laterally homogeneous embedding,

$$\gamma_r(x_\mu,\zeta,\alpha_\nu,s)=\gamma^0(x_3,\alpha_\nu)+\gamma^1_r(x_\mu,\zeta,\alpha_\nu,s)\ \text{ if }\ \zeta\in[x'_3,x_3]\,. \tag{7.69}$$

First, let us expand the vertical slowness perturbation, asymptotically in the magnitude of medium perturbation, i.e.,

$$\gamma^1_r(x_\mu,\zeta,\alpha_\nu,s)\sim\sum_{n=1}^{\infty}\chi^n\,\eta^{[n]}(x_\mu,\zeta,\alpha_\nu,s)\,. \tag{7.70}$$

This expansion bears resemblance with the Born series expansion.

Second, we expand the series (7.70) further in terms of the smoothness of the medium perturbation,

$$\eta^{[n]}(x_\mu,\zeta,\alpha_\nu,s)\sim\sum_{m=0}^{\infty}\Omega^m\,\eta^{[n]}_{[1-m]}(x_\mu,\zeta,\alpha_\nu,s)\,, \tag{7.71}$$

where the $\eta^{[n]}_{[1-m]}=(\eta_{ij}{}^{[n]}_{[1-m]})$ are 3×3 matrices. The leading term of this expansion represents the high-frequency approximation or the principal part. We shall suppress the dependencies on ζ and s in our notation.

7.5.6 Recursive solution procedure

While substituting expansions (7.70) and (7.71) into equation (7.66), we observe that for $k\geq 1$,

$$\begin{aligned}
&(+\mathrm{i}\partial_{\alpha'_\sigma}D_{x'_\sigma})^k\gamma_r(x_\mu,\alpha'_\sigma)\gamma_r(x'_\sigma,\alpha_\nu)\Big|_{(x'_\mu,\alpha'_\nu)=(x_\mu,\alpha_\nu)}=\\
&\sum_{\ell=0}^{k}\binom{k}{l}(\mathrm{i})^k[(\partial^{k-\ell}_{\alpha_1}\partial^{\ell}_{\alpha_2}\gamma^0)(x_\mu,\alpha_\nu)+(\partial^{k-\ell}_{\alpha_1}\partial^{\ell}_{\alpha_2}\gamma^1_r)(x_\mu,\alpha_\nu)]\,(D^{k-\ell}_{x_1}D^{\ell}_{x_2}\gamma^1_r)(x_\mu,\alpha_\nu)\\
&=\sum_{\ell=0}^{k}\left(\begin{array}{c}k\\ \ell\end{array}\right)(\mathrm{i})^k\Omega^k\sum_{n'=1}^{\infty}\chi^{n'}\sum_{m'=0}^{\infty}\Omega^{m'}(\mathsf{D}^{k-\ell}_{x_1}\mathsf{D}^{\ell}_{x_2}\eta^{[n']}_{[1-m']})(x_\mu,\alpha_\nu)\\
&\qquad\left[(\partial^{k-\ell}_{\alpha_1}\partial^{\ell}_{\alpha_2}\gamma^0)(x_\mu,\alpha_\nu)+\sum_{n=1}^{\infty}\chi^n\sum_{m=0}^{\infty}\Omega^m\,(\partial^{k-\ell}_{\alpha_1}\partial^{\ell}_{\alpha_2}\eta^{[n]}_{[1-m]})(x_\mu,\alpha_\nu)\right]\,.
\end{aligned}$$

Upon substituting expansions (7.70) and (7.71) into equation (7.66), we collect terms of equal order in χ. These terms are then separated in orders of Ω. We shall carry out our analysis up to $\mathcal{O}(\Omega^2)$.

The terms $\mathcal{O}(\chi^0)$ yield equation (7.68), namely

$$(\gamma^0)^2 = a^{[0]}_{[2]} \qquad [k=0] \quad (7.72)$$

which is $\mathcal{O}(\Omega^0)$. The terms $\mathcal{O}(\chi)$ decompose into [cf., De Hoop *et al.* (2000)]

$$\gamma^0\ \eta^{[1]}_{[1]} + \eta^{[1]}_{[1]}\ \gamma^0 = a^{[1]}_{[2]} \qquad [k=0] \quad (7.73)$$

which is $\mathcal{O}(\Omega^0)$, and

$$\gamma^0\ \eta^{[1]}_{[0]} + \eta^{[1]}_{[0]}\ \gamma^0 + \mathrm{i}\,(\partial_{\alpha_\sigma}\gamma^0)\,(\mathsf{D}_{x_\sigma}\eta^{[1]}_{[1]}) = a^{[1]}_{[1]} \qquad [k=0,1] \quad (7.74)$$

which is $\mathcal{O}(\Omega)$, and

$$\begin{aligned} &\gamma^0\ \eta^{[1]}_{[-1]} + \eta^{[1]}_{[-1]}\ \gamma^0 + \mathrm{i}\,(\partial_{\alpha_\sigma}\gamma^0)\,(\mathsf{D}_{x_\sigma}\eta^{[1]}_{[0]}) \qquad [k=0,1] \quad (7.75)\\ &-\tfrac{1}{2}[(\partial^2_{\alpha_1}\gamma^0)(\mathsf{D}^2_{x_1}\eta^{[1]}_{[1]}) + 2(\partial_{\alpha_1}\partial_{\alpha_2}\gamma^0)(\mathsf{D}_{x_1}\mathsf{D}_{x_2}\eta^{[1]}_{[1]}) + (\partial^2_{\alpha_2}\gamma^0)(\mathsf{D}^2_{x_2}\eta^{[1]}_{[1]}) = a^{[1]}_{[0]}[k=2] \end{aligned}$$

which is $\mathcal{O}(\Omega^2)$. The terms $\mathcal{O}(\chi^2)$ decompose into

$$(\eta^{[1]}_{[1]})^2 + \gamma^0\ \eta^{[2]}_{[1]} + \eta^{[2]}_{[1]}\ \gamma^0 = a^{[2]}_{[2]} \qquad [k=0] \quad (7.76)$$

which is $\mathcal{O}(\Omega^0)$,

$$\begin{aligned} &\eta^{[1]}_{[1]}\eta^{[1]}_{[0]} + \eta^{[1]}_{[0]}\ \eta^{[1]}_{[1]} + \gamma^0\ \eta^{[2]}_{[0]} + \eta^{[2]}_{[0]}\ \gamma^0 + \mathrm{i}\,(\partial_{\alpha_\sigma}\gamma^0)\,(\mathsf{D}_{x_\sigma}\eta^{[2]}_{[1]}) \qquad [k=0,1] \quad (7.77)\\ &\quad +\mathrm{i}\,(\partial_{\alpha_\sigma}\eta^{[1]}_{[1]})\,(\mathsf{D}_{x_\sigma}\eta^{[1]}_{[1]}) = a^{[2]}_{[1]} \qquad [k=0,1] \end{aligned}$$

which is $\mathcal{O}(\Omega)$, and

$$\begin{aligned} &\gamma^0\ \eta^{[2]}_{[-1]} + \eta^{[2]}_{[-1]}\ \gamma^0 + (\eta^{[1]}_{[0]})^2 + \eta^{[1]}_{[1]}\ \eta^{[1]}_{[-1]} + \eta^{[1]}_{[-1]}\ \eta^{[1]}_{[1]} \qquad [k=0] \quad (7.78)\\ &+\mathrm{i}\,[(\partial_{\alpha_\sigma}\gamma^0)\,(\mathsf{D}_{x_\sigma}\eta^{[2]}_{[0]}) + (\partial_{\alpha_\sigma}\eta^{[1]}_{[1]})\,(\mathsf{D}_{x_\sigma}\eta^{[1]}_{[0]}) + (\partial_{\alpha_\sigma}\eta^{[1]}_{[0]})\,(\mathsf{D}_{x_\sigma}\eta^{[1]}_{[1]})] \qquad [k=1]\\ &-\tfrac{1}{2}[(\partial^2_{\alpha_1}\gamma^0)(\mathsf{D}^2_{x_1}\eta^{[2]}_{[1]}) + 2(\partial_{\alpha_1}\partial_{\alpha_2}\gamma^0)(\mathsf{D}_{x_1}\mathsf{D}_{x_2}\eta^{[2]}_{[1]}) + (\partial^2_{\alpha_2}\gamma^0)(\mathsf{D}^2_{x_2}\eta^{[2]}_{[1]}) \qquad [k=2]\\ &+(\partial^2_{\alpha_1}\eta^{[1]}_{[1]})(\mathsf{D}^2_{x_1}\eta^{[1]}_{[1]}) + 2(\partial_{\alpha_1}\partial_{\alpha_2}\eta^{[1]}_{[1]})(\mathsf{D}_{x_1}\mathsf{D}_{x_2}\eta^{[1]}_{[1]}) + (\partial^2_{\alpha_2}\eta^{[1]}_{[1]})(\mathsf{D}^2_{x_2}\eta^{[1]}_{[1]})] \qquad [k=2]\\ &= a^{[2]}_{[0]} \end{aligned}$$

which is $\mathcal{O}(\Omega^2)$. Higher order terms can be obtained, if desired.

7.5.7 The vertical slowness right symbol

The preceding analysis yields the (asymptotic) construction of the symbol γ_r. Here, we give the formulae for the first three terms of the principal part of the vertical slowness symbol, γ_1. Equations (7.72)-(7.78) can be solved by means of the diagonalization

$$\gamma^0 = M^0 \pi^0 [M^0]^{-1} , \tag{7.79}$$

where M^0 and $[M^0]^{-1}$ are given in equations (7.64)-(7.65). We express the terms $\eta^{[n]}_{[1-m]}$ in the eigenvector basis, i.e., $\eta^{[n]}_{[1-m]} = M^0 \vartheta^{[n]}_{[1-m]} [M^0]^{-1}$. The term $\vartheta^{[1]}_{[1]} = (\vartheta_{ij}{}^{[1]}_{[1]})$ then follows from equation (7.73) as

$$\begin{aligned}
\vartheta_{11}{}^{[1]}_{[1]} &= \frac{[c_S^0]^{-2}}{2\pi_{11}^0}(\epsilon_S + \epsilon_\rho) , \quad \vartheta_{13}{}^{[1]}_{[1]} = \frac{[c_{PS}^0]^{-2} c_S^0 \sqrt{\alpha_\nu \alpha_\nu}}{\pi_{11}^0 + \pi_{33}^0} (\epsilon_S + \epsilon_\rho) , \\
\vartheta_{22}{}^{[1]}_{[1]} &= \frac{[c_S^0]^{-2}}{2\pi_{22}^0}(\epsilon_S + \epsilon_\rho) , \quad \vartheta_{33}{}^{[1]}_{[1]} = \frac{[c_P^0]^{-2}}{2\pi_{33}^0}(\epsilon_P + \epsilon_\rho) , \\
\vartheta_{31}{}^{[1]}_{[1]} &= -\frac{[c_{PS}^0]^{-2} c_S^0 \sqrt{\alpha_\nu \alpha_\nu}\,(1 - 2[c_S^0]^2(\alpha_\nu \alpha_\nu))}{2(\pi_{11}^0 + \pi_{33}^0)} (\epsilon_S + \epsilon_\rho)
\end{aligned}$$

the other entries being zero. This term is used in the first-order GS approximation. The term $\vartheta^{[2]}_{[1]}$ can be found in Appendix O. Note that the diagonal entries of $\vartheta^{[1]}_{[1]}$ correspond with the first-order term of the mode-wise scalar screen expansion (De Hoop *et al.*, 2000; Le Rousseau & De Hoop, 2001b). Likewise, the diagonal entries of $\vartheta^{[2]}_{[1]}$ in Appendix O contain the second-order term of the mode-wise scalar screen expansion. The off-diagonal entries of $\vartheta^{[1]}_{[1]}$ and $\vartheta^{[2]}_{[1]}$ contribute to the mode coupling.

The recursion for the solution of the vertical slowness right symbol described by equations (7.72)-(7.78) and Figure 7.5 reveals that the expansion in χ implies a separation in the phase space coordinates, x_μ and α_ν, of the constituent symbols in equation (7.71):

$$\vartheta_{ij}{}^{[n]}_{[1-m]}(x'_\mu, \alpha_\nu) = \sum_\lambda \xi_{ij}{}^{[n]\lambda}_{[1-m]}(x'_\mu)\, \varphi_{ij}{}^{[n]\lambda}_{[1-m]}(\alpha_\nu) , \tag{7.80}$$

which is required for the screen reduction of the one-way propagator (De Hoop *et al.*, 2000).

Figure 7.6 illustrates the real and imaginary parts of the principal slowness surfaces (as a function of the horizontal slowness $p = \sqrt{-\alpha_\nu \alpha_\nu}$) for a pure P constituent in a constant-perturbation medium. Figure 7.7 illustrates the real and imaginary parts of the principal slowness surfaces for a pure S constituent in a constant perturbation medium. GSP0 stands for the vertical slowness symbol associated with the background medium, γ_0. The ratio between the medium properties (here P and S wave speeds) of the actual medium and the background medium is 1/3 here. The vector split-step Fourier approximation corresponds to a vertical shift of the slowness surface to match the true one in the vicinity of vertical propagation (as in the acoustic case (Stoffa *et al.*, 1990)). The labels (1) and (2) correspond to the choice of matrix M that separates the P and S constituents of the wave matrix. In

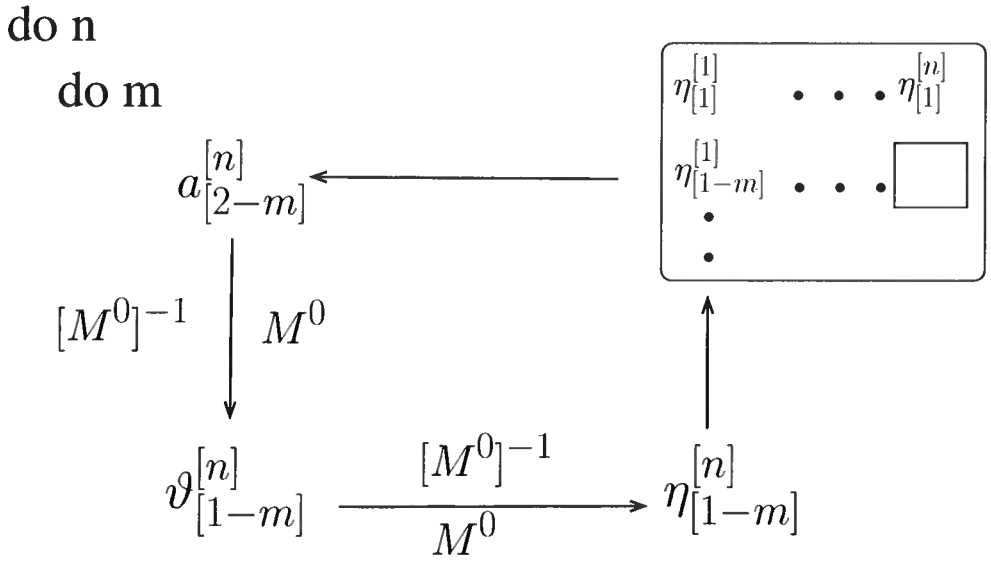

Figure 7.5. Computation of $\gamma_r^1 = \sum_{n,m} \eta^{[n]}_{[1-m]}$ with the recursion procedure.

case (1) the diagonalization is carried out in the actual medium, whereas in case (2) it is carried out in the background medium [see equation (7.64)]. Figures 7.6 and 7.7 illustrate that separating the P and S constituent in the background medium result in an acceptable approximation. GPS1 stands for the first-order screen approximation, i.e., the GS expansion of the vertical slowness symbol is truncated after the term $\vartheta^{[1]}_{[1]}$. Adding higher-order terms to the GS expansion, the *shape* of the slowness surface is improved and, hence, the accuracy for wider-angle propagation is increased.

7.6 The elastic generalized-screen propagator

In this section we substitute the background and contrast terms for the square-root Hamiltonian appearing in the phase of the thin-slab propagator (Section 7.6.1); we then separate (approximately) the P and S constituents in the embedding (Section 7.6.1); the embedding term is left in the exponential. The exponential containing the contrast terms is expanded about vertical propagation (first-order Taylor) and we obtain an explicit split-step and contrast contributions (Section 7.6.2); we finally substitute the GS expansion for the vertical slowness right symbol in the contrast contribution of the propagator (Section 7.6.3); we renormalize to restore unitarity after the expansion of the exponential in Section 7.6.2 (Section 7.6.4).

7.6.1 Symbol substitution and separation of P and S constituents

We shall now return to the basic symbol decomposition (7.69) and analyze what this implies for the thin-slab propagator, see equation (7.50). In general, with decomposi-

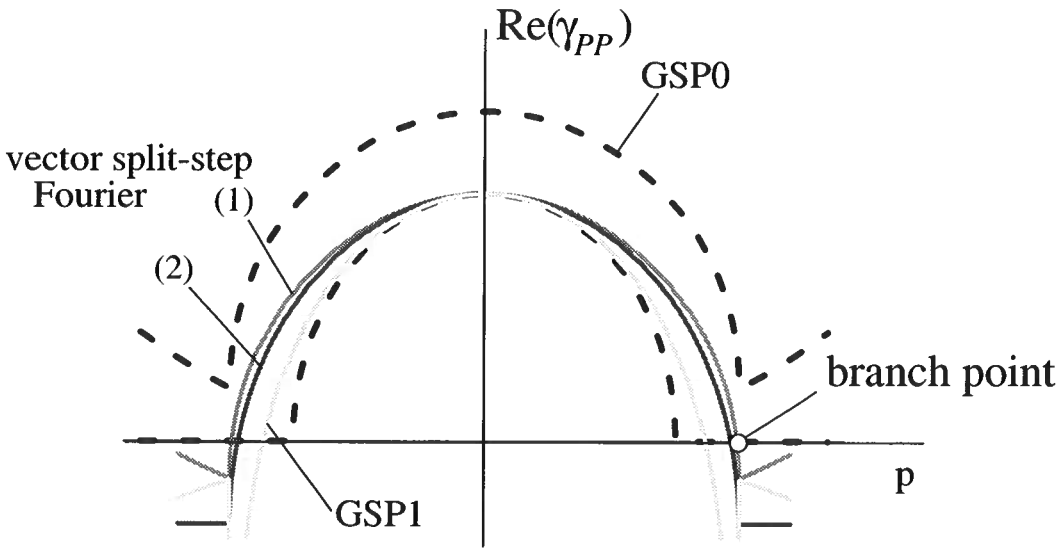

(a)

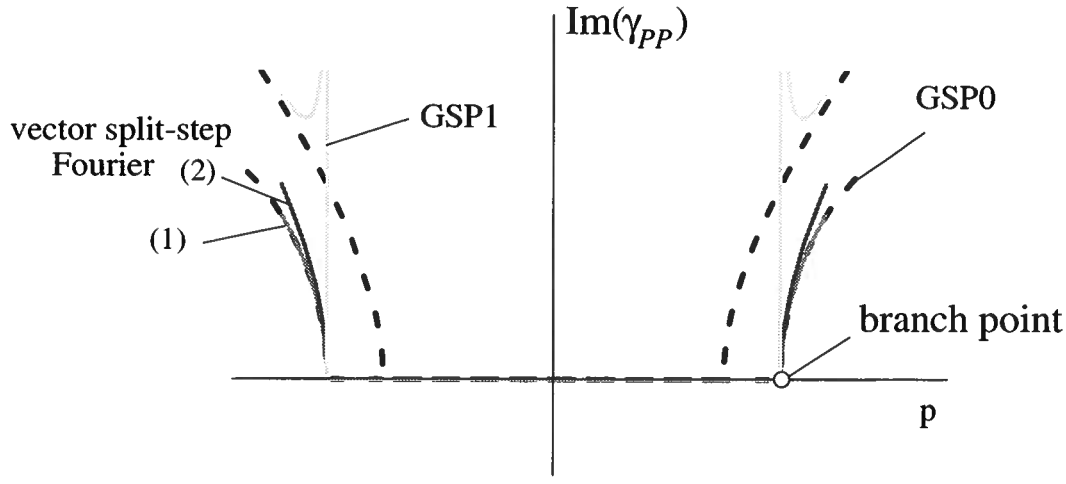

(b)

Figure 7.6. (a) Real and (b) imaginary parts of the principal parts of the generalized-screen vertical slowness for P constituents: zero-order (GSP0) and first-order (GSP1). Also shown is the principal part of the vertical slowness for the split-step Fourier method with P and S constituents separated in (1) the actual medium and in (2) the background medium. The principal part of the exact vertical slowness is shown with the inner dashed curve.

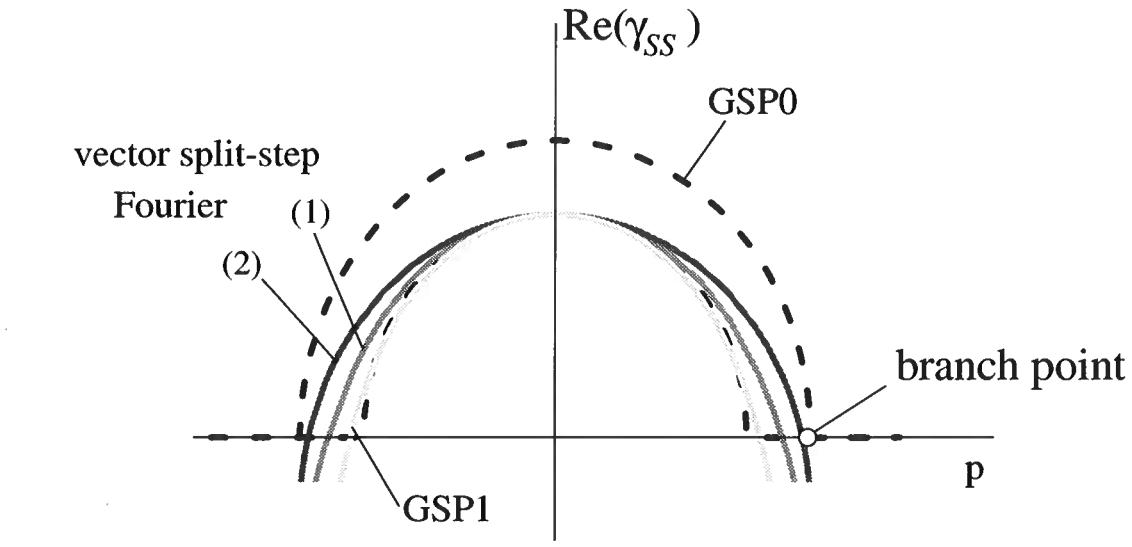

(a)

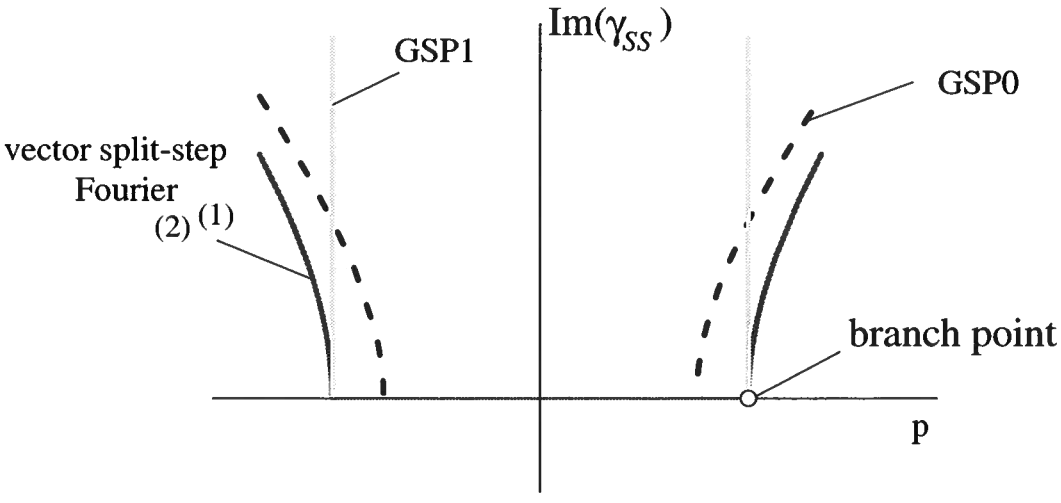

(b)

Figure 7.7. (a) Real and (b) imaginary parts of the principal parts of the generalized-screen vertical slowness for S constituents: zero-order (GSP0) and first-order (GSP1). Also shown is the principal part of the vertical slowness for the split-step Fourier method with P and S constituents separated in (1) the actual medium and in (2) the background medium. The principal part of the exact vertical slowness is shown with the inner dashed curve.

tion (7.69) we obtain

$$\int \mathrm{d}x_1'\mathrm{d}x_2'\, g^{(\pm)}(x_\mu, x_3; x_\nu', x_3')(\cdot) \simeq \int (s/2\pi)^2 \mathrm{d}\alpha_1''\mathrm{d}\alpha_2'' \exp[-\mathrm{i}s\,\alpha_\sigma'' x_\sigma]\ (\mathcal{K}(\cdot))(\bar{x}_3, \alpha_\nu'')\ , \tag{7.81}$$

where

$$(\mathcal{K}(\cdot))(\bar{x}_3, \alpha_\nu'') = \int \mathrm{d}x_1'\mathrm{d}x_2' \exp[\mathrm{i}s\,\alpha_\sigma'' x_\sigma'] \exp[\mp s\Delta x_3\,\{\gamma^0(\bar{x}_3, \alpha_\nu'') + \gamma_r^1(x_\mu', \bar{x}_3, \alpha_\nu'')\}](\cdot)\ , \tag{7.82}$$

and $x_3' = x_3 - \Delta x_3$, $\bar{x}_3 = x_3 - \frac{1}{2}\Delta x_3$. Note that equations (7.81) and (7.82) reveals the structure of the propagator induced by the use of the right symbol. The symbol matrices γ^0 and γ_r^1 do not commute in general. Yet, as Δx_3 tends to zero,

$$\exp[\mp s\,(\gamma^0 + \gamma_r^1)\Delta x_3] = \exp[\mp s\,\gamma^0 \Delta x_3] \exp[\mp s\,\gamma_r^1 \Delta x_3] + \mathcal{O}(s\Delta x_3)^2\ . \tag{7.83}$$

This yields the following simplification of equation (7.82)

$$(\mathcal{K}(\cdot))(\bar{x}_3, \alpha_\nu'') \simeq \exp[\mp s\Delta x_3\,\gamma^0(\bar{x}_3, \alpha_\nu'')] \int \mathrm{d}x_1'\mathrm{d}x_2'\ \exp[\mathrm{i}s\,\alpha_\sigma'' x_\sigma'] \times \exp[\mp s\Delta x_3\,\gamma_r^1(x_\mu', \bar{x}_3, \alpha_\nu'')](\cdot)\ . \tag{7.84}$$

As before, we diagonalize the symbol matrix γ^0 using equation (7.79) and transform the perturbation accordingly as $\gamma_r^1 = M^0 \pi_r^1 [M^0]^{-1}$. Equation (7.84) then takes the form

$$(\mathcal{K}(\cdot))(\bar{x}_3, \alpha_\nu'') \simeq M^0(\bar{x}_3, \alpha_\nu'') \exp[\mp s\Delta x_3\,\pi^0(\bar{x}_3, \alpha_\nu'')] \times \int \mathrm{d}x_1'\mathrm{d}x_2'\ \exp[\mathrm{i}s\,\alpha_\sigma'' x_\sigma'] \exp[\mp s\Delta x_3\,\pi_r^1(x_\mu', \bar{x}_3, \alpha_\nu'')][M^0]^{-1}(\bar{x}_3, \alpha_\nu'')(\cdot)\ . \tag{7.85}$$

In this form we separate (approximately) the P and S constituents. (This decomposition is carried out in the background medium and not in the actual medium.)

7.6.2 Expansion of $\exp(\mp s\Delta x_3\,\pi_r^1)$

We then expand $\exp[\mp s\Delta x_3\,\pi_r^1(x_\mu', \bar{x}_3, \alpha_\nu'')]$ about vertical propagation ($\alpha_\nu \alpha_\nu = 0$),

$$\begin{aligned}\exp[\mp s\Delta x_3\,\pi_r^1(x_\mu', \bar{x}_3, \alpha_\nu'')] &= \exp[\mp s\Delta x_3\,\pi_r^1(x_\mu', \bar{x}_3, 0)] \\ &\quad \times \exp[\mp s\Delta x_3\,\{\pi_r^1(x_\mu', \bar{x}_3, \alpha_\nu'') - \pi_r^1(x_\mu', \bar{x}_3, 0)\}] \\ &\simeq \exp[\mp s\Delta x_3\,\pi_r^1(x_\mu', \bar{x}_3, 0)][1 \mp s\Delta x_3\,\{\pi_r^1(x_\mu', \bar{x}_3, \alpha_\nu'') - \pi_r^1(x_\mu', \bar{x}_3, 0)\}]\ .\end{aligned} \tag{7.86}$$

Note that approximations (7.83) and (7.86) are consistent with the assumption that Δx_3 is small (thin slab). Expansion (7.86) accounts both for P and S wave propagation and

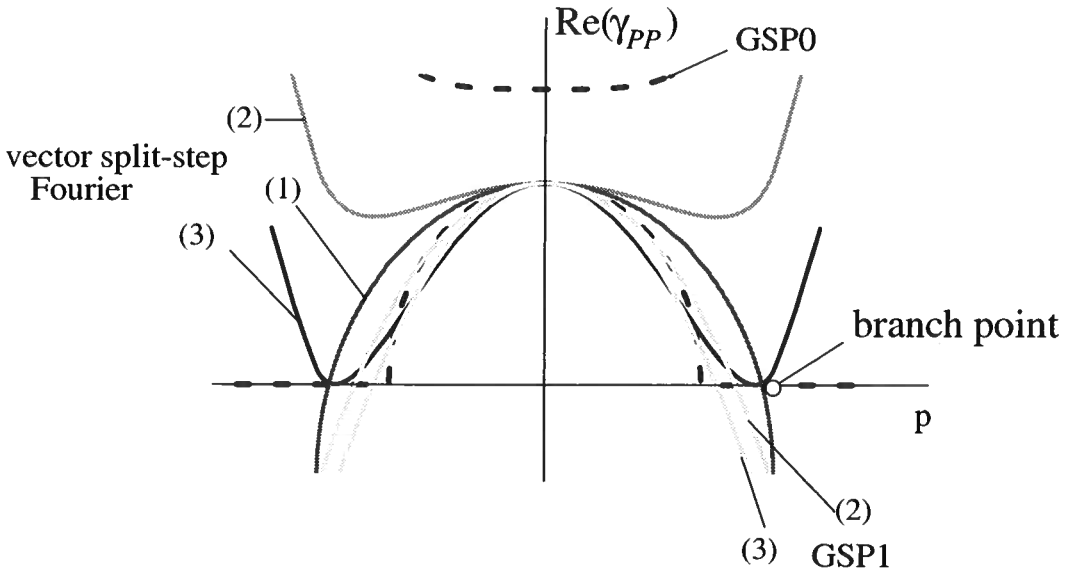

Figure 7.8. Real part of the vertical slowness symbols associated with propagator (7.84) with $\exp[\mp s\Delta x_3\,\gamma_r^1]$ expanded (1),(2) after separation of P and S constituents, (3) before mode separation in the background medium. (1) corresponds to a separation in the actual medium, (2) in the background medium. In Figures 7.6 and 7.7, cases (1) and (2) are consistent with the present figure.

its structure resembles the one for scalar waves (De Hoop *et al.*, 2000; Le Rousseau & De Hoop, 2001b). Thus, we have expanded $\exp[\mp s\Delta x_3\,\pi_r^1]$ about vertical propagation rather than $\exp[\mp s\Delta x_3\,\gamma_r^1]$. In the process of truncating the expansion this makes a difference as illustrated in Figure 7.8.

Substituting expansion (7.86) into equation (7.81) results in a decomposition of the thin-slab propagator, i.e.,

$$g^{(\pm)}(x_\mu, x_3; x'_\nu, x'_3) \simeq g^{0\,(\pm)}(x_\mu, x_3; x'_\nu, x'_3) + g^{1\,(\pm)}(x_\mu, x_3; x'_\nu, x'_3)\ , \tag{7.87}$$

where

$$\begin{aligned}\int \mathrm{d}x'_1\mathrm{d}x'_2\ g^{N(\pm)}(x_\mu, x_3; x'_\nu, x_3 - \Delta x_3)(\cdot) = \int (s/2\pi)^2 \mathrm{d}\alpha''_1\mathrm{d}\alpha''_2 \exp[-\mathrm{i}s\,\alpha''_\sigma x_\sigma] \qquad (7.88)\\ \times M^0(\bar{x}_3, \alpha''_\nu)\exp[\mp s\Delta x_3\,\pi^0(\bar{x}_3, \alpha''_\nu)]\ \mathcal{X}^N(x'_\mu, \bar{x}_3, \alpha''_\nu)\\ \times \int \mathrm{d}x'_1\mathrm{d}x'_2\ \exp[\mathrm{i}s\,\alpha''_\sigma x'_\sigma]\exp[\mp s\Delta x_3\,\pi_r^1(x'_\mu, \bar{x}_3, 0)][M^0]^{-1}(\bar{x}_3, \alpha''_\nu)(\cdot)\ ,\end{aligned}$$

for $N = 0, 1$, where $\mathcal{X}^0 = 1$ and

$$\mathcal{X}^1(x'_\mu, \bar{x}_3, \alpha''_\nu) = (\mp)s\Delta x_3\{\pi_r^1(x'_\mu, \bar{x}_3, \alpha''_\nu) - \pi_r^1(x'_\mu, \bar{x}_3, 0)\}\ . \tag{7.89}$$

When $N = 0$, propagator (7.88) is denoted as the vector split-step Fourier approximation. Here the vector screen is implicitly given by $M^0(\bar{x}_3, \alpha''_\nu)\pi^1_r(x'_\mu, \bar{x}_3, 0)[M^0]^{-1}(\bar{x}_3, \alpha''_\nu)$.

7.6.3 Substitution of the generalized-screen expansion

We shall now invoke the GS expansion for $\pi^1_r(x'_\mu, \bar{x}_3, \alpha''_\nu) - \pi^1_r(x'_\mu, \bar{x}_3, 0)$. To this end, we reconsider

$$\pi^1_r = [M^0]^{-1}\gamma^1_r M^0 = \sum_{n,m}[M^0]^{-1}\eta^{[n]}_{[1-m]}M^0 = \sum_{n,m}\vartheta^{[n]}_{[1-m]} ,$$

which upon substitution in equation (7.89) gives

$$\mathcal{X}^1(x'_\mu, \bar{x}_3, \alpha''_\nu) = \mp s\Delta x_3 \sum_{n,m}\{\vartheta^{[n]}_{[1-m]}(x'_\mu, \bar{x}_3, \alpha''_\nu) - \vartheta^{[n]}_{[1-m]}(x'_\mu, \bar{x}_3, 0)\} . \tag{7.90}$$

Invoking the screen reduction (7.80), we obtain

$$\int \mathrm{d}x'_1\mathrm{d}x'_2\, g^{1\,(\pm)}(x_\mu, x_3; x'_\nu, x'_3)(\cdot) = \int (s/2\pi)^2\mathrm{d}\alpha''_1\mathrm{d}\alpha''_2 \exp[-\mathrm{i}s\,\alpha''_\sigma x_\sigma]$$
$$\times M^0(\bar{x}_3, \alpha''_\nu)(\mp)s\Delta x_3 \exp[\mp s\Delta x_3\, \pi^0(\bar{x}_3, \alpha''_\nu)] \sum_{m,n}\sum_{\lambda}[\Upsilon^{[n]\lambda}_{[1-m]}(\cdot)](x_\mu, x_3; \alpha''_\nu) , \tag{7.91}$$

where $\Upsilon^{[n]\lambda}_{[1-m]}$ is the operator defined by

$$[\Upsilon^{[n]\lambda}_{[1-m]}(\cdot)]_i\,(x_\mu, x_3; \alpha''_\nu) = \sum_{j,k=1}^{3}\Big\{(\varphi_{ik})^{[n]\lambda}_{[1-m]}(\bar{x}_3, \alpha''_\nu) - (\varphi_{ik})^{[n]\lambda}_{[1-m]}(\bar{x}_3, 0)\Big\}\int \mathrm{d}x'_1\mathrm{d}x'_2$$
$$\times \exp[\mathrm{i}s\,\alpha''_\sigma x'_\sigma]\exp[\mp s\Delta x_3\, \pi^1_r(x'_\mu, \bar{x}_3, 0)](\xi_{ik})^{[n]\lambda}_{[1-m]}(x_\mu, \bar{x}_3)[M^0_{kj}]^{-1}(\bar{x}_3, \alpha''_\nu)\,(\cdot)_j . \tag{7.92}$$

Equation (7.91) combined with equation (7.92) reveals the following structure: multiplication, Fourier transform, multiplication, inverse Fourier transform. The key simplification is, that the forward Fourier transform with respect to x'_ν *no longer* has to be evaluated for each α''_ν *separately*; compare propagator (7.93) with propagator (7.50). This feature was inherited from the GS expansion of the vertical-slowness right symbol: The functions $\xi^{[n]\lambda}_{[1-m]}(x_\mu)$ in equation (7.80) constitute a family of 'generalized screens', while the functions $\varphi^{[n]\lambda}_{[1-m]}(\alpha_\nu)$ extend the concept of 'phase shift' (De Hoop *et al.*, 2000).

7.6.4 Normalization

The GS thin-slab propagator is finally defined as

$$\int \mathrm{d}x_1'\mathrm{d}x_2'\, g_{GSP}^{(\pm)}(x_\mu, x_3; x_\nu', x_3 - \Delta x_3)(\cdot) = \int (s/2\pi)^2 \mathrm{d}\alpha_1''\mathrm{d}\alpha_2'' \exp[-\mathrm{i}s\,\alpha_\sigma'' x_\sigma] \tag{7.93}$$
$$\times M^0(\bar{x}_3, \alpha_\nu'') \exp[\mp s\Delta x_3\, \pi^0(\bar{x}_3, \alpha_\nu'')]$$
$$\times \mathcal{N}\left\{ \int \mathrm{d}x_1'\mathrm{d}x_2' \exp[\mathrm{i}s\,\alpha_\sigma'' x_\sigma'] \exp[\mp s\Delta x_3\, \pi_r^1(x_\mu', \bar{x}_3, 0)]\, [M_{kj}^0]^{-1}(\bar{x}_3, \alpha_\nu'')(\cdot) \right.$$
$$\left. \times(\mp)s\Delta x_3 \sum_{m,n} \sum_{\lambda} [\Upsilon_{[1-m]}^{[n]\lambda}(\cdot)](x_\mu, x_3; \alpha_\nu'') \right\} .$$

In this expression we have introduced a normalization operator $\mathcal{N}$ to restore the amplitude behavior that was destroyed by Taylor expanding the exponential in equation (7.86), (De Hoop *et al.*, 2000). $\mathcal{N}$ acts on a component of the wave matrix separated into P and S constituents. We apply the normalization for each constituent separately in accordance with (De Hoop *et al.*, 2000)

$$\mathcal{N}\{y(1+p+\mathrm{i}q)\} = y\exp(\mathrm{i}q) \left|1 + \frac{p}{1+\mathrm{i}q}\right|^{-1} \left[1 + \frac{p}{1+\mathrm{i}q}\right] , \quad |y| = 1 . \tag{7.94}$$

Above (see section on contrast formulation), we pointed out the necessity of introducing two background media. We set up two parallel computations, one in the background c_P^0, c_S^0, and one in the background c_S^0, c_S^0, see Figure 7.9. Note that we have written the diagonalization in terms of c_S^0 and hence both computations have the diagonalization procedure in common. The parallel computations are initiated by separating the wave matrix into P and S constituents. In one computation, a computational S is introduced (S'). In the parallel computation, a computational P is introduced (P'). The computational P' and S' constituents affect the physical P and S constituents through mode coupling only. In fact, as shown in Figure 7.9, the wave matrix is reconstructed by extracting the physical P and S constituents from the parallel computation.

The case of a constant medium perturbation provides insight into how wavefronts evolve based on Huygens' principle (Huygens, 1690; Arnold, 1978; Hörmander, 1990). Let the ratio between the medium properties (here P and S wave speeds) of the actual medium and the background medium be 1/3. Figure 7.10 and Figure 7.11 show (instantaneous) wavefronts constructed as the polar reciprocal of the local slowness surfaces shown in Figures 7.6 and 7.7. We have generalized here the results obtained with the GS method in the acoustic case (De Hoop *et al.*, 2000; Le Rousseau & De Hoop, 2001b). For non-horizontal propagation, including large angle propagation, any accuracy can be obtained by increasing the order of the GS approximation chosen.

As the *computational complexity* of the downward continuation in the split-step Fourier method is proportional to $3 \cdot 2 \cdot N_1 N_2 \log_2 N_1 N_2$ (N_μ denoting the numbers of samples in the x_μ-direction), the complexity of the GS approach is proportional to $2 \cdot 3 \cdot (2 +$

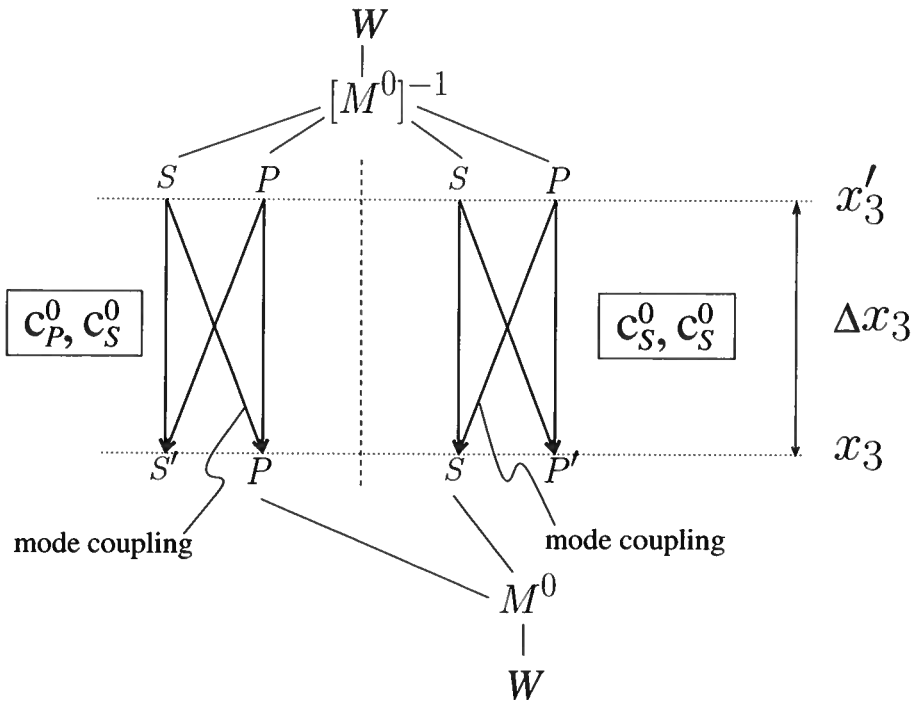

Figure 7.9. Practical implementation of the two backgrounds for the GS propagator. The actual P constituent along with a computational S' constituent is computed in the background characterized by c_P^0, and c_S^0. The actual S constituent along with a computational P' constituent is computed in the background medium characterized by c_S^0, and c_S^0.

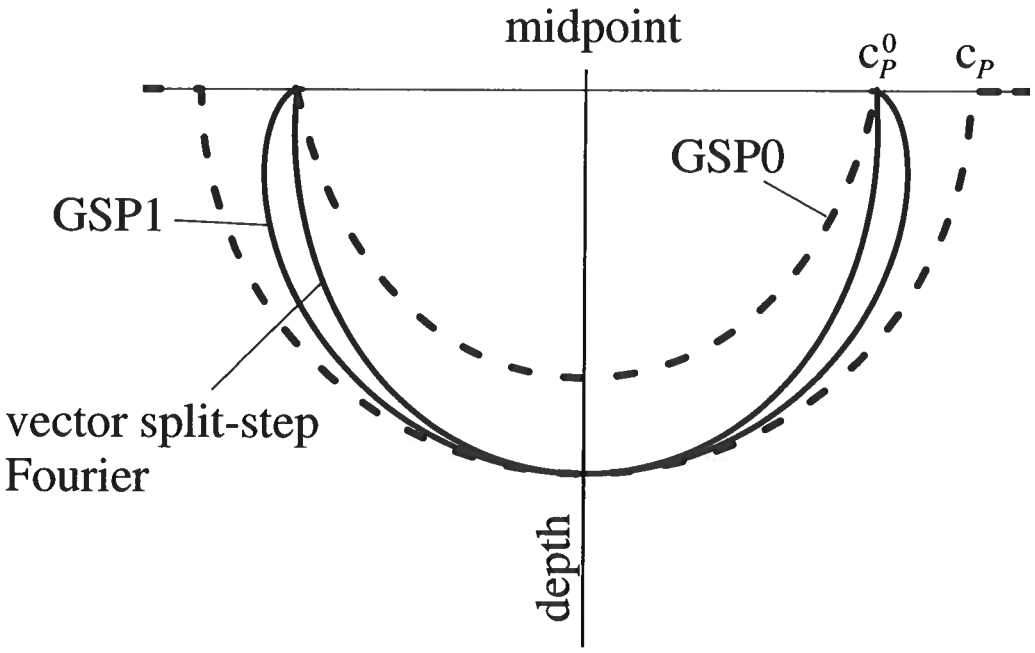

Figure 7.10. Wavefronts in a constant-perturbation medium for a pure P constituent associated with the first-order (GSP1) GS approximation and split-step Fourier, as calculated as polar reciprocal of the slowness surfaces shown in Figure 7.6; the exact and background wavefronts are shown dashed.

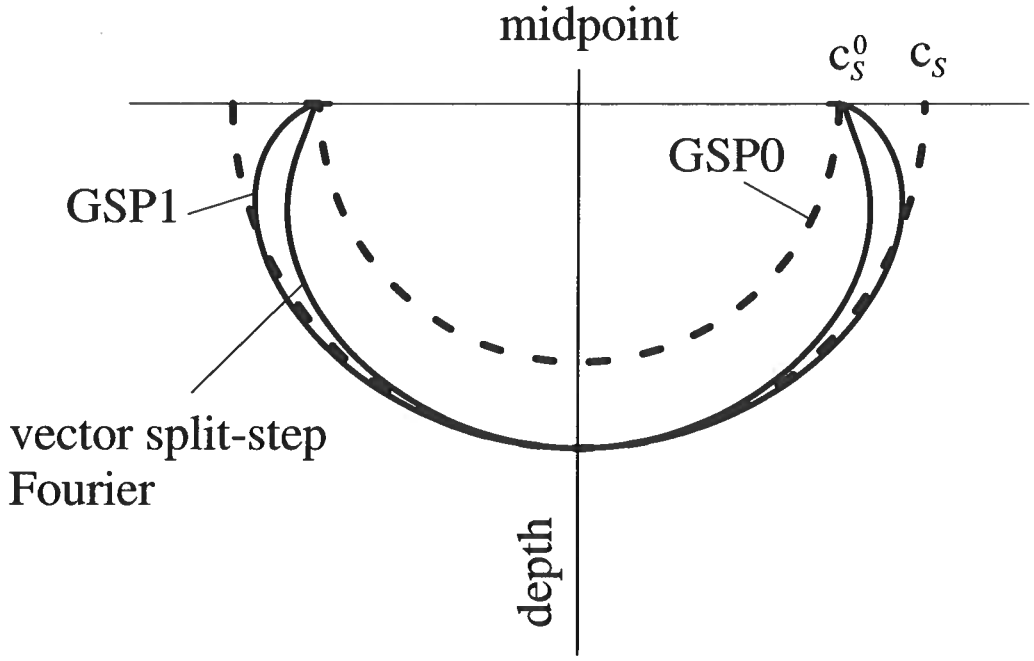

Figure 7.11. Wavefronts in a constant-perturbation medium for a pure S constituent associated with the first-order (GSP1) GS approximation and split-step Fourier, as calculated as polar reciprocal of the slowness surfaces shown in Figure 7.7; the exact and background wavefronts are shown dashed.

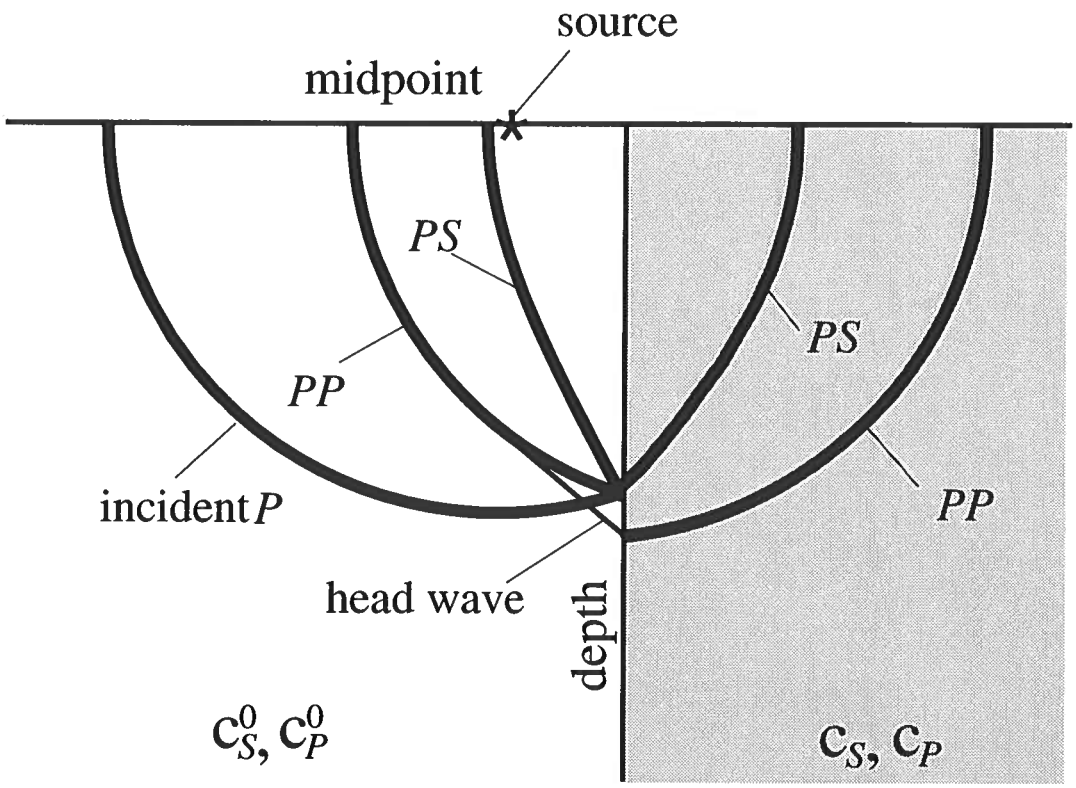

Figure 7.12. Model used in the numerical computations shown in Figure 7.13. A source is exited near a vertical interface where both P and S wave speeds increase. The wavefront of an incident P wavefield is shown after it has reached the interface.

$\binom{n}{3}) N_1 N_2 \log_2 N_1 N_2$ (the first factor of 2 arises from the introduction of two background media), where n is the number of terms used in the GS expansion of the right vertical slowness symbol. Here we only considered the computational complexity for the GS propagator associated with the GS expansion of the principal part of the vertical slowness symbol.

7.7 Numerical results

We illustrate the behavior of the generalized-screen propagator in a simple, yet, representative situation. Recall that the action of the (pseudodifferential) vertical slowness operator accounts for transverse scattering only. Hence, consider a medium characterized by a vertical interface (simplified salt flank) representing an increase (from left to right) in both P and S wave speeds. A source is located in the low wave speed region. Figure 7.12 shows the geometry of the problem and the behavior of the wavefront of an incident P wave when encountering the interface. A reflected and a transmitted P wave appear as well as a reflected and a transmitted S wave. Note the discontinuity of the body wavefront at the

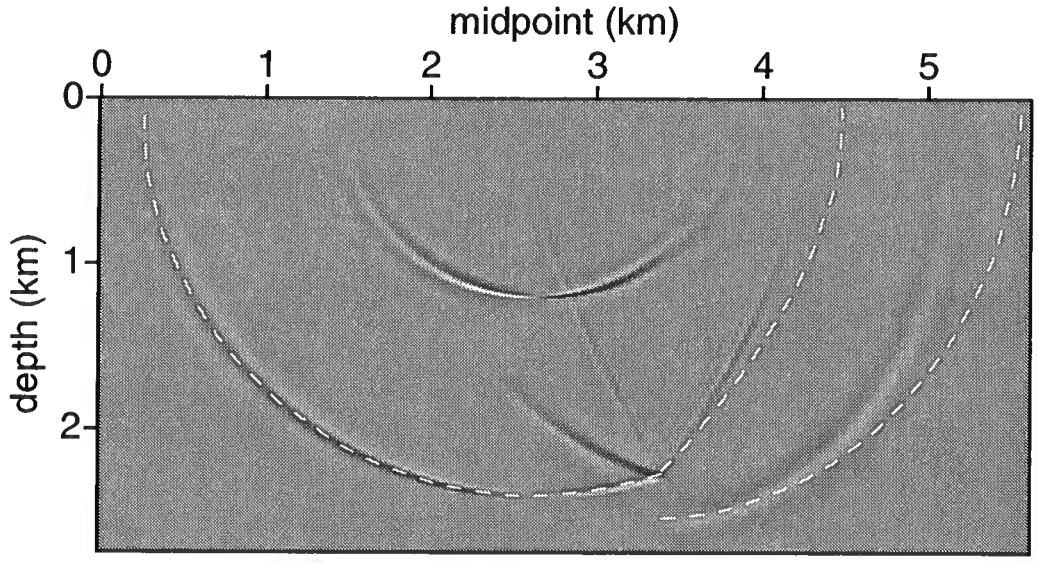

(a)

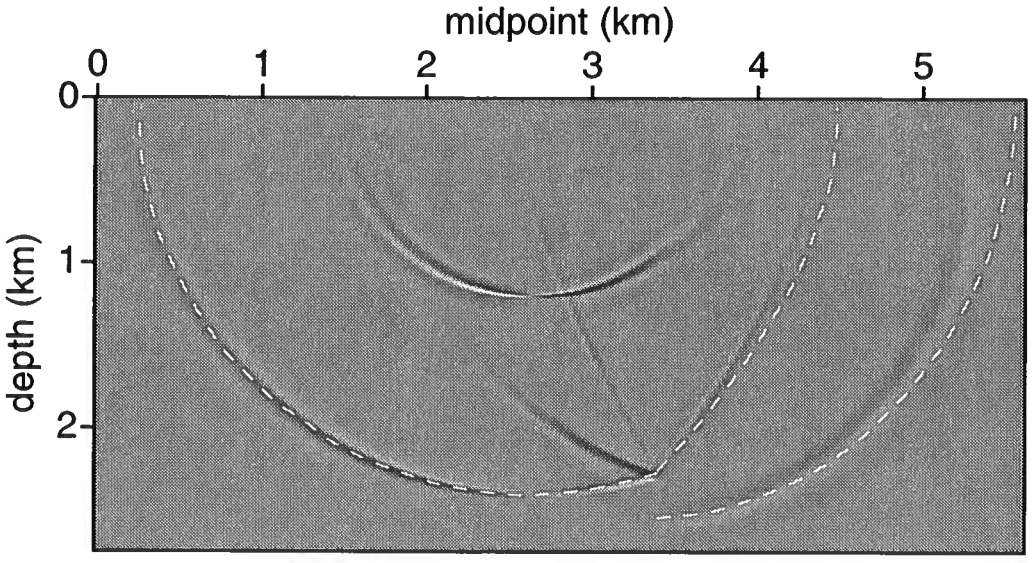

(b)

Figure 7.13. Numerical wavefront of the vertical particle velocity for (a) the vector split-step Fourier method and (b) the first-order GS method, in the geometry described by Figure 7.12 with a source characterized by a horizontal point force. Exact parts of the wavefront are shown dashed.

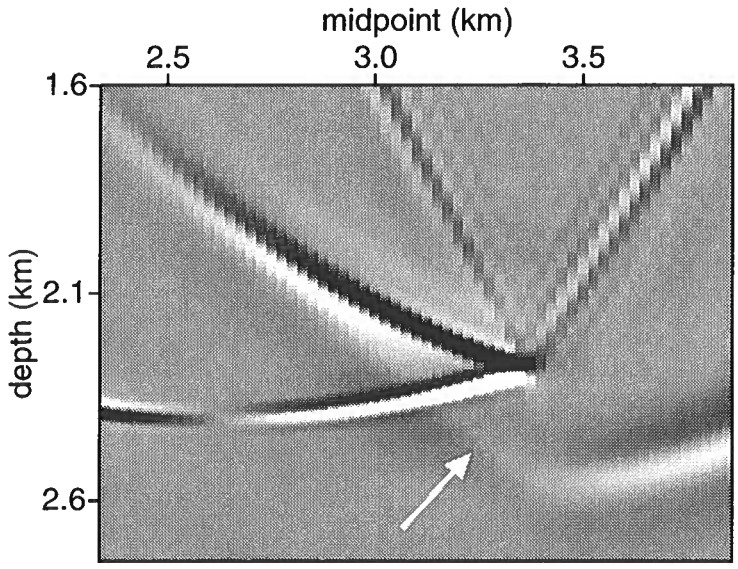

Figure 7.14. Enlargement of Figure 7.13(b) to illustrate the prediction of a headwave (see white arrow).

interface, which implies the creation of a head wave. The medium on the left of the interface is used as the reference medium in the computation of the GS propagator. Inaccuracies in the GS propagator therefore occur in the medium on the right of the interface. We illustrate the accuracy with the number of terms in the GS representation of the vertical slowness symbol in Figure 7.13(a) and Figure 7.13(b). In these figures the source is characterized by a horizontal point force and the vertical particle velocity is computed. As expected, the propagator in the (left) background region gives a close to perfect result. In Figures 7.13(a) and 7.13(b) the white dashed lines follow the wavefront set of Figure 7.12. In both figures, in the right region, the accuracy decreases with propagation angle as predicted by Figures 7.6 to 7.11. As expected from the previous analysis, the first-order GS propagator matches more accurately the true wavefront set than the vector split-step Fourier propagator. In Figure 7.14 we show an enlargement of Figure 7.13(b) to point out the presence and position of the head wave connecting the two P constituents of the wavefront.

Note that *continuous* mode coupling within the GS thin-slab propagator induces the mode conversions at the vertical interface.

The source in Figures 7.13(a) and 7.13(b) is a (regularized) Dirac distribution as it occurs on the right hand side of equation (7.47). Radiation patterns are not imposed to show the action of the propagator only; hence the decay of amplitude at horizontal propagation, even for the incident wavefront.

To illustrate the S to P mode coupling we place the source closer to the vertical interface and only consider an incoming S wave. The numerical results of the vector split-step Fourier and GS methods are shown in Figure 7.15(a) and Figure 7.15(b). The source used to create

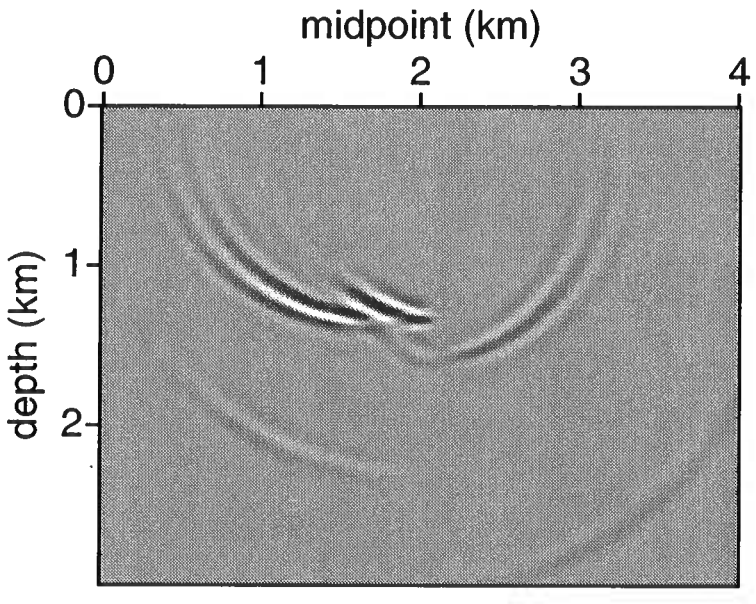

(a)

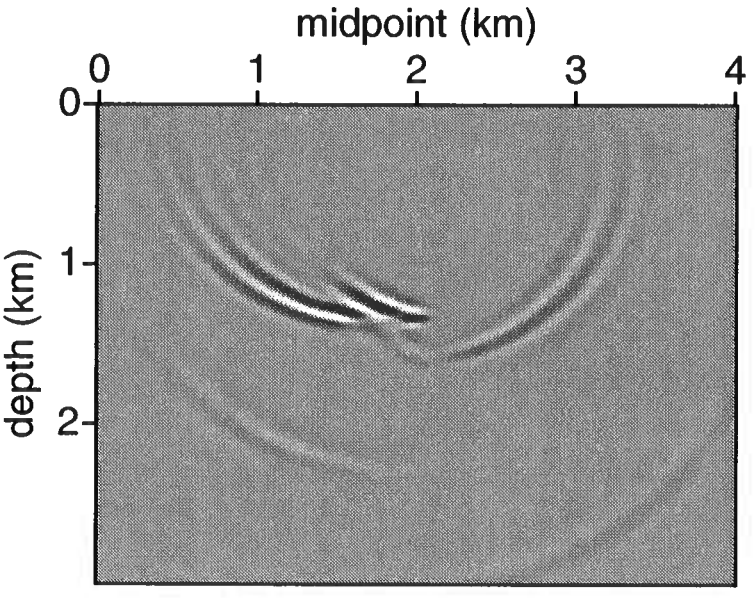

(b)

Figure 7.15. Numerical wavefront of the horizontal particle velocity for (a) the vector split-step Fourier method and (b) the first-order GS method, with an incoming shear wave at a vertical interface with a source characterized by a horizontal point force.

these figures was a horizontal point source while the horizontal particle velocity is computed. To clearly show the transmitted and reflected P waves we enhanced the contrast. Note the prediction of the head wave in the S wavefront.

7.8 Discussion

For large scale geophysical configurations, efficient 3D propagation algorithms are in demand. On the one hand, full-wave 3D finite-difference and finite-element methods are costly. One the other hand, the phase-screen approach, though approximate, yields a much more efficient algorithm in 3D. The phase-screen approximation breaks down at large-angle scattering associated with significant lateral heterogeneity. In this chapter, we have developed the elastic generalized-screen propagator that extends the phase-screen approach. It allows for larger medium fluctuations and wider-angle propagation. Similarities with the acoustic case were found. In the basis of P and S polarization vectors (in the background medium), we have recognized the diagonal entries of the first order term in the GS expansion (of the principal part of the vertical slowness symbol) as that of the mode-wise scalar GS expansion. The off-diagonal entries of contribute to the mode coupling. Similar observations can be made for higher-order terms. The number of terms used in the generalized-screen expansion yields a hierarchy of increasingly accurate approximations of the one-way wave propagator. We have given an explicit recursion for the computation of the terms in the GS expansion. The GS method represents a reduction of the computational complexity of the 'exact' thin-slab propagator: its complexity is proportional to the complexity of a (fast) Fourier transform and the number of terms used in the generalized-screen expansion of the vertical slowness symbol.

The GS method stays close to the path-integral representation for wave propagation. It has no difficulty to account for continuous mode coupling between P and S. Since multi-pathing is naturally contained in the path integral, the GS method does not require following the formation of caustics. This is a particular advantage if caustics and pseudocaustics (i.e., a caustics in the slowness variables) are closely spaced. Uniform asymptotic methods such as the Maslov representation for wave propagation (Maslov & Fedoriuk, 1981; Kendall & Thomson, 1993; De Hoop & Brandsberg-Dahl, 2000) do not account naturally for these effects.

Chapter 8

Concluding remarks

Wave-equation imaging and inversion rely on wave extrapolation operations. The exact propagator (Trotter) exhibits a high computational complexity. The wave front set of the exact propagator depends on its phase function. In the phase function, the vertical slowness symbol is responsible for the transverse left-right scattering. It is then responsible for phenomena such as focusing and defocusing, i.e., multipathing. By modifying the exact symbol we alter the prediction of such scattering. In the GS expansion of the vertical slowness symbol the lowest terms give exact propagation in the vertical direction while additional terms yield an increasing accuracy for wide-angle propagation. For processes associated with a preferred direction of propagation such as seismic data imaging (vertical direction) the GS expansion offers a range of adapted approximations. If the medium becomes complex, wide angle propagation along with multipathing becomes significant. Higher-order terms in the GS expansion of the vertical slowness symbol are then necessary to predict such multipathing phenomena. It this sense, we may say that the GS expansion of the vertical slowness symbol allows one to control the microlocal properties of the propagator and to keep the wave front set of the computed wavefield as close as required to the true one. An extensive quantitative analysis of the accuracy of the GS approximation was provided. This enables to understand the propagation of errors.

We have illustrated the accuracy of the GS propagator with modeling and imaging. We have compared the GS approach with some of its competitive algorithms. One-way (split-step Fourier, PSPI, filter), two-way (finite differences). All these algorithms account, to a certain degree, for multipathing. We have in addition tested the performance of the GS propagator for imaging on field data using TotalFinaElf's L7D data set from the North Sea. The main feature of this 3D marine data set is the presence of an intrusive salt body surrounded by a sedimentary sequence. For this data set we have shown enhanced resolution, improved positioning of faults and some reflectors. We have confirmed with this dataset that the accurate prediction of and the accounting for multipathing is key to an optimal imaging in complex regions.

The success of the GS analysis we carried out relies on some microlocal techniques, namely the calculus of pseudodifferential operators. It allows us to avoid ad hoc techniques such as the introduction of the Born approximation to account for transverse left-right scattering and further paraxial approximations in each extrapolation (thin) slab (Wu, 1994). In addition the subsequent 'GS' calculus for the vertical slowness symbol yields a hierarchy of increasing accuracy for the propagation of waves through (geologically) complex structure, e.g., salt bodies. The extension of the GS approach to elastic waves relies on the 'GS'

calculus of the (matrix) vertical slowness symbol. Again such calculus keeps the microlocal approximation of the exact symbol under control while allowing for a proper treatment of multipathing, and the *continuous* mode-coupling between the P and S polarizations. This continuous coupling between P and S waves can not be honored by asymptotic methods.

Wave-equation imaging was shown to be equivalent to (Maslov-)Kirchhoff on the wave front set of the image. This was further illustrated by results on field data where the two approaches yield mainly differences in texture in the images. In addition the high-frequency analysis of the wave-equation imaging yields a condition on the vertical extrapolation step and on the lateral medium variations to avoid missing caustics. This ensures a proper treatment of multipathing. Finally, this high-frequency analysis yields similar scattering-angle/azimuth common image point gathers (ACIGs) as those introduced in Kirchhoff-style imaging procedures. ACIGs are used for amplitude inversion as well as in tomography. This analysis opens the door to *wave-equation*-based tomographic algorithms where differential semblance can be used as a mismatch criterion.

Following the high frequency analysis of the wave-equation imaging we have shown how the common-azimuth approximation reduces the computational complexity of the imaging operator. Such an approximation is made at the cost of approximating some of the 3D scattering effects on the wave front of the imaging kernel itself (see Appendix D). Such an approach calls for improvements, i.e., a better approximation of the wave front set. High-frequency analysis of the wave-equation imaging procedure with the help of microlocal analysis will be necessary for such an undertaking.

In this thesis we only addressed the imaging procedure leaving out the normal operator necessary for the inversion. The study of the normal operator and the full inversion procedure in the microlocal framework naturally constitute a further direction of investigation. The hope is to be able to approximate the full inverse yielding some local operation.

Seismic data imaging is based on a single scattering approximation, i.e., ignores internal multiples. For the treatment of field data, prior to an imaging-inversion, multiples are usually attenuated. While a proper treatment of multipathing is a key step towards improved imaging, the question remains whether the inclusion of internal multiples could further improve the imaging.

References

Abraham, R., & Marsden, J. E. 1978. *Foundations of Mechanics.* The Benjamin/Cummings publishing company Inc., Reading, MA.

Achenbach, J. D. 1973. *Wave propagation in elastic solids.* North-Holland, Amsterdam.

Alkhalifah, T. 1998a. Acoustic approximations for processing in transversely isotropic media. *Geophysics*, **63**(2), 623–631.

Alkhalifah, T. 1998b. An acoustic wave equation for anisotropic media. *Pages 1913–1916 of: Expanded Abstracts.* Soc. Expl. Geophys.

Arnold, V. I. 1978. *Mathematical methods of classical mechanics.* Springer-Verlag, Berlin.

Berkhout, A. J. 1982. *Seismic migration : imaging of acoustic energy by wave field extrapolation.* Elsevier Science Publ. Co., Inc.

Berry, M. V. 1979. Diffractals. *J. Phys. A: Math. Gen.*, **12**, 781–796.

Biondi, B., & Palacharla, G. 1996. 3-D prestack migration of common-azimuth data. *Geophysics*, **61**, 1822–1832.

Blacquière, G., Debeye, H. W. J., Wapenaar, C. P. A., & Berkhout, A. J. 1989. 3D table-driven migration. *Geophys. Prosp.*, **37**, 925–958.

Bostock, M. G., & Rondenay, S. 1999. Migration of scattered teleseismic body waves. *Geophys. J. Int.*, **137**, 732–746.

Bourbaki, N. 1966. *General topology.* Hermann, Paris; Addison-Wesley Pub. Co, Reading, Mass.

Bourgeois, A., Bourget, M., Lailly, P., Poulet, M., Ricarte, P., & Versteeg, R. 1991. Marmousi, model and data. *Proc. 1990 EAEG workshop on Practical Aspects of Seismic Data Inversion.*

Bramley, E. N. 1977. The accuracy of computing ionospheric radiowave scintillation by the thin-phase screen approximation. *J. Atmos. Terr. Phys.*, **39**, 367–373.

Brandsberg-Dahl, S., O'Brien, M. J., Whitmore, D., Etgen, J. T., & Murphy, G. E. 1999. Multicomponent Modelling of the Valhall Field. *In: Expanded Abstracts.* Eur. Assoc. Expl. Geophys.

Brandsberg-Dahl, S., De Hoop, M. V., & Ursin, B. 2000. Focusing in dip and AVA compensation on scattering-angle/azimuth common image gathers. *Center for Wave Phenomena, Colorado School of Mines, CWP-349.*

Brandsberg-Dahl, S., Ursin, B., & De Hoop, M. V. 2001. Seismic velocity analysis in the scattering-angle/azimuth domain. *Center for Wave Phenomena, Colorado School of Mines, CWP-391.*

Buckley, R. 1975. Diffraction by a random phase-changing screen: a numerical experiment. *J. Atmos. Terr. Phys.*, **37**, 1431–1446.

Burridge, R., De Hoop, M. V., Miller, D., & Spencer, C. 1998. Multiparameter inversion in anisotropic elastic media. *Geophys. J. Int*, **134**, 757–777.

Chazarain, J., & Piriou, A. 1982. *Introduction to the theory of linear partial differential equations.* North-Holland, Amsterdam.

Choquet-Bruhat, Y., DeWitt-Morette, C., & Dillard-Bleick, M. 1996. *Analysis, manifolds and physics.* North Holland.

Claerbout, J. 1970. Coarse grid calculations of wave in inhomogeneous media with application to delineation of complicated seismic structure. *Geophysics*, **35**, 407–418.

Claerbout, J. 1986. *Imaging the Earth's interior.* Blackwell Scientific Publications, Inc.

Clayton, R. W. 1978. *Common midpoint migration.* Tech. rept. *SEP*-14. Stanford University. pp. 21-36.

Cohen-Tannoudji, C., Diu, B., & Laloë, F. 1977. *Mécanique quantique.* Vol. 1. Hermann, Paris.

Collins, M. D. 1989. Applications and time-domain solution of higher-order parabolic equations in underwater acoustics. *J. Acoust. Soc. Am.*, **86**, 1097–1102.

Dahlen, F. A., & Tromp, J. 1998. *Theoretical Global Seismology.* Princeton University Press, Princeton.

De Bruin, C. G. M., Wapenaar, C. P. A., & Berkhout, A. J. 1990. Angle-dependent reflectivity by means of prestack migration. *Geophysics*, **55**, 1223–1234.

De Hoop, A. T. 1991. Convergence criterion for the time-domain iterative Born approximation to scattering by an inhomogeneous, dispersive object. *J. Opt. Soc. Am.*, **A 8**, 1256–1260.

De Hoop, M. V. 1996. Generalization of the Bremmer coupling series. *J. Math. Phys.*, **37**, 3246–3282.

De Hoop, M. V. 1998. Direct, leading-order asymptotic, inverse scattering based on the generalized Bremmer series. *Pages 249–253 of:* DeSanto, J.A. (ed), *Mathematical and numerical aspects of wave propagation.*

De Hoop, M. V., & Brandsberg-Dahl, S. 2000. Maslov asymptotic extension of generalized Radon transform inversion in anisotropic elastic media: a least-squares approach. *Inverse Problems*, **16**, 519–562.

De Hoop, M. V., & De Hoop, A. T. 1992. Scalar space-time waves in their spectral-domain first- and second-order Thiele approximations. *Wave Motion*, **15**, 229–265.

De Hoop, M. V., & De Hoop, A. T. 1994. Elastic wave up/down decomposition in inhomogeneous and anisotropic media: an operator approach and its approximations. *Wave Motion*, **20**, 57–82.

De Hoop, M. V., & De Hoop, A. T. 2000. Wavefield reciprocity and optimization in remote sensing. *Proc. Roy. Soc. London, Ser. A*, **456**, 641–682.

De Hoop, M. V., & Gautesen, A. K. 2000. Uniform asymptotic expansion of the generalized Bremmer series. *SIAM J. Appl. Math.*, **60**, 1302–1329.

De Hoop, M. V., & Gautesen, A. K. 2001. Uniform asymptotic expansion of the square-root Helmholtz operator and the one-way propagator. *SIAM J. of Appl. Math.*

De Hoop, M. V., Le Rousseau, J. H., & Wu, R.-S. 2000. Generalization of the phase-screen approximation for the scattering of acoustic waves. *Wave Motion*, **31**, 43–70.

De Hoop, M. V., Le Rousseau, J. H., & Biondi, B. 2001a. Symplectic structure of wave-equation imaging: a path-integral approach based on the double-square root equation. *Geophys. J. Int., submitted.*

De Hoop, M. V., Symes, W., Brandsberg-Dahl, S., & Ursin, B. 2001b. Tomographic migration velocity analysis by differential semblance opticmization with respect to scattering-angle/azimuth in anisotropic elastic media. *Center for Wave Phenomena, Colorado School of Mines CWP-374.*

De Witte-Morette, C., Maheshwari, A., & Nelson, B. 1979. Path integration in non-relativistic quantum mechanics. *Physics Reports*, **50**, 255–372.

Deregowski, S. M., & Rocca, F. 1981. Geometrical optics and wave theory of constant offset sections in layered media. *Geophys. Prosp.*, **29**, 374–406.

Dieudonné, J. 1969. *Treatise on analysis.* Vol. 1. Academic Press, New York.

Dieudonné, J. 1972. *Treatise on analysis.* Vol. 3. Academic Press, New York.

Dowker, J. S. 1976. Path integrals and ordering rules. *J. Math. Phys.*, **17**, 1873–1874.

Dubrulle, A. A. 1983. Numerical methods for the migration of constant-offset sections in homogeneous and horizontally layered media. *Geophysics*, **48**, 1195–1203.

Duistermaat, J. J. 1996. *Fourier integral operators.* Progress in Mathematics, vol. 130. Birkhäuser, Boston.

Duitermaat, J. J., & Hörmander, L. 1972. Fourier integral operators II. *Acta Math.*, **128**, 183–269.

Ekren, B. O., & Ursin, B. 1999. True-amplitude frequency-wavenumber constant-offset migration. *Geophysics*, **64**, 915–924.

Feit, M. D., & Fleck, J. A. 1978. Light propagation in graded-index optical fibers. *Appl. Opt.*, **17**, 3990–3998.

Filice, J. P. 1984. *Studies of the microscale density fluctuations in the solar wind using the power law phase screen model.* Ph.D. thesis, Univ. of Calif. San Diego, La Jolla.

Fishman, L., & McCoy, J. J. 1984a. Derivation and application of extended parabolic wave theories I. The factorized Helmholtz equation. *J. Math. Phys.*, **25**, 285–296.

Fishman, L., & McCoy, J. J. 1984b. Derivation and application of extended parabolic wave theories II. Path integral representations. *J. Math. Phys.*, **25**, 297–308.

Fishman, L., De Hoop, M. V., & Van Stralen, M. J. N. 2000. Exact construction of square-root Helmholtz operator symbols: The focusing quadratic profile. *J. Math. Phys.*, **41**, 4881–4938.

Fisk, M. D., & McCartor, G. D. 1991. The phase screen method for vector elastic waves. *J. Geophys. Res.*, **96**, 5985–6010.

Fisk, M. D., Charrette, E. E., & McCartor, G. D. 1992. A comparison of phase screen and finite difference calculations for elastic waves in random media. *J. Geophys. Res.*, **97**, 12409–12423.

Flatté, S. M., Dashen, R., Munk, W. H., Watson, K. M., & Zachariasen, F. 1979. *Sound transmission through a fluctuating ocean.* Cambridge University Press, New York.

Folland, G. B. 1989. *Harmonic analysis in phase space.* Princeton University Press, Princeton NJ.

Folland, G. B. 1995. *Introduction to partial differential equations.* 2nd. edn. Princeton University Press, Princeton, N.J.

Friedlander, F. G. 1998. *Introduction to the theory of distribution.* 2nd. edn. Cambridge University Press.

Gazdag, J. 1978. Wave equation migration with the phase-shift method. *Geophysics*, **43**, 1342–1351.

Gazdag, J., & Sguazzero, P. 1984. Migration of seismic data by phase shift plus interpolation. *Geophysics*, **49**, 124–131.

Hadley, G. R. 1992. Wide-angle beam propagation using Padé approximant operator. *Opt. Lett.*, **17**, 1426–1428.

Hale, D. 1991a. Migration via McClellan transformations. *Geophysics*, **56**(11), 1778–1785.

Hale, D. 1991b. Stable explicit depth extrapolation of seismic wavefields. *Geophysics*, **56**(11), 1770–1777.

Hirsch, M. W., & Smale, S. 1974. *Differential equations, dynamical systems, and linear algebra.* Academic Press, New York.

Holberg, O. 1988. Towards optimum one-way wave propagation. *Geophys. Prosp.*, **36**, 99–114.

Hörmander, L. 1985a. *The analysis of linear partial differential operators.* Vol. 3. Springer-Verglad, Berlin.

Hörmander, L. 1985b. *The analysis of linear partial differential operators.* Vol. 4. Springer-Verglad, Berlin.

Hörmander, L. 1971. Fourier integral operators I. *Acta Math.*, **127**, 79–183.

Hörmander, L. 1979. The Weyl calculus of pseudo-differential operators. *Comm. Pure Appl. Math.*, **32**, 359–443.

Hörmander, L. 1990. *The analysis of linear partial differential operators.* 2nd. edn. Vol. 1. Springer-Verlag, Berlin.

Huang, L.-J., & Wu, R.-S. 1996. 3D prestack depth migration with acoustic pseudo-screen propagators. *Pages 40–51 of:* Hassanzadeh, S. (ed), *Proc. SPIE 2822.*

Huang, L.-J., Fehler, M. C., & Wu, R.-S. 1999. Extended local Born Fourier migration method. *Geophysics*, **64**, 1524–1534.

Hudson, J. A. 1980. A parabolic approximation for elastic waves. *Wave Motion*, **2**, 207–215.

Huygens, C. 1690. *Traité de la lumière.* Pierre van der Aa, Leyden. Translated reprint (*Treatise on light*), Dover, New York, 1962.

Jones, L. E. A., & Wang, H. F. 1981. Ultrasonic velocities in Cretaceous shales from the Williston basin. *Geophysics*, **46**, 288–297.

Kendall, J.-M., & Thomson, C. J. 1993. Maslov ray summation, pseudo-caustics, Lagrangian equivalence and transient seismic waveforms. *Geophys. J. Int*, **113**, 186–214.

Kennett, B. L. N. 1985. *Seismic wave propagation in stratified media.* Cambridge University Press, Cambridge.

Knepp, D. L. 1983. Multiple phase screen calculation of the temporal behavior of stochastic waves. *Proc. IEEE*, **71**, 722–737.

Landers, T., & Claerbout, J.F. 1972. Numerical calculation of elastic waves in laterally inhomogeneous media. *J. Geophys. Res.*, **77**, 1476–1482.

Le Rousseau, J. H., & De Hoop, M. V. 1998. Modeling and imaging with the generalized screen algorithm. *Pages 1937–1940 of: Expanded Abstracts.* Soc. Explor. Geophys.

Le Rousseau, J. H., & De Hoop, M. V. 2001a. Generalized-screen approximation and algorithm for the scattering of elastic waves. *Q. J. Mech. Appl. Math., accepted for publication.*

Le Rousseau, J. H., & De Hoop, M. V. 2001b. Modeling and imaging with the scalar generalized-screen algorithms in isotropic media. *Geophysics*, **66**, 1551–1568.

Le Rousseau, J. H., & De Hoop, M. V. 2001c. Scalar generalized-screen algorithms in transversely isotropic media with a vertical symmetry axis. *Geophysics*, **66**, 1538–1550.

Le Rousseau, J. H., De Hoop, M. V., & Olhoeft, G. R. 2000. Generalized-screen approximation for the scattering of electromagnetic waves in isotropic, frequency dependent media. *In: Proc. 8th Internat. Conf. on Ground Penetrating Radar, Gold Coast, Australia, May 23-26, 2000.*

Le Rousseau, J. H., Hörmann, G., & De Hoop, M. V. 2001. Trotter product and Fourier integral operators. *in prep.*

Martin, J.M., & Flatté, S. M. 1988. Intensity images and statistics from numerical simulation of wave propagation in 3-D random media. *Appl. Opt.*, **27**, 2111–2125.

Maslov, V. P., & Fedoriuk, M. V. 1981. *Semi-classical approximation in quantum mechanics.* Dordrecht, Reidel.

Mayes, I. W., & Dowker, J. S. 1972. Canonical functional integrals in general coordinates. *Proc. R. Soc. Lond. A*, **327**, 131–135.

McClellan, J. H. 1973. The design of two-dimensional digital filters by transformations. *Pages 247–251 of: Proc. 7th Ann. Princeton Conf. on Inform. Sci. and Syst.*

McCoy, J. J., & Frazer, L. N. 1987. Pseudodifferential operators, operator orderings, marching algorithms and path integrals for one-way equations. *Wave Motion*, **9**, 413–427.

Mercier, R. P. 1962. Diffraction by a screen causing large random phase fluctuations. *Proc. Cambridge Philos. Soc.*, **58**, 382–400.

Michor, P. 1991. *Foundations of differential geometry.* Lecture Notes,. University of Vienna, Austria. Available electronically at
`http://www.mat.univie.ac.at/people/michor/listpubl.html#books`.

Mosher, C. C., Foster, D. J., & Hassanzadeh, S. 1997. Common angle imaging with offset plane waves. *Pages 1379–1382 of: Expanded Abstracts.* Soc. Explor. Geophys.

Popovici, A. M. 1996. Prestack migration by split-step DSR. *Geophysics*, **61**, 1412–1416.

Ratcliffe, J. A. 1956. Some aspects of diffraction theory and their application to the ionosphere. *Rep. Prog. Phys.*, **19**, 190–263.

Robbin, J., & Salamon, D. 1993. Phase functions and path integrals. *Pages 203–226 of:* Salamon, D. (ed), *Symplectic geometry.* London Math. Soc., LN series, vol. 192. Cambridge University Press, Cambridge.

Saint Raymond, X. 1991. *Elementary introduction to the theory of pseudodifferential operators.* CRC Press, Boca Raton.

Schlottmann, R. B. 1999. A path integral formulation of acoustic wave propagation. *Geophys. J. Int.*, **137**, 353–363.

Schoenberg, M., & De Hoop, M. V. 2000. Approximate dispersion relations for qP-qSV waves in transversely isotropic media. *Geophysics*, **65**, 919–933.

Schulman, L. S. 1981. *Techniques and Applications of path integration.* John Wiley and Sons, New York.

Schwartz, L. 1966a. *Mathematics for the physical sciences.* Hermann, Paris; Addison-Wesley Pub. Co, Reading, Mass.

Schwartz, L. 1966b. *Théorie des distributions.* 2nd edn. Hermann, Paris.

Shubin, M. A. 1987. *Pseudodifferential Operators and Spectral Theory.* Springer-Verlag New York.

Spivak, M. 1965. *Calculus on manifolds.* Addison-Wesley, Reading, Mass.

Stoffa, P. L., Fokkema, J. T., de Luna Freire, R. M., & Kessinger, W. P. 1990. Split-step Fourier Migration. *Geophysics*, **55**, 410–421.

Stolk, C. C., & De Hoop, M. V. 2000. Microlocal analysis of seismic inverse scattering in anisotropic elastic medi. *Comm. Pure Appl. Math., submitted.*

Stolt, R. H. 1978. Migration by Fourier transform. *Geophysics*, **43**, 23–48.

Tappert, F. D. 1977. The parabolic approximation method. *Pages 224–287 of:* Keller, J.B., & Papadakis, J.S. (eds), *Wave propagation and underwater acoustics.* Lecture Notes in Physics, vol. 70. Springer-Verlag, New York.

Thomsen, L. 1986. Weak elastic anisotropy. *Geophysics*, **51**, 1954–1966.

Thomsen, L. 1998. *personal communication.*

Thomsen, L. A., Barkved, O., Haggard, B., Kommedal, J. H., & Rosland, B. 1997. Converted-wave imaging of Valhall reservoir. *In: Expanded Abstracts.* Eur. Assoc. Expl. Geophys.

Thomson, D. J., & Chapman, N. R. 1983. A wide-angle split-step algorithm for the parabolic equation. *J. Acoust. Soc. Am.*, **74**, 1848–1854.

Treves, F. 1967. *Topological vector spaces, distributions and kernels.* Academic Press, New York.

Treves, F. 1975. *Basic linear partial differential equations.* Academic Press, New York.

Treves, F. 1980a. *Introduction to pseudodifferential and Fourier integral operators.* Vol. 1. Plenum Press, New York.

Treves, F. 1980b. *Introduction to pseudodifferential and Fourier integral operators.* Vol. 2. Plenum Press, New York.

Tsvankin, I. 1996. P-wave signatures and notation for transversely isotropic media: an overview. *Geophysics*, **61**(2), 467–483.

Van Stralen, M. J. N., De Hoop, M. V., & Blok, H. 1998. Generalized Bremmer series with rational approximation for the scattering of waves in inhomogeneous media. *J. Acoust. Soc. Am.*, **104**(4), 1943–1963.

Wapenaar, C. P. A., & Berkhout, A. J. 1989. *Elastic wave field extrapolation. Redatuming of single- and multi-component seismic data.* Elsevier Science Publ. Co., Inc.

Widder, D. V. 1946. *The Laplace transform.* Princeton University Press, Princeton.

Wild, A. J., & Hudson, J. A. 1998. A geometrical approach to the elastic complex screen. *J. Geoph. Res.*, **103**, 707–725.

Wu, R.-S. 1994. Wide-angle elastic wave one-way propagation in heterogeneous media and an elastic wave complex-screen method. *J. Geophys. Res.*, **99**, 751–766.

Wu, R.-S., & Huang, L.-J. 1992. Scattered field calculation in heterogeneous media using phase-screen propagation. *Pages 1289–1292 of: Expanded Abstracts.* Soc. Of Expl. Geophys.

Wu, R.-S., & Huang, L.-J. 1995. Reflected wave modeling in heterogeneous acoustic media using the de Wolf approximation. *Pages 176–186 of:* Hassanzadeh, S. (ed), *Proc. SPIE 2571.*

Wu, R.-S., & Jin, S. 1997. Windowed GSP (generalized screen propagators) migration applied to SEG-EAEG salt model data. *Pages 1746–1749 of: Expanded Abstracts.* Soc. Explor. Geophys.

Wu, R.-S., & Xie, X.-B. 1994. Multi-screen backpropagator for fast 3D elastic prestack migration. *Pages 181–193 of:* Hassanzadeh, S. (ed), *Proc. SPIE 2301.*

Appendix A

Fundamental concepts and tools of microlocal analysis

Microlocal analysis is the study of *singularities* (of a wave field for instance) as well as their *'high-frequency' orientations* (directions of propagation); the two combined form the wave front set. In direct and inverse wave propagation problems, microlocal analysis provides mathematical tools to follow the propagation of singularities, even in rather complex media (in the presence of caustics). In a remote sensing experiment, most of the information is contained in the wave front set of the data. Microlocal analysis thus offers a suitable framework for inverse scattering theory.

Microlocal tools are often used to construct parametrices of some partial differential equations (PDEs), e.g elliptic and strongly hyperbolic. A parametrix is a fundamental solution E up to a smooth contribution[1] (Treves, 1980a). In the case of elliptic PDEs parametrices can be obtained using pseudodifferential operators (ΨDOs). For strongly hyperbolic PDEs[2] parametrices can be obtained with the aid of Fourier integral operators (FIOs). For constructions of such parametrices see for instance Treves (1980a; 1980b). In this thesis we use ΨDOs to construct the square-roots of elliptic partial differential operators.

In this appendix we also present concepts from the fields of symplectic geometry and differential geometry which are of 'every-day' use in microlocal analysis. These concepts are especially important to understanding the propagation of singularities, which is at the heart of the (inverse) scattering theory and its applications to seismic data processing.

For basic references on the theory of distribution we refer the reader to Schwartz (1966a), and Friedlander (1998). For more advanced treatments see Schwartz (1966b), Treves (1967), and Hörmander (1990). A good review of definitions and properties of distributions can be found in Chazarain and Piriou (1982).

Let Ω be an open set of $\mathbb{R}^n$. We recall that distributions on Ω, $\mathcal{D}'(\Omega)$ are continuous linear maps on the space of smooth compactly supported function on Ω, $C_c^\infty(\Omega)$. We denote by $\mathcal{E}'(\Omega)$ the space of distribution with compact support on Ω.

[1] By smooth we mean infinitely differentiable everywhere.

[2] For definitions of strongly hyperbolic PDEs see Treves (1980b), Chpt.6 Def. 1.1, Treves (1975), Sects. 15 and 16, or Hörmander (1985a), Chpt. 23

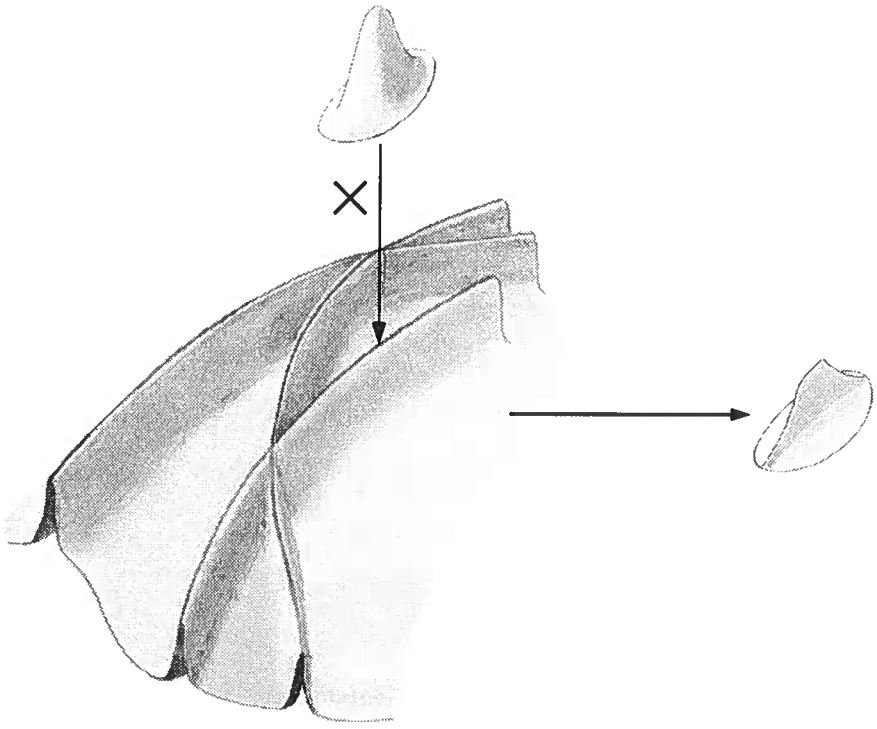

Figure A.1. Localization of a distribution. A smooth function with compact support is multiplied to the distribution leaving out most of the distribution. This allows to isolate the singular behavior at a particular point.

A.1 The wave front set of a distribution

The wave front set is one of the most fundamental notions in microlocal analysis and its application to seismic data analysis. In reflection seismic data the information exploited in both inverse and imaging methods as well as in subsequent interpretations is primarily contained in the wave front set of the data. The wave front set represents the high-frequency information in the data. Once the source wavelet is (approximately) suppressed from the data by deconvolution, the events in the seismic data are characterized by the singular support of the data, which corresponds to the so-called reflectivity series. The notion of wave front set further introduces the orientations of those singularities. This includes information such as slopes and so-called 'move-out'.

Distributions in $\mathbb{R}^n$ can be localized to a neighborhood V of a point $x \in \mathbb{R}^n$ by multiplying them by a test function $\varphi \in C_c^\infty(\mathbb{R}^n)$, i.e., φ is smooth and compactly supported, such that $\operatorname{supp}\varphi \subset V$. The singular support of a distribution u on $\mathbb{R}^n$ is the set where the distribution is not smooth (sc. C^∞): $x \notin \operatorname{singsupp} u$, if and only if there exists $\varphi \in C_c^\infty(\mathbb{R}^n)$ with $\varphi(x) \neq 0$ such that $\varphi u \in C_c^\infty(\mathbb{R}^n)$. The localization procedure is illustrated in Figure A.1. In this figure one sees that the localization allows to focus on some of the

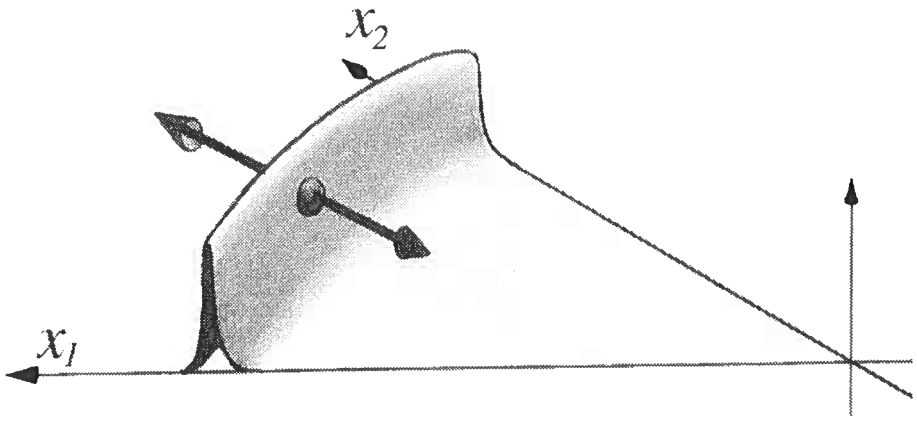

Figure A.2. The wave front set.

singularities of the distribution. This is needed for the identification of the orientation of the singularities by means of a Fourier transform.

Once a distribution u is localized in the neighborhood of a point x, if we take its Fourier transform, then the orientations of the singularities will be identified with the set of directions of non-rapid decay at ∞, denoted by $\Sigma(\varphi u)$: $\xi_0 \notin \Sigma(\varphi u)$ if and only if $\xi_0 \neq 0$ and there exists a conic neighborhood V of ξ_0, i.e., a neighborhood invariant by positive scaling, such that

$$\forall N \in \mathbb{N}, \ \sup_{\xi \in V} (1 + |\xi|)^N |\widehat{\varphi u}(\xi)| < \infty \ ,$$

where $\widehat{\varphi u}$ is the Fourier transform of φu. Note that $\Sigma(\varphi u)$ is closed and conic in $\mathbb{R}^n$.

If we want to identify the directions of the singularities at the point x rather than in a neighborhood of x, we have to shrink the support of φ to $\{x\}$ or more precisely we define the cone $\Sigma_x(u)$ as

$$\Sigma_x(u) = \bigcap_{\varphi} \Sigma(\varphi u) \ ,$$

where the intersection is taken over all test functions φ such that $\varphi(x) \neq 0$. Finally, we are ready to define the *wave front set* of u as

$$\mathrm{WF}(u) = \{(x, \xi) \in \mathbb{R}^n \times (\mathbb{R}^n \backslash 0) \mid \xi \in \Sigma_x(u)\} = \bigcup_{x \in \mathbb{R}^n} \{x\} \times \Sigma_x(u) \ .$$

The projection of the wave front set onto the base space naturally yields the singular support of the distribution. In Figure A.2 we give an illustration of what the wave front set is in a simple case. In Figure A.1 It should be observed that some points x can be associated

with more than one singular direction ξ. This naturally occurs in the presence of caustics in some wavefield.

In summary, we localize the singularities, i.e., the high frequency information, in space with the help of test functions and in the wave number domain by identifying the directions of non-rapid decay.

For a detailed treatment of wave front sets and examples see Hörmander (1990, Chpt. 8).

A.2 Pseudodifferential operators

A.2.1 Basic definitions, symbols, amplitudes, composition

ΨDOs generalize partial differential operators (PDOs), hence their name. Define $D_j = -\mathrm{i}\,\partial_j$, $1 \le j \le n$. In multi-index notation (Treves, 1980a) with $\alpha = (\alpha_1, \cdots, \alpha_n)$ we have $D^\alpha = D_1^{\alpha_1} D_2^{\alpha_2} \cdots D_n^{\alpha_n}$. Define also $|\alpha| = \sum_j \alpha_j$. Consider now the PDO, $P(x,D) = \sum_{|\alpha| \le m} a_\alpha(x) D^\alpha$. For instance the Laplace operator, Δ, is written as $-D_1^2 - D_2^2 - \cdots - D_n^2$. The action of a PDO on a test function, φ, can be written with the help of the Fourier transform $\widehat{\varphi}$ of φ as

$$\begin{aligned} P(x,D)\varphi(x) &= (2\pi)^{-n} \int e^{\mathrm{i}\langle x|\xi\rangle} p(x,\xi)\, \widehat{\varphi}(\xi)\, \mathrm{d}\xi \\ &= (2\pi)^{-n} \iint e^{\mathrm{i}\langle x-y|\xi\rangle} p(x,\xi)\, \varphi(y)\, \mathrm{d}\xi\, \mathrm{d}y\,, \end{aligned}$$

with $p(x,\xi) = \sum_{|\alpha| \le m} a_\alpha(x)\xi^\alpha$. ΨDOs are a generalization of such a representation which allow for more general forms of $p(x,\xi)$. For this purpose we define, $\mathcal{S}^m = \mathcal{S}^m(\mathbb{R}^n \times \mathbb{R}^n)$, the space of *symbols* of order m as the set of all $a \in C^\infty(\mathbb{R}^n \times \mathbb{R}^n)$ such that for all α, β (multi-indices), and for all compact $K \subset \mathbb{R}^n$, there exists $C_{\alpha,\beta,K}$ such that

$$|\partial_\xi^\alpha \partial_x^\alpha a(x,\xi)| \le C_{\alpha,\beta,K}(1+|\xi|)^{m-\alpha}\,,\ x \in K\,,\ \xi \in \mathbb{R}^n\,. \tag{A.1}$$

For example, a polynomial of order m in ξ is a symbol of order m. Note that the terms of the polynomial are homogeneous of degree equal to their order ($a_\alpha(x)(\lambda\xi)^\alpha = \lambda^\alpha a_\alpha(x)\xi^\alpha$). Estimate (A.1) generalizes the concept of homogeneity. Noting that $\mathcal{S}^m \subset \mathcal{S}^{m'}$ if $m \le m'$, we define

$$\mathcal{S}^{-\infty} = \bigcap_{m \in \mathbb{R}} \mathcal{S}^m\,.$$

For $a \in \mathcal{S}^m$ we define the operator $\mathrm{Op}(a)$ as

$$\mathrm{Op}(a)\varphi(x) = (2\pi)^{-n} \iint e^{\mathrm{i}\langle x-y|\xi\rangle} a(x,\xi)\, \varphi(y)\, \mathrm{d}\xi\, \mathrm{d}y\,,\ \varphi \in C_c^\infty(\mathbb{R}^n)\,. \tag{A.2}$$

The operator $\mathrm{Op}(a)$ is called the ΨDO associated with the symbol a, while a is called the (left) symbol of $\mathrm{Op}(a)$. Note that for all $\varphi \in C_c^\infty(\mathbb{R}^n)$ $\mathrm{Op}(a)\varphi$ is a smooth function because of estimate (A.1). Furthermore, a ΨDO can be extended to map $\mathcal{E}'(\mathbb{R}^n)$ into $\mathcal{D}'(\mathbb{R}^n)$. Note

that the (left) symbol depends on the output variable, x. On the other hand, there exists a symbol a_r such that the same operator can be rewritten as

$$\mathrm{Op}(a)\varphi(x) = (2\pi)^{-n} \iint e^{\mathrm{i}\langle x-y|\xi\rangle} a_r(y,\xi)\, \varphi(y)\, \mathrm{d}\xi\, \mathrm{d}y\ .$$

Note that the symbol depends then on the input variable, y; a_r is called right or dual symbol and the relation between left and right symbol is given by (Treves, 1980a)

$$a(x,\xi) = e^{\mathrm{i}\langle D_y, D_\xi\rangle} a_r(y,\xi)\big|_{y=x}\ .$$

We now define amplitudes as symbols on $\mathbb{R}^{2n} \times \mathbb{R}^n$. Amplitudes also can be used to define ΨDOs. A ΨDO, B, with amplitude $b(x,y,\xi)$ is defined by its action on a test function ϕ:

$$B\varphi(x) = (2\pi)^{-n} \iint e^{\mathrm{i}\langle x-y|\xi\rangle} b(x,y,\xi)\, \varphi(y)\, \mathrm{d}\xi\, \mathrm{d}y\ .$$

Such an operator can always be put in the form of definition (A.2) (Treves, 1980a). We therefore recover the previous definition. A ΨDO can thus have more than one amplitude. Note that amplitudes of ΨDOs depend generally both on the input point, y, and the output point, x. Left and right symbols are both admissible amplitudes for a ΨDO. However, up to $\mathcal{S}^{-\infty}$ contributions the left and right symbols of a ΨDO are uniquely defined (Treves, 1980a; Hörmander, 1985a). We thus see that the same operator can have various representations depending on the choice to use left or right symbols or an admissible amplitude.

The so-called Weyl symbol, a_w, is a particular case of an amplitude which allows the operator A to be written in the form

$$A\varphi(x) = (2\pi)^{-n} \iint e^{\mathrm{i}\langle x-y|\xi\rangle} a_w(\frac{x+y}{2},\xi)\, \varphi(y)\, \mathrm{d}\xi\, \mathrm{d}y\ .$$

In the case of (classical) polyhomogeneous symbols, i.e., symbols that are asymptotic series of homogeneous terms with decreasing integer orders going to $-\infty$, we define the principle part as the term with the highest degree of homogeneity. A principal part may also be defined for more general symbols. Since we mainly deal with polyhomogeneous symbols here (e.g., the generalized-screen expansion of the vertical slowness symbol), we refer the reader to Hörmander (1985a) for such a definition. Note that the principal symbol is the same for both left and right symbols.

The composition of two ΨDOs, $\mathrm{Op}(a_1)$ and $\mathrm{Op}(a_2)$, yields a ΨDO with symbol given by (Hörmander, 1985a, Thm. 18.1.8)

$$a(x,\xi) = e^{\mathrm{i}\langle D_y, D_\eta\rangle} a_1(x,\eta) a_2(y,\xi)\big|_{\eta=\xi,\ y=x}\ . \tag{A.3}$$

Note than if one restricts oneself to the principal part only, the composition formula (A.3) is then simply the product of the two principal symbols. In the case of the composition of two PDOs, note that the series representation of equation (A.3) naturally truncates.

A.2.2 Action on wave front sets

We now present microlocal properties of ΨDOs, i.e., how they affect wave front sets. For this purpose, we first define the characteristic set of a ΨDO. If a_m is the principal symbol of A, a ΨDO of order m, A is said to be non-characteristic at $(x_0, \xi_0) \in \mathbb{R}^n \times \mathbb{R}^n$ (i.e., (x_0, ξ_0) not in the characteristic set of A) if there exists a neighborhood V of (x_0, ξ_0) , such that

$$|a_m(x,\xi)| \geq c|\xi|^m \text{ for large } |\xi| \,, \quad (x,\xi) \in V \,.$$

If a_m is homogeneous this definition is then equivalent to $a_m(x_0, \xi_0) \neq 0$. Such a definition is therefore compatible with that of the characteristic set of PDOs. The set of characteristic points is denoted Char$A$. When the characteristic set of a ΨDO is empty, it is called an elliptic ΨDO. We then have the microlocal property of ΨDOs (Hörmander, 1985a):

$$\forall\, u \in \mathcal{E}'(\mathbb{R}^n) \,, \quad \mathrm{WF}(Au) \subset \mathrm{WF}(u) \subset \mathrm{WF}(Au) \cup \mathrm{Char}A \,.$$

Such an estimate shows how the singularities of the right-hand side of a pseudodifferential equation propagate in the solution. In the case of an elliptic ΨDO we then have:

$$\forall\, u \in \mathcal{E}'(\mathbb{R}^n) \,, \quad \mathrm{WF}(Au) \subset \mathrm{WF}(u) \subset \mathrm{WF}(Au) \,,$$

i.e., the classical result that there is no propagation of singularities associated with an elliptic operator. An example of an elliptic operator is the Laplace operator.

A.2.3 Particular notations

In various chapters of the thesis, we have changed variables, $\boldsymbol{\alpha} = \boldsymbol{\xi}/s$, in the original Fourier transform. The symbol h of a ΨDO H is then defined as

$$(H\varphi)(\boldsymbol{x}) = (s/2\pi)^n \iint \exp[-\mathrm{i}s(x_\sigma - y_\sigma)\alpha_\sigma]\, h(\boldsymbol{x}, \boldsymbol{\alpha})\, \varphi(y)\, \mathrm{d}\boldsymbol{y}\, \mathrm{d}\boldsymbol{\alpha} \,.$$

Then the symbol of $D_\nu = -s^{-1}\partial_\nu$, i.e. the differentiation operator in the lateral directions x_ν, $\nu = 1, 2$, scaled by the Laplace parameter s (cf. Chapter 3), is $\mathrm{i}\alpha_\nu$. For instance the symbol of the transverse Helmholtz operator of Chapter 3,

$$\hat{\mathrm{A}} = -D_\nu D_\nu + \kappa\rho - \rho^{-1}(D_\nu\rho)\, D_\nu - \rho^{-1}(D_\nu^2\rho) + \rho^{-2}(D_\nu\rho)^2 \,,$$

as found in equation (3.70), is

$$\hat{\mathrm{A}} = \alpha_\nu\alpha_\nu + \kappa\rho - \rho^{-1}(D_\nu\rho)\, \mathrm{i}\alpha_\nu - \rho^{-1}(D_\nu^2\rho) + \rho^{-2}(D_\nu\rho)^2 \,.$$

For elementary introductions to the subject of ΨDOs see Saint Raymond (1991) and Folland (1995). For more advanced treatments, see Treves (1980a), Hörmander (1985a), and Shubin (1987).

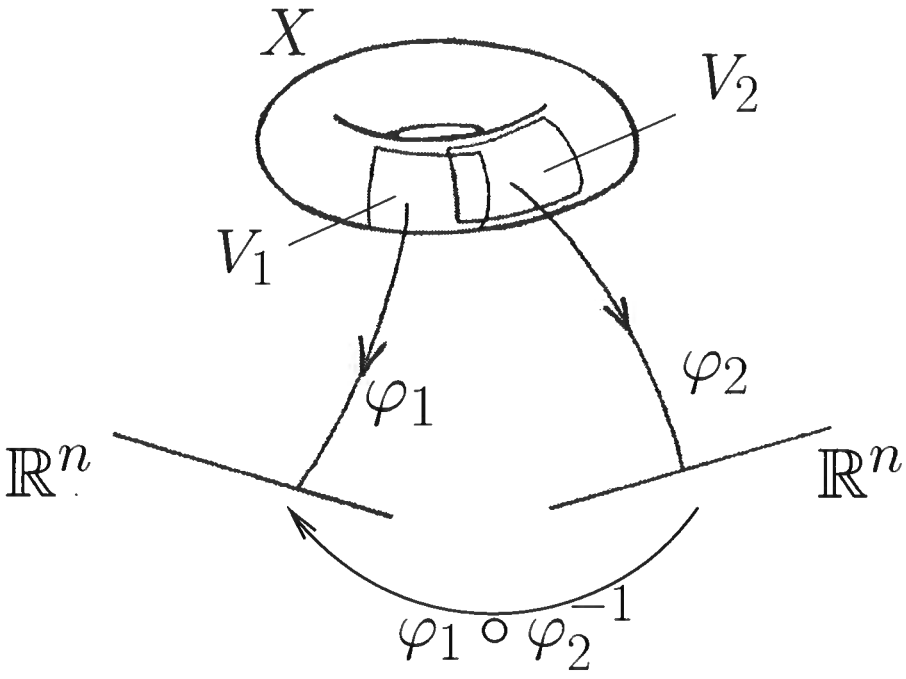

Figure A.3. Two charts on a manifold.

A.3 Some concepts from differential and symplectic geometry

For basic references on manifolds and differential geometry see Spivak (1965) and Choquet-Bruhat *et al.* (1996). For more advanced sources we refer the reader to Dieudonné (1972) and Michor (1991). For a treatment of symplectic geometry we refer the reader to Abraham and Marsden (1978) and Hömander (1985a, chapter 21)

A.3.1 Manifolds

Manifolds generalize the concept of surfaces. A Hausdorff[3] topological space X is called a manifold of dimension n if every point of X has a neighborhood homeomorphic to $\mathbb{R}^n$, i.e., if V is such a neighborhood, there exists a mapping φ from V onto $\mathbb{R}^n$ that is invertible (bijective), continuous and its inverse is also. A pair (V, φ) is called a chart of X; V is called the domain of the chart. A family of charts $(V_i, \varphi_i)_{i \in I}$ such that the domains $(V_i)_{i \in I}$ cover X is called an atlas. If furthermore for all $i, j \in I$, $\varphi_i \circ \varphi_j^{-1}$ is a diffeomorphism of $\varphi_j(V_i \cap V_j)$ onto $\varphi_i(V_i \cap V_j)$ (i.e., a mapping that is invertible and such that it is infinitely differentiable and its inverse is also) the atlas and the manifold X are said to be smooth. Those notions are illustrated in Figure A.3. Consider a chart (V, φ). We

[3]By Hausdorff it is meant that two points on X can be separated in the topology of X [see for instance Treves (1967) or Bourbaki (1966).]

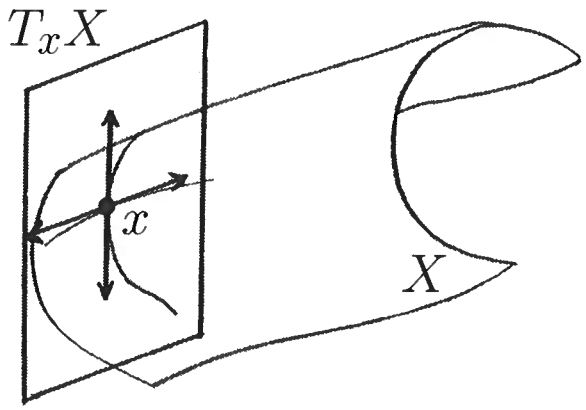

Figure A.4. The tangent space of X at x.

only consider smooth manifolds here. For all $x \in V$, we can write $\varphi(x) = (x_1(x), \cdots x_n(x))$. The functions x_k, $1 \leq k \leq n$ are called the coordinate functions for the chart (V, φ).

A manifold X of dimension k, which is a subset of a manifold Y of dimension n, is called a submanifold of Y if for all $x \in X$ there exist a chart (V, φ) of Y, such that $x \in V$ and in this chart X is defined by $x_1 = \cdots = x_{n-k} = 0$.

A map f from a manifold X with atlas $(V_i, \varphi_i)_{i \in I}$ into a manifold Y with atlas $(W_j, \psi_j)_{j \in J}$ is said to be a C^r diffeomorphism if it is bijective and for all x in X, and for all $(i, j) \in I \times J$ with $x \in V_i$ and $f(x) \in W_j$, $\psi_j \circ f \circ \varphi_i^{-1}$ is r times continuously differentiable at $\varphi_i(x) \in \varphi_i(V_i)$ and its inverse at $\psi_j(f(x)) \in \psi_j(W_j)$ is also.

A.3.2 Tangent and cotangent bundles

At every point x of a manifold X we can define the tangent space, T_xX. This can be done by defining the tangent space as the set of all vectors tangent, at x, to smooth curves on X passing through x. We then define the *tangent bundle* of X as

$$TX = \bigcup_{x \in X} \{x\} \times T_xX \, .$$

For $\mathbb{R}^n$ we naturally have $T\mathbb{R}^n \simeq \mathbb{R}^n \times \mathbb{R}^n$. Every tangent bundle locally has such a structure. One should however keep in mind that generally the tangent bundle is not globally a Cartesian product. Figure A.4 illustrates the intuitive notion of tangent space.

The tangent space of X at x is a vector space of dimension n . One can therefore introduce its dual T_x^*X. One can then define the so-called *cotangent bundle* as

$$T^*X = \bigcup_{x \in X} \{x\} \times T_x^*X \, .$$

For $\mathbb{R}^n$ we have $T^*\mathbb{R}^n \simeq \mathbb{R}^n \times \mathbb{R}^n$. In the forward and inverse Fourier transforms we

encounter the inner product $\langle x, \xi \rangle$. Since on $\mathbb{R}^n$ the tangent space is identified with the space itself, ξ is then considered as a dual variable of x, i.e., the cotangent variable. This allows us to define the wave front set of a distribution on $\mathbb{R}^n$ as a subspace of $T^*\mathbb{R}^n$. Noting that the wave font set is geometrically invariant, i.e., does not depend on the local chart used, this further enables us to define the wave front set of a distribution on a manifold (Hörmander, 1990, Chpt. 8.1).

If X is a submanifold of Y, we can view the tangent space of X at x, T_xX, as a subspace of the tangent space of Y at x, T_xY. In the cotangent space of Y at x, T_x^*Y, there are then vectors orthogonal to those in T_xX. We denote this set as N_xX and define the conormal bundle of X as

$$NX = \bigcup_{x \in X} \{x\} \times N_xX \, .$$

NX is then a submanifold of T^*X and its dimension is the same as that of Y.

A.3.3 Symplectic and Lagrangian manifolds

The archetypical example of a symplectic manifold is given by $T^*\mathbb{R}^n$ along with the 2-form σ with the local representation

$$\sigma = \sum_i \mathrm{d}\xi_i \wedge \mathrm{d}x_i \, ,$$

i.e., if (u, v) and (u', v') are in the tangent plane of $T^*\mathbb{R}^n$ at (x, ξ), $T_{(x,\xi)}T^*\mathbb{R}^n$,

$$\sigma((u, v), (u', v')) = \langle u', v \rangle - \langle u, v' \rangle \, .$$

More generally a manifold S of dimension $2n$ along with a 2-form σ is said to be symplectic if σ is smooth, non-degenerate, and closed. By non-degenerate we mean that

$$\forall x \in S, \forall u \in T_xS, \quad (\forall v \in T_xS, \quad \sigma(u, v) = 0) \Rightarrow (u = 0) \, ,$$

and by closed we mean that $\mathrm{d}\sigma = 0$ where d is the exterior derivative (Choquet-Bruhat *et al.*, 1996; Abraham & Marsden, 1978). The symplectic manifold (S, σ) has locally the same symplectic structure as $T^*\mathbb{R}^n$ (Darboux theorem) (Hörmander, 1985a, theorem 21.1.6). A subset Γ of $T^*\mathbb{R}^n$ is said to be conic is it is not affected by positive scaling in the ξ direction, i.e., if $(x, \xi) \in \Gamma$ then for all $t > 0$ $(x, t\xi) \in \Gamma$.

Let (S, σ) be a symplectic manifold, say $T^*\mathbb{R}^n$, a submanifold $\mathcal{L}$ is Lagrangian if its dimension is n, i.e., half the dimension of S, and $\sigma \mid_{\mathcal{L}} = 0$, i.e., for all $x \in \mathcal{L}$, $T_x\mathcal{L}$ is its own orthogonal with respect to σ. An example of a Lagrangian submanifold of $T^*\mathbb{R}^n$ is the conormal bundle NX of a submanifold X of $\mathbb{R}^n$.

If (S_1, σ_1) and (S_2, σ_2) are two symplectic manifolds, a Lagrangian submanifold of $S_1 \times S_2$ with respect to the symplectic form $\sigma_1 - \sigma_2$ is called a *canonical relation* from S_2 to S_1. With 'Lagrangian submanifolds' we usually refers to those associated with the symplectic 2-form $\sigma_1 + \sigma_2$.

A.3.4 A fundamental example

We show the importance of canonical relation with an example relevant to seismic modeling and imaging. High-frequency methods make use of the (bi)characteristics of the wave equation. To do so one solves the corresponding Hamiltonian system with travel time as the flow parameter. Such a system is solved in the cotangent bundle of $\mathbb{R}^n$. In local coordinates, (x,ξ), x corresponds to the position while ξ corresponds to the momentum. (See Hirsch and Smale (1974) for a simple explanation of the cotangent nature of the momentum in classical mechanics.) If we write the Hamiltonian flow as $F_t(x_0,\xi_0) = (F_{t,x}(x_0,\xi_0), F_{t,\xi}(x_0,\xi_0))$ then for all admissible time t

$$C_t = \{(F_{t,x}(x_0,\xi_0), F_{t,\xi}(x_0,\xi_0); x_0,\xi_0) \mid (x_0,\xi_0) \in T^*(\mathbb{R}^n)\}$$

is a canonical relation because Hamiltonian vector fields preserve the symplectic form, σ on $T^*(\mathbb{R}^n)$ (Abraham & Marsden, 1978). One could also include travel time and frequency in the canonical relation (Stolk & De Hoop, 2000). We omit those for simplicity.

It is common to refer to the cotangent bundle T^*X as phase-space. When solving for the Hamiltonian flow, i.e., tracing rays in phase-space, one actually builds a correspondence 'table' between points in phase-space. Two points (x_1,ξ_1) and (x_2,ξ_2) are related to each other if there is a ray that connects them with travel time t, in other words if $(x_2,\xi_2;x_1,\xi_1) \in C_t$. The canonical relation C_t therefore gives such a correspondence and as shown in Section A.4 yields all the information necessary to follow the propagation of singularities, i.e. the evolution of the wave front set.

The canonical relation, C_t, is of dimension $2n$ in the present example. It is a submanifold of $T^*(X\times X)$. Projections on spaces of lower dimensions can be singular. If one chooses to ignore the dimensions associated to momentums, i.e., projects C_t into $X\times X$, singularities of such a projection correspond to caustics. This is illustrated in Figure A.5. One sees that on caustics one needs cotangent (momentum) variables to smoothly parameterize the canonical relation.

Canonical relations are therefore important geometrical objects that control the propagation of singularity. Their high dimensionality make them cumbersome to handle directly and projections to lower dimensional space can be singular. The introduction of phase functions can be a cure to those issues.

A.3.5 phase functions

Let X be a manifold of dimension n, e.g., $\mathbb{R}^n$, and $\phi(x,\theta)$ a smooth real valued function in an open conic set $\Gamma \subset X\times(\mathbb{R}^N\backslash 0)$ which is homogeneous of degree 1 in θ, i.e., $\phi(x,\lambda\theta) = \lambda\phi(x,\theta)$ for all $\lambda\in\mathbb{R}$. Then ϕ is called a *clean* phase function if $\mathrm{d}\phi \neq 0$ and the *stationary point set*

$$S_\phi = \{(x,\theta) \mid \partial_\theta\phi(x,\theta) = 0\}$$

is a smooth manifold with tangent space defined by the equations $\mathrm{d}(\partial_\theta\phi) = 0$. If the number of linearly independent equations $\mathrm{d}(\partial_\theta\phi) = 0$ is $N-e$ we call e the excess of the phase. The phase is said to be non-degenerate if $e = 0$. The dimension of the stationary point set, S_ϕ,

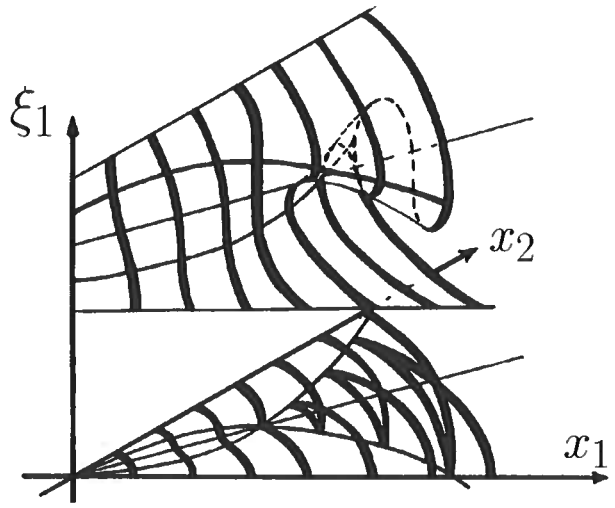

Figure A.5. Caustics and singular projections of the canonical relations.

is $n + e$. Furthermore the set

$$\Lambda_\phi = \{(x,\xi) \mid \xi = \partial_x\phi(x,\theta), \partial_\theta\phi(x,\theta) = 0 \text{ for some } \theta \in \mathbb{R}^N \backslash 0\}$$

has dimension n and is a locally conic Lagrangian submanifold of T^*X.

Conversely, given a conic Lagrangian submanifold Λ in T^*X, for every point of Λ, say (x,ξ) in local coordinates, we can locally parameterize Λ by a non-degenerate phase function ϕ in a conic neighborhood of (x,ξ) (Hörmander, 1985a, theorem 21.2.16). Hence a high dimensional object such as a Lagrangian submanifold (or a canonical relation) can be locally represented by a single function. This remarkable property is exploited in chapter 2.

Let X and Y be two manifolds. If $\phi(x,y,\theta)$ is a phase function on $X \times Y \times (\mathbb{R}^N \backslash 0)$ then

$$\Lambda_\phi = \{(x,\xi,y,\eta) \mid \xi = \partial_x\phi(x,y,\theta), \eta = \partial_y\phi(x,y,\theta), \partial_\theta\phi(x,y,\theta) = 0 \text{ for some } \theta \in \mathbb{R}^N \backslash 0\}$$

is a Lagrangian submanifold in $T^*X \times T^*Y$ for the symplectic 2-form $\sigma_x + \sigma_y$.

$$C_\phi = \{(x,\xi,y,\eta) \mid (x,\xi,y,-\eta) \in \Lambda_\phi\}$$

is then a canonical relation from T^*Y to T^*X. Canonical relations are sometimes called twisted Lagrangian submanifolds (they are Lagrangians associated with $\sigma_1 - \sigma_2$). When a canonical relation is a graph it is called a canonical transformation. Canonical relations are the geometrical objects used to characterize the propagation of singularities through the application of Fourier integral operators.

A.4 Fourier integral operators and oscillatory integrals

We start this brief introduction to FIOs with the definition of so-called oscillatory integrals (OIs). Let Ω be an open set of $\mathbb{R}^n$. OIs are (finite) distributions on Ω with an integral representation that makes sense via regularization (see Hörmander (1990, Sect. 7.8), (1971, Sect. 1.2)and see below). Let ϕ be a phase function on a open cone Γ of $\Omega \times (\mathbb{R}^N \backslash 0)$ for some N, i.e., $\phi(x,\theta)$ is real[4] smooth, homogeneous of degree 1 in θ, and non critical in Γ ($\mathrm{d}\phi \neq 0$). Let also $a \in \mathcal{S}^m(\Omega \times \mathbb{R}^N)$, i.e., a symbol of order m (see estimate (A.1)).

The symbol a is also chosen to have support in some closed cone, $F \subset \Gamma \cup (X \times \{0\})$. Then for $u \in C_c^\infty(\Omega)$ the integral

$$I_\phi(au) = \iint e^{i\phi(x,\theta)}\, a(x,\theta)\, u(x)\mathrm{d}x\mathrm{d}\theta\ ,$$

is well defined. It is clearly defined if, for instance, a is rapidly decreasing and from this it can be extended to all symbols in a unique manner. Such an integral is then called an OI. The symbol a is also referred to as the amplitude of the OI. In addition, the linear form, $\mathcal{I}$, on $C_c^\infty(\Omega)$

$$\mathcal{I}:\ u \mapsto I_\phi(au)$$

is a distribution of order $\leq k$ with $m + N < k$. One can further prove that if the phase ϕ and the symbol a depend continuously on a parameter, the OI does also. It is thus remarkable that in the framework of OIs, many integration procedures become licit (change in integration order, differentiation under the integral sign).

The regularization procedure can be performed in several different manners. On one hand, if $\chi \in C_c^\infty(\mathbb{R}^N)$, we have

$$I_\phi(au) = \lim_{t\to\infty} \iint e^{i\phi(x,\theta)}\, a(x,\theta)\, \chi(\theta/t)\, u(x)\mathrm{d}x\mathrm{d}\theta\ .$$

On the other hand, one can construct a first-order differential operator L such that $e^{i\phi}$ is left invariant by ${}^tL$. Then

$$I_\phi(au) = \iint e^{i\phi(x,\theta)}\, L^k(a(x,\theta)\, u(x)\mathrm{d}x\mathrm{d}\theta\ , \quad k \in \mathbb{N}\ ,$$

which is well defined for large enough k [use estimate (A.1)]. Note that similar definitions and analysis of OIs can be done for more general symbols (Hörmander, 1990, Def. 7.8.1) as well as different types of phase functions.

The stationary-point set,

$$S_\phi = \{(x,\theta) \in \Gamma \mid \partial_\theta \phi(x,\theta) = 0\}\ ,$$

[4] or of positive imaginary part

gives an estimate of the singular support of the OI as the projection of $S_\phi \cap F$ on Ω. Such an estimate is sharp and the actual singular support depends on the behavior of the symbol a on S_ϕ (Hörmander, 1971, Props. 1.2.4 and 1.2.5). The stationary point set also leads to an estimate for the wave front set of the OI:

$$\mathrm{WF}(\mathcal{I}) \subset \{(x, \partial_x \phi(x,\theta)) \mid (x,\theta) \in S_\phi \cap F\} .$$

When the phase is clean the stationary point set, S_ϕ, of the phase function is a submanifold (Hörmander, 1985a, Def. 21.2.15). Then

$$\Lambda_\phi = \{(x, \phi'_x(x,\theta) \mid (x,\theta) \in S_\phi\} ,$$

is *locally* a Lagrangian submanifold of $T^*(\Omega)$. In the case when $\Omega = X \times Y$, with X and Y open subsets of $\mathbb{R}^m$ and $\mathbb{R}^p$ for some m and p ($m+p=n$), the OI defined by such a phase function, ϕ, as well as a symbol, a, may be viewed as the kernel of an operator (Schwartz, 1966b; Treves, 1967; Hörmander, 1990), A, from $C_c^\infty(Y)$ into $\mathcal{D}'(X)$. Such an operator is called a (local) FIO. If ϕ has no stationary point as a function of (y,θ) for all $x \in X$, A maps $C_c^\infty(Y)$ into $C^\infty(X)$. If ϕ has no stationary point as a function of (x,θ) for all $y \in Y$, A can then be extended from $\mathcal{E}'(Y)$ into $\mathcal{D}'(X)$. A phase function that satisfies both these properties is called an operator phase function (Hörmander, 1971, Def. 1.4.4).

To the Lagrangian submanifold, Λ_ϕ, one can associate the canonical relation,

$$C_\phi = \{(x,\xi,y,-\eta) \mid (x,\xi,y,\eta) \in \Lambda_\phi\} .$$

This canonical relation gives the proper geometric tool to follow the propagation of singularities through the application of the FIO:

$$\mathrm{WF}(Au) \subset C_\phi \circ \mathrm{WF}(u) .$$

Two properly supported FIOs associated with operator phases can be composed, and the resulting operator will be an FIO if the two canonical relations compose cleanly (Hörmander, 1985b; Treves, 1980b).

For a given conic Lagrangian submanifold Λ in $T^*(\Omega)\backslash 0$, the space of Lagrangian distributions of order m, $I^m(\Omega,\Lambda)$, is defined via regularity properties along Λ. A distribution $u \in I^m(\Omega,\Lambda)$ if and only if

$$L_1 \cdots L_M \, u \in {}^\infty H^{loc}_{(-m-n/4)}(\Omega) ,$$

where the L_j's are first-order ΨDOs with principal symbols vanishing on Λ (for details on Besov spaces ${}^pH^{loc}_{(s)}$, $s \in \mathbb{R}$, $1 \le p \le \infty$, see Hörmander (1985a, Appx. B.1)). Elements of $I^m(\Omega,\Lambda)$ have their wave front set contained in Λ and they can be (locally) represented by OIs with clean phase functions that (locally) characterize Λ. One can associate to these Lagrangian distributions a principal symbol in an geometrically invariant way. This symbol appears as a section of the Maslov bundle over Λ tensored with the half-density bundle over Λ (Treves, 1980b; Hörmander, 1985a; Hörmander, 1985b; Duistermaat, 1996). In

Section A.3.5 it has been seen that a Lagrangian submanifold can be locally parameterized by a clean phase function. When no causitcs are present, i.e., the projection π into the base manifold X is onto, then no phase variable are required. However, in the presence of caustics the minimum number of phase variables required is given by the corank of π. Passing from a local representation with no phase variables to a local representation where phase variables are required and passing back to a local representation with no phase variables, i.e., going through a caustics, affects the Maslov index (Hörmander, 1985a; Hörmander, 1985b). This is observed in the Maslov bundle component of the FIO amplitude, i.e., the FIO amplitude naturally carries the change of phase when passing through caustics. Those effects are described in Duistermaat (1996).

If $\Lambda \subset T^*(X)\backslash 0 \times T^*(Y)\backslash 0$ and is closed in $T^*(X \times Y)\backslash 0$, operator with kernels in $I^m(\Omega, \Lambda)$ are called (global) FIOs (Hörmander, 1985b, Sect. 25.2). Because of the properties imposed on Λ, such operators map $C_c^\infty(Y)$ into $C^\infty(X)$ and can be readily extended to map $\mathcal{E}'(Y)$ into $\mathcal{D}'(X)$. In the particular case where Λ is the conormal bundle of a submanifold of Ω, $I^m(\Omega, \Lambda)$ is the space of conormal distributions. If $X = Y$, conormal distributions are essentially kernels of ΨDOs (Hörmander, 1985a, Sect. 18.2).

For a complete treatment of the subject of FIOs see Hörmander (1971), Duistermaat and Hörmander (1972), Hörmander (1985a; 1985b), Duistermaat (1996). For a more physical perspective see Maslov and Fedoriuk (1981).

Appendix B

Non degeneracy of the phase function

For ϕ in equation (2.39) to be a clean phase function, we have to check that the stationary point set, Σ_ϕ, is a submanifold. We do so by checking that the system of differentials $\mathrm{d}(\phi')_\theta$, for all the parameters θ of the phase function, has constant rank. If so, the number of linearly independent differentials is then equal to $4M - 1 - e$, with e the excess. Then Λ_ϕ, as defined in equation (2.44) is a Lagrangian submanifold of dimension 7, and the stationary point set, Σ_ϕ, is of dimension $7 + e$ (Hörmander, 1985a, p.292). We shall prove here that the excess, e, is even zero, i.e., the phase function is non-degenerate, for M large enough in a sense that we shall precise.

The structure of the matrix of the components of the differentials $\mathrm{d}(\phi')_\theta$ is shown in Figure B.1. The block matrices with the stars in Figure B.1 are given by

$$\begin{pmatrix} -1 - M^{-1}\Delta x_3 (K_3^{\mathrm{prin}''})_{x_1 K_1}(x_\mu^{(l)}, \bar{\zeta}_l, K_\nu^{(l)}, \omega) & \\ -M^{-1}\Delta x_3 (K_3^{\mathrm{prin}''})_{x_1 K_2}(x_\mu^{(l)}, \bar{\zeta}_l, K_\nu^{(l)}, \omega) & \\ & -M^{-1}\Delta x_3 (K_3^{\mathrm{prin}''})_{x_2 K_1}(x_\mu^{(l)}, \bar{\zeta}_l, K_\nu^{(l)}, \omega) \\ & -1 - M^{-1}\Delta x_3 (K_3^{\mathrm{prin}''})_{x_2 K_2}(x_\mu^{(l)}, \bar{\zeta}_l, K_\nu^{(l)}, \omega) \end{pmatrix}.$$

If we can enforce these blocks to have a dominant diagonal by choosing M large enough, the columns of the matrix in Figure B.1 are then linearly independent. To this end, it is sufficient to prove that

$$(K_3^{\mathrm{prin}''})_{x_\mu K_\nu} = \frac{\omega^2 K_\nu}{K_3^{\mathrm{prin}}}\, c^{-1}\, \frac{\partial c^{-1}}{\partial x_\mu} \tag{B.1}$$

is bounded. In the scattering region considered, $\partial c^{-1}/\partial x_\mu$ is bounded, and so is c^{-1}. Also, $\omega^2 K_\nu / K_3^{\mathrm{prin}}$ is homogeneous of degree 0 in (ω, K_ν) for K_ν and ω large, and bounded for K_ν and ω small since we restrict ourselves to an open region on the canonical relation which closure is away from the 'turning' rays, i.e., where $K_3^{\mathrm{prin}} \geq \varepsilon_1 > 0$[1]. The second order derivative $(K_3^{\mathrm{prin}''})_{x_\mu K_\nu}$ is therefore bounded, which completes the proof.

Remark – The same argument proves that one can globally parameterize the stationary point set, and subsequently the canonical relation, by $(x_{1,2}^{(M)}, x_3, K_{1,2}^{(M+1)}, t, \omega)$ by use

[1] such restriction is accomplished with the help of a cut-off function χ multiplied to the amplitude in equation (2.38)

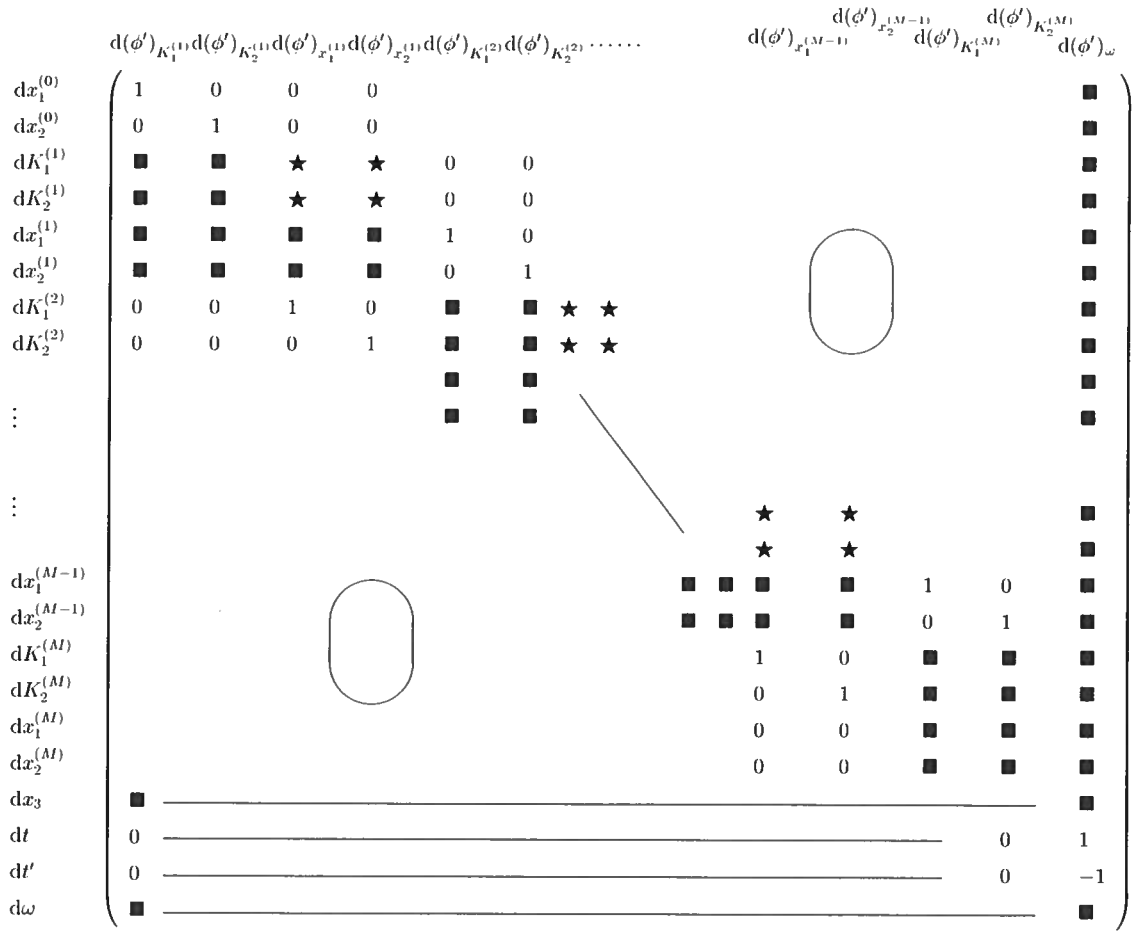

Figure B.1. Matrix of the differentials of $(\phi')_\theta$.

of the implicit function theorem applied to the discrete square-root Hamiltonian system of equation (2.43) characterizing the stationary point set, Σ_ϕ. Because of this global parameterization of the canonical relation we do not have to explicitly account for caustics, as needs to be done with asymptotic methods.

Appendix C

Approximation of the cotangent vector $(\phi')_{x_3}$ on the canonical relation

First, recall that

$$\bar{\zeta}_k = (k - \tfrac{1}{2})M^{-1}(x_3 - x_3') + x_3' \,. \tag{C.1}$$

The partial derivative of the phase function with respect to x_3 is then given by

$$\begin{aligned}(\phi')_{x_3} &= -M^{-1}\sum_{k=1}^{M} K_3^{\text{prin}}(x_\mu^{(k)}, \bar{\zeta}_k, K_\nu^{(k)}, \omega) \\ &\quad -M^{-1}(x_3 - x_3')\sum_{k=1}^{M} M^{-1}(k - \tfrac{1}{2})(K_3^{\text{prin}'})_{x_3}(x_\mu^{(k)}, \bar{\zeta}_k, K_\nu^{(k)}, \omega) \\ &= -M^{-1}\left\{\sum_{k=1}^{M} K_3^{\text{prin}}(x_\mu^{(k)}, \bar{\zeta}_k, K_\nu^{(k)}, \omega) + (\bar{\zeta}_k - x_3')(K_3^{\text{prin}'})_{x_3}(x_\mu^{(k)}, \bar{\zeta}_k, K_\nu^{(k)}, \omega)\right\} \,.\end{aligned} \tag{C.2}$$

We may interpret the $(x_3 - x_3')(\phi')_{x_3}$ as a Riemann sum along the bicharacteristic, $\mathcal{B}$, parametrized by ζ (as it is in the present square-root Hamiltonian system), which gives us the limit as $M \to \infty$:

$$\lim_{M\to\infty}(\phi')_{x_3} = -(x_3 - x_3')^{-1}\int_{\mathcal{B}}[K_3^{\text{prin}} + (\zeta - x_3')(K_3^{\text{prin}'})_{x_3}](x_\mu(\zeta), \zeta, K_\nu(\zeta), \omega)\mathrm{d}\zeta \,. \tag{C.3}$$

Note that, here, we face two limiting processes: one corresponds to the Riemann sum converging to the integral, the other one to the discrete bicharacteristics approaching the 'true' bicharacteristics.

Now, on the bicharacteristics we have

$$\begin{aligned}\frac{\mathrm{d}}{\mathrm{d}\zeta}\left[(\zeta - x_3')K_3^{\text{prin}}(x_\mu(\zeta), \zeta, K_\nu(\zeta), \omega)\right] = \\ [K_3^{\text{prin}} + (\zeta - x_3')(K_3^{\text{prin}'})_{x_3}](x_\mu(\zeta), \zeta, K_\nu(\zeta), \omega) \,,\end{aligned} \tag{C.4}$$

since

$$(K_3^{\text{prin}'})_{x_\sigma} \frac{\mathrm{d}x_\sigma}{\mathrm{d}\zeta} + (K_3^{\text{prin}'})_{K_\sigma} \frac{\mathrm{d}K_\sigma}{\mathrm{d}\zeta} = 0 \tag{C.5}$$

(set up the Hamiltonian system for F defined in equations (2.53)-(2.56)). We therefore obtain

$$\lim_{M\to\infty} (\phi')_{x_3} = -K_3^{\text{prin}}(x_\mu(x_3), x_3, K_\nu(x_3), \omega) \; . \tag{C.6}$$

For M large enough (in the compact region considered) we therefore have the following approximation:

$$(\phi')_{x_3} \simeq -K_3^{\text{prin}}(x_\mu^{(M)}, \bar{\zeta}_M, K_\nu^{(M+1)}, \omega) \; . \tag{C.7}$$

Appendix D

The common-azimuth approach

As a special case of the analysis presented in this paper, let us consider data (the scattered field) that is restricted to $h_2 = 0$ ('common azimuth'). After the restriction, we apply the imaging operator with kernel equation (2.73) to the data, subject to

$$h_{1,2}^{\mathrm{im}} = 0\,, \quad M = 1\,.$$

Removing the radation patterns, for the sake of simplification, we obtain

$$\begin{aligned}\mathcal{I}^1(x_{1,2}, z; y_{1,2}, h_1, 0, t; 0, 0) = &\int_{\mathbb{R}} (1/2\pi)\mathrm{d}\omega \\ &\times \tfrac{1}{16}\int_{\mathbb{R}^4} (1/2\pi)^2 \mathrm{d}K_1^{(1)}\mathrm{d}K_2^{(1)}(1/2\pi)^2\mathrm{d}k_1^{(1)}\mathrm{d}k_2^{(1)} \\ &\times \exp(\mathrm{i}\omega t)\exp\Big[-\mathrm{i}\{K_\sigma^{(1)}x_\sigma - K_\sigma^{(1)}y_\sigma - k_1^{(1)}h_1 + \\ &\Big[K_3(x_\mu, \bar{\zeta}_1, \tfrac{1}{2}(K_\nu^{(1)} - k_\nu^{(1)}), \omega) + K_3(x_\mu, \bar{\zeta}_1, \tfrac{1}{2}(K_\nu^{(1)} + k_\nu^{(1)}), \omega)\Big]\Delta x_3\}\Big]\,.\end{aligned} \tag{D.1}$$

We will now integrate out the phase variable $k_2^{(1)}$ with the aid of stationary phase. The stationary phase condition follows simply from equation (2.82):

$$(K_3^{\mathrm{prin}'})_{K_2}(x_\mu, \bar{\zeta}_1, \tfrac{1}{2}(K_\nu^{(1)} - k_\nu^{(1)}), \omega) = (K_3^{\mathrm{prin}'})_{K_2}(x_\mu, \bar{\zeta}_1, \tfrac{1}{2}(K_\nu^{(1)} + k_\nu^{(1)}), \omega), \tag{D.2}$$

which can be rewritten as

$$\frac{K_2^{(1)} - k_2^{(1)}}{K_3^{\mathrm{prin}}(x_\mu, \bar{\zeta}_1, \tfrac{1}{2}(K_\nu^{(1)} - k_\nu^{(1)}), \omega)} = \frac{K_2^{(1)} + k_2^{(1)}}{K_3^{\mathrm{prin}}(x_\mu, \bar{\zeta}_1, \tfrac{1}{2}(K_\nu^{(1)} + k_\nu^{(1)}), \omega)}\,. \tag{D.3}$$

On the wavefront set, this equality implies that the slowness (cotangent) vectors associated with the rays from the source and the receiver at depth $\bar{\zeta}_1$ restricted to the $(2,3)$-plane must have the same direction.

The solution $\widehat{k_2^{(1)}}$ for $k_2^{(1)}$ is given by

$$\widehat{k_2^{(1)}} = K_2^{(1)}\,\frac{K_3^{\mathrm{prin}}(x_\mu, \bar{\zeta}_1, \tfrac{1}{2}(K_1^{(1)} + k_1^{(1)}), 0, \omega) - K_3^{\mathrm{prin}}(x_\mu, \bar{\zeta}_1, \tfrac{1}{2}(K_1^{(1)} - k_1^{(1)}), 0, \omega)}{K_3^{\mathrm{prin}}(x_\mu, \bar{\zeta}_1, \tfrac{1}{2}(K_1^{(1)} + k_1^{(1)}), 0, \omega) + K_3^{\mathrm{prin}}(x_\mu, \bar{\zeta}_1, \tfrac{1}{2}(K_1^{(1)} - k_1^{(1)}), 0, \omega)}\,.$$

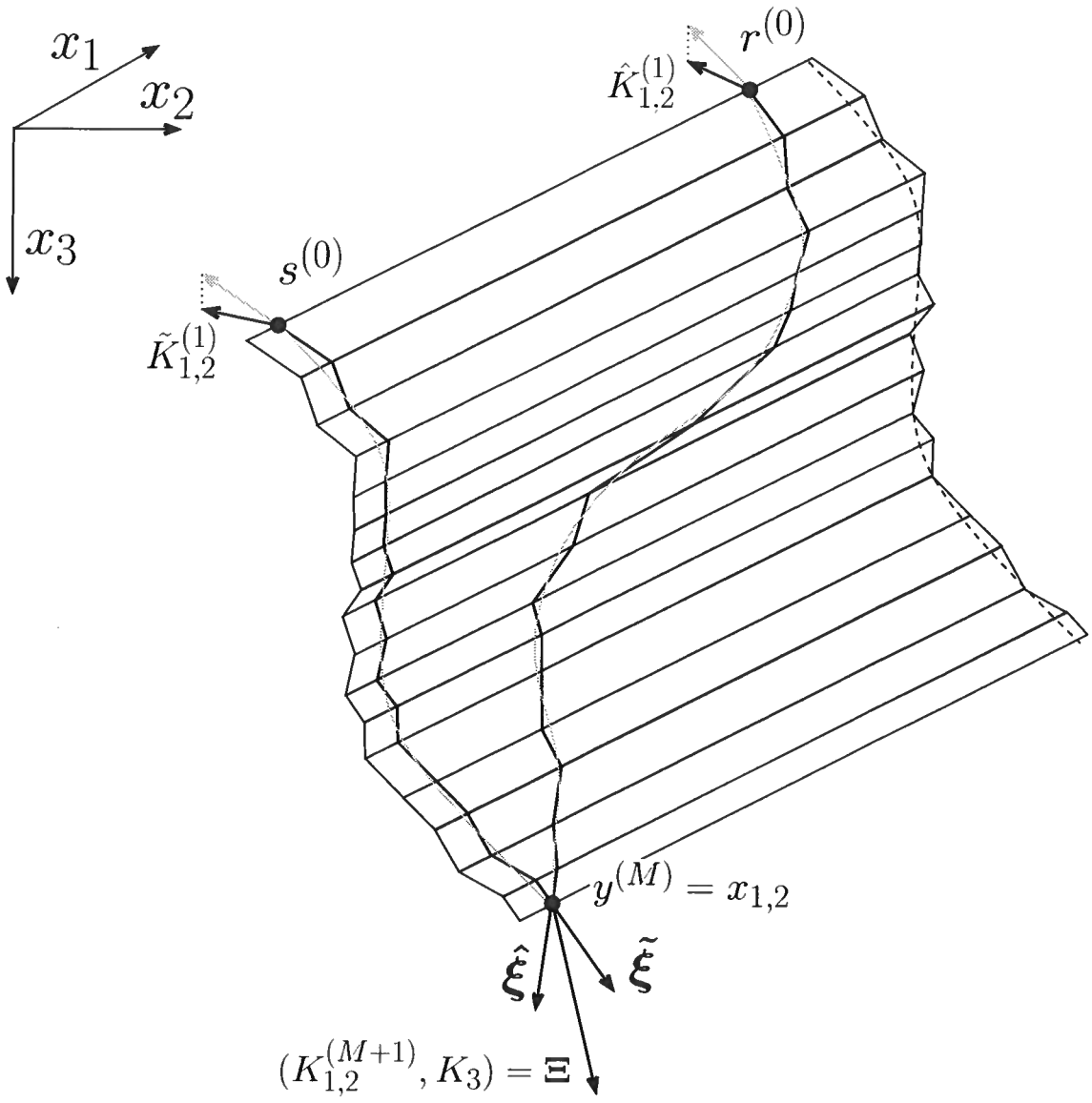

Figure D.1. Bicharacteristics satisfying the common azimuth assumption.

We leave the computation of the Hessian to the reader.

Extending these results to $M > 1$ invokes the assumption that on the stationary point set,

$$h_2^{(k)} = h_2^{(0)} = h_2 = 0 \quad \text{for } 2 \leq k \leq M-1 \ ,$$

i.e., $h_2^{(k)}$ does not change (Biondi & Palacharla, 1996). Then the expression between braces in equation (2.82) must vanish. This requires that, on the stationary point set, the relation

$$\widehat{k_2^{(k)}} = K_2^{(k)} \frac{P^{(k,-)}}{P^{(k,+)}} \ , \tag{D.4}$$

where

$$\begin{aligned} P^{(k,\pm)} \ = \ & K_3^{\text{prin}}(y_\mu^{(k)} + h_\mu^{(k)}, \bar{\zeta}_k, \tfrac{1}{2}(K_1^{(k)} + k_1^{(k)}), 0, \omega) \\ & \pm K_3^{\text{prin}}(y_\mu^{(k)} - h_\mu^{(k)}, \bar{\zeta}_k, \tfrac{1}{2}(K_1^{(k)} - k_1^{(k)}), 0, \omega) \ . \end{aligned}$$

holds. On the wavefront set, this equality implies that the slowness (cotangent) vectors associated with the rays from the source and the receiver at any depth $\bar{\zeta}_k$ restricted to the $(2,3)$-plane must have the same direction (but jointly could differ from one depth level to another), see figure D.1.

An alternative approximation is the offset-plane-wave approach (Mosher *et al.*, 1997). There the assumption is invoked that, on the stationary point set,

$$k_{1,2}^{(k)} = k_{1,2}^{(0)} \quad \text{for } 2 \leq k \leq M \ .$$

Then the expression between braces in equation (2.81) must vanish, which is certainly possible in a horizontally layered medium.

Appendix E

Comparison of the wide-angle-screen with the local-Born approximations

Dividing up the propagation range into thin slabs, and applying a Born approximation to each of them, Wu and Huang (1992) found the following spectral-domain propagator,

$$\tilde{g}^{(+)}(\alpha_\mu, x_3; \alpha'_\nu, x'_3) \simeq \exp[-s\gamma^0(x_3, \alpha_\mu)x_3] \left\{\delta(\alpha_\mu - \alpha'_\mu) + \frac{(-s)}{2\,[c^0(x_3)]^2\gamma^0(x_3, \alpha_\mu)}\,\Delta x_3\,\tilde{\mathsf{f}}(\alpha_\mu, x_3, \alpha'_\nu, x'_3)\right\} \exp[s\gamma^0(x_3, \alpha'_\nu)x'_3] ,$$

where

$$\tilde{\mathsf{f}}(\alpha_\mu, x_3, \alpha'_\nu, x'_3) = -\tilde{\tilde{\epsilon}}_\kappa(\alpha_\mu - \alpha'_\mu, \gamma^0(x_3, \alpha_\mu) - \gamma^0(x_3, \alpha'_\nu)) + [c^0(x_3)]^2[\alpha_\sigma\alpha'_\sigma + \gamma^0(x_3, \alpha_\mu)\gamma^0(x_3, \alpha'_\nu)]\,\tilde{\tilde{\epsilon}}_\rho(\alpha_\mu - \alpha'_\mu, \gamma^0(x_3, \alpha_\mu) - \gamma^0(x_3, \alpha'_\nu)) ,$$

arising from the contrast-source radiation patterns, and in which

$$\tilde{\tilde{\epsilon}}_\kappa = \frac{1}{\Delta x_3}\int_{\zeta=x'_3}^{x_3} \mathrm{d}\zeta\, \exp[\mathrm{i}s\alpha_3\zeta]\,\tilde{\epsilon}_\kappa(\alpha_\mu, \zeta) , \quad \tilde{\tilde{\epsilon}}_\rho = \frac{1}{\Delta x_3}\int_{\zeta=x'_3}^{x_3} \mathrm{d}\zeta\, \exp[\mathrm{i}s\alpha_3\zeta]\,\tilde{\epsilon}_\rho(\alpha_\mu, \zeta)$$

are windowed Fourier transforms with respect to the vertical coordinate.

Applying a lowest order *difference* paraxial approximation to the perturbation term in the thin slab propagator, viz.,

$$\gamma^0(x_3, \alpha_\mu) - \gamma^0(x_3, \alpha'_\mu) = \mathcal{O}(\alpha_\mu - \alpha'_\mu) , \tag{E.1}$$

$$\alpha_\sigma\alpha'_\sigma + \gamma^0(x_3, \alpha_\mu)\gamma^0(x_3, \alpha'_\nu) = [c^0(x_3)]^{-2} + \mathcal{O}(\alpha_\mu - \alpha'_\mu) , \tag{E.2}$$

we arrive at

$$\tilde{\mathsf{f}} \simeq \tilde{\tilde{\epsilon}}_\rho(\alpha_\mu - \alpha'_\mu, 0) - \tilde{\tilde{\epsilon}}_\kappa(\alpha_\mu - \alpha'_\mu, 0) .$$

Upon comparing now the spectral-domain propagator with equations.(3.36)-(3.36), we find an expression,

$$\gamma^0(x_3, \alpha_\mu) + \frac{1}{\gamma^0(x_3, \alpha_\mu)}\,\frac{\tilde{\mathsf{f}}(\alpha_\mu, x_3, \alpha'_\nu, x'_3)}{2\,[c^0(x_3)]^2} .$$

which, in view of equation (E.1), is directly related to the cokernel [equation (3.102)] asso-

ciated with the wide-angle approximation equation (3.103). Out of the expression for the cokernel, we can extract the screen $S_{c^{-1}}$ [cf., equation (3.85)]

$$\tilde{\gamma}(\alpha_\mu - \alpha'_\mu, x_3 - \tfrac{1}{2}\Delta x_3, \alpha'_\nu, s) \simeq \gamma^0(x_3, \alpha'_\nu) + \frac{1}{\gamma^0(x_3, \alpha'_\nu)} \frac{\tilde{S}_{c^{-1}}(\alpha_\mu - \alpha'_\mu, x_3)}{[c^0(x_3)]^2} \,. \tag{E.3}$$

Appendix F

Comparison of the wide-angle-screen approximation with linearized transmission coefficients

To account for horizontal medium variations, we introduced the leading-order scattering correction equation (3.103):

$$\hat{\gamma}_1 - \gamma^0 \sim \frac{\hat{a}_2^1}{2\,\gamma^0} \sim 2\gamma^0 \, \frac{(c^0)^{-1}\epsilon_{c^{-1}}}{2c^0\,(\gamma^0)^2} \, . \tag{F.1}$$

In comparison, the scattering due to vertical medium variations is given by equation (3.126), i.e.,

$$\frac{1}{2\hat{\gamma}_1}\,(\partial_3\hat{\gamma}_1) \sim \frac{\partial_3[\hat{a}_2^0 + \hat{a}_2^1]}{4\,(\gamma^0)^2} \sim \frac{(\partial_3 c^{-1})}{2c^0\,(\gamma^0)^2} \, , \tag{F.2}$$

which constitutes the linearized transmission(/reflection) coefficient.

Upon discretizing the vertical derivative, the two expressions above become directly related.

Appendix G

Relationship between one-way Green's function and propagator

The propagator, $g^{(\pm)}$, associated with the one-way wave equation satisfies the pseudodifferential equation

$$[\partial_3 \pm s\Gamma]\, g^{(\pm)}(x_\mu, x_3; x'_\upsilon, x'_3) = 0 \,, \tag{G.1}$$

complemented with the initial condition

$$g^{(\pm)}(x_\mu, x_3 = x'_3; x'_\upsilon, x'_3) = \delta(x_\mu - x'_\mu) \,. \tag{G.2}$$

Let us consider a function $\phi(x_\mu, x_3)$ that satisfies the one-way wave equation also. With properties (G.1) and (G.2), we have

$$\phi(x_\mu, x_3) = \int \mathrm{d}x'_1 \mathrm{d}x'_2 \; g^{(\pm)}(x_\mu, x_3; x'_\upsilon, x'_3)\; \phi(x'_\upsilon, x'_3) \,, \tag{G.3}$$

hence the terminology propagator. We now prove that the function $\mathcal{G}^{(\pm)}(x_\mu, x_3; x'_\upsilon, x'_3)$ defined as

$$\mathcal{G}^{(\pm)}(x_\mu, x_3; x'_\upsilon, x'_3) = \pm H(\pm[x_3 - x'_3])\; g^{(\pm)}(x_\mu, x_3; x'_\upsilon, x'_3) \,, \tag{G.4}$$

is a Green's function associated with the one-way wave equation. H is the Heaviside function. Applying the one-way operator to expression (G.4) yields

$$\begin{aligned}[\partial_3 \pm s\Gamma]\, \mathcal{G}^{(\pm)}(x_\mu, x_3; x'_\upsilon, x'_3) = {} & \pm g^{(\pm)}(x_\mu, x_3; x'_\upsilon, x'_3)\; \partial_3\, H(\pm[x_3 - x'_3]) \\ & \pm H(\pm[x_3 - x'_3])\, [\partial_3 \pm s\Gamma]\, g^{(\pm)}(x_\mu, x_3; x'_\upsilon, x'_3) \,.\end{aligned} \tag{G.5}$$

The second term in equation (G.5) vanishes because of property (G.1), hence

$$\begin{aligned}[\partial_3 \pm s\Gamma]\, \mathcal{G}^{(\pm)}(x_\mu, x_3; x'_\upsilon, x'_3) &= \pm g^{(\pm)}(x_\mu, x_3; x'_\upsilon, x'_3)\, [\pm\delta(x_3 - x'_3)] \\ &= g^{(\pm)}(x_\mu, x_3 = x'_3; x'_\upsilon, x'_3)\; \delta(x_3 - x'_3) \\ &= \delta(x_\mu - x'_\mu)\; \delta(x_3 - x'_3) \,,\end{aligned} \tag{G.6}$$

which is the defining equation for the one-way Green's function. The occurrence of the Heaviside function, enforces the Green's function to be causal; the propagator is not.

In this paper, we define a one-way Green's function with respect to the preferred spatial direction (x_3). In the field of Quantum mechanics, the same arguments are used to define the one-way Green's function in time using the propagator that satisfies the Schrödinger equation (Cohen-Tannoudji *et al.*, 1977).

Appendix H

Reduction to the principal parts

Using the composition rule for symbols of pseudodifferential operators (Treves, 1980a), the operator equation,

$$\Gamma^2 = \mathrm{A} \,, \tag{H.1}$$

is transformed into an equation for the corresponding left symbols (De Hoop, 1996):

$$\exp\left[-i\,\partial_{\alpha'_\sigma} D_{x'_\sigma}\right]\, \gamma(x_\mu;\alpha'_\sigma)\gamma(x'_\sigma;\alpha_\nu)\Big|_{(x'_\mu,\alpha'_\nu)=(x_\mu,\alpha_\nu)} = \mathrm{a}(x_\mu;\alpha_\nu) \,, \tag{H.2}$$

where γ is the left symbol of Γ and a is the left symbol of A, i.e.,

$$\begin{aligned}
\Gamma(x_\mu, x_3; D_\nu)\, \exp(\mathrm{i}s\alpha_\sigma x_\sigma) &\equiv \gamma(x_\mu, x_3; \alpha_\nu) \exp(\mathrm{i}s\alpha_\sigma x_\sigma) \,, \\
\mathrm{A}(x_\mu, x_3; D_\nu)\, \exp(\mathrm{i}s\alpha_\sigma x_\sigma) &\equiv \mathrm{a}(x_\mu, x_3; \alpha_\nu) \exp(\mathrm{i}s\alpha_\sigma x_\sigma) \,.
\end{aligned}$$

From the form of A in the acoustic-pressure-normalization analog of equation (4.4) (De Hoop, 1996) we have

$$\mathrm{a} = \kappa\rho + \alpha_\nu\alpha_\nu - \rho^{-1}(D_\nu\rho)\mathrm{i}\alpha_\nu - \rho^{-1}(D_\nu D_\nu\rho) - \rho^{-2}(D_\nu\rho)(D_\nu\rho) \,. \tag{H.3}$$

As $s \to \infty$ the composition of symbols tends to an ordinary multiplication, and the solution of equation (H.2) reduces to the principal parts, γ_1 and a_2 respectively, of the symbols:

$$\gamma_1(x_\mu;\alpha_\nu)\gamma_1(x_\mu;\alpha_\nu) = \mathrm{a}_2 = \kappa\rho + \alpha_\nu\alpha_\nu = c^{-2} + \alpha_\nu\alpha_\nu \,. \tag{H.4}$$

Referring to the contrast formulation made here and in De Hoop *et al.* (2000), the 'high-frequency' approximation of equation (H.4) can also be expressed by assuming that the vertical-slowness symbol depends only on the magnitude (ϵ) of the medium perturbation, but not on the smoothness (Ω) of the medium perturbation, i.e., γ_1 is $\mathcal{O}(\Omega^0)$.

Appendix I

The generalized-screen representation of the reflection operator

The thin-slab propagator given in equation (4.8) is the one associated with the one-way wave equation. To recover the two-way wave propagation one has to make use of the Bremmer series, as described by De Hoop (1996). The first term of the series is the one-way wavefield; the second term is the first (class one) multiple; the third term is the second multiple, etc. The evaluation of each term of the Bremmer series requires the use of the reflection operator given as

$$R = \tfrac{1}{2}\Gamma^{-1}(\partial_3\Gamma) \,, \tag{I.1}$$

for constant density and a continuous medium. We associate to R its left symbol, r,

$$R\phi(x_\mu, x_3) = \int (s/2\pi)^2 \mathrm{d}\alpha_1 \mathrm{d}\alpha_2 \int \mathrm{d}x_1' \mathrm{d}x_2' \; r(x_\mu, x_3; \alpha_\nu) \; \exp[-\mathrm{i}s(x_\sigma - x_\sigma')\alpha_\sigma] \; \phi(x_\upsilon', x_3) \,.$$

In the framework of the present 'high-frequency' approximation, R reduces to its principal part R_1, with r reducing to its principal symbol r_1.

In a similar fashion as in Appendix B, one can show that such reduction to principal symbol, yields

$$r_1 = \frac{\partial_3 \gamma_1}{2\gamma_1} \,. \tag{I.2}$$

At a horizontal interface, the reflection symbol is simply the reflection coefficient, but this is not true for a non-horizontal interface. For a non-horizontal interface, the reflection of an incoming wave is split between the one-way propagation operator and the reflection operator. The reflection operator is responsible for the interaction between the up- and downgoing constituents of the wavefield. The one-way wave operator describes the transverse scattering.

Like γ_1, the reflection symbol r_1 can be expanded by introducing the same background medium and perturbation as within the thin slab through which propagation takes place. Here, we present the GS expansion of the reflection symbol in a medium sampled at discrete

points. At an interface located at x_3, the reflection symbol can be expressed as

$$r_1(x_\mu, x_3; \alpha_\nu)\Delta x_3 = \frac{\gamma_1(x_\mu, x_3^+; \alpha_\nu) - \gamma_1(x_\mu, x_3^-; \alpha_\nu)}{\gamma_1(x_\mu, x_3^+; \alpha_\nu) + \gamma_1(x_\mu, x_3^-; \alpha_\nu)} , \tag{I.3}$$

where

$$x_3^- = x_3 - \tfrac{1}{2}\Delta x_3 ,$$

and

$$x_3^+ = x_3 + \tfrac{1}{2}\Delta x_3 .$$

Upon introducing a background medium and a perturbation on both sides of the interface, i.e.,

$$u(x_\mu, x_3^-) = [c(x_\mu, x_3^-)]^{-2} - [c^0(x_3^-)]^{-2} ,$$

and

$$u(x_\mu, x_3^+) = [c(x_\mu, x_3^+)]^{-2} - [c^0(x_3^+)]^{-2} ,$$

one can expand the reflection principal symbol with respect to these two perturbations. In the GS expansion of the one-way thin-slab propagator, the expansion of the exponential in equation (4.24) yields accuracy in the vicinity of vertical propagation. We want to enforce such accuracy for the expansion of the reflection operator as well, and thus write

$$r_1(x_\mu, x_3; \alpha_\nu) = r_1(x_\mu, x_3; 0) + [r_1(x_\mu, x_3; \alpha_\nu) - r_1(x_\mu, x_3; 0)] . \tag{I.4}$$

We denote $r_1^0(x_3; \alpha_\nu)$ the reflection symbol associated with the upper and lower background media. We then expand $r_1(x_\mu, x_3; \alpha_\nu) - r_1(x_\mu, x_3; 0)$ with respect to the perturbations u at x_3^- and x_3^+, which, to first order, yields

$$\begin{aligned} r_1(x_\mu, x_3; \alpha_\nu) \simeq\ & r_1(x_\mu, x_3; 0) - r_1^0(x_3; 0) + r_1^0(x_3; \alpha_\nu) \\ & + a_1^-(x_3; \alpha_\nu) u(x_\mu, x_3^-) + a_1^+(x_3; \alpha_\nu) u(x_\mu, x_3^+) , \end{aligned} \tag{I.5}$$

with

$$\begin{aligned} a_1^-(x_3; \alpha_\nu) = & \frac{-\frac{\gamma^0(x_3^+, \alpha_\nu)}{\gamma^0(x_3^-, \alpha_\nu)} \left(\left[c^0(x_3^+)\right]^2 + \left[c^0(x_3^-)\right]^2 \right) + c^0(x_3^-) c^0(x_3^+) + \frac{[c^0(x_3^-)]^3}{c^0(x_3^+)}}{\sigma(x_3^+, x_3^-, \alpha_\nu)} \\ & + \frac{2\alpha_\nu \alpha_\nu \left[c^0(x_3^-)\right]^3 c^0(x_3^+) \left(1 + \frac{\gamma^0(x_3^+, \alpha_\nu)}{\gamma^0(x_3^-, \alpha_\nu)}\right)}{\sigma(x_3^+, x_3^-, \alpha_\nu)} , \end{aligned} \tag{I.6}$$

and

$$a_1^+(x_3;\alpha_\nu) = \frac{\frac{\gamma^0(x_3^-,\alpha_\nu)}{\gamma^0(x_3^+,\alpha_\nu)}\left(\left[c^0(x_3^+)\right]^2+\left[c^0(x_3^-)\right]^2\right) - c^0(x_3^-)c^0(x_3^+) - \frac{\left[c^0(x_3^+)\right]^3}{c^0(x_3^-)}}{\sigma(x_3^+,x_3^-,\alpha_\nu)}$$
$$-\frac{2\alpha_\nu\alpha_\nu\left[c^0(x_3^+)\right]^3 c^0(x_3^-)\left(1+\frac{\gamma^0(x_3^-,\alpha_\nu)}{\gamma^0(x_3^+,\alpha_\nu)}\right)}{\sigma(x_3^+,x_3^-,\alpha_\nu)}\,, \tag{I.7}$$

where

$$\sigma(x_3^+,x_3^-,\alpha_\nu) = \Delta x_3\left[\gamma^0(x_3^+,\alpha_\nu)+\gamma^0(x_3^-,\alpha_\nu)\right]^2\left[c^0(x_3^+)+c^0(x_3^-)\right]^2\,.$$

The superscript '$-$' refers to the upper medium and the superscript '$+$' to the lower one, whereas the subscript refers to the order in the GS expansion. We have

$$a_1^-(x_3;0) = 0\,,\quad a_1^+(x_3;0) = 0\,.$$

Figure I.1 illustrates the GS expansion of the real part of the reflection symbol at an interface where the upper medium is characterized by a constant perturbation and the lower medium by a zero perturbation. In the top of the figure, the exact reflection symbol (dashed) and the first two GS approximations are shown as a function of the horizontal slowness $p = \sqrt{-\alpha_\nu\alpha_\nu}$. The bottom part of Figure I.1 shows the relative error of the first two GS approximations. Note the increasing angular accuracy as the order of the GS expansion increases. This accuracy will be required to predict multiple scattering at large offset. However, in the vicinity of the critical angle, all orders break down.

Note that to compute the n^{th} term in the Bremmer series, the reflection operator is only applied n times to the wavefield while a cascade of thin-slab GS propagators is applied for each of the terms. Such cascade implies an accumulation of errors associated with the inaccuracies of the thin-slab GS propagator (e.g., propagation very close to the horizontal direction). Such accumulation of error does not occur when applying the GS reflection operator, since we usually consider the first few terms in the Bremmer series only.

The GS representation (here, first order) of the principal part of the reflection operator then follows as

$$(R_1\phi)(x_\mu,x_3) \simeq \int (s/2\pi)^2 \mathrm{d}\alpha_1\mathrm{d}\alpha_2 \int \mathrm{d}x_1'\mathrm{d}x_2'\ \exp[-\mathrm{i}s(x_\sigma - x_\sigma')\alpha_\sigma] \tag{I.8}$$
$$\cdot\left[r_1(x_\mu,x_3;0) - r_1^0(x_3;0) + r_1^0(x_3;\alpha_\nu) + a_1^-(x_3;\alpha_\nu)u(x_\mu,x_3^-)\right.$$
$$\left.+a_1^+(x_3;\alpha_\nu)u(x_\mu,x_3^+)\right]\ \phi(x_\nu',x_3)\,,$$

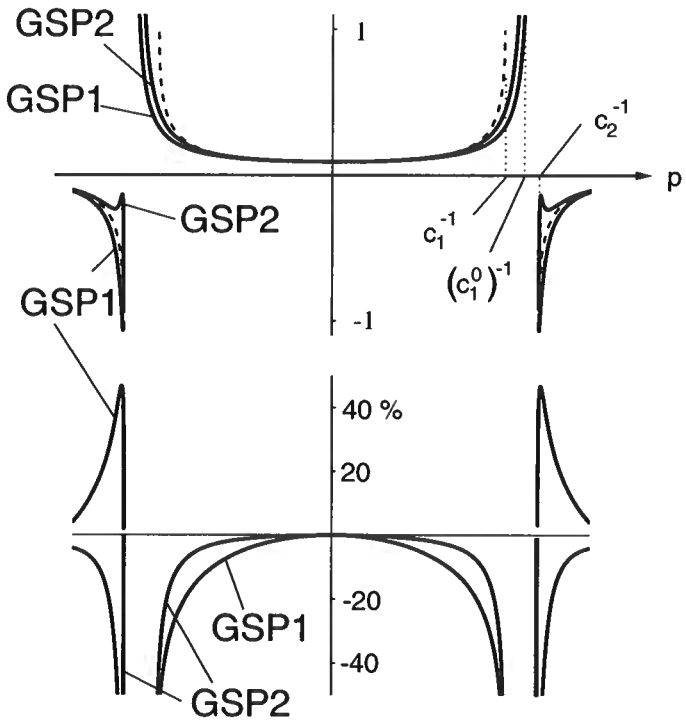

Figure I.1. Top: real part of the principal parts of the generalized-screen reflection symbols: first-order (GSR1) and second-order (GSR2) as a function of horizontal slowness p. The principal part of the exact symbol is shown dashed. Bottom: relative error of the first-order and second-order GS approximations.

which can be written as

$$
\begin{aligned}
(R_1\phi)(x_\mu, x_3) \simeq\ & (r_1(x_\mu, x_3; 0) - r_1^0(x_3; 0))\ \phi(x_\mu, x_3) \\
& + \int (s/2\pi)^2 \mathrm{d}\alpha_1 \mathrm{d}\alpha_2 \int \mathrm{d}x_1' \mathrm{d}x_2'\ r_1^0(x_3; \alpha_\nu)\ \exp[-\mathrm{i}s(x_\sigma - x_\sigma')\alpha_\sigma]\ \phi(x_\upsilon', x_3) \\
& + u(x_\mu, x_3^-) \int (s/2\pi)^2 \mathrm{d}\alpha_1 \mathrm{d}\alpha_2 \int \mathrm{d}x_1' \mathrm{d}x_2'\ a_1^-(x_3; \alpha_\nu)\ \exp[-\mathrm{i}s(x_\sigma - x_\sigma')\alpha_\sigma]\ \phi(x_\upsilon', x_3) \\
& + u(x_\mu, x_3^+) \int (s/2\pi)^2 \mathrm{d}\alpha_1 \mathrm{d}\alpha_2 \int \mathrm{d}x_1' \mathrm{d}x_2'\ a_1^+(x_3; \alpha_\nu)\ \exp[-\mathrm{i}s(x_\sigma - x_\sigma')\alpha_\sigma]\ \phi(x_\upsilon', x_3)\ ,
\end{aligned}
\tag{I.9}
$$

yielding the reflection operator (Schwartz) kernel $\mathcal{R}_1$ (Schwartz, 1966b; Treves, 1967; De Hoop *et al.*, 2000)

$$
\begin{aligned}
\mathcal{R}_1(x_\mu, x_\upsilon', x_3) \simeq\ & (r_1(x_\mu, x_3; 0) - r_1^0(x_3; 0))\ \delta(x_\mu - x_\mu') \\
& + \int (s/2\pi)^2 \mathrm{d}\alpha_1 \mathrm{d}\alpha_2\ r_1^0(x_3; \alpha_\nu)\ \exp[-\mathrm{i}s(x_\sigma - x_\sigma')\alpha_\sigma] \\
& + u(x_\mu, x_3^-) \int (s/2\pi)^2 \mathrm{d}\alpha_1 \mathrm{d}\alpha_2\ a_1^-(x_3; \alpha_\nu)\ \exp[-\mathrm{i}s(x_\sigma - x_\sigma')\alpha_\sigma] \\
& + u(x_\mu, x_3^+) \int (s/2\pi)^2 \mathrm{d}\alpha_1 \mathrm{d}\alpha_2\ a_1^+(x_3; \alpha_\nu)\ \exp[-\mathrm{i}s(x_\sigma - x_\sigma')\alpha_\sigma]\ .
\end{aligned}
\tag{I.10}
$$

The concept of reflection kernel was introduced by Berkhout (1982, sections 4.6 and 6.2), Wapenaar and Berkhout (1989, section III.3.3), De Bruin *et al.*(1990). Equations (I.9) and (I.10) can directly be cast into a numerical algorithm. Each additional term in the GS expansion of the reflection operator requires two additional Fourier transforms.

Appendix J

Comparison with the filter-McClellan approach

Another approach to approximate the one-way propagator (4.10) is the filter approach. Like our approach, the filter approach aims at approximating the propagation of singularities. Unlike our approach, it does not yield a comprehensive recursion that generates increasingly accurate one-way propagators on and away from the wavefront set.

Here, we compare the accuracy and efficiency of the GS method with the explicit extrapolation induced by the filter approach introduced by Holberg (1988) and Blacquière *et al.* (1989), and extended to 3D by Hale (1991b; 1991a). In 2D ($\mu, \nu \cdots = 1$) this approach is based on the construction of a finite-length filter,

$$\sum_{(-N+1)/2}^{(N-1)/2} h_n \, \delta(x_1 - n\Delta x_1) \, ,$$

which matches the *local* thin-slab propagator. The matching is carried out in the Fourier domain and hence

$$H(k') = h_0 + 2 \sum_{n=1}^{N_h-1} h_n \cos(k'n) \, , \tag{J.1}$$

where k' is the wave number scaled by the sampling rate, i.e., $k' = -s\alpha_1 \, \Delta x_1$, and $N_h = (N+1)/2$ is the number of independent coefficients (imposing appropriate symmetries amongst the h_n's), should resemble

$$\exp[-s \, \gamma_1(x_1, \bar{x}_3; \alpha_1)\Delta x_3] \, ,$$

upon applying transformations (4.5)-(4.6). With the aid of Chebychev polynomials, T_n, $H(k')$ can be written as a function of $\cos k'$, viz.,

$$H(k') = h_0 + 2 \sum_{n=1}^{N_h-1} T_n(\cos k') = J(\cos k') \, . \tag{J.2}$$

In 3D, $k' = \sqrt{k'^2_1 + k'^2_2}$. To preserve the algorithm's efficiency, the same 2D filter is used but is now combined with an approximation of $\cos k'$ proposed by McClellan (1973) – to

obtain an approximate circular filter:

$$\cos(k') \simeq G(k'_1, k'_2) = -1 + \tfrac{1}{2}(1 + \cos k'_1)(1 + \cos k'_2) \; . \tag{J.3}$$

Hale's (1991a) improvement of this expression is given by

$$\cos(k') \simeq G(k'_1, k'_2) = -1 + \tfrac{1}{2}(1 + \cos k'_1)(1 + \cos k'_2) - \tfrac{c}{2}(1 - \cos 2k'_1)(1 - \cos 2k'_2) \; , \tag{J.4}$$

where $c \simeq 0.0255$.

We now seek to associate a vertical slowness symbol with the filter. Because of the match, this symbol should be given by

$$\gamma_H(x_\mu, \alpha_\nu) = -\frac{1}{s\Delta x_3} \log J(G(-s\,\alpha_1\,\Delta x_1, -s\,\alpha_2\,\Delta x_2)) \quad \text{with } \Delta x_2 = \Delta x_1 \; , \tag{J.5}$$

where the dependency on the transverse directions, x_μ is contained in the coefficients h_n's. We observe that the dispersion relation which characterizes the propagator is dependent on the frequency and the spatial sampling rate. Note also that the use of a circular filter requires the same sampling rate in the inline and crossline directions (different sampling rates would require the design of an elliptic filter).

In Figures J.1 and J.2, we illustrate both the accuracy of the filter and the accuracy of the McClellan transformation for two different sampling rates. In Figure J.1, grazing incidence corresponds to half Nyquist which yields the accuracy claimed in Hale's examples (Hale, 1991b). In Figure J.1, grazing incidence corresponds to 0.8 Nyquist and one can see the degradation of the accuracy of the McClellan transformation at large propagation angle. In these examples, we use all the coefficients h_n's to match the thin-slab propagator. In practice this cannot be done for it implies a non-unitary propagator. Hale (1991b) solved this problem decreasing the amplitude smoothly to zero beyond half Nyquist. This impacts the propagation of energy at wide angle, in view of the cascade of extrapolations. Figures (J.3) and (J.4) show the computations of the wavefront sets associated with the vertical slownesses shown in Figures J.1 and J.2. The wavefront sets are truncated when the vertical slownesses become complex, which does not happen in our GS approach. Note that in both Figures J.1 and J.2, the vertical slownesses become complex where their real parts depart from the exact one. Also note that the present analysis yields wavefront sets resembling the numerical wavefronts given by Hale (1991a).

Concerning the filter-McClellan approach the following can be said: (i) the filter will not be exact even in an (almost) homogeneous medium, (ii) the accuracy of the filter will depend on the sampling rate which for fixed frequency will depend on the local medium properties, i.e., the accuracy will vary with location, (iii) the same remarks apply to the McClellan transformation, (iv) intrinsic instability enforces dense sampling . These features are avoided in the GS method. As far as the computational complexity is concerned, the filter-McClellan and GS methods compare as follows, $52N_h - 46$ (Hale, 1991a) versus $(2 + n) \log_2 N_1 N_2$. Typically, $N_h = 20$, $n = 2$, $N_1 = N_2 = 10^3$, whence the filter-McClellan approach is more than 10 times less efficient than the GS method.

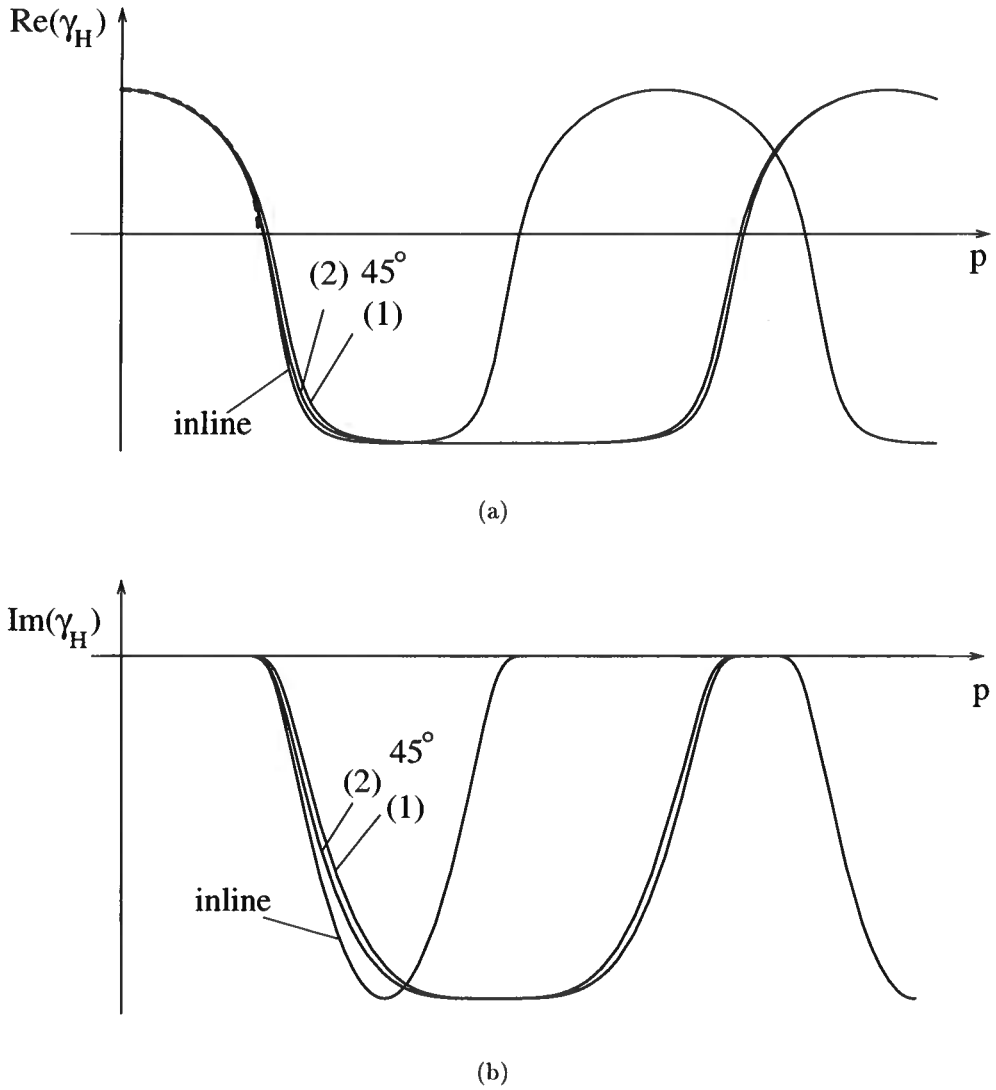

Figure J.1. (a) Real and (b) imaginary parts of the vertical slownesses associated with the filter-McClellan approach. The 'inline' curve correspond to the 2D filter (J.1) The '45°' curves correspond to the 2D filter combined (1) with approximation (J.3) and (2) with approximation (J.4) at a 45° azimuth. The true vertical slowness is shown dashed. In the present case grazing incidence corresponds to half Nyquist. Compare with Figure J.2.

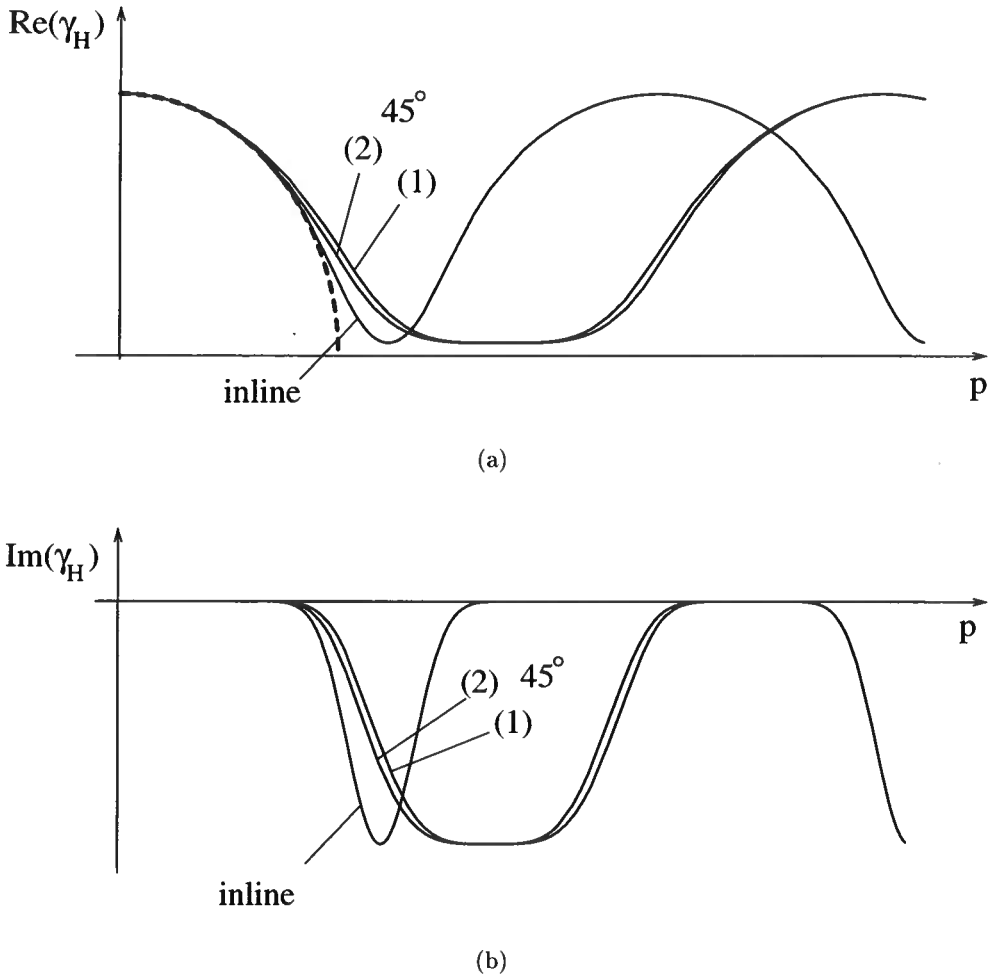

Figure J.2. (a) Real and (b) imaginary parts of the vertical slownesses associated with the filter-McClellan approach. The 'inline' curve correspond to the 1D filter, The '45°' curves correspond to the 1D filter combined (1) with McClellan's and (2) with Hale's approximations of the circular filter at a 45° azimuth (Hale, 1991a). The true vertical slowness is shown dashed. In the present case grazing incidence corresponds to 0.8 Nyquist. (c) Wavefronts computed as polar reciprocals of the slowness surfaces; the exact wavefront is shown dashed. Note the truncation of the wavefronts.

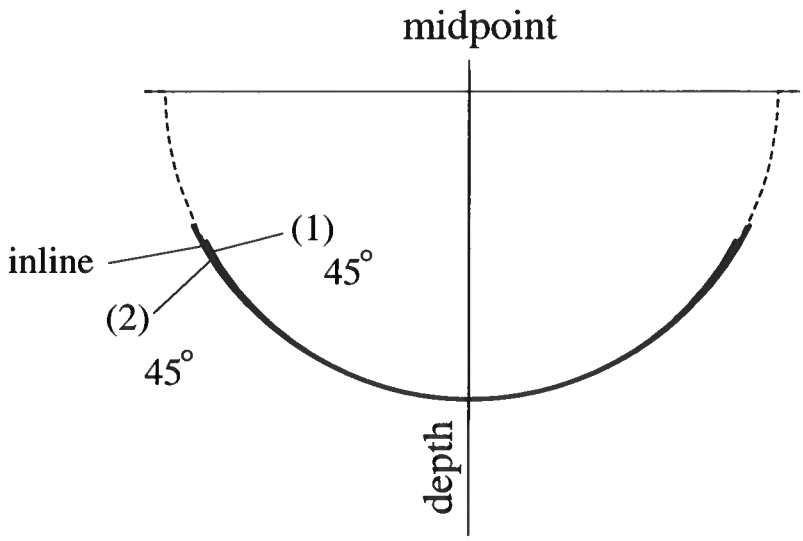

Figure J.3. Wavefronts computed as polar reciprocals of the slowness surfaces shown in Figure J.1; the exact wavefront is shown dashed.

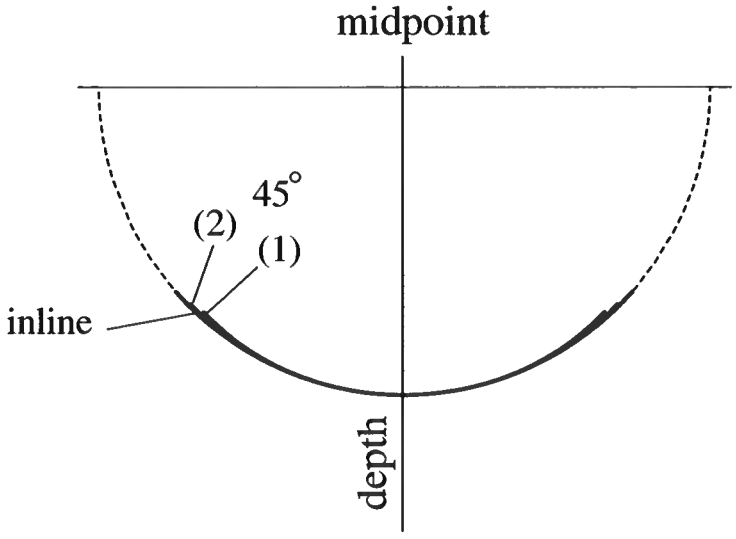

Figure J.4. Wavefronts computed as polar reciprocals of the slowness surfaces shown in Figure J.2; the exact wavefront is shown dashed.

Appendix K

Equivalent 'acoustic' system of equations for VTI *qP*-wave propagation

VTI media are essentially elastic media. Yet, in various applications the propagation of *qP* waves only is treated as if the medium were acoustic. Following the concept introduced by Alkhalifah (1998a) and the methodology of Schoenberg and De Hoop (2000), we introduce an equivalent 'acoustic' system of equations for VTI *qP*-wave propagation. This first-order system rather than the induced second-order wave equation, is required to arrive at the appropriate directional wavefield decomposition procedure that leads to the one-way wave equation and its associated propagator. We show the accuracy of the equivalent 'acoustic' system for the *qP*-wave propagation not only for the dispersion relation (Alkhalifah, 1998a, (A-9)), i.e., the wavefront set (Hörmander, 1990), but also for the polarization vectors.

K.1 Exact VTI system and limiting equivalent 'acoustic' system

The medium being VTI, we work in a vertical plane without loss of generality. In an elastic medium, the wave equation is given by the second-order hyperbolic system

$$\rho\partial_t^2 u_i - \partial_j\left(C_{ijkl}\,\partial_l u_k\right) = f_i\ ,\ \text{for}\ \ i = 1,3, \tag{K.1}$$

where u_i=particle displacement (m), ρ=volume density of mass (kg/m^3), C_{ijkl}=stiffness tensor (Pa), and f_i=volume source density of force (N/m^3). In the VTI case, system (K.1) reduces to

$$\rho\partial_t^2 u_1 - \partial_1\left(c_{11}\partial_1 u_1 + c_{13}\partial_3 u_3\right) - \partial_3\left(c_{55}(\partial_3 u_1 + \partial_1 u_3)\right) = f_1\ , \tag{K.2}$$

$$\rho\partial_t^2 u_3 - \partial_3\left(c_{13}\partial_1 u_1 + c_{33}\partial_3 u_3\right) - \partial_1\left(c_{55}(\partial_3 u_1 + \partial_1 u_3)\right) = f_3\ , \tag{K.3}$$

according to the stiffness matrix (5.1) and the Voigt notation.

Let $a = c_{13} + 2c_{55}$ be fixed. Alkhalifah (1998a) and Schoenberg and De Hoop (2000) propose then the following transformation

$$c_{13} \to a\ , \tag{K.4}$$

$$c_{55} \to 0\ . \tag{K.5}$$

Taking the vertical *qSV*-wave speed equal to zero yields an equivalent 'acoustic' system; however, as noticed by Schoenberg and De Hoop (2000), keeping $c_{13} + 2c_{55}$ constant, as is

done here, does not affect dramatically the shape of the qP-slowness surface in the case of 'mild' anisotropy. The second-order system (K.2)-(K.3) thus becomes

$$\rho\partial_t^2 u_1 - \partial_1 \left(c_{11}\partial_1 u_1 + a\partial_3 u_3\right) = f_1 \ , \tag{K.6}$$
$$\rho\partial_t^2 u_3 - \partial_3 \left(a\partial_1 u_1 + c_{33}\partial_3 u_3\right) = f_3 \ . \tag{K.7}$$

We define a pseudo-pressure, p, as

$$p \equiv -\left(a\partial_1 u_1 + c_{33}\partial_3 u_3\right) \ . \tag{K.8}$$

Then equation (K.7) takes the form

$$\rho\partial_t^2 u_3 + \partial_3 p = f_3 \ , \tag{K.9}$$

which is an equation that appears in the isotropic acoustic case also (De Hoop, 1996, (II.6)). From equation (K.8) one can extract $\partial_3 u_3$,

$$\partial_3 u_3 = -\frac{1}{c_{33}} p - \frac{a}{c_{33}} \partial_1 u_1 \ , \tag{K.10}$$

which upon substitution in equation (K.6) yields

$$\left\{\rho\partial_t^2 - \partial_1 \left[\left(c_{11} - \frac{a^2}{c_{33}}\right)\partial_1 \cdot\right]\right\} u_1 + \partial_1 \left(\frac{a}{c_{33}} \cdot\right) p = f_1 \ , \tag{K.11}$$

which we rewrite as

$$O\, u_1 + \partial_1 \left(\frac{a}{c_{33}} \cdot\right) p = f_1 \ , \tag{K.12}$$

with

$$O(\partial_t, \partial_1) = \rho\partial_t^2 - \partial_1 \left[\left(c_{11} - \frac{a^2}{c_{33}}\right)\partial_1 \cdot\right] \ . \tag{K.13}$$

The principal part, O_2, of the differential operator O is given by

$$O_2(\partial_t, \partial_1) = \rho\partial_t^2 - \left(c_{11} - \frac{a^2}{c_{33}}\right)\partial_1^2 \ , \tag{K.14}$$

and its principal symbol, o_2, follows, upon replacing ∂_t and ∂_1 by their respective symbols, s^2 and $-\mathrm{i}s\alpha$, in the Laplace-Fourier domain, as

$$o_2(s, \alpha) = \rho s^2 + \left(c_{11} - \frac{a^2}{c_{33}}\right)\alpha^2 \ . \tag{K.15}$$

In the case where $a^2 < c_{11}c_{33}$, which we assume here, the differential operator O is strongly

elliptic[1]. We can therefore invert it (Treves, 1980a), and hence with equation (K.12),

$$u_1 = -O^{-1}\left[\partial_1\left(\frac{a}{c_{33}}\cdot\right)\right]p + O^{-1}f_1\ . \tag{K.16}$$

Substituting equation (K.16) into the definition (K.8) of the pseudo-pressure, p, we obtain

$$\partial_3 u_3 + \left\{\frac{1}{c_{33}} - \frac{a}{c_{33}}\partial_1\, O^{-1}\left[\partial_1\left(\frac{a}{c_{33}}\cdot\right)\right]\right\}p = -\frac{a}{c_{33}}\partial_1 O^{-1} f_1\ . \tag{K.17}$$

Using the particle velocity, $\boldsymbol{v}$, instead of the particle displacement, $\boldsymbol{u}$, we obtain the system of equations

$$\rho\partial_t v_3 + \partial_3 p = f_3\ , \tag{K.18}$$

$$\partial_3 v_3 + \left\{\frac{1}{c_{33}} - \frac{a}{c_{33}}\partial_1\, O^{-1}\left[\partial_1\left(\frac{a}{c_{33}}\cdot\right)\right]\right\}\partial_t p = -\frac{a}{c_{33}}\partial_1\, O^{-1}\partial_t f_1\ . \tag{K.19}$$

Defining the 'acoustic' field matrix, F_I, I=1,3, as

$$F_1 = p\ , \tag{K.20}$$

$$F_3 = v_3\ , \tag{K.21}$$

we obtain the matrix differential equation

$$(\partial_3\delta_{I,J} + A_{I,J}\partial_t)F_J = N_I\ , \tag{K.22}$$

where the elements of the acoustic system operator matrix, $A_{I,J}$, are given by

$$A_{1,1} = 0\ , \tag{K.23}$$

$$A_{1,2} = \rho\ , \tag{K.24}$$

$$A_{2,1} = \left\{\frac{1}{c_{33}} - \frac{a}{c_{33}}\partial_1\, O^{-1}\left[\partial_1\left(\frac{a}{c_{33}}\cdot\right)\right]\right\}\ , \tag{K.25}$$

$$A_{2,2} = 0\ . \tag{K.26}$$

The source matrix, N_I, $I = 1, 3$, is given by

$$N_1 = f_3\ , \tag{K.27}$$

$$N_3 = -\frac{a}{c_{33}}\partial_1\, O^{-1}\partial_t f_1\ . \tag{K.28}$$

Observe that in the limiting case $c_{11} = c_{33} = a$, we recover the exact form of the acoustic-matrix differential equation for an isotropic-acoustic medium (De Hoop, 1996, (II-9) through (II-16)); then the linear operator O reduces to $\rho\,\partial_t^2$.

[1]Note that the case $a^2 > c_{11}c_{33}$ would induce a pole in expression (K.31) for the vertical slowness γ_1, i.e., the phase velocity would have a zero.

K.2 Dispersion relation for the equivalent 'acoustic' system

To obtain the dispersion relation, i.e., to derive the (micro-local) eikonal equation, we consider a (locally) constant medium ('high-frequency' approximation). Then the linear operator O reduces to its principal part O_2. Upon applying a Fourier transform in the spatial coordinates, x_1 and x_3, and a Laplace transform in time, t, to system (K.22) thus replacing ∂_t, ∂_3, ∂_1, and O_2 by their respective symbols, s^2, $-s\gamma_1$, $-\mathrm{i}s\alpha$, and o_2, we set the determinant of system (K.22) equal to zero:

$$\rho s^2 \left[\frac{a^2}{c_{33}^2} o_2^{-1} s^2 \alpha^2 + \frac{1}{c_{33}} \right] - s^2 \gamma_1^2 = 0 \,, \tag{K.29}$$

which can be written as

$$\gamma_1^2 = \frac{\frac{\tilde{a}^2}{\tilde{c}_{33}^2}\alpha^2}{1 + \tilde{c}_{11}\alpha^2 - \frac{\tilde{a}^2}{\tilde{c}_{33}}\alpha^2} + \frac{1}{\tilde{c}_{33}} \,. \tag{K.30}$$

Note that the term $\tilde{c}_{ij}$ represents the elastic moduli c_{ij} normalized by density, ρ. The previous equation simplifies to

$$\gamma_1^2 = \frac{1 + \tilde{c}_{11}\alpha^2}{\tilde{c}_{33}\left(1 + \left(1 - \frac{\tilde{a}^2}{\tilde{c}_{11}\tilde{c}_{33}}\right)\alpha^2\right)} \,, \tag{K.31}$$

which yields

$$\left[1 - \left(1 - \frac{\tilde{a}^2}{\tilde{c}_{11}\tilde{c}_{33}}\right) X\right] Z = 1 - X \,, \tag{K.32}$$

when carrying out the change of variables (5.8). The dispersion relation defines the slowness surface (γ_1 as a function of $-\mathrm{i}\alpha$), and hence the phase velocity, as the reciprocal of the slowness. Figure K.1(a) illustrates the relative error between the approximate phase velocity given by equation (5.11) and the exact dispersion relation using the measured moduli of Greenhorn shale (Jones & Wang, 1981); the stiffness coefficients in $(\mathrm{km/s})^2$ are

$$c_{11} = 14.47 \,, \quad c_{33} = 9.57 \,, \quad c_{55} = 2.28 \,, \quad c_{13} = 4.51 \,.$$

See also the papers by Alkhalifah (1998a; 1998b).

K.3 Polarization angle

Here, we study the (micro-local) behavior of the polarization vector. Upon applying a Fourier transform in the spatial coordinates, x_1 and x_3, and a Laplace transform in time, t, to system (K.22) thus replacing ∂_t, ∂_3, and ∂_1 by their respective symbols, s^2, $-s\gamma_1$, and $-\mathrm{i}s\alpha$, we can derive the polarization angle, Υ, of the qP wave in the framework of the

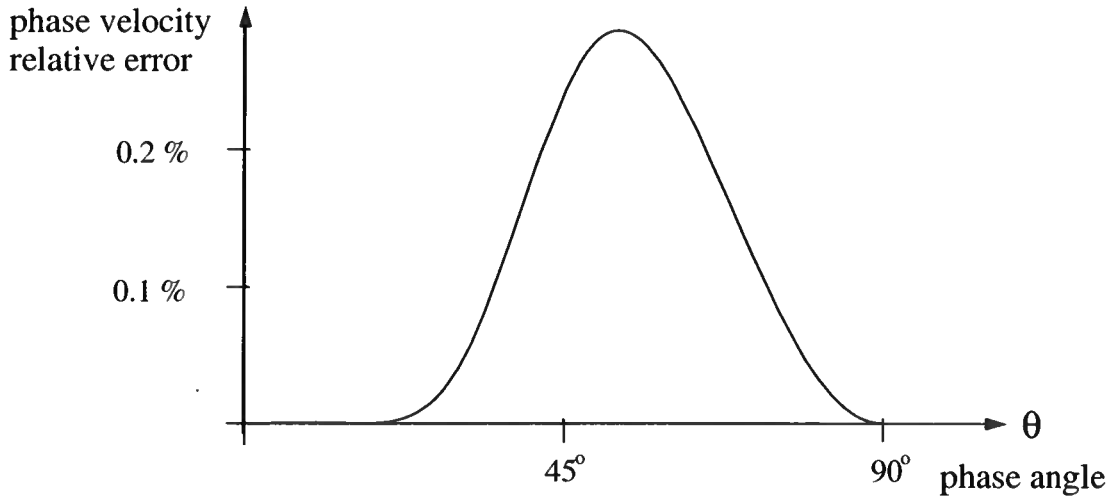

(a)

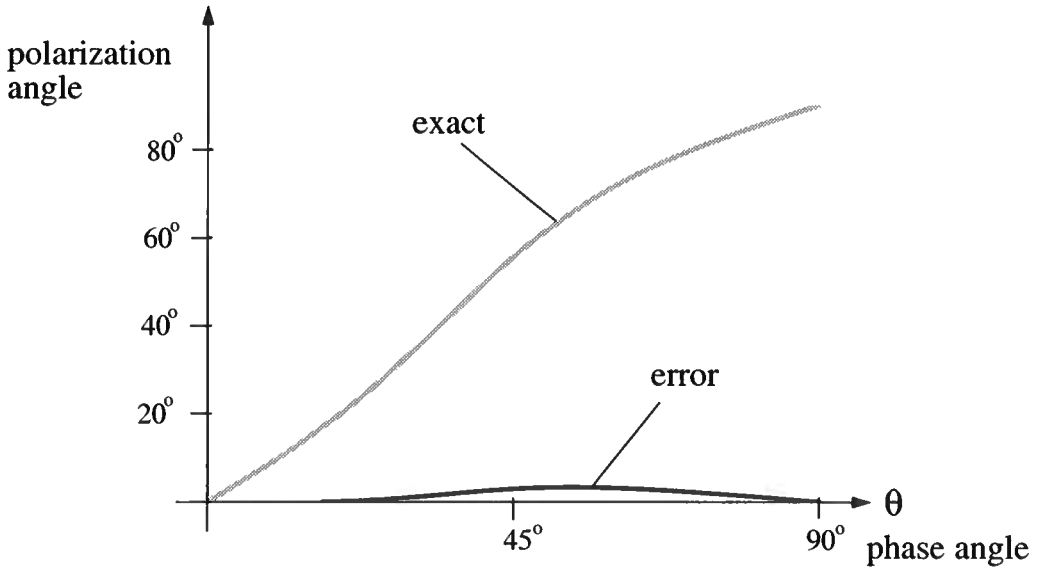

(b)

Figure K.1. (a) Relative error between the approximate phase velocity as given by dispersion relation (5.11) and the exact phase velocity as a function of the phase angle θ, in the case of Greenhorn shale. (b) Gray curve: exact polarization angle as a function of the phase angle θ, in the case of Greenhorn shale; black curve: Error in degrees between the approximate polarization angle as given equation (K.33) and the exact polarization angle.

approximation proposed by Schoenberg and De Hoop (2000)

$$\tan \Upsilon = \frac{u_1}{u_3} = \frac{\mathrm{i}\alpha\gamma_1\tilde{a}}{1+\tilde{c}_{11}\alpha^2} \,. \tag{K.33}$$

Note that the polarization angle given by equation (K.33) is the limit of the exact polarization angle in VTI media for the qP wave (Tsvankin, 1996, (42)) when applying transformations (K.4) and (K.5). In the current notation, the exact polarization angle is indeed given by

$$\tan \Upsilon^e = \frac{(\tilde{c}_{13}+\tilde{c}_{55})\mathrm{i}\alpha\gamma_1}{1+\tilde{c}_{11}\alpha^2-\tilde{c}_{55}\gamma_1^2} \,. \tag{K.34}$$

Figure K.1(b) illustrates the degree of accuracy offered by the approximation proposed by Schoenberg and De Hoop (2000) for the polarization angle in the case of Greenhorn shale (Jones & Wang, 1981).

From the value of the polarization angle in the 'mild' anisotropy approximation, Υ, we can recover the exact polarization angle, Υ^e, as

$$\tan \Upsilon^e = \frac{(c_{13}+c_{55})\mathrm{i}\alpha\gamma_1^e}{\mathrm{i}\alpha a\gamma_1 - c_{55}(\gamma_1^e)^2 \tan \Upsilon} \tan \Upsilon \,, \tag{K.35}$$

where γ_1^e is the vertical slowness principal symbol in the exact VTI case. Using the fact that $\gamma_1 \simeq \gamma_1^e$, i.e., that the dispersion relation is weakly affected by the present approximation, this relation simplifies to

$$\tan \Upsilon^e = \frac{(c_{13}+c_{55})\mathrm{i}\alpha}{\mathrm{i}\alpha a - c_{55}\gamma_1 \tan \Upsilon} \tan \Upsilon \,. \tag{K.36}$$

The fractional term can be shown to be quasi insensitive to transformations (K.4) and (K.5) in the case of 'mild' anisotropy.

Appendix L

Directional decomposition of the wavefield in the 'acoustic' VTI approximation

L.1 Characteristic equation for the vertical slowness operator

Directional wavefield decomposition maps the 'two-way' wavefield into counterpropagating constituents that satisfy a coupled system of 'one-way' wave equations. The directional decomposition procedure exposed in De Hoop (1996) can readily be applied to the equivalent 'acoustic' system of equations (K.22) derived in Appendix A. In the time-Laplace (s) domain, the one-way wave operators follow as

$$\partial_3 \pm s\Gamma \,, \tag{L.1}$$

where Γ is obtained from the characteristic equation, $\Gamma^2 = \mathrm{A}$, and is given by

$$\Gamma = \mathrm{A}^{\frac{1}{2}} \,, \tag{L.2}$$

where A is called the transverse Helmholtz operator and is here given by

$$\mathrm{A} = \left\{ \frac{1}{c_{33}}\rho - \frac{a}{c_{33}}\partial_1 O^{-1}\left[\partial_1\left(\frac{a}{c_{33}}\rho\,\cdot\right)\right]\right\} \,. \tag{L.3}$$

The characteristic equation (L.2) transforms into a characteristic equation for left symbols:

$$\exp\left[-\mathrm{i}\,\partial_{\alpha'} D_{x_1'}\right]\ \gamma(x_1;\alpha')\gamma(x_1';\alpha)\Big|_{(x_1',\alpha')=(x_1,\alpha)} = \mathrm{a}(x_1;\alpha) \,, \tag{L.4}$$

as given by symbol calculus of pseudodifferential operators (Treves, 1980a; Hörmander, 1985a; De Hoop, 1996, equation (A12)). In this paper, we freeze the medium locally, i.e., we apply a 'high-frequency' approximation; then the symbols γ and a reduce to their principal parts γ_1 and a_2 respectively. Up to principal symbols, this characteristic equation thus becomes the dispersion relation

$$\gamma_1^2 = \mathrm{a}_2 = \frac{1 + \tilde{c}_{11}\alpha^2}{\tilde{c}_{33}\left(1 + \left(1 - \frac{\tilde{a}^2}{\tilde{c}_{11}\tilde{c}_{33}}\right)\alpha^2\right)} \,. \tag{L.5}$$

This explains the subscript 1 in γ_1 in the dispersion relation (5.6). The symbol γ_1 is the vertical component of the slowness vector and hence we can then interpret Γ as the *vertical slowness* operator.

L.2 Mapping between acoustic field matrix components and observable

To obtain the equivalent 'acoustic' system, we have used a pseudo-pressure that is not observable. The introduction of p allows a wavefield decomposition. Yet, as given by equation (K.10), we can map the two field matrix components, p and v_3, to the particle velocity according to:

$$v_3 = v_3 \,, \tag{L.6}$$

$$\partial_1 v_1 = -\frac{1}{a}\partial_t p - \frac{c_{33}}{a}\partial_3 v_3 \,, \tag{L.7}$$

with appropriate initial conditions.

Appendix M

Second term of the polyhomogeneous expansion of the right symbol of the characteristic operator

Here, we show the term $a_{r[1]}$. It is computed with the aid of equation (7.46). we have $a_{r[1]} = (a_{r,ij_{[1]}})$ where

$$
\begin{aligned}
a_{r,11_{[1]}} &= -\rho^{-1}(D_2\rho)\mathrm{i}\alpha_2 + [2\kappa_S^{-1}\rho^{-1}\kappa_P - 3\rho^{-1}](D_1\rho)\mathrm{i}\alpha_1 - 2\kappa_S^{-1}(D_1\kappa_P)\mathrm{i}\alpha_1 \qquad \text{(M.1)}\\
&\quad +[4\kappa_S^{-2}\kappa_P - \kappa_S^{-1}](D_1\kappa_S)\mathrm{i}\alpha_1 \,,\\
a_{r,12_{[1]}} &= [\kappa_S^{-1}\rho^{-1}\kappa_P - \rho^{-1}](D_2\rho)\mathrm{i}\alpha_1 + [\kappa_S^{-1}\rho^{-1}\kappa_P + \rho^{-1}](D_1\rho)\mathrm{i}\alpha_2 \qquad \text{(M.2)}\\
&\quad -2\kappa_S^{-1}(D_2\kappa_P)\mathrm{i}\alpha_1 + [5\kappa_S^{-2}\kappa_P - \kappa_S^{-1}](D_2\kappa_S)\mathrm{i}\alpha_1 - \kappa_S^{-2}\kappa_P(D_1\kappa_S)\mathrm{i}\alpha_2 \,,\\
a_{r,13_{[1]}} &= \Big[-(8(D_2\kappa_P) + 2(D_2\kappa_S))\,\kappa_S^{-3/2}\rho^{-1/2} + 12\kappa_S^{-5/2}\rho^{-1/2}\kappa_P(D_2\kappa_S) \qquad \text{(M.3)}\\
&\quad +4\kappa_S^{-3/2}\rho^{-3/2}\kappa_P(D_2\rho) - 4\kappa_S^{-1/2}\rho^{-3/2}(D_2\rho)\Big]\,\alpha_1\alpha_2\\
&\quad + \Big[-8\kappa_S^{-3/2}\rho^{-1/2}(D_1\kappa_P) + 10\kappa_S^{-5/2}\rho^{-1/2}\kappa_P(D_1\kappa_S)\\
&\quad +6\kappa_S^{-3/2}\rho^{-3/2}\kappa_P(D_1\rho) - 6\kappa_S^{-1/2}\rho^{-3/2}(D_1\rho)\Big]\,\alpha_1^2\\
&\quad + \Big[-2\kappa_S^{-5/2}\rho^{-1/2}\kappa_P(D_1\kappa_S) - 2\kappa_S^{-3/2}\rho^{-1/2}(D_1\kappa_S) + 2\kappa_S^{-3/2}\rho^{-3/2}\kappa_P(D_1\rho)\\
&\quad -2\kappa_S^{-1/2}\rho^{-3/2}(D_1\rho)\Big]\,\alpha_2^2 - \kappa_S^{-3/2}\rho^{1/2}\kappa_P(D_1\kappa_S) + \kappa_S^{-1/2}\rho^{1/2}(D_1\kappa_S)\\
&\quad +\kappa_S^{-1/2}\rho^{-1/2}\kappa_P(D_1\rho) \,,\\
a_{r,31_{[1]}} &= -\kappa_S^{-1/2}\rho^{1/2}(D_1\kappa_P) + 2\kappa_S^{-3/2}\kappa_P\rho^{1/2}(D_1\kappa_S) \,, \qquad \text{(M.4)}\\
a_{r,33_{[1]}} &= 4(\kappa_S^{-1} - \kappa_S^{-2}\kappa_P)[(D_1\kappa_P)\mathrm{i}\alpha_1 + (D_2\kappa_P)\mathrm{i}\alpha_2] \,. \qquad \text{(M.5)}
\end{aligned}
$$

Appendix N

Higher-order terms in the expansion of the right symbol of A in medium contrast and smoothness

Here, we show higher-order terms in the polyhomogeneous expansion of the right symbol of the characteristic operator, A. The term $a^{[1]}_{[2]} = (a_{r,ij}{}^{[1]}_{[2]})$, first order in medium contrast, zero order in operator order, is given by

$$a_{r,11}{}^{[1]}_{[2]} = -2[c_P^0]^{-2}[c_S^0]^2\alpha_1^2\epsilon_P + \left([c_S^0]^{-2} + 2[c_P^0]^{-2}[c_S^0]^2\alpha_1^2\right)\epsilon_S + [c_S^0]^{-2}\epsilon_\rho\,, \tag{N.1}$$

$$a_{r,12}{}^{[1]}_{[2]} = -2[c_P^0]^{-2}[c_S^0]^2\alpha_1\alpha_2(\epsilon_P - \epsilon_S)\,, \tag{N.2}$$

$$\begin{aligned} a_{r,13}{}^{[1]}_{[2]} = {} & \left(4[c_P^0]^{-2}[c_S^0]^3\mathrm{i}(\alpha_1^3 + \alpha_1\alpha_2^2) + 2[c_P^0]^{-2}c_S^0\mathrm{i}\alpha_1\right)\epsilon_P \\ & + \left(2([c_S^0]^{-2} - 3[c_P^0]^{-2})[c_S^0]^3\mathrm{i}(\alpha_1^3 + \alpha_1\alpha_2^2) - [c_S^0]^{-1}\mathrm{i}\alpha_1 - [c_P^0]^{-2}c_S^0\mathrm{i}\alpha_1\right)\epsilon_S \\ & + \left(2[c_{PS}^0]^{-2}[c_S^0]^3\mathrm{i}(\alpha_1^3 + \alpha_1\alpha_2^2) + [c_P^0]^{-2}c_S^0\mathrm{i}\alpha_1 - [c_S^0]^{-1}\mathrm{i}\alpha_1\right)\epsilon_\rho\,, \end{aligned} \tag{N.3}$$

$$\begin{aligned} a_{r,31}{}^{[1]}_{[2]} = {} & -\left(\tfrac{1}{2}c_S^0[c_P^0]^{-2} + \tfrac{1}{2}[c_S^0]^{-1}\right)\mathrm{i}\alpha_1\epsilon_S + [c_P^0]^{-2}c_S^0\mathrm{i}\alpha_1\epsilon_P \\ & -\tfrac{1}{2}[c_{PS}^0]^{-2}c_S^0\mathrm{i}\alpha_1\epsilon_\rho\,, \end{aligned} \tag{N.4}$$

$$a_{r,33}{}^{[1]}_{[2]} = [c_P^0]^{-2}(\epsilon_P + \epsilon_\rho) + 2[c_P^0]^{-2}[c_S^0]^2(\alpha_1^2 + \alpha_2^2)(\epsilon_P - \epsilon_S)\,. \tag{N.5}$$

The term $a^{[2]}_{[2]} = (a_{r,ij}{}^{[2]}_{[2]})$, second order in medium contrast, zero order in operator order, is given by

$$
\begin{aligned}
a_{r,11}{}^{[2]}_{[2]} &= 2[c_P^0]^{-2}[c_S^0]^2\alpha_1^2\epsilon_S(\epsilon_P-\epsilon_S)+[c_S^0]^{-2}\epsilon_S\epsilon_\rho\,, && \text{(N.6)}\\
a_{r,12}{}^{[2]}_{[2]} &= 2[c_P^0]^{-2}[c_S^0]^2\alpha_1\alpha_2\epsilon_S(\epsilon_P-\epsilon_S)\,, && \text{(N.7)}\\
a_{r,13}{}^{[2]}_{[2]} &= \tfrac{1}{4}(3[c_P^0]^{-2}+[c_S^0]^{-2})c_S^0\mathrm{i}\alpha_1\epsilon_S^2 && \text{(N.8)}\\
&\quad +\tfrac{1}{2}(15[c_P^0]^{-2}-[c_S^0]^{-2})[c_S^0]^3\mathrm{i}(\alpha_1^3+\alpha_1\alpha_2^2)\epsilon_S^2\\
&\quad -\tfrac{1}{2}([c_P^0]^{-2}+[c_S^0]^{-2})c_S^0\mathrm{i}\alpha_1\epsilon_S\epsilon_\rho\\
&\quad +(3[c_P^0]^{-2}-[c_S^0]^{-2}))[c_S^0]^3\mathrm{i}(\alpha_1^3+\alpha_1\alpha_2^2)\epsilon_S\epsilon_\rho\\
&\quad -[c_P^0]^{-2}(c_S^0\mathrm{i}\alpha_1+6[c_S^0]^3\mathrm{i}(\alpha_1^3+\alpha_1\alpha_2^2))\epsilon_P\epsilon_S\\
&\quad +[c_{PS}^0]^{-2}(-\tfrac{1}{4}c_S^0\mathrm{i}\alpha_1+\tfrac{3}{2}[c_S^0]^3\mathrm{i}(\alpha_1^3+\alpha_1\alpha_2^2))\epsilon_\rho^2\,,\\
a_{r,31}{}^{[2]}_{[2]} &= \tfrac{1}{2}[c_P^0]^{-2}c_S^0\mathrm{i}\alpha_1\epsilon_P(\epsilon_\rho-\epsilon_S)+(\tfrac{1}{8}[c_S^0]^{-2}+\tfrac{3}{8}[c_P^0]^{-2})c_S^0\mathrm{i}\alpha_1\epsilon_S^2 && \text{(N.9)}\\
&\quad -(\tfrac{1}{4}[c_S^0]^{-2}+\tfrac{1}{4}[c_P^0]^{-2})c_S^0\mathrm{i}\alpha_1\epsilon_S\epsilon_\rho-\tfrac{1}{8}[c_{PS}^0]^{-2}c_S^0\mathrm{i}\alpha_1\epsilon_\rho^2\,,\\
a_{r,33}{}^{[2]}_{[2]} &= [c_P^0]^{-2}\epsilon_P\epsilon_\rho+2[c_P^0]^{-2}[c_S^0]^2(\alpha_1^2+\alpha_2^2)\epsilon_S(\epsilon_S-\epsilon_P)\,. && \text{(N.10)}
\end{aligned}
$$

The term $a^{[1]}_{[1]} = (a_{r,ij}{}^{[1]}_{[1]})$, first order in medium contrast, first order in operator order, is given by

$$
\begin{aligned}
a_{r,11}{}^{[1]}_{[1]} &= 2[c_P^0]^{-2}[c_S^0]^2(2D_1\epsilon_S+D_1\epsilon_P)\mathrm{i}\alpha_1\epsilon_P && \text{(N.11)}\\
&\quad +[c_P^0]^{-2}\left[[c_P^0]^2D_1\epsilon_S+2[c_S^0]^2(D_1\epsilon_P-4D_1\epsilon_S-D_1\epsilon_\rho)\right]\mathrm{i}\alpha_1\epsilon_S\\
&\quad +\left[(3-2[c_P^0]^{-2}[c_S^0]^2)(D_1\epsilon_\rho)\mathrm{i}\alpha_1+(D_2\epsilon_\rho)\mathrm{i}\alpha_2\right]\epsilon_\rho\,,\\
a_{r,12}{}^{[1]}_{[1]} &= [c_P^0]^{-2}[c_S^0]^2\left[(5D_2\epsilon_P+D_2\epsilon_\rho)\mathrm{i}\alpha_1+(D_1\epsilon_\rho-D_1\epsilon_S)\mathrm{i}\alpha_2\right]\epsilon_P && \text{(N.12)}\\
&\quad +[c_P^0]^{-2}\left[[c_P^0]^2(D_2\epsilon_S)\mathrm{i}\alpha_1+[c_S^0]^2(2D_2\epsilon_P-10D_2\epsilon_S-D_2\epsilon_\rho)\mathrm{i}\alpha_1\right.\\
&\quad \left.+[c_S^0]^2(2D_1\epsilon_P-D_1\epsilon_\rho)\mathrm{i}\alpha_1\right]\epsilon_S\\
&\quad -[c_S^0]^2[c_{PS}^0]^{-2}\left[(D_2\epsilon_\rho)\mathrm{i}\alpha_1+(D_1\epsilon_\rho)\mathrm{i}\alpha_2\right]\epsilon_\rho\,,
\end{aligned}
$$

$$
\begin{aligned}
a_{r,13}{}^{[1]}_{[1]} \;=\; & c_S^0[c_P^0]^{-2}\Big[4[c_S^0]^2(3D_2\epsilon_S + D_2\epsilon_\rho)\alpha_1\alpha_2 - D_1\epsilon_S(1-2[c_S^0]^2(5\alpha_1^2-\alpha_2^2)) \\
& +D_1\epsilon_\rho(1+2[c_S^0]^2(3\alpha_1^2+\alpha_2^2))\Big]\,\epsilon_P \\
& +\tfrac{1}{2}[c_P^0]^{-2}[c_S^0]^{-1}\Big[-[c_S^0]^2\Big(12[c_S^0]^2\alpha_1(-2D_1\epsilon_P\alpha_1 + (5D_2\epsilon_S - 2D_2\epsilon_P + D_2\epsilon_\rho)\alpha_2) \\
& +(D_1\epsilon_S)(-3+10[c_S^0]^2(5\alpha_1^2-\alpha_2^2)) + (D_1\epsilon_\rho)(1+6[c_S^0]^2(3\alpha_1^2+\alpha_2^2))\Big) \\
& +[c_P^0]^2\Big((D_1\epsilon_S)(-1+6[c_S^0]^2\alpha_1^2) + 2[c_S^0]^2[(3D_2\epsilon_S + 2D_2\epsilon_\rho)\alpha_1\alpha_2 \\
& +(D_1\epsilon_\rho)(3\alpha_1^2+\alpha_2^2)]\Big)\Big]\,\epsilon_S \\
& +\tfrac{1}{2}[c_P^0]^{-2}[c_S^0]^{-1}\Big[-[c_S^0]^2\Big(-8[c_S^0]^2(D_1\epsilon_P)\alpha_1^2 \\
& -4[c_S^0]^2(2D_2\epsilon_P - 3(D_2\epsilon_S + D_2\epsilon_\rho))\alpha_1\alpha_2 \\
& +(D_1\epsilon_S)(1+2[c_S^0]^2(5\alpha_1^2-\alpha_2^2)) + (D_1\epsilon_\rho)(1+6[c_S^0]^2(3\alpha_1^2+\alpha_2^2))\Big) \\
& +[c_P^0]^2\Big((D_1\epsilon_S)(1+2[c_S^0]^2\alpha_1^2) \\
& +2[c_S^0]^2((D_2\epsilon_S + 6D_2\epsilon_\rho)\alpha_1\alpha_2 + 3(D_1\epsilon_\rho)(3\alpha_1^2+\alpha_2^2))\Big)\Big]\,\epsilon_\rho\,,
\end{aligned}
\tag{N.13}
$$

$$
a_{r,31}{}^{[1]}_{[1]} \;=\; [c_P^0]^{-2}c_S^0\Big(2(D_1\epsilon_S)\epsilon_P + \tfrac{1}{2}(D_1\epsilon_P - 6D_1\epsilon_S)\epsilon_S - \tfrac{1}{2}(D_1\epsilon_P - 2D_1\epsilon_S)\epsilon_\rho\Big)\,, \tag{N.14}
$$

$$
\begin{aligned}
a_{r,33}{}^{[1]}_{[1]} \;=\; & 4[c_P^0]^{-2}[c_S^0]^2\Big([(D_1\epsilon_S)\mathrm{i}\alpha_1 + (D_2\epsilon_S)\mathrm{i}\alpha_2]\,\epsilon_P \\
& -[(D_1\epsilon_P - 2D_1\epsilon_S)\mathrm{i}\alpha_1 + (D_2\epsilon_P - 2D_2\epsilon_S)\mathrm{i}\alpha_2]\epsilon_S\Big)\,.
\end{aligned}
\tag{N.15}
$$

Appendix O

Second-order term in medium contrast of the principal part of the vertical slowness symbol

The evaluation of $\vartheta^{[2]}_{[1]} = (\vartheta_{ij}{}^{[2]}_{[1]})$, according to (7.76), results in

$$\vartheta_{11}{}^{[2]}_{[1]} = -\frac{1}{2\pi^0_{11}}\left[\frac{[c^0_S]^{-4}(\epsilon_S+\epsilon_\rho)^2}{4[\pi^0_{11}]^2} - [c^0_S]^{-2}\epsilon_S\epsilon_\rho + ([c^0_S]^2 - [c^0_P]^2)(\alpha_\nu\alpha_\nu)\right.$$
$$\left.\times(1-2[c^0_S]^2(\alpha_\nu\alpha_\nu))\left(\tfrac{1}{2}[c^0_P]^{-2}(\epsilon_S+\epsilon_\rho)^2 - [c^0_{PS}]^{-2}\frac{[c^0_P]^{-2}}{2(\pi^0_{11}+\pi^0_{33})^2}(\epsilon_\rho+\epsilon_S)^2\right)\right],$$

$$\vartheta_{13}{}^{[2]}_{[1]} = \frac{\sqrt{\alpha_\nu\alpha_\nu}}{\pi^0_{11}+\pi^0_{33}}\left[[c^0_P]^{-2}c^0_S\left(\epsilon_S\epsilon_P+\epsilon_P^2+\epsilon_P\epsilon_\rho\right) + [c^0_S]^{-1}\epsilon_S\epsilon_\rho\right.$$
$$+c^0_S[c^0_{PS}]^{-2}(1-4[c^0_S]^2(\alpha_\nu\alpha_\nu))\left(\tfrac{1}{4}\epsilon_S^2+\tfrac{1}{2}\epsilon_S\epsilon_\rho+\tfrac{1}{4}\epsilon_\rho^2\right)$$
$$\left.-\frac{c^0_S[c^0_{PS}]^{-2}}{2\pi^0_{11}(\pi^0_{11}+\pi^0_{33})}\left([c^0_P]^{-2}(\epsilon_S+\epsilon_\rho)(\epsilon_P+\epsilon_\rho)+[c^0_S]^{-2}(\epsilon_S+\epsilon_\rho)^2\right)\right],$$

$$\vartheta_{22}{}^{[2]}_{[1]} = \frac{1}{2\pi^0_{22}}\left[[c^0_S]^{-2}\epsilon_S\epsilon_\rho + \frac{[c^0_S]^{-4}(\epsilon_S+\epsilon_\rho)^2}{4[\pi^0_{22}]^2}\right],$$

$$
\begin{aligned}
\vartheta_{31}{}^{[2]}_{[1]} &= \frac{\sqrt{\alpha_\nu \alpha_\nu}}{\pi^0_{11}+\pi^0_{33}} \Bigg[\tfrac{1}{2}[c^0_P]^{-2} c^0_S(-1+2[c^0_S]^2(\alpha_\nu\alpha_\nu))\epsilon_S\epsilon_P \\
&\quad -\tfrac{1}{8}c^0_S[c^0_{PS}]^{-2}(1+6[c^0_S]^2(\alpha_\nu\alpha_\nu)-8[c^0_S]^4(\alpha_\nu\alpha_\nu)^2)(\epsilon_S\epsilon_\rho)^2 \\
&\quad +\tfrac{1}{2}(1-2[c^0_S]^2(\alpha_\nu\alpha_\nu))\left([c^0_P]^{-2}c^0_S(\epsilon_S^2-\epsilon_P\epsilon_\rho)+[c^0_S]^{-1}\epsilon_S\epsilon_\rho\right) \\
&\quad +\frac{c^0_S[c^0_{PS}]^{-2}(1-2[c^0_S]^2(\alpha_\nu\alpha_\nu))}{4\pi^0_{11}(\pi^0_{11}+\pi^0_{33})} \\
&\qquad \times\left([c^0_P]^{-2}(\epsilon_S+\epsilon_\rho)(\epsilon_P+\epsilon_\rho)+[c^0_S]^{-2}(\epsilon_S+\epsilon_\rho)^2\right)\Bigg] , \\
\vartheta_{33}{}^{[2]}_{[1]} &= -\frac{1}{2\pi^0_{33}}\Bigg[\frac{[c^0_P]^{-4}(\epsilon_P+\epsilon_\rho)^2}{4[\pi^0_{33}]^2}-[c^0_P]^{-2}\epsilon_P\epsilon_\rho-([c^0_S]^2-[c^0_P]^2)(\alpha_\nu\alpha_\nu) \\
&\quad \times(1-2[c^0_S]^2(\alpha_\nu\alpha_\nu))\left(\tfrac{1}{2}[c^0_P]^{-2}(\epsilon_S+\epsilon_\rho)^2+[c^0_{PS}]^{-2}\frac{[c^0_P]^{-2}}{2(\pi^0_{11}+\pi^0_{33})^2}(\epsilon_\rho+\epsilon_S)^2\right)\Bigg] .
\end{aligned}
$$

This term builds up the second-order GS approximation.